Experimental Studies of the Effects of Magnetic Fields on Radical Recombination Reactions in Vesicular and Micellar Environments



Philip G. Thomas

A Thesis presented for the degree of Doctor of Philosophy

Wolfson College

Trinity Term 2004



EXPERIMENTAL STUDIES OF THE EFFECTS OF MAGNETIC FIELDS ON RADICAL RECOMBINATION REACTIONS IN VESICULAR AND MICELLAR ENVIRONMENTS

A Thesis Submitted for the Degree of Doctor of Philosophy

Philip G. Thomas

Wolfson College Trinity Term 2004

ABSTRACT

This thesis is concerned with an experimental study into the effects of weak static magnetic fields on radical recombination reactions, weak magnetic fields being defined as those which are similar to the average hyperfine coupling of the radical pair. It is the aim of this thesis to examine the effect of these weak magnetic fields on the recombination reactions of neutral radical pairs, as influenced by the microenvironments in which they are created, using the technique of time resolved optical absorption spectroscopy.

In the introductory chapters the theoretical concepts underlying the phenomenon of magnetic field effects (MFEs) are presented, and experimental methods applied to study these effects are discussed. A variety of structures used to confine the radical pairs after creation are introduced, and their relevant properties are listed. A discussion of the experimental apparatus used to study the MFEs in neutral radical pairs is presented, alongside the methods used for data analysis.

The opening two results chapters are concerned with neutral radical pairs contained in synthetic micelles. A variety of minor alterations to both the radical pair and the micelle structure are introduced, such as addition of hydrogen donor molecules to the micelle, and deuteration of one or both members of the radical pair. An experimental investigation is also presented which tests the theoretical prediction that changing the magnetic field strength from absolute zero magnetic field to a very weak field will lead to a large alteration in radical recombination rate.

For the first time at weak magnetic field strengths MFEs are demonstrated in synthetic vesicles, and optimised as a function of concentration and temperature, both above and below the phase transition temperature of the vesicle.

Lysophospholipid micelles, formed by phospholipid derivatives are investigated, and form a stepping stone between the synthetic micelles and vesicles investigated in earlier chapters and the biologically relevant vesicles formed by phospholipid molecules. A new probe molecule is introduced, and the MFEs are investigated as a function of chemical concentration and solution temperature.

Finally, MFEs are investigated in phospholipid vesicles. Experiments are performed in systems of differing chemical composition, and the effect of solution preparation is evaluated.

ACKNOWLEDGEMENTS

Firstly I would like to extend a huge thank-you to Chris for everything over the past five years. Hopefully being your first supervisee hasn't put you off too much for the future. Thanks for the support, the explanations, and the advice above and beyond the call of duty.

For my studentship, financial support, and some interesting conferences in London, I am grateful to acknowledge the EMF Biological research Trust.

I also want to thank all the people in the lab who have contributed to this work, and made my time there more enjoyable. Keith, Rob, and Esther all put in a vast amount to the experimental side of things. Ailsa provided theoretical simulations and some very good meals, Chris R supplied the computational know-how behind the kinetic simulations. Janet was an excellent 'next desk neighbour' and always somebody to talk to. Nic provided a whole bunch of good meals, and also a floor, which I am very grateful for. Iain produced a lot of cake and jokes of questionable humour. Anthony provided his own unique contribution. There are many more people who have been members of the CRT/PJH groups during my time in the lab, and not enough room to thank them all individually.

I think Pid deserves his own special section, as the last five years would have been immeasurably less fun and interesting without his input. All the places we went, and the stuff we did was boony, what more can I say.

My parents deserve a huge thank-you for all the love and support they have shown me over my time in Oxford, and I am very happy to be able to do so here. This wouldn't have been possible without you both.

Finally I would like to acknowledge Em, for everything. It's much too hard to fit it all into such a small space, but there's no way I would have achieved this, or so many other things, without you.

CONTENTS

		PAGE
	Abstract	i
	Acknowledgements	ii
	Table of Contents	iii
	List of Figures	vii

CHAPTER 1	INTRODUCTION	PAGE	1
1.1	**Radicals**		2
1.1.1	Radical Pairs		4
1.1.2	The Exchange and Dipolar Interactions		7
1.1.3	The Vector Model		10
1.2	**The Radical Pair Mechanism**		12
1.2.1	Coherent Spin Mixing		13
1.2.2	Incoherent Spin Mixing		18
1.2.3	The Role of Diffusion		20
1.2.4	Geminate and F Pairs		21
1.2.5	The Reaction Scheme		24
1.3	**Weak Magnetic Fields**		26
1.3.1	MFEs at Different Magnetic Field Strengths		26
1.3.2	The Low Field Effect		28
1.4	**Experimental Strategies for Observing MFEs**		32

CHAPTER 2	STRUCTURES OF MICELLES AND VESICLES	PAGE	35
2.1	**The Hydrophobic Effect**		36
2.2	**Micelles**		37
2.2.1	Adding Substrates to Micelles		40
2.2.2	Synthetic Micelles – Negatively Charged Head Groups		41
2.2.3	Synthetic Micelles – Positively Charged Head Groups		42
2.2.4	'Biological' Micelles		43
2.2.5	Properties of Micelles		44
2.3	**Vesicles**		45
2.3.1	Phase Transitions in Vesicles		47
2.3.2	Synthetic Vesicles		48
2.3.3	Biological Vesicles		50
2.3.4	Properties of Vesicles		51

CHAPTER 3	METHODS AND MATERIALS	PAGE	54
3.1	**Concentration and Extinction Coefficient**		56
3.2	**Experimental Apparatus**		56
3.3	**Solution Preparation**		59
3.4	**Absorption Specificity**		60
3.5	**Typical Measurements and Results**		63
3.5.1	Manually Calculated MFEs		67
3.6	**Evolution of the Experiment**		68
3.6.1	The Cell		69
3.6.2	The Lamp		72
3.7	**Experimental Uncertainties**		72
3.8	**Kinetic Analysis**		73
3.8.1	Effects of Rate Constants		79
3.8.2	Fractional Lifetimes		81

CHAPTER 4	SYNTHETIC MICELLES – NEGATIVELY CHARGED HEAD GROUPS	PAGE	83
4.1	**Experimental Section**		83
4.1.1	Abbreviations Used in this Chapter		84
4.2	**Hydrogen Donors**		84
4.3	**Deuteration**		96
4.3.1	SDS/BP		98
4.3.2	SDS/BP/THF		101
4.3.3	SDS/BP/PrOH		105
4.4	**True Zero Magnetic Field**		108
4.4.1	Theoretical Model		109
4.4.2	Experimental Results		110
4.5	**Conclusions**		113

CHAPTER 5	SYNTHETIC MICELLES – POSITIVELY CHARGED HEAD GROUPS	PAGE	114
5.1	**Experimental Section**		114

5.2	**Carbon Chain Length**	115
5.2.1	Zero Field Results	115
5.2.2	Magnetic Field Effects	119
5.3	**Hydrogen Donors**	123
5.3.1	Hydrogen Donors with DTAC/BP	123
5.3.2	Hydrogen Donors with CTAC/BP	126
5.3.3	Comparing Chain Length Effects in the Presence of CHD	130
5.4	**Radical Quenchers**	133
5.5	**Conclusions**	136

CHAPTER 6	**SYNTHETIC VESICLES – DODAC**	**PAGE**	138

6.1	**Experimental Section**	138
6.1.1	Solution Preparation	139
6.1.2	Reproducibility	140
6.2	**Concentration Studies**	143
6.2.1	Time Curves	143
6.2.2	MARY Curves	148
6.3	**Hydrogen Donors**	151
6.3.1	Lower CHD Concentrations	155
6.4	**Looking for Low Field Effects**	157
6.5	**Temperature Effects**	159
6.6	**Conclusions**	162

CHAPTER 7	**BIOLOGICAL MICELLES – LYSOPHOSPHOLIPIDS**	**PAGE**	**163**

7.1	**Experimental Section**	163
7.1.1	Wavelength Studies	164
7.1.2	Buffered Solutions	164
7.2	**A Change of Probe Molecule**	165
7.2.1	Initial Experiments with BP	165
7.2.2	Experiments with 2-Benzoyl Thiophene	168
7.2.3	Using BT with Lysophospholipids	175
7.2.4	Experiments with BP-4F and BP-COOH	177
7.2.5	Solubility of BP-COOH	183
7.3	**Low Field Effects with BP-COOH**	186

7.4	**BP-COOH in LPC**	190
7.4.1	Initial Experiments	190
7.4.2	BP-COOH Concentration and Temperature Effects	192
7.4.3	LFE in LPC/BP-COOH	197
7.5	**Comparison Between SDS and LPC Micelles**	198
7.6	**Conclusions and Future Lysophospholipid Work**	201

CHAPTER 8 — BIOLOGICAL VESICLES – PHOSPHOLIPIDS — PAGE 203

8.1	**Experimental Section**	203
8.1.1	Purity and Nomenclature of Phospholipids	203
8.1.2	Solution Preparation	204
8.2	**Concentration of Phospholipids**	206
8.3	**Probe Molecules**	208
8.4	**Stronger Magnetic Fields**	209
8.4.1	Horseshoe Magnet	210
8.5	**Purity of Phospholipids**	215
8.6	**Experiments with PC_C Phospholipids**	218
8.7	**Conclusions and Future Phospholipid Work**	222

SUMMARY — PAGE 224

REFERENCES — PAGE 230

APPENDIX — PAGE 235

LIST OF FIGURES

CHAPTER 1	INTRODUCTION	
1.1	Energy dependence of singlet and triplet states on magnetic field strength	5
1.2	Energy dependence of singlet and triplet states on distance	8
1.3	Vector representation of radical pair spin states	11
1.4	The distinction between geminate and F pair recombination	22
1.5	Flow diagram of reaction scheme	25
1.6	Variation of S-T mixing with magnetic field strength	26

CHAPTER 2	STRUCTURES OF MICELLES AND VESICLES	
2.1	Cross-section through an anionic micelle	38
2.2	The structure of an SDS monomer	41
2.3	The generic structure of a trimethylammonium chloride monomer	42
2.4	The structure of an LPC monomer	43
2.5	The structure of a vesicle	46
2.6	The structure of a DODAC monomer	49
2.7	The structure of phosphatidyl choline monomer	50

CHAPTER 3	METHODS AND MATERIALS	
3.1	Flow diagram of experimental apparatus	57
3.2	The timing of the magnetic field and laser trigger signal	58
3.3	Transient absorption spectra of BP-COOH/MeCN, and SDS/BP-COOH	61
3.4	Typical time curve showing the two regions of radical recombination	64
3.5	Time curves showing how MFE is calculated	65
3.6	Typical MARY curve	66
3.7	Cross-section of original cell design	69
3.8	Depletion of signal during the course of an experiment	70
3.9	Cross-section of new cell design	71
3.10	Reaction scheme for kinetic analysis	75
3.11	Simulated time curves with fixed rate constants	80
3.12	Simulated time curves showing effect of changing individual rate constants	80

CHAPTER 4	SYNTHETIC MICELLES – NEGATIVELY CHARGED HEAD GROUPS	
4.1	Zero field time curves of SDS/BP with various hydrogen donors	87
4.2	Zero field time curve of SDS/BP/TEA at longer timescales	88
4.3	Zero field time curves of SDS/BP with various hydrogen donors	89
4.4	Normalised zero field time curves of SDS/BP with various hydrogen donors	90
4.5	MARY curves of SDS/BP with various hydrogen donors	95
4.6	Normalised zero field time curves of SDS/BP, and SDS/BP_{d10}	99
4.7	MARY curves of SDS/BP and SDS/BP_{d10}	100
4.8	Normalised zero field time curves of SDS/BP/THF showing effect of deuteration	101

4.9	MARY curves of SDS/BP/THF showing effect of deuteration	104
4.10	Zero field time curves of SDS/BP/PrOH and SDS/BP/$PrOH_{d8}$	106
4.11	MARY curves of SDS/BP/PrOH and SDS/BP/$PrOH_{d8}$	107
4.12	Simulation for one proton radical pair	109
4.13	Time curves of SDS/BP inside mu metal box	111

CHAPTER 5	**SYNTHETIC MICELLES – POSITIVELY CHARGED HEAD GROUPS**	
5.1	Normalised zero field time curves of BP in cationic micelles	116
5.2	MARY curves of BP in cationic micelles	120
5.3	Time curves of DTAC/BP and CTAC/BP at various magnetic field strengths	121
5.4	Effect of CHD on DTAC/BP	124
5.5	Effect of CHD and THF on CTAC/BP	127
5.6	Time curves of CTAC/BP/CHD at various magnetic fields strengths	129
5.7	Zero field time curves of BP/CHD in DTAC and CTAC micelles	130
5.8	MARY curves of BP/CHD in DTAC and CTAC micelles	132
5.9	MARY curves of SDS/BP showing effect of additional cations	133
5.10	MARY curves of DTAC/BP showing effect of additional cations	135

CHAPTER 6	**SYNTHETIC VESICLES – DODAC**	
6.1	Zero field time curves of DODAC/BP showing signal loss	140
6.2	Normalised zero field time curves of DODAC/BP showing signal loss	141
6.3	Effect of flowing sample through apparatus	142
6.4	Zero field time curves of 2 mM BP and DODAC at various concentrations	143
6.5	Normalised zero field time curves of 2 mM BP and DODAC at various concentrations	144
6.6	Normalised zero field time curves of 2.5 mM BP and DODAC at various concentrations	145
6.7	Zero field time curves of DODAC at various BP concentrations	146
6.8	Normalised zero field time curves of DODAC at various BP concentrations	147
6.9	MARY curves of 2 mM BP and DODAC at various concentrations	149
6.10	MARY curves of 2.5 mM BP and DODAC at various concentrations	149
6.11	MARY curves of DODAC at various BP concentrations	150
6.12	Zero field time curves of DODAC/BP showing effect of CHD	152
6.13	Normalised zero field time curves of DODAC/BP showing effect of CHD	153
6.14	MARY curves of DODAC/BP showing effect of CHD	154
6.15	Normalised zero field time curves of DODAC/BP showing effect of CHD	156
6.16	MARY curve of DODAC/BP concentrating on LFE region	157
6.17	Time curves of DODAC/BP concentrating on LFE region	158
6.18	Zero field time curves of DODAC/BP at 25 °C and 60 °C	160
6.19	MARY curves of DODAC/BP at 25 °C and 60 °C	161

CHAPTER 7	BIOLOGICAL MICELLES – LYSOPHOSPHOLIPIDS	
7.1	Zero field time curves of LPC/BP, DODAC/BP, and SDS/BP	165
7.2	MARY curve of LPC/BP	166
7.3	UV/vis absorption spectra of LPC and DODAC/BP	167
7.4	Structure of 2-benzoyl thiophene	168
7.5	Transient absorption spectra of SDS/BT, BT/MeCN, and SDS/BT/CHD	170
7.6	Transient absorption spectra of SDS/BT with excitation from XeCl and YAG lasers	171
7.7	MARY curves of SDS/BT and SDS/BT/CHD	172
7.8	Normalised transient absorption spectra of SDS/BT and SDS/BT/CHD	174
7.9	Time curves of LPC/BT/CHD at various magnetic field strengths	175
7.10	MARY curve of LPC/BT/CHD	176
7.11	Structures of BP-COOH and BP-4F	177
7.12	UV/vis absorption spectra of SDS/BP, SDS/BP-COOH, and SDS/BP-4F	178
7.13	Transient absorption spectra of SDS/BP-COOH and SDS/BP-4F	179
7.14	Transient absorption spectra of BP-COOH/MeCN and SDS/BP-COOH	180
7.15	Normalised transient absorption spectra of BP-COOH/MeCN and SDS/BP-COOH	181
7.16	Time curves of SDS/BP-COOH and SDS/BP-4F at various magnetic field strengths	182
7.17	Zero field time curves of SDS/BP-COOH at various pH values	184
7.18	MARY curves of SDS/BP-COOH at various pH values	185
7.19	MARY curve of SDS/BP-COOH concentrating on LFE region	187
7.20	Time curves of SDS/BP-COOH showing lack of LFE	188
7.21	Zero field time curves of LPC/BT/CHD and LPC/BP-COOH	190
7.22	Time curves of LPC/BP-COOH at various magnetic field strengths	191
7.23	MARY curve of LPC/BP-COOH	192
7.24	Zero field time curves of LPC/BP-COOH at two temperatures and two BP-COOH concentrations	195
7.25	Normalised zero field time curves of LPC/BP-COOH at two temperatures	196
7.26	MARY curve of LPC/BP-COOH concentrating on LFE region	197
7.27	Zero field time curves of SDS/BP-COOH and LPC/BP-COOH	198
7.28	MARY curves of SDS/BP-COOH and LPC/BP-COOH	200

CHAPTER 8	BIOLOGICAL VESICLES – PHOSPHOLIPIDS	
8.1	Zero field time curves of PC_A/BP-COOH at various PC_A concentrations	207
8.2	Zero field time curves of BP-COOH, BP-4F, and BT/CHD in PC_A	208
8.3	Configuration of horseshoe magnet in relation to cell	210
8.4	Time curves of PC_A/BP-COOH in absence and presence of permanent magnet	211
8.5	Time curves of SDS/BP-COOH in absence and presence of permanent magnet	213
8.6	Time curves of PC_A/BP-COOH/CHD and PC_A/BP-COOH/THF in absence and presence of permanent magnet	214
8.7	Zero field time curves of PC_A and PC_B with BP-COOH	215
8.8	Time curves for PC_B/BP-COOH at various magnetic field strengths	217
8.9	MARY curve of PC_B/BP-COOH	218
8.10	Zero field time curves of PC_B and PC_C with BP-COOH	219

8.11 Zero field time curve of PC_C/BP-COOH at longer timescales 220
8.12 Zero field time curves of PC_C/BP-COOH at two temperatures 221

SUMMARY

S1 Fractional lifetimes showing effect of CHD addition 226
S2 Correlation between $T_{3/4}$ and MFE size 227

1:INTRODUCTION

This thesis is concerned with the effect of magnetic fields on a certain class of chemical reactions, those that proceed through a radical pair intermediate. The effect of magnetic fields on this class of reaction has been well studied, and there are several reviews on the subject [1-5].

The effects of magnetic fields on chemical reactions have been of interest for a long time, but it is only comparatively recently that the theories governing these phenomena were proposed [6,7], and have been used to design experiments to investigate these effects. Most of the experimental and theoretical studies so far have focused on investigating the effects of strong magnetic fields [*e.g.* 1,8,9], but recently a lot of interest has been devoted to the study of the effect of much weaker magnetic fields (of the order of a few mT) [10-14]. There are numerous stimuli driving research into this area of science; there is concern about the potentially harmful impact of magnetic fields on human health, with public anxiety over the detrimental effects of mobile phones and overhead power lines. In 1998 the World Health Organisation estimated that concerns about electromagnetic fields and health cost the US economy US$ 1 billion [15]. A number of epidemiological studies on the potentially hazardous influence of overhead power lines and other sources of magnetic fields on human health have been undertaken [16-18] but so far without conclusive results.

Furthermore, magnetic fields are known to be involved in the navigation of animals [19,20]. The discussion as to which mechanism underlies these navigation phenomena is still ongoing, but recent research [21] has suggested that in some bird species (namely European robins) a magnetically sensitive chemical reaction underlies the avian magnetic compass. Several biological processes proceed through radical pair

intermediates, and magnetic fields have been found to influence some of these processes. The best studied of these are the radical species that form the electron transfer chain in the primary steps of photosynthesis (where magnetic field effects are observed when the forward electron transfer is blocked) [22]. Magnetic field effects have also been observed on enzymatic reactions which procede through radical pair intermediates, such as those involving ethanolamine ammonia lyase [23].

Most effects of magnetic fields on radical reactions have been observed, however, in non-biological systems, with a particular focus on systems in which the movement of the radical pair is confined in some way, either by caging the radicals in microreactors such as micelles [*e.g.* 24], hampering radical movement by working in high viscosity solvents [*e.g.* 25], or by using radical ion pairs which are held together by electrostatic forces [*e.g.* 26]. It is the aim of this work to shed some light on the significance of the confinement of the radicals by systematically changing their caging conditions. Studying the magnetic field effects as a function of the reaction medium will help in the design of future experiments, and facilitate the prediction of magnetic field effect dependence in known chemical and biological environments such as membranes.

This chapter introduces the concepts governing radical pair characteristics and discusses the behaviour of these species in both the absence and presence of applied magnetic fields.

1.1 Radicals

Radicals are defined as chemical species that contain an unpaired electron, and hence possess non-zero spin angular momentum. Consequently the energy of the radical is influenced by a magnetic field, in the same way as that of a free electron.

The spin of an electron is an intrinsic property, and is described as a type of angular momentum. Spin angular momentum is labelled with the quantum number s, with projection on the z-axis m_s, where the z-axis is normally taken to coincide with the direction of the applied magnetic field. The magnitude of the spin angular momentum is $(s(s+1))^{1/2}\hbar$, with m_s limited to $2s+1$ values. For an electron $s = ½$, so $m_s = +½$ or $-½$. The $+½$ state is referred to as the α state, and the $-½$ state is the β state.

The spin angular momentum of the electron causes a magnetic moment, μ, which is antiparallel to the spin angular momentum. For an electron, the magnetic moment due to its spin is given by:

$$\mu = -g_e\mu_B s \qquad (1.1)$$

where g_e is the g-value of a free electron, and μ_B is the Bohr magneton. The magnetic moment in the direction of an applied magnetic field is therefore given by:

$$\mu_z = -g_e\mu_B m_s. \qquad (1.2)$$

In a magnetic field the magnetic moments will align with the field direction so that they are either parallel or antiparallel to it. Hence when a magnetic field is applied the two states of an electron are no longer degenerate, and their energies are given by:

$$E = g_e\mu_B m_s B. \qquad (1.3)$$

The energy gap between the two states of the electron in a magnetic field is known as the Zeeman splitting,

$$\Delta E = E_\alpha - E_\beta = g_e \mu_B B. \qquad (1.4)$$

When the electron spin is due to the unpaired electron on a radical, and not a free electron, the magnetic field that it experiences will not necessarily be identical to the applied magnetic field. Additional magnetic fields, such as those caused by spin orbit coupling, or hyperfine interactions, contribute to the overall magnetic field experienced by the electron. The actual, local magnetic field experienced by the electron can be described as B_{loc}, which is made up of two components, the applied magnetic field, B_{app}, and the induced magnetic field, B_{ind}. This is usually accounted for by replacing g_e with g, so that the energy gap between the two states becomes:

$$\Delta E = g_e \mu_B B_{loc} = g_e \mu_B (B_{app} + B_{ind}) = g \mu_B B_{app} \qquad (1.5)$$

where g has a value specific to the radical in question. The g-value of a specific radical is not necessarily homogeneous around the unpaired electron, and hence the anisotropy can be described by replacing the g value with a three-dimensional tensor **g**.

1.1.1 Radical Pairs

Radicals are usually generated in pairs; a chemical bond is made of two electrons, so if a bond is broken homolytically, a radical pair (RP) is formed. RPs are also formed following electron transfer between non-radical species, following atom transfer, or when two radicals encounter. In a radical pair, when the radicals are close enough, their spins couple to each other and instead of considering each radical spin

individually, the spin state of the pair as a whole can be described. Each electron has a spin angular momentum of ½ (*i.e.* $s = ½$), so they can couple to give a total spin angular momentum quantum number, S, of 1 or 0. The state with $S = 0$ can have only one value of the magnetic spin angular momentum quantum number M_S ($M_S = 0$) and is called the singlet state. When $S = 1$, M_S can have any of three values ($M_S = +1, 0, -1$) and these are the triplet states. In the absence of a magnetic field (and non-zero dipolar interaction between the spins) all three triplet states are degenerate, but this degeneracy is lifted when a magnetic field is applied. In the case of a high strength magnetic field the triplet states are labelled according to their value of M_S, the states with $M_S = +1$, 0, and -1 are called T_+, T_0, and T. respectively. The singlet state is labelled S, which is not to be confused with the total spin angular momentum quantum number, S. Figure 1.1 shows how the energy of all four states depends on the magnetic field strength.

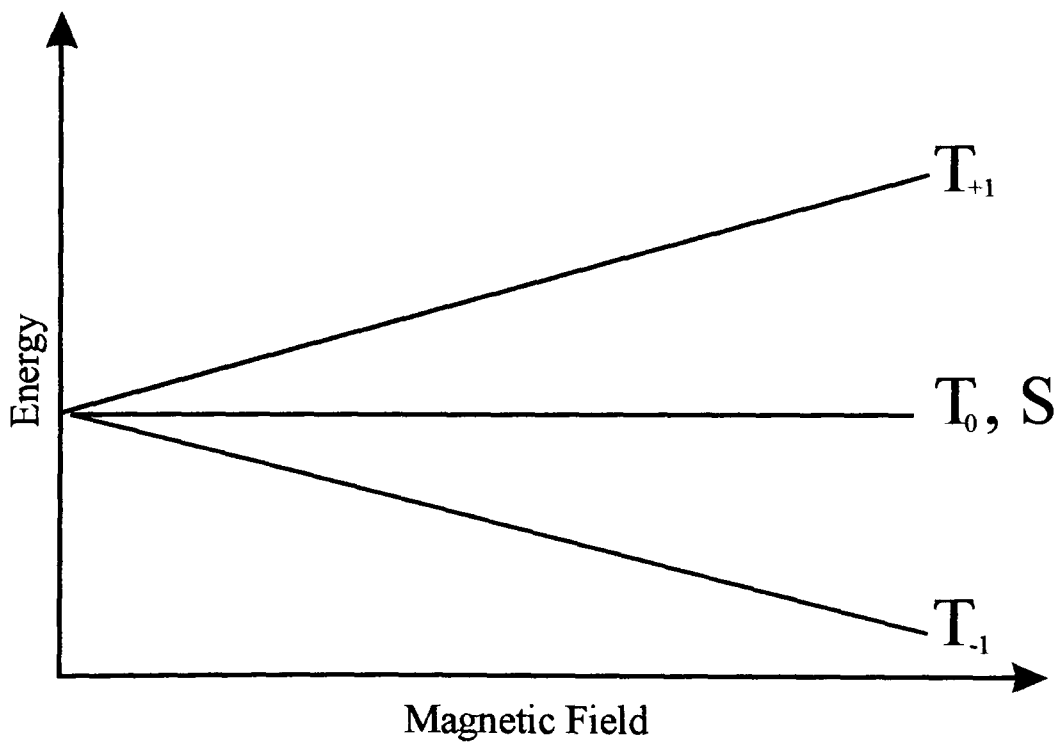


Figure 1.1: Dependence of energies of singlet and triplet states on magnetic field strength (assuming inter-radical distance is large enough for exchange and dipolar interactions to be negligible)

The energies of the S and T_0 states are independent of the applied magnetic field, as neither state has a component of spin angular momentum in the direction of the magnetic field. The splitting in energy of the T_+ and T. states from the T_0 state is due to the Zeeman splitting.

The Hamiltonian that describes the electronic Zeeman interaction is given by:

$$\hat{H}_Z = \mu_B \hat{\boldsymbol{S}}_1 \cdot \mathbf{g} \cdot \mathbf{B} \qquad (1.6)$$

where $\hat{\boldsymbol{S}}_1$ is the operator of the electron spin angular momentum of electron 1.

Furthermore, the initial spin state of a radical pair is determined by the molecular precursor which forms the RP. The total electron spin angular momentum is conserved in chemical reactions. A singlet molecule, with antiparallel, paired electron spins, dissociates to yield a RP, which at the instant of its formation also has paired electron spins, and so is in a singlet state [27]. This is also true for reactions such as electron transfer or atom transfer, the total angular momentum of the two reactants is conserved during the reaction, such as during the hydrogen abstraction reaction by benzophenone (BP) from hydrocarbon molecules. Excited triplet BP abstracts a hydrogen atom from a suitable donor (in its singlet state) to form the $BPH^{\bullet}$ hydroxydiphenyl methyl radical (henceforward known as the benzophenone ketyl radical). The total spin angular momentum before the reaction is 1 (the precursors consist of a triplet, ^{3}BP, with $S = 1$ and a molecular singlet, the hydrogen donor, with total spin angular momentum $S = 0$), and so the spin angular momentum of the RP that is formed must also be 1, *i.e.* the RP is formed in the triplet state.

A radical pair which is in a singlet or triplet state is known as a spin correlated radical pair, *i.e.* a radical pair in which the electron spins are mutually orientated in a certain way. Uncorrelated radical pairs are those which have their electron spins orientated in a random manner, *e.g.* a radical pair that forms from the encounter of two radicals in solution.

1.1.2 The Exchange and Dipolar Interactions

The exchange interaction determines the energy separation between the singlet and triplet states of the radical pair, and thus plays an important part in the behaviour of RPs. The exchange interaction originates in the Pauli exclusion principle, and its magnitude is dependent on the separation of the RP. Consider a radical pair formed by two hydrogen atoms. As the two hydrogen atom radicals approach each other their wavefunctions overlap and the electron spins on each radical align with an antiparallel (singlet state) or parallel (triplet states) configuration. The singlet state is associated with the bonding orbital, and the triplet states with the antibonding orbital, thus the singlet state is lower in energy than the triplet states, and the energy gap between the singlet and triplet manifolds is given by 2J(r). Figure 1.2 shows in a diagrammatic form the energy variation of the four states of a RP with distance, at a non-zero magnetic field strength, meaning that the three triplet states are not degenerate.

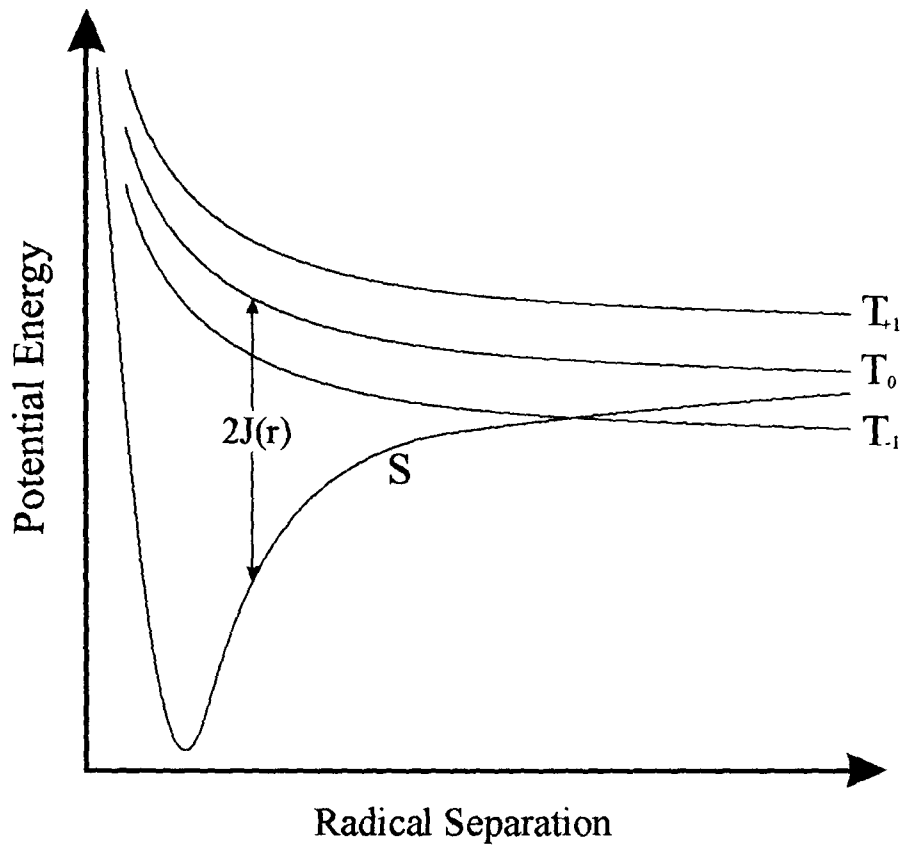


Figure 1.2: A schematic depiction of the energy variation with radical separation of the four states of a RP at non-zero magnetic field. (Not to scale)

Using the same model of two hydrogen atom radicals, the exchange interaction can be calculated explicitly from the overlap of the two 1s orbitals as the radicals approach one another in an isolated system. This calculation gives an exponential form for the exchange interaction:

$$J(r) = J_0 e^{-(r/r_J)} \qquad (1.7)$$

where r is the distance between the two radicals [28]. This exponential form is usually assumed in solution, and for RPs other than this simple case. The exchange interaction falls off rapidly with radical separation, and is assumed to be of negligible magnitude at separations greater than 1 nm [29]. After formation of the RP the separation of the radicals to distances exceeding this value occurs within some hundreds of picoseconds in liquids with viscosities similar to that of water, and consequently for the greater part of the RP lifetime the radicals do not experience the effect of the exchange interaction [28]. However, for RPs in higher viscosity solutions, or RPs constrained in

some manner (*e.g.* in micelles, or for biradicals) the exchange interaction has the potential to play a much larger role.

In solution the exchange interaction can be considered to be isotropic, due to fast molecular tumbling, however for RPs that have a fixed arrangement with respect to each other it is possible that the exchange interaction could be anisotropic. Nevertheless, it is very difficult to distinguish between the anisotropic part of the exchange interaction from the anisotropic part of the dipolar interaction. For theoretical simulations of RP behaviour the exchange interaction is normally described as a purely isotropic parameter, and any anisotropy is ascribed to the dipolar interaction.

The Hamiltonian that describes the isotropic exchange interaction is given by:

$$\hat{H}_E = 2\mathrm{J(r)}\hat{\boldsymbol{S}}_1 \cdot \hat{\boldsymbol{S}}_2 . \qquad (1.8)$$

The dipolar interaction results from interaction between the magnetic dipoles of the two radicals in the RP. In the case of non-negligible dipole-dipole interactions the dipolar interaction causes splittings between the energy levels of the radical pair, meaning that even at zero magnetic field the triplet levels are no longer degenerate. The magnitude of the dipolar interaction is inversely proportional to the cube of the distance between the radicals (strictly the distance between the point magnetic dipoles of the radicals), and hence is normally of longer range than the exchange interaction. As with the exchange interaction the dipolar interaction is anisotropic, and for two radicals in solution fast molecular tumbling leads to the translational motion of one radical about the other, causing the dipolar interaction to average to zero.

The Hamiltonian that describes the dipolar interaction is given by:

$$\hat{H}_D = \hat{\boldsymbol{S}} \cdot \mathbf{D} \cdot \hat{\boldsymbol{S}} \qquad (1.9)$$

where $\hat{\boldsymbol{S}}$ is the total spin operator, and is given by $\hat{\boldsymbol{S}} = \hat{\boldsymbol{S}}_1 + \hat{\boldsymbol{S}}_2$, and **D** is the dipolar tensor.

1.1.3 The Vector Model

The vector model provides a classical, pictorial representation of spin angular momentum in strong magnetic fields (in practice those which are stronger than 10 mT) [30]. Section 1.1 described the spin angular momentum of a single electron in a magnetic field as aligned either parallel or antiparallel to the field direction. This electron spin can be illustrated by a vector of length $(s(s+1))^{1/2}\hbar$, which precesses around the field direction, and has a projection on the magnetic field axis of either $+\frac{1}{2}\hbar$ or $-\frac{1}{2}\hbar$. Since the spin vector precesses around the magnetic field direction the orthogonal components in the perpendicular directions to the magnetic field vary continuously in time at the precession frequency, and average to zero in any particular orthogonal direction over time.

The precession frequency of the vectors around the magnetic field direction is called the Larmor frequency, ω_L, which is given by:

$$\omega_L = g\mu_B B_{loc} / \hbar. \qquad (1.10)$$

In a radical pair the spins of the two electrons couple together and can be in either a triplet or singlet state, as described in section 1.1.1. The angular momentum vector now has length $(S(S+1))^{1/2}\hbar$, and in the triplet state it has three projections in the direction of the applied magnetic field given by $M_S\hbar$, where $M_S = +1$, 0, or -1. In the presence of a magnetic field these are of different energy due to the Zeeman effect, since two have equal but opposite magnetic moments, while the third has no magnetic moment in the direction of the magnetic field.

Figure 1.3, below shows the vector representation of the four RP spin states in a strong magnetic field, where R_1 and R_2 are the vectors representing the individual electron spins. From the diagram it is apparent that in the S and T_0 states the resultant component in the direction of the magnetic field is zero, whereas it is non-zero for the other two. T_0 differs from S in having a non-zero resultant perpendicular to the field, which rotates at the precession frequency. In the singlet state the electrons precess 180° out of phase to each other and so have no resultant in any direction. Thus the S and T_0 states differ only in the relative phase of their electron spin vectors.

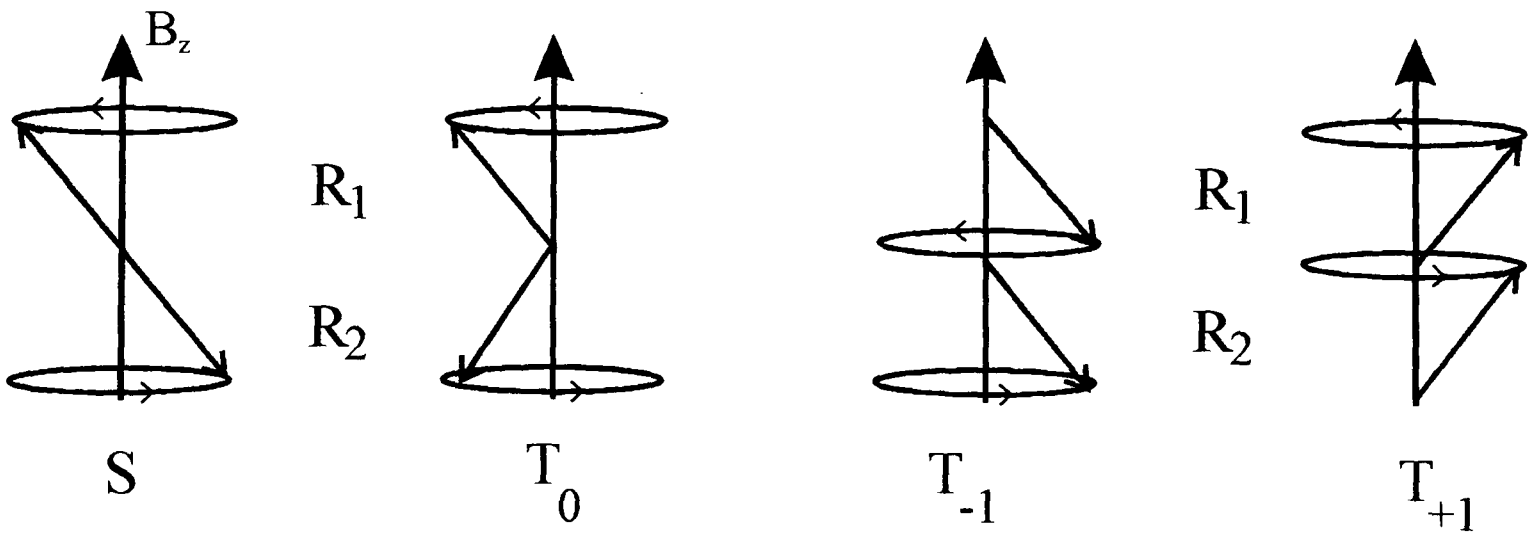


Figure 1.3: Vector representation of singlet and triplet spin states of a RP in a strong magnetic field.

1.2 The Radical Pair Mechanism

From the previous section it has been seen that the application of a magnetic field can affect the energy levels of some states of a radical pair, but it has not yet been established how the magnetic field can influence a chemical reaction. From energetic considerations it is hard to see how a magnetic field can alter a reaction. The energy difference between the two states of an electron in a 1 T magnetic field is 11.2 J mol^{-1}, for comparison kT is around 2300 J mol^{-1} at room temperature. This implies that a magnetic field can have little effect on the position of equilibrium of a chemical reaction. However, many processes are kinetically, rather than thermodynamically controlled. If a reaction is kinetically controlled a magnetic field can only change the rate of formation of a product, and not its nature, but if competing reaction pathways are present the relative proportions of different products can be changed. However, this should not be taken to imply that all, or even most, kinetically controlled reactions show a magnetic field dependence. One or more of the reaction pathways needs to have a rate that is magnetic field dependent, *e.g.* that the activation energy for one of the pathways is affected by a magnetic field.

Hence, for magnetic field effects (MFEs) to be seen in a chemical reaction there needs to be a mechanism whereby changing the magnetic field strength causes a change in the relative positions of the energy levels of the reaction intermediates. This has been demonstrated in section 1.1 with the magnetic field dependence of the energy levels of the radical pair spin states. However, there also needs to be at least one mechanism that causes the mixing between these spin states, otherwise the magnetic field will have no effect. There are two different classes of spin mixing, coherent and incoherent, and they are described below.

1.2.1 Coherent Spin Mixing

Coherent spin mixing is the process whereby a constant interaction drives one state of the spin correlated RP smoothly into another. There are three different mechanisms by which coherent spin mixing can occur, the Δg mechanism, the hyperfine mechanism, and the level crossing mechanism.

1.2.1a The Δg Mechanism

As stated above, and in equation 1.10, the frequency of precession of the electron spin around the field direction at strong magnetic fields is given by the Larmor frequency. If the unpaired electrons on the two radicals in a RP have different g values then they will have different Larmor frequencies. This means that the RP will oscillate between the T_0 and S states in a time Δt, which is determined by the difference in precession frequencies:

$$\Delta t = \hbar\pi / \Delta g \mu_B B_{loc}. \qquad (1.11)$$

The differences in g values for organic radicals are very small, typically of the order of 10^{-4}, for example the difference in g values between a benzophenone ketyl radical and a t-butyl radical is 0.0004 (g values of 2.003 and 2.0026 respectively). This means that the time taken to convert from a S to a T_0 state (or vice versa) in a 20 mT magnetic field (which is one of the strongest considered in this thesis) is $\Delta t = 4.5$ μs.

The Δg mechanism is assumed to be negligible at the magnetic field strengths considered in this thesis. However, the fact that the mixing time is inversely proportional to the applied magnetic field means that this mechanism becomes important, and eventually dominant at high magnetic field strengths.

The mixing due to coherent precession between the T_0 and S states at high magnetic field strengths can be illustrated using the vector model introduced in section 1.1.3. The pure T_0 and S states differ in the constant phase differences of the spins, which are in phase in the former, and exactly out of phase in the latter. If the two spin vectors R_1 and R_2 have different Larmor frequencies then one spin will precess faster than the other and mixing will occur. In between the two extremes of T_0 and S the RP possesses both T_0 and S character. If the radicals re-encounter, then the likelihood that the RP will react from the singlet state is given by the singlet character of the state (see section 1.2.3).

1.2.1b The Hyperfine Mechanism

The electrons are not the only species in a radical that can have spin angular momentum, radicals contain nuclei which may also have non-zero spin. Nuclei are made up of protons and neutrons, which are both fermions, and so some nuclei possess a non-zero spin angular momentum. Examples of these magnetic nuclei, with non-zero spin, are ^{1}H ($I = ½$), ^{13}C ($I = ½$), ^{14}N ($I = 1$), and ^{2}H ($I = 1$). Nuclei with zero spin include ^{12}C and ^{16}O.

The spin quantum number for nuclei is labelled I and is a non-negative integer, or half integer. If a nucleus has spin quantum number I then it has an angular momentum of magnitude $(I(I+1))^{1/2}\hbar$. The component of angular momentum on the z-axis is given by m_I where m_I can take $2I+1$ values between $+I$ and $-I$. If $I > 0$ then the nucleus will have a magnetic moment with an orientation dependent on the value of m_I. This magnetic moment will interact with the electron spin of the unpaired electron in the radical, a mechanism called the hyperfine interaction. The magnetic field generated by the nucleus will either add or subtract from the applied field so that:

$$B_{loc} = B_{app} + a m_I \qquad (1.12)$$

where a is hyperfine coupling constant. If the two electrons in the RP are subject to different hyperfine interactions then they will experience different local magnetic fields, and hence will undergo spin mixing. To examine this further, consider the one proton radical pair, this is a RP that consists of radical 1, which has hyperfine coupling to a single hydrogen nucleus ($R_1H^\bullet$) and radical 2 that has no source of spin beside the unpaired electron ($R_2^\bullet$). In the case of a Δg value of zero $R_1H^\bullet$ will precess around the field direction with a frequency $\omega_1 = \omega_L \pm {}^a/_2$ (depending on the spin state of the hydrogen nucleus) and $R_2^\bullet$ will have a frequency of $\omega_2 = \omega_L$. Using the vector model it is obvious to see that this will mix the S and T_0 states of the radical pair, with a mixing frequency of ${}^a/_2$. At high magnetic field strengths the hyperfine interaction does not mix the S state with the T_+ and T_- states.

In a weak magnetic field the electron spins precess around a magnetic field that is a combination of the applied field and the hyperfine-induced field. This total field is not in the same direction as the applied magnetic field, and the electrons now precess around this total field direction. Hence the projection of the electron spin onto the

applied field direction can alter as a function of time, and interconversion becomes possible between the S and the T_+ and T_- states.

The hyperfine coupling between magnetic nuclei and electrons is comprised of two separate spin coupling mechanisms. The Fermi contact interaction, which describes the probability of finding the electron at the nucleus, and the dipole-dipole interaction, which describes the magnetic interaction between the electronic and nuclear dipoles, and is the hyperfine analogue of the dipolar interaction described in section 1.1.2. As with the dipolar interaction the hyperfine interaction is anisotropic, but in solutions with fast molecular tumbling the anisotropy averages out and the hyperfine interaction can be assumed to be isotropic.

The Hamiltonian that describes the isotropic hyperfine interaction is given by:

$$\hat{H}_H = \sum_i a_i \hat{\boldsymbol{S}}_1 \cdot \hat{\boldsymbol{I}}_i \qquad (1.13)$$

where a_i are the hyperfine coupling constants and $\hat{\boldsymbol{I}}_i$ the nuclear spin operators for nucleus i.

Most RP phenomena at magnetic fields below several tesla, including zero field, are dominated by the hyperfine interaction.

1.2.1c Magnetic Isotope Effects

One consequence of hyperfine interactions causing mixing between spin states is that kinetic changes are expected if magnetic isotopes are substituted into the RP, for example changing a non-magnetic nucleus such as ^{12}C for a magnetic nucleus such as ^{13}C. Effects are also seen when both the size of the hyperfine coupling and the spin quantum number I are altered, *e.g.* substituting deuterium for hydrogen (hydrogen has $I = ½$, deuterium has $I = 1$, and the hyperfine coupling constant of hydrogen is approximately 6.5 times larger than that of deuterium). These effects have been seen experimentally [31-33] and are known as magnetic isotope effects (MIEs). MIEs can also be seen in radical ensembles that contain magnetic nuclei in natural abundance. Radicals that contain these magnetic nuclei will react at different rates from those which do not, due to the altered rates of spin mixing. Studies have also shown that MIEs can be enhanced by the application of external magnetic fields. For example Wakasa et al. [34] showed that a magnetic field of 20 mT can enrich the relative proportion of the magnetic isotope of germanium, ^{73}Ge, from samples of natural isotropic abundance in a solution of Ph_3MeGe in micellar solution by 42%, compared to a 14% enrichment at zero magnetic field.

1.2.1d The Level Crossing Mechanism

As described in section 1.1.2 the exchange interaction determines the magnetic field independent energy separation of the singlet and triplet states, with the magnitude of the exchange interaction dependent on the separation of the RP. For radical pairs with a fixed, non-zero value of the exchange interaction (*e.g.* biradicals, which can have a

fixed separation) there will be no mixing at zero magnetic field if the singlet and triplet states are separated too far by the exchange energy. However, as the magnetic field strength is increased the T_+ and T_- energy levels are no longer degenerate with the T_0 state, due to the Zeeman effect, and there is a specific value of the magnetic field strength where the difference in energy between the singlet state and one of the triplet states (either T_+ or T_-, depending on the sign of the exchange interaction) due to the exchange interaction, and the energy difference between the same two states due to the Zeeman splitting is the same. This leads to spin mixing between these two states at the level-crossing magnetic field strength, B_{LC}, given by:

$$B_{LC} = 2J(r) / g\mu_B. \qquad (1.14)$$

However, if the individual radicals in the RP are free to move with respect to each other then the value of the energy splitting due to the exchange energy will change with radical separation. Movement through this level-crossing region is often too fast for spin mixing to occur, but if the RP is held together (*e.g.* in a biradical, [35]) then mixing due to the level crossing mechanism can be seen.

1.2.2 Incoherent Spin Mixing

The equilibrium population of spin states for a radical pair is given by the Boltzmann distribution. However, when a radical pair is formed, because the spin state of the molecular precursor is conserved, the spin states of the RPs immediately after RP creation do not have a Boltzmann population distribution, and are said to be polarised. Relaxation is the process which re-establishes the equilibrium (Boltzmann)

populations of the spin states. It is a stimulated process, caused by fluctuations in the local magnetic field experienced by the radicals due to random molecular motion.

Relaxation falls into two categories, spin-lattice relaxation and spin-spin relaxation. Spin lattice relaxation occurs between the T_+, T. states, and the T_0, S states, *i.e.* (T_+, T.) ↔ (T_0, S). The rate of spin-lattice relaxation is the rate at which the equilibrium populations of spin in the magnetic field direction are obtained. Spin-lattice relaxation is also called longitudinal relaxation, and the reciprocal of this rate of relaxation gives a time constant called T_1, or the longitudinal relaxation time.

The second category of relaxation is spin-spin relaxation and causes mixing between the T_0 and S states of the RP. This form of relaxation is also called transverse relaxation and is the loss of spin polarisation in the plane perpendicular to the direction of the magnetic field. The inverse of the spin-spin relaxation rate gives the transverse relaxation time T_2.

In normal aqueous, homogeneous solutions relaxation times are of the order of microseconds, and so are expected to be slower than the coherent spin mixing processes. This is also expected to be the case for relaxation in the interior of micelles. Relaxation acts to randomly change the spin state of the RP, and so will mask any effects due to coherent spin mixing. For MFEs to be observed the coherent spin mixing must happen at a faster rate than the relaxation.

1.2.3 The Role of Diffusion

In solution the radical pair is not fixed in space, and the individual radicals of the pair are not fixed in relation to one another. The distance between the members of the RP hence varies as both radicals diffuse throughout the solution after creation.

As mentioned in section 1.1.1 spin angular momentum is conserved on creation of a RP, therefore a RP formed from a singlet molecular precursor will initially be in the singlet state. Conservation of spin angular momentum also applies when two radicals combine. Radical reaction is spin selective, and in the majority of cases (including all those described in this thesis) the recombination product is the singlet ground state. This means that RPs which are created in the triplet state must first undergo spin evolution to the singlet state before they can recombine. For most of the time the RP is in a quantum mechanically mixed state exhibiting both singlet and triplet character. Reaction of the radical pair occurs upon re-encounter with a probability that depends on the singlet character of the radical pair at that time. The mixed state has a wavefunction that can be written as a time dependent linear combination of the two pure states. In the case of high magnetic field strengths, where the T_+ and T_- states are energetically removed from the S and T_0 states, the mixed wavefunction can be written as:

$$\psi(t) = \left[c_S(t)|S\rangle + c_{T_0}(t)|T_0\rangle\right]\varphi_N \qquad (1.15)$$

where φ_N is a nuclear wavefunction which describes the nuclear spin states of the two radicals. The probability that the RP is in a singlet state at a time, t, is given by the

square of the modulus of the time dependent singlet coefficient, $|c_S(t)|^2$. This probability that the RP is in a singlet state is also known as the singlet character of the RP.

1.2.4 Geminate and F Pairs

Until the 1950's it was believed that in solution chemistry the fastest category of reactions were those which were diffusion controlled, *i.e.* with reaction at each encounter and occurring on the microsecond to millisecond timescale. However, it was demonstrated by direct observation of iodine atom recombination in solution by Chuang et al. [36] that an ultrafast reaction precedes the diffusion controlled process, with approximately 90% of the atoms recombining in the first 500 ps after the photolysis flash which created them. This very fast stage occurs between atoms or radicals created together, and is known as the geminate reaction (geminate meaning born together). Radicals that are created together from a molecular precursor and are termed geminate radical pairs. In a homogeneous solvent the RP is held in a solvent cage, which means that, after initial separation, the radicals can diffuse back together to form the geminate product. If either member of the RP escapes from the geminate stage without reaction then the radicals enter the bulk solution, where they may encounter radicals from other geminate pairs. Such RPs are termed freely diffusing pairs (or F pairs). This process is illustrated in figure 1.4.

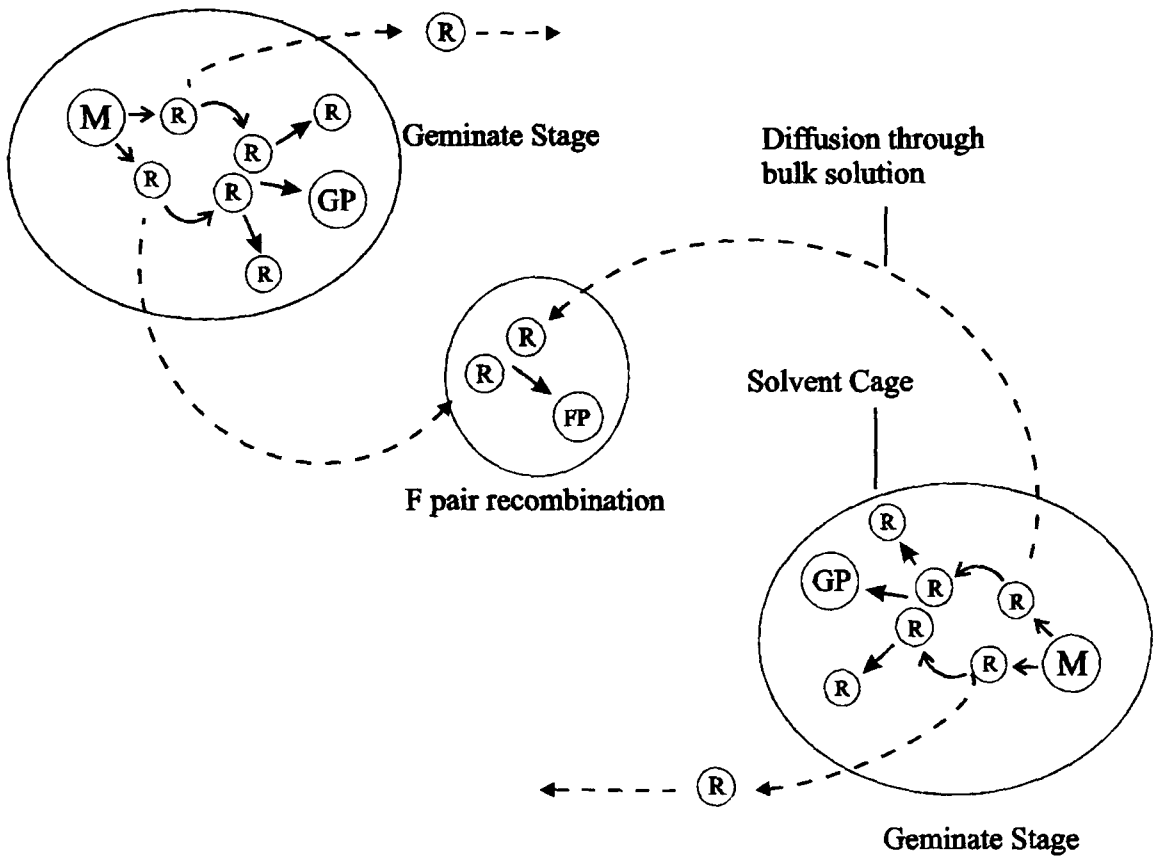


Figure 1.4: The distinction between geminate and F pair recombination

As geminate RPs are those in which the two radicals are created together from a common precursor, spin correlation exists at the moment of formation of the RP and they will be in either a triplet or singlet state. For F pairs spin correlation is established upon encounter.

For geminate RPs to undergo spin evolution they must diffuse apart to a distance where the exchange interaction becomes smaller than the interactions causing singlet-triplet interconversion (such as the hyperfine coupling mechanism). However, for radicals to recombine they not only need to be in the correct spin state, but they also need to come into close enough contact for reaction to occur. It is of no consequence if the RP is in the correct spin state, but never encounters, as the recombination can never occur. Thus for MFEs to be observed diffusion plays a vital role. The RP must diffuse apart far enough for spin mixing to occur, but also have a geminate lifetime long enough for sufficient spin mixing to occur before re-encounter or further separation. The dependence of MFE on both spin mixing and diffusion can

be seen from one theoretical model for the probability of reaction of a radical pair, in equation 1.16, where P_R is the probability of reaction [37].

$$P_R = \lambda \int P_E(t)\, P_S(t)\, dt \qquad (1.16)$$

where λ is the probability of reaction given that the two radicals encounter in the singlet state, $P_E(t)$ is the encounter probability at time t, and $P_S(t)$ is the probability that the RP is in the singlet state at a time t, and is given by $|c_S(t)|^2$ as described in section 1.2.3. Equation 1.16 treats the state mixing and diffusion as separate processes which is not strictly true, however it does make calculations simpler. The diffusion and spin mixing can be considered together by using the density matrix, $\rho(r,t)$ which characterises the spin state of the RP at a time when the radicals are a distance r apart. The time evolution of this matrix is described by the stochastic Liouville equation (SLE). It is not discussed any further in this thesis, but the approach is explained in [1].

Application of a magnetic field changes the proportion of the overall reaction that occurs in the geminate and F pair periods. The magnetic field does not change the chemical nature of products, just the proportion of geminate and escape products. The molecular dynamics of the reaction processes in geminate and F pair periods are not changed by changing the magnetic field strength, however the molecular dynamics governs the separation and any subsequent re-encounter of the RP and so plays a vital role in the effect any magnetic field may have.

In summary, for a magnetic field to have a significant effect on a RP reaction the following conditions must be satisfied [13]:

1) The radical pair must be created in an electron spin correlated singlet or triplet state from a molecular precursor of the same multiplicity, or, if the two radicals encounter at random, spin correlation must be generated by a spin selective reaction.
2) The singlet and triplet states of the RP must be coherently interconverted by some spin mixing mechanism.
3) Recombination reactions, diffusive separation of the radicals, and spin relaxation should be slow enough to permit appreciable S-T interconversion to take place.
4) Singlet and triplet pairs must have different chemical fates. They must either react to form different products, or, if triplet pairs do not recombine directly they should diffuse apart to give free radicals.

1.2.5 The Reaction Scheme

The majority of this thesis is concerned with a radical pair formed from benzophenone (or a derivative) and a hydrogen donor molecule (R), as shown in the reaction scheme in figure 1.5.

The singlet benzophenone molecule is excited by laser light to an excited singlet state, which subsequently undergoes intersystem crossing (ISC) into an excited triplet state. This excited triplet BP abstracts a hydrogen atom from a suitable hydrogen donor and a triplet radical pair is formed (under conservation of spin angular momentum).

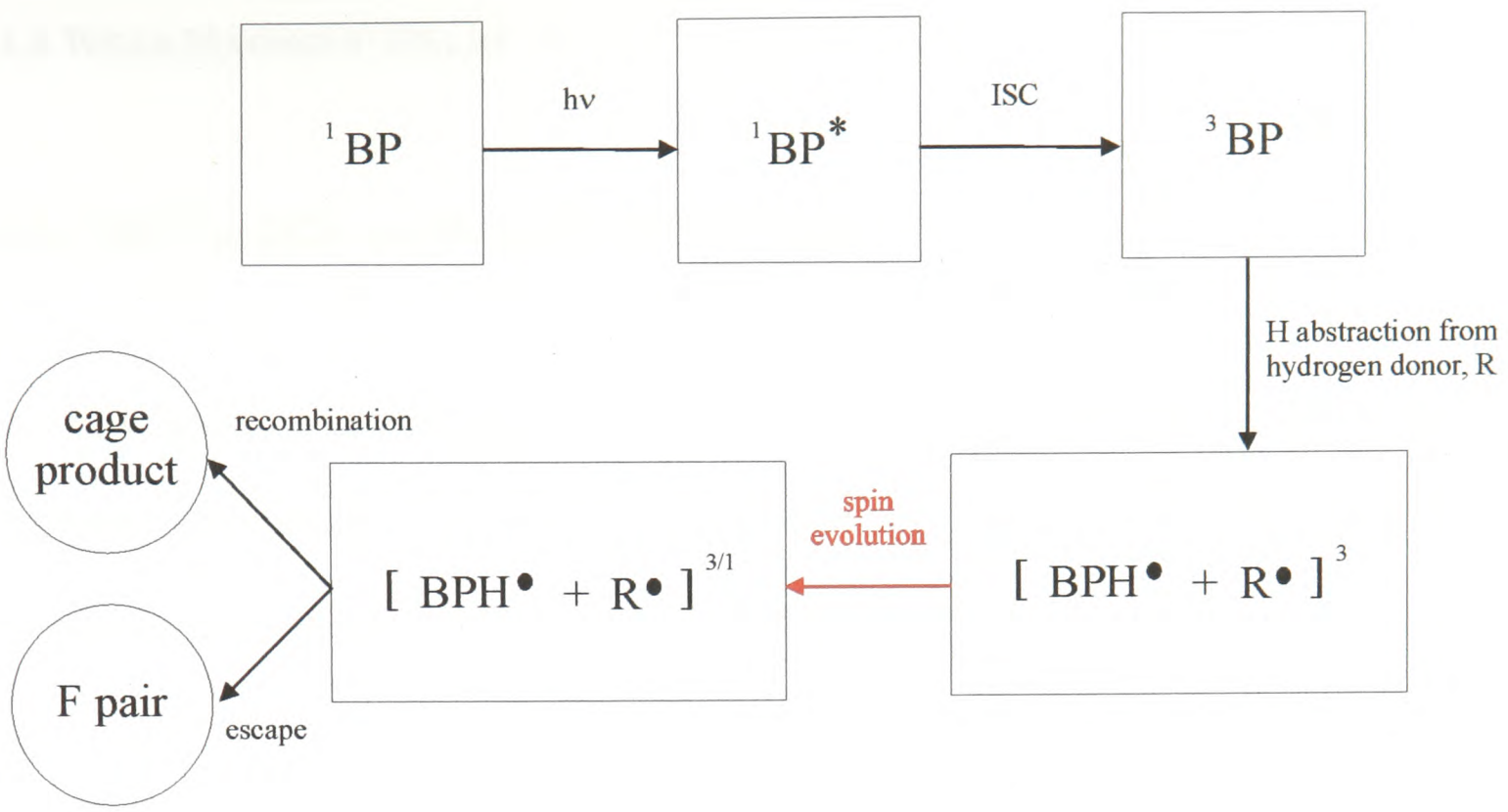


Figure 1.5: Flow diagram of reaction scheme

Hence, for any recombination to occur the triplet RP must undergo evolution to the singlet state. The rate of spin mixing decreases with increasing energy difference between the triplet and singlet states, and this is the key to understanding how magnetic fields can affect the reaction. The case at magnetic field strengths close to zero is exceptional, and is discussed in section 1.3.2. The spin mixing state is highlighted in red on the diagram and it is the rate of this step in the reaction pathway that is dependent on the strength of the applied magnetic field.

The cage product can only be formed from the singlet state of the geminate RP, whereas both the singlet and triplet states can undergo escape to form F pairs. Therefore, although the rate of formation of the cage product from the singlet state RP is not dependent on the magnetic field strength, the proportion of the RPs which are in the singlet state will determine the rate of formation of the cage product. The effect of the magnetic field can therefore be observed by either the change in rate of formation of the cage products, or the change in rate of loss of the radical pair.

1.3 WEAK MAGNETIC FIELDS

1.3.1 MFEs at Different Magnetic Field Strengths

As the magnetic field strength is increased from zero magnetic field the extent of the different mechanisms of spin mixing will change, and hence the total extent of spin mixing will also change. This is shown in a qualitative way in the diagram below.

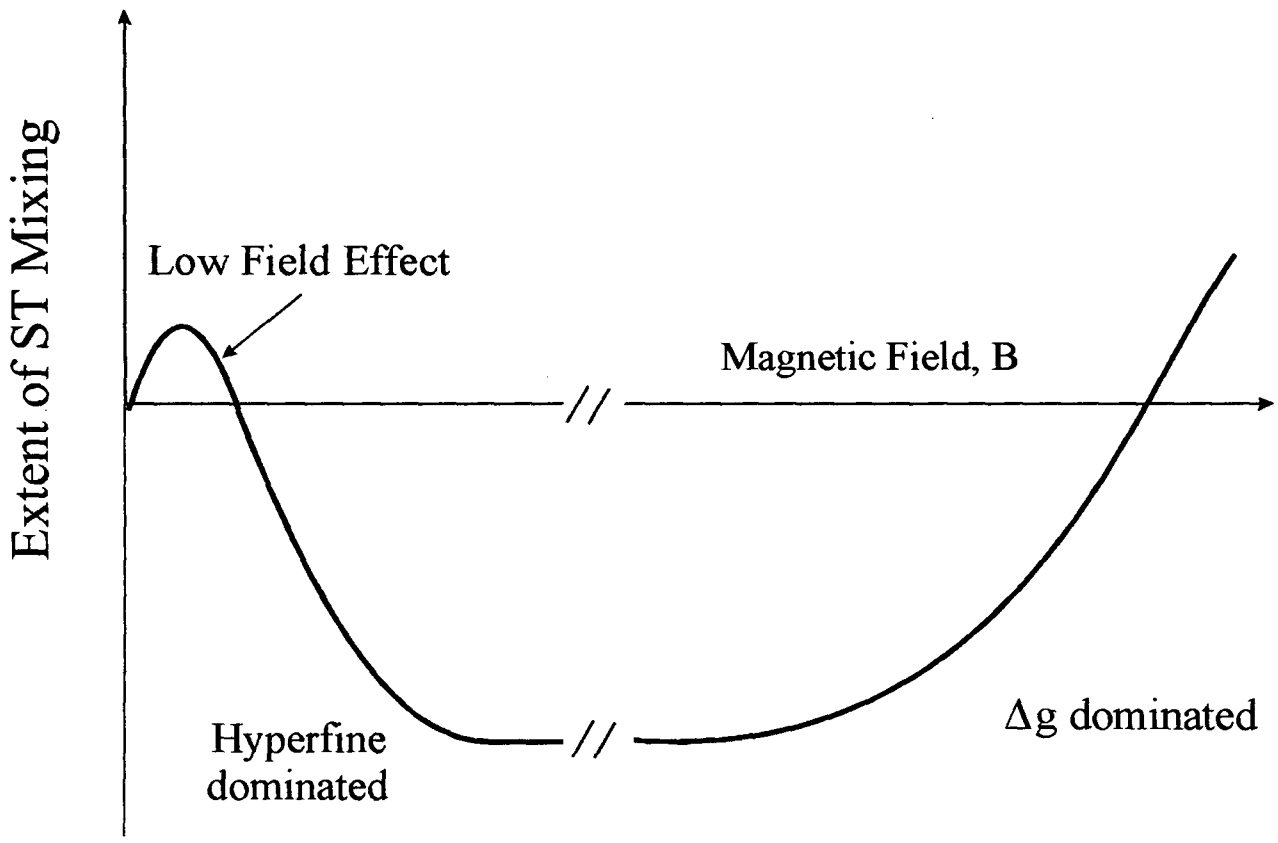


Figure 1.6: Variation of S–T mixing with magnetic field strength (not to scale)

There are three distinct regions to the diagram, the Δg dominated region, the hyperfine dominated region and the Low Field Effect (LFE) region. These will all be discussed in turn.

At high magnetic field strengths the hyperfine interaction cannot cause mixing between the T_+ and T_- states and the T_0 and S states due to the large energy difference caused by the Zeeman interaction. However, the magnetic field is strong enough for

Δg mixing between the S and T_0 states, and this rate of mixing increases as the magnetic field strength increases, as described in equation 1.11. As the magnetic field strength decreases the mixing due to the Δg mechanism becomes less important, until the magnetic field strength is not large enough for mixing to occur during the lifetime of the radical pair using this mechanism. This is the plateau region where the T_+ and T. states are energetically too far removed from the T_0 and S states for mixing to occur, but the magnetic field is too weak for mixing via the Δg mechanism to occur during the RP lifetime. As the magnetic field strength decreases still further the Zeeman splitting becomes smaller, and the difference is small enough for mixing to occur between all four spin states due to the hyperfine mechanism. The peak of S-T mixing at magnetic field strengths only just larger than zero is due to the LFE, which is discussed below.

The diagram in figure 1.6, and the discussion above describe what happens in the absence of relaxation. As relaxation processes generally happen on a longer timescale than coherent mixing this is an adequate description for RPs with a short lifetime. However RPs with longer lifetimes can exhibit behaviour that is best described by the relaxation mechanism [8]. The main effect is to reduce the plateau region seen in figure 1.6, as spin mixing between the T_+, T. states and the T_0, S states is still possible due to spin-lattice relaxation. Relaxation causes an increase in spin mixing in the same sense as the Δg mechanism at high strength magnetic fields, but the two effects can be separated using paramagnetic ions, which quench the effect from the relaxation mechanism, but not the Δg mechanism [38].

1.3.2 The Low Field Effect

Until the magnetic field strength is large enough for the Δg mechanism to become significant, the rate of S-T mixing decreases with increasing magnetic field strength. This is due to the separation of the T_+ and T_- states from the T_0 and S states due to Zeeman splitting. For a radical pair created as a triplet, the rate of recombination (for which the RP must be in the singlet state) decreases with increasing magnetic field strength due to a decrease in the efficiency of spin mixing.

However, at weak magnetic fields (those weaker than the average radical pair hyperfine coupling) the opposite is true, the rate of spin mixing is increased relative to the zero magnetic field case. This is called the low field effect, and was first predicted in 1976 [39], when it was shown that in the absence of chemical reactions the probability of a RP being in a singlet state is the sum of several constant terms plus a number of time dependent ones, which oscillate at frequencies corresponding to gaps between the energy levels of the spin system. The origin of the LFE can be described in two different, but equivalent, ways, both of which are outlined below.

1.3.2a Selection Rules

The selection rules for conservation of spin angular momentum are different at zero and non-zero magnetic field [12]. The easiest way to display this is to consider the one proton radical pair introduced in section 1.2.1b. In the singlet state the resultant electron angular momentum is zero, and so the total angular momentum, F, (including the proton spin) for the RP is $^1/_2$. In the T_0, T_+, and T_- states the components of the electron spin in the direction of the magnetic field are 0, +1, and −1 respectively. With

the proton spin the total spin angular momentum, F, becomes $^1/_2$ and $^3/_2$. In zero magnetic field the selection rule requires that both the total angular momentum and its component in a given direction are conserved, *i.e.* $\Delta F = 0$ and $\Delta F_z = 0$. For a triplet born RP, only the pairs that have a total angular momentum of $^1/_2$ can convert to the singlet state. In high magnetic field strengths the selection rules are different and only the component of the angular momentum which is in the direction of the magnetic field has to be conserved, *i.e.* only $\Delta F_z=0$. This means that triplet states that have a total angular momentum of $^3/_2$ can convert to the singlet state as long as the spin angular momentum in the direction of the magnetic field is conserved. For the one proton RP these selection rules mean that for triplet born RPs with equal population in each of the six triplet states only two can convert to one of the two singlet states, so the maximum statistical proportion of the RPs that can recombine either directly (S), or after allowed conversion into the singlet state is $^1/_3$. When a magnetic field is applied the selection rules change so that four of the six triplet states can now convert to one of the two singlet states, and so the total proportion of RPs that can recombine directly, or after allowed conversions is now $^2/_3$. These are the statistical results for recombination probabilities, and assume that the RP can only recombine from the singlet state, that spin mixing occurs to the maximum possible extent, and that the geminate period lasts for a sufficient time for re-encounters to occur after complete spin mixing. It also neglects the effect of relaxation.

In intermediate strength magnetic fields there is a gradual change from one set of rules to the other, so from these conditions it would seem that the S-T mixing would increase with increasing magnetic field strength. However, as the magnetic field strength increases the T_+ and T_- states are becoming further and further removed in energy from the T_0 and S states due to the Zeeman splitting. The LFE maximum in

spin mixing is caused by a combination of these two effects. At a certain magnetic field strength there is a maximum in the mixing where the selection rules have become sufficiently relaxed for a significant degree of mixing between the S and T_+, T. states, but where the Zeeman splitting is not so strong that these levels are too far apart in energy for the mixing to occur.

1.3.2b Removal of Zero Field Coherences

The second way of explaining the LFE is to consider the energy levels of the spin states using a quantum mechanical approach [39]. At low strength magnetic fields there is no classical model that can describe spin mixing. The vector model only holds true at high magnetic field strengths. Also in zero, or weak strength magnetic fields the initial states are not the simple high magnetic field ones, but their wavefunctions can be written as linear combinations of these states. The increase in mixing between states in zero and weak magnetic fields can be seen as a consequence of the removal of zero field degeneracies between the spin states of the radical pair by an applied magnetic field. To consider these statements in more detail it is useful to consider the one proton radical pair again. At high magnetic field strengths this RP has eight states, corresponding to two hyperfine states for each of the four electronic states, T_+, T_-, T_0, and S. This implies that there are also eight states at zero magnetic field. If the energy of these eight states at zero magnetic field is calculated by solving the Schrödinger equation it is found that six of the energy levels are degenerate, with energy of $^{a}/_{4}$, where a is the hyperfine coupling constant between the electron and the proton on radical $R_1H^{\bullet}$. The other two states are also degenerate, and have an energy of $^{-3a}/_{4}$. The energy levels are populated to a different extent on RP formation depending on

whether the RP is formed from a singlet or triplet precursor and the singlet or triplet character of each of the energy levels. Mixing can occur at zero magnetic field through the hyperfine interaction, but only between energy levels which are non-degenerate. The presence of even a small applied magnetic field removes some of the zero field degeneracies unlocking coherences between the states which lay dormant in zero field. These coherences now lead to increased singlet-triplet mixing at a frequency that is determined by the splitting between the states. The latter is proportional to the Larmor precession frequency of the electrons in the applied field (see equation 1.10) so as the magnetic field strength is increased this mixing occurs at a faster rate. However, the rate of mixing between energy levels is also dependent on the difference in energy of the states, so as the magnetic field strength increases the energy gaps between levels increase and this slows down the mixing rate. The combination of these two factors leads to the LFE maximum in the rate of spin mixing at low magnetic field strengths.

For RPs with more than one hyperfine coupling there will be different numbers of energy levels, and different amounts of degeneracy, and so the size of the LFE will vary between systems.

Theoretical investigations into the LFE [13,40] have shown that weak magnetic fields can decrease the singlet yield of a singlet born radical pair by up to 40%, where the singlet yield is defined as the proportion of the initial radical pairs that form the singlet recombination product after infinite time. It was found that the size of the LFE is strongly dependent on the RP lifetime, with the condition that $\tau^{-1} << a$ (where τ is the RP lifetime, and a the average hyperfine coupling of the RP) for the greatest effects to be seen. For all radical pairs considered in [40] the LFE was shown to be at least 10% (in the limit $a>>B>>\tau^{-1}$), irrespective of the number of magnetic nuclei,

whether the nuclei are equivalent or inequivalent, or whether one or both radicals have significant hyperfine couplings. It was also shown that the size of the LFE decreases drastically with the rate of radical recombination, interaction between the radicals (*e.g.* the exchange and dipolar reactions), and spin relaxation.

The LFE is the only reproducible and understood way in which a weak magnetic field has been shown to affect chemical reactions.

1.4 Experimental Strategies for Observing MFEs

In most situations overall product yields are comparatively unaffected by the presence of applied magnetic fields, especially if a number of competing reactions occur, and so it is more productive to observe the transient radicals themselves. Product studies have been utilised to observe the effect of magnetic fields [1,41], but direct observation of the RP provides the most information on what is happening as a result of applying the magnetic field. The most common method for direct observation of the radicals is to use optical methods such as fluorescence or absorbance. These are described in more detail in the following section.

The probability of geminate reaction occurring depends on two separate processes; singlet-triplet interconversion and molecular diffusion. At low magnetic field strengths S-T conversion is slow and requires ca. 100-300 ns in organic systems to affect the reaction yield appreciably [12] (for magnetic field strengths of the order of 0.1 mT). This means that for MFEs, and particularly LFEs, to be observable in a system a method of extending the geminate lifetime of the RP is needed. In the past

the two most common ways of achieving this experimentally have been to use radical ion pairs [26,42-45] or to constrain the RP within other structures *e.g.* micelles [14,24,46-48], vesicles [49,50], or other systems, such as zeolites or porous silica [51-53]. There are two reasons for radical ion pairs being so extensively used for experimental studies; firstly the Coulomb interaction between the oppositely charged ions prolongs the lifetime of the geminate pair and enhances the LFE by increasing the probability of re-encounter after sufficient time for spin mixing has occurred. Secondly, many photochemical radical ion pair reactions result in an exciplex whose fluorescence provides a convenient method for detection of the RP concentration. Also, as the exciplex is stable only in an excited electronic state the products of fluorescence are the initial reactants, so experiments can be performed without having to constantly renew the sample. Fluorescence is a useful detection technique, as it occurs against a zero background, *i.e.* the signal with no fluorescence present is zero, and a small signal is relatively easy to detect.

However, the purpose of this work is to study neutral radical pairs, as the ultimate aim is to investigate radical pair reactions in analogues of biological systems, and, with a few notable exceptions (*e.g.* photosynthesis), the radical pairs which are found in these biological systems are neutral [2]. This statement must, however, come with the caveat that there are very few known RPs in biological systems, and there is no inherent reason that any that are present have to be composed of neutral radicals.

Neutral radicals do not form exciplexes, and neither do the products of their reactions, as the reaction energy is too small to populate excited electronic states. It is possible to excite fluorescence in neutral radicals using a laser flash [54] (separate from the source of radical creation) but this is technically difficult, and hence rarely done. The only other method of optical detection is transient absorption, where light at a

particular wavelength is passed through a solution containing the radicals and their concentration is calculated from the amount of light that is absorbed. This is the technique that has been utilised in this study, and is described in greater detail in the following chapters.

2: Structures of Micelles and Vesicles

In order for magnetic field effects to be observed it is often the case that the geminate lifetime of the radical pair must be extended over that seen for neutral RPs in homogeneous solution (which is typically of the order of 10 ns [1]). The most common way for this to be achieved is to encapsulate the RP inside a structure, thus limiting the diffusion of the RP and extending its lifetime, as discussed in section 1.4 (other methods of extending the RP lifetime, and references are also listed in this section). The structures that have been used in this work are all self-assembling, and are formed from amphiphilic molecules. Their properties, and the structures that they form are outlined below.

An amphiphilic molecule is defined as one that contains both hydrophilic and hydrophobic domains within the same molecule. The hydrophilic part can be either ionic, non-ionic, or zwitterionic, and is referred to as the 'head' of the molecule. The hydrophobic part of the molecule is non-polar, and is referred to as the 'tail' of the molecule. At low concentrations, in aqueous solutions, these amphiphiles tend to congregate at the air-water interface, where the head group will be in contact with the water and the tail will be in the air to minimise unfavourable interactions between the non-polar tail and the water.

If an amphiphile is added to water the surface tension of the solution decreases with addition of amphiphile until a critical value is reached, when the addition of more amphiphile no longer results in the lowering of the surface tension. It is at this critical concentration that the amphiphile molecules begin to aggregate into structures within

the bulk of the solution. For micelles this is termed the critical micelle concentration (CMC). The value of the CMC can be measured by a discontinuity in properties such as conductivity or surface tension. The reason for the aggregation of amphiphilic molecules into structures such as micelles and vesicles is the hydrophobic effect.

2.1 The Hydrophobic Effect

Hydrophobic substances are defined as those that are readily soluble in many non-polar solvents, but only sparingly soluble in water. They are distinct from substances that have generally low solubility in all solvents because hydrophobic substances form solids with strong intermolecular cohesion. This distinction means that hydrophobic molecules expelled from water tend to remain in a fluid, deformable state.

The thermodynamic reason for unfavourable interaction between hydrophobic molecules and water is not only due to the enthalpy of mixing (which is usually considered to be positive, but close to zero at room temperature [2]), but also entropic contributions. At temperatures around 25 °C the dominant contribution to the large, positive change in free energy of adding hydrophobic molecules to water is from the entropy [2]. The addition of a hydrophobic molecule to an aqueous solution disrupts the hydrogen-bonded network of water molecules, resulting in a 'cage' of water molecules surrounding the hydrophobic molecule. This ordering of water molecules around the hydrophobic molecule results in a decrease in entropy that outweighs the increase in entropy caused by the mixture of solute and water molecules. With polar solutes the decrease in entropy caused by the rearrangement of the water structure around the solute molecule is outweighed by the decrease in enthalpy caused by the

strong ion-dipole interactions between the water molecules and the polar solute molecules, and hence the polar molecules are not hydrophobic.

For straight chain aliphatic hydrocarbon molecules the change of free energy on transfer from water to a purely hydrocarbon solvent is a linear function of the number of CH_2 groups in the chain [3]. More generally it is approximately proportional to the surface area of the cavity created in the solvent by the hydrophobic solute, or to the number of water molecules forced to be in contact with the hydrophobic molecule. This effect means that if two hydrophobic molecules come together in an aqueous solution the total number of water molecules needed to surround the aggregate is lower than the number of water molecules needed to surround each hydrophobic molecule separately. This release of water molecules back to the bulk solution leads to an increase in the entropy of the solution, and hence aggregation of hydrophobic molecules in an aqueous solution is a favourable process.

2.2 MICELLES

Micelles are structures composed of many amphiphile monomers that, in aqueous solutions, group their tails together to form an oil-like microphase, which excludes water. The head groups are on the surface of this structure, in contact with the water. The cross section of a typical ionic micelle is shown in figure 2.1.

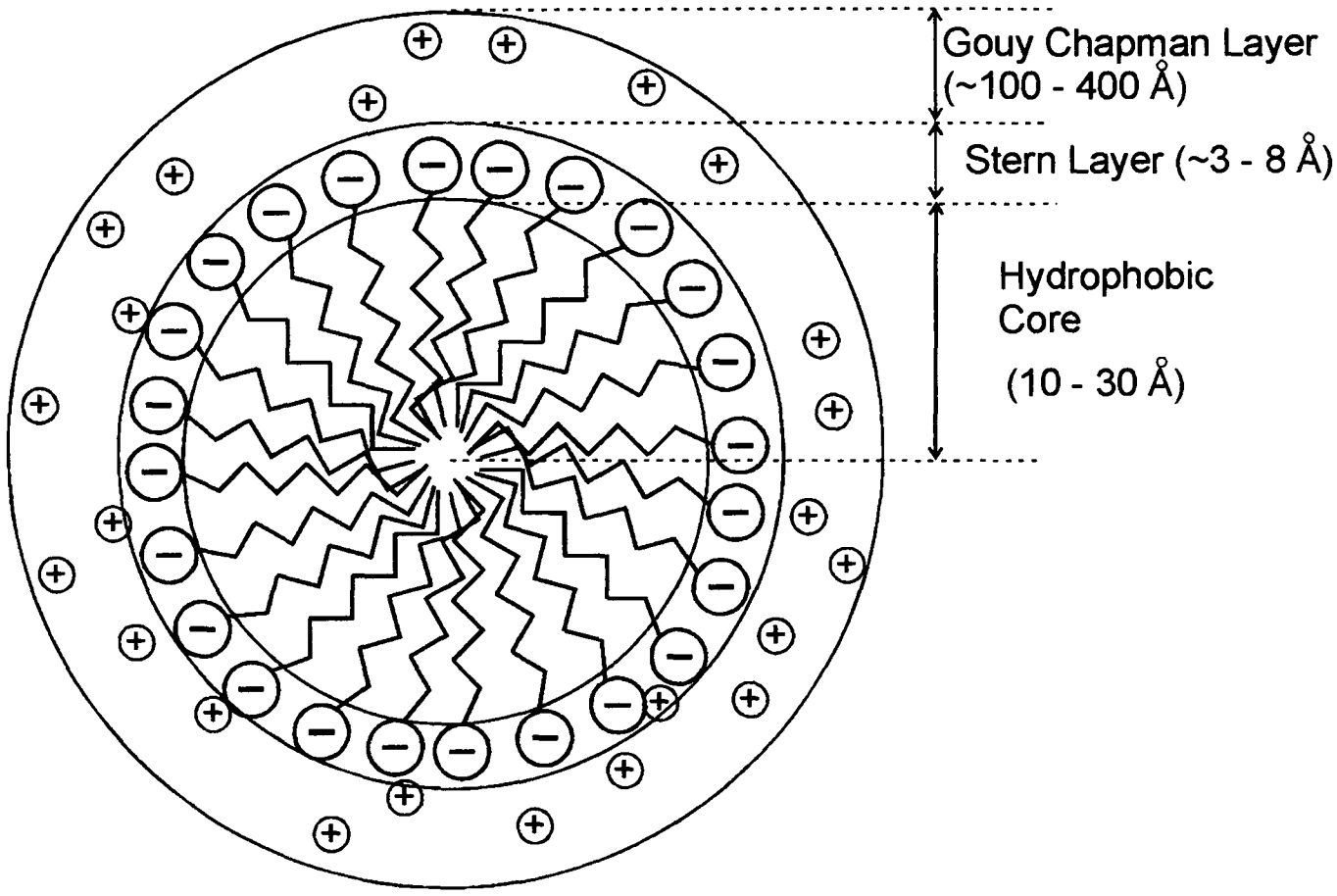


Figure 2.1: Cross-section through an anionic micelle (not to scale)

The hydrophobic core contains the tails of the amphiphilic groups. NMR analysis has shown that these tails are mobile, but their movement is more restricted than a solution of pure hydrocarbon of the same chain length [4]. This is due to the anchoring of the head groups in the Stern layer. The Stern layer defines the location of the charged head groups, and is the closest the water molecules get to the centre of the micelle. The Gouy-Chapman layer contains the counter-ions for the head group, and can be defined as the co-ordination sphere of the micelle.

The number of amphiphile monomers contained in a micelle is known as the aggregation number (N_{agg}), and for ionic micelles at room temperature is usually in the range of 50-100 [5]. The aggregation number of a micelle is an average, for in solution the micelles will have a distribution of aggregation numbers, centred on N_{agg}. Micelles are also dynamic, exchanging monomers with the solution on a microsecond timescale [3]. The aggregation number of a micelle is the result of a competition

between the hydrophobic effect and repulsion between the charged head groups. For effective expulsion of water there needs to be a minimum number of molecules in the micelle. If water molecules are present inside the hydrophobic region then there is no thermodynamic gain from aggregation. The upper limit to the aggregation number of micelles comes primarily from repulsion between the head groups. In ionic micelles this is due to electrostatic repulsion between the charged head groups; as the aggregation number is increased the head groups are forced closer together, and eventually a limit is reached where the thermodynamic gain in removing the hydrophobic tail from the aqueous solution is outweighed by the amount of energy needed to overcome the electrostatic repulsion of the head groups.

As well as a minimum concentration of amphiphile needed for micelle formation there is also a minimum temperature below which micelles will not form, this is known as the Krafft temperature. At temperatures lower than the Krafft temperature the saturated amphiphile solution will be in equilibrium with solid amphiphile. Whereas the CMC is primarily determined by the nature of the hydrophobic group, the Krafft temperature depends on the nature of the head group and the length of the hydrophobic chain. The tails of the molecules must be in a liquid state for micelles to form, which means the Krafft temperature increases with chain length. However, solidification can be hindered if the size of the head group prevents the hydrophobic tails of the molecules coming in close contact. For this reason an increase in head group size leads to a decrease in the Krafft temperature.

2.2.1 Adding Substrates to Micelles

Micelles can be used to solubilise a wide range of hydrophobic molecules in aqueous solutions, since the micelles contain an aliphatic core where the hydrophobic molecule is shielded from interactions with water molecules. This is advantageous for studying RP reactions, due to the increase in geminate lifetime over homogeneous solutions of the same viscosity. When the RP is formed in the interior of the micelle, the cage formed by the micelle encloses the RP, and limits the diffusion to a greater extent than would be seen with homogeneous solutions.

The solubilised hydrophobic molecules are distributed amongst the micelles with a Poisson-Boltzmann distribution:

$$P(n) = m^n \frac{e^{-n}}{n!} \qquad (2.1)$$

where $P(n)$ is the probability of finding n solute molecules in a given micelle, when the mean occupation number of solute molecules per micelle is m, where m is defined as:

$$m = \frac{N_{agg}[\text{solute}]}{[\text{amphiphile}] - \text{CMC}}. \qquad (2.2)$$

In some experiments described in this thesis a large number of molecules (used as hydrogen donors, see section 4.2) were added to the micelles, sometimes as many as 60 substrate molecules per micelle. This will cause a change in micellar properties in some, perhaps drastic, way. Research has been undertaken investigating the effect of

adding butane to aqueous SDS solutions [5A], where it was shown that when the concentration of butane is increased from 10% to 40% of the SDS concentration, the radius of the SDS micelles is only increased by approximately 8%. However, to fully understand the effect of the high concentration of substrate molecules on the micelle structure in the MFE experiments the micelles should have been characterised in the presence of these molecules.

The molecules used to form micelles in this work can be divided into two categories, those which can be found in biological systems and those which are entirely synthetic. The synthetic micelle category can then be divided into two further categories, those with negatively charged head groups and those with positively charged head groups. It is also possible to form micelles from molecules with neutral head groups (*e.g.* the Brij family of micelles) but as these have not been used in the studies presented here, they will not be discussed.

2.2.2 Synthetic Micelles – Negatively Charged Head Groups

The most common micelle used for the study of magnetic field effects on radical pair reactions is sodium dodecyl sulfate (SDS), the structure of which is shown in figure 2.2.

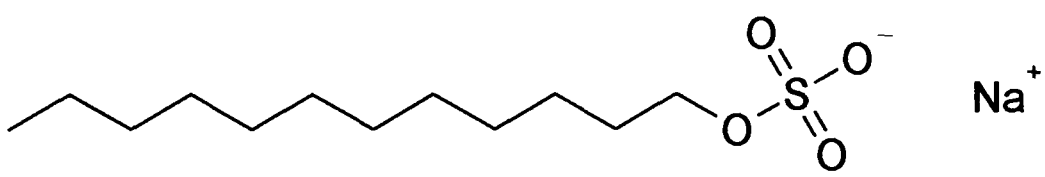


Figure 2.2: The structure of an SDS monomer

SDS micelles have been used to contain RPs to investigate MFEs at magnetic field strengths ranging from those as weak as the Earth's magnetic field [6] up to magnetic field strengths of 30 T [7]. In this work SDS has been used as the standard with which to compare other micellar and vesicular systems, as it gives the best signal to noise ratio of all systems investigated, and is also the easiest to prepare. Of all micellar systems used in RP studies SDS is the most commonly employed in the literature, which means that data are easily available.

2.2.3 Synthetic Micelles – Positively Charged Head Groups

The second class of synthetic micelles is those with positively charged head groups. In chapter five a series of cationic micelles is studied, which have the same head group, but differing lengths of alkyl chain. The generic structure is shown in figure 2.3, the micelles studied have values of n ranging from twelve to eighteen.

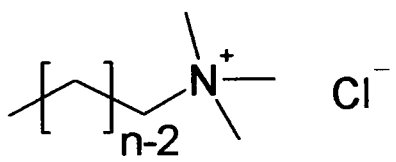


Figure 2.3: The generic structure of a trimethylammonium chloride monomer

The four alkyl trimethyl chlorides used are dodecyl trimethylammonium chloride (DTAC, n = 12), tetradecyl trimethylammonium chloride (TTAC, n = 14), hexadecyl trimethylammonium chloride (CTAC, n = 16), and octadecyl trimethylammonium chloride (OTAC, n = 18). The most commonly used cationic micelle in MFE studies is CTAC *e.g.* [8-11].

2.2.4 'Biological' Micelles

The molecule used to form these micelles is lysophosphatidyl choline (LPC), the structure of which is shown in figure 2.4. LPC is a natural constituent of many biological membranes, so is a good candidate for studying MFEs in systems of a more biological nature than synthetic micelles.

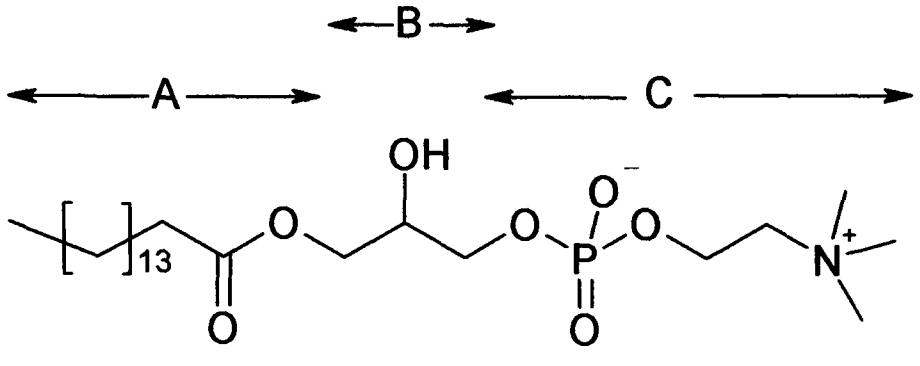


Figure 2.4: The structure of an LPC monomer, with a 16 carbon hydrophobic tail

The structure of the molecule can be divided into three parts, the hydrophobic alkyl chain (section A), the glycerol group (section B), and the large zwitterionic, polar head group (section C) based on the alcohol choline bonded to the glycerol backbone via a phosphate ester. The hydrophobic chain in figure 2.4 has a length of sixteen carbons, but chain lengths of 12 to 18 carbons are common in nature. LPC micelles with a single chain length are known by the traditional name for the length of the chain, for example the LPC in figure 2.4 is palmitoyl LPC. The hydrocarbon tail can also be esterified at the *sn*-2 position of the glycerol backbone, and it has been found that at equilibrium the ratio of acyl chains in the *sn*-1 to the *sn*-2 position is about 9 to 1 over the range pH 6.2 and 9.0 [12]. The rate constant for the migration is about $4 \times 10^{-4}\ M^{-1}\ s^{-1}$ for the acid catalysed reaction between pH 1.0 and 2.0, and about $160\ M^{-1}\ s^{-1}$ for the base catalysed reaction between pH 6.2 and 9.0 [12]. LPC is a member of a class of molecules known as lysophospholipids, which consist of a

hydrophobic chain attached to a glycerol backbone and a phosphate ester linkage to a hydrophilic group. Some common hydrophilic groups include those based on choline, ethanolamine, glycerol, and serine.

Whilst LPC is a natural constituent of many biological membranes, micelles formed from LPC only are not found in nature. LPC is found to form between about 0.5% and 6.0% [13] of many biological membranes, and indeed lysophospholipids are formed by the action of phospholipases on phospholipid molecules in membranes. Lysophospholipids have been used in this study as an intermediate step between well-studied synthetic micelles, such as SDS, and more complicated, biologically relevant structures such as phospholipid vesicles.

2.2.5 Properties of Micelles

The physical properties of micelles vary greatly depending on factors such as the identity of the head and tail groups, and experimental conditions such as temperature and the ionic strength of the solution.

	SDS	DTAC	TTAC	CTAC	OTAC	LPC[A]
Head group charge	Negative	Positive	Positive	Positive	Positive	Zwitter-ionic
N_{agg}	65[14]	51[15]	69[15]	89[15]		139[16]
CMC / mM	8.3[17]	16[18]	5.4[18]	1.3[19]	0.39[20]	0.0076[21]
Microviscosity / cP	19[22]	18[22]		42[22]		10.4[23]
Micelle radius / Å	17.5[24]	17[25]	19[25]	22[25]		26.7[26]

Table 2.1: Physical properties of micelles used in this thesis. (A: for a chain length of 16)

In the cationic micelle series the only change in structure is an increase in the hydrophobic chain length, and table 2.1 highlights trends such as the increase in N_{agg} and the decrease in CMC with increasing chain length. Microviscosity data is only available for two of the cationic species studied, but it has been noted [27] that, as in normal hydrocarbon liquids, the viscosity of the local environment in the local hydrocarbon core increases with increasing alkyl chain length as a result of an increased probability for these interchain entanglement processes.

In general for micelles an increase in the temperature of the solution leads to a decrease in N_{agg}, as can be seen in table 2.2 for SDS micelles.

Temperature / °C	20	31.7	41.5	51.4
N_{agg}	75	68	59	49

Table 2.2: Variation of N_{agg} with temperature. ([SDS] = 100 mM, Krafft temp. = 9 °C) [28]

2.3 VESICLES

Not all amphiphiles assemble to form micelles; some molecules have a geometry that precludes micelle formation. To effectively form a micelle the constituent molecules need to have a roughly conical shape, with the head group as the base of the cone, tapering towards the end of the hydrocarbon tail and allowing the formation of spherical micelles. For amphiphilic molecules with a more bulky hydrophobic region this is not possible, and many of these types of molecules form vesicles, whose structure is shown in figure 2.5.

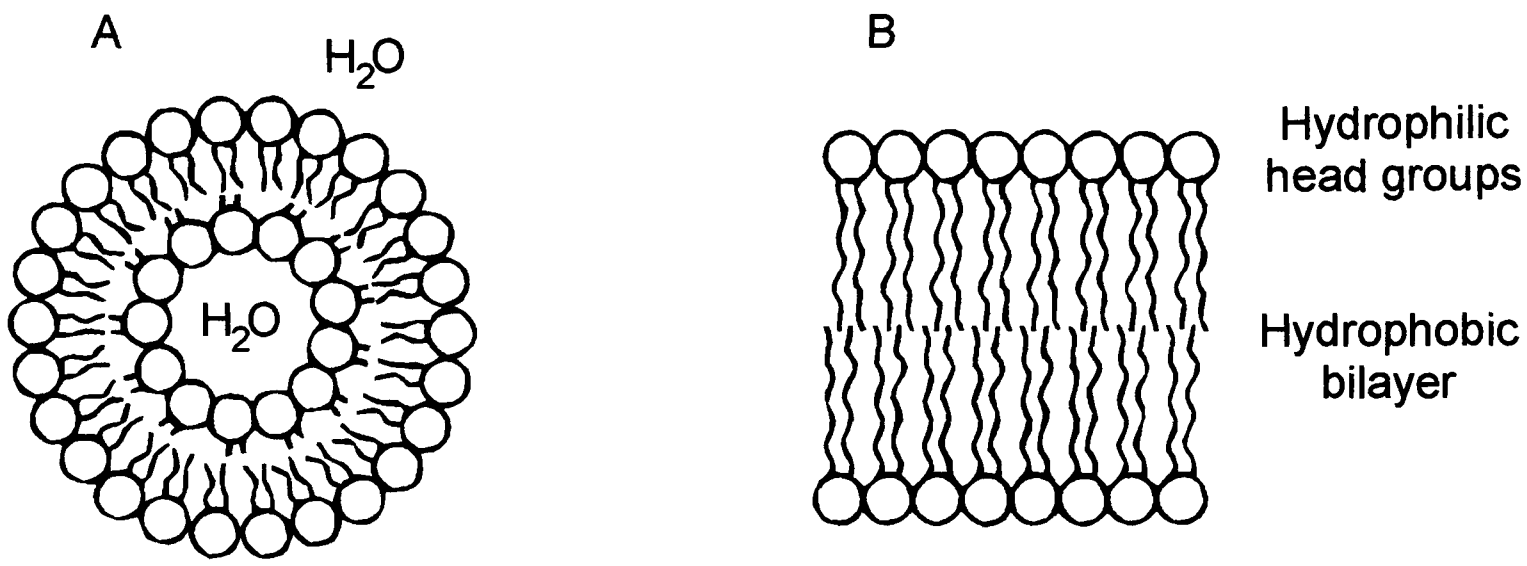


Figure 2.5: A) Cross-section through a vesicle, and B) close up of the bilayer (not to scale)

Vesicular systems have three well-defined regions, the entrapped water core, the hydrophobic bilayer, and the bulk water phase external to the vesicle. Lateral diffusion of phospholipid monomers is much faster than transverse diffusion across the bilayer as transverse diffusion requires the polar head group to diffuse through the hydrophobic region of the bilayer. For phospholipid membranes the rate of change of lipids between opposing layers of vesicle has been measured to have a half life of between 6.5 hours [29] and 16 to 69 days [30], depending on the composition of the membrane.

Not all vesicles have the exact structure shown in figure 2.5, which has only one bilayer in the structure and is called unilamellar, or single-walled. Vesicles can also be formed which are multilamellar and have several bilayers sandwiched one on top of the other, with an aqueous phase separating each bilayer. Dissolving vesicle-forming amphiphiles in water tends to lead to multilamellar vesicles, but (as first observed in 1962 [31]) sonication of these solutions leads to small, unilamellar vesicles being formed. It has been shown that increasing the sonication time results in a decrease in the viscosity and turbidity of the solution down to a point where further sonication has no appreciable effect. This point is considered to correspond to the appearance of

single compartment, unilamellar vesicles [32]. All the vesicles used in this thesis have undergone experiments to determine the length of sonication needed to achieve the point where further sonication ceases to have an effect on the results, and are therefore assumed to be unilamellar.

The high curvature of the vesicle wall makes the external area of the bilayer three times as large as the internal area, and it causes the hydrocarbon chains entering from the external side to extend into a space of continuously decreasing radius, while those entering from the inside extend into a radially expanding space. As a result of this unavoidable asymmetry there are more than twice as many molecules in the outer half of the bilayer than in the inner half. The outer half is thicker than the inner half because the increasing constriction forces the hydrocarbon chains to be more fully extended, and the area per head group is substantially larger on the outside than on the inside. [3]

Due to the increased size of the hydrophobic region, the CMCs of vesicle forming molecules are much smaller than those of comparable micelle forming molecules, for example dipalmitoyl phosphatidyl choline (a phospholipid that forms vesicles) has a CMC of 4.7×10^{-10} M [33], but palmitoyl lysophosphatidyl choline (a lysophospholipid that forms micelles) has a CMC of 7×10^{-6} M [34].

2.3.1 Phase Transitions in Vesicles

Another difference between micelles and vesicles is that at all temperatures above the Krafft temperature the hydrocarbon chains in the hydrophobic core of micelles are in a liquid-like state. Vesicles have a characteristic phase transition temperature where the

hydrocarbon chains in the hydrophobic bilayer change from a gel-like state to a liquid-like state as the temperature is increased. This phase change corresponds to a rapid change in the freedom of rotation about the C-C bonds of the hydrocarbon chains over a small temperature range. Whereas in the gel state the tails are in an extended, all-*trans* configuration, in the liquid-like state the chains are all highly disordered. Since freedom of rotation about C-C bonds in a particular chain requires the neighbouring chains to be fluid (for simple steric reasons), the melting transition is therefore co-operative. The phase transition in vesicles happens over a small range of temperature. This contrasts with a 'classical' phase transition, which occurs sharply at a single temperature, with the two phases of the substance co-existing in equilibrium only at this one temperature [35]. The transition temperature of the vesicle increases with increasing chain length, and the degree of saturation of the hydrocarbon chains.

As with the micelles two types of vesicle were used in this study, one synthetic and one of a more biological nature.

2.3.2 Synthetic Vesicles

The synthetic vesicle used in this study is dioctadecyl dimethylammonium chloride (DODAC). The structure of this molecule resembles that of OTAC, but with one of the methyl groups replaced by another octadecyl hydrocarbon chain. The structure of DODAC is shown in figure 2.6.

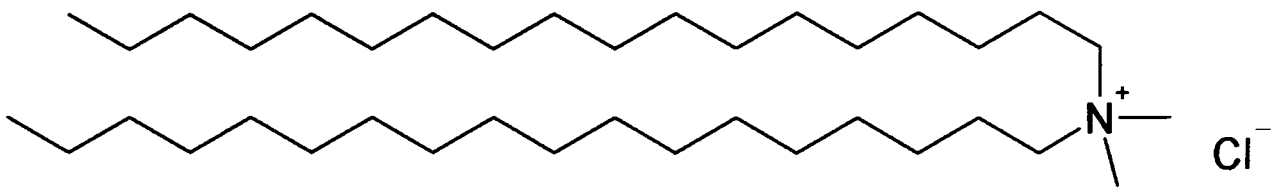


Figure 2.6: The structure of a DODAC monomer

Phase transitions of DODAC vesicles have been established to occur between 30 °C and 36 °C [36]. Below 30 °C DODAC vesicles are likely to consist of a bilayer with the hydrocarbon chains fully extended and somewhat tilted [37]. Between 30 °C and 36 °C the fully extended surfactant molecules are distorted by periodic undulations. At 36 °C the hydrocarbon chains 'melt' by assuming mobile liquid-like arrangements [32].

MFEs on RPs in vesicles have been studied far less than those in micelles. Studies have been undertaken in DODAC using product studies and laser flash photolysis to investigate the behaviour of RPs derived from 1,1-diphenylacetone, (DPA) and 1,1,3,3-tetraphenylacetone, (TPA) [38], and dibenzyl ketone (DBK) [39]. MFEs were seen with TPA and DBK, but not with DPA. The strengths of the magnetic fields used in these studies were of the order of 100 mT, or greater. Studies at lower magnetic field strengths have not been performed before. All the molecules used in references [38] and [39] photolyse to form the RPs, and previous to this thesis there have been no studies on the effect of magnetic fields on RPs formed by hydrogen abstraction in DODAC.

2.3.3 Biological Vesicles

The molecules used in this work to form biological vesicles belong to a class of molecules named phospholipids. They are related to the lysophospholipids seen earlier, but have two hydrophobic alkyl chains where the lysophospholipids have only one. The structure of a typical phospholipid molecule is shown in figure 2.7.

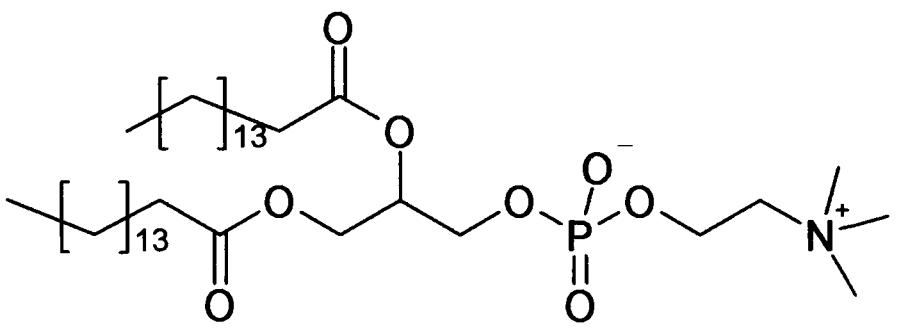


Figure 2.7: The structure of PC monomer, with two 16:0 hydrocarbon chains

As with the LPC, the hydrophilic head group on the phospholipids used in this work is made from choline, attached to the glycerol backbone by a phosphate ester. This type of phospholipid is called phosphatidyl choline (PC), and is the most common type of phospholipid found in animal cell membranes. The human red blood cell contains at least twenty different molecular species of PC, and a total of some 150-200 chemically distinct lipid molecules [40]. The two hydrophobic chains in phospholipids do not have to be of identical length, and can consist of saturated or unsaturated chains. They are labelled X:Y, where X is the number of carbon atoms, and Y is the number of C=C double bonds in the chain, so for example dipalmitoyl PC, which has two saturated sixteen carbon chains would be labelled 16:0.

Phospholipid molecules generally form vesicles in aqueous solutions, but if the two hydrocarbon chains are very short (5 carbon atoms, or shorter) they will form micelles instead [3].

Pure anhydrous phospholipids are solids with very high melting points. The melting points are unrelated to hydrocarbon chain length, or degree of unsaturation. This in itself suggests that hydrocarbon chains are already in a liquid-like state at the melting point, and that the melting process primarily reflects the disruption of intermolecular bonds between head groups. Support for this conclusion is provided by the observation of a major phase transition within the solid state at temperatures below the true melting point. Similar phase transitions, but at temperatures below those at which they occur in the anhydrous solid, are observed in aqueous phospholipid dispersions and in small single-walled vesicles [3].

MFEs have been observed in phospholipid vesicles, and have been used to investigate the molecular dynamics and phase transitions of bilayers [41, 42]. Linked radical ion pairs consisting of zinc porphyrin, and viologen, linked by various 'spacer' hydrophobic chains were incorporated into phosphatidyl choline vesicles, and the effect of magnetic fields on the recombination kinetics was studied at magnetic field strengths of up to 240 mT. It was found that increasing the magnetic field strength led to a decrease in the recombination rate of the RPs. As with the DODAC vesicles no MFE studies of RPs formed by hydrogen abstraction inside phospholipid vesicles have been undertaken, before the work described in this thesis.

2.3.4 Properties of Vesicles

Table 2.3 shows some properties of the vesicles discussed in sections 2.3.2 and 2.3.3.

	DODAC	PC
N_{agg}	19100[43]	2450[32]
Microviscosity / cP	144[44]	291[44]
Bilayer thickness / Å	50[43]	37[45]
Hydrated vesicle radius / Å	396[43]	105[45]

Table 2.3: Physical properties of vesicles used in this thesis

Comparing tables 2.3 and 2.1 it can be seen that vesicles form much larger structures than micelles, as would be expected. The microviscosity inside the vesicles is also larger than that in the micelles, so the diffusion of RPs in vesicles is expected to be slower than in micelles. This may impact on the magnetic field effects in a number of ways; the increased viscosity will lead to slower separation of the RP and hence the exchange interaction could have a larger effect. Slower diffusion in vesicles than in micelles could also lead to faster relaxation of the RP and smaller MFEs in vesicles. However, the larger viscosity and size of vesicles over micelles will also lead to slower escape rates of the RP from the geminate stage, which could in turn lead to an increased re-encounter rate, and larger MFEs. Escape from the geminate RP in micelles usually implies escape of one of the members of the RP into the bulk solution, however, the larger size of vesicles, and their double layer structure means that the individual members of the RP do not necessarily have to escape into the bulk solution to escape from the geminate RP. One other consideration is the number of RPs per structure. The smaller size, and lower aggregation numbers of micelles means that even with the order of one RP per micelle the absorption signal is large enough to detect MFEs. If vesicles were to have an occupation number of the same order either the concentration of vesicles would be so large that the amphiphilic molecules would not dissolve, or the concentration of hydrogen abstracting probe molecule would be too small for any absorption to be detected. For this reason higher occupation numbers have been used in the study of MFEs in vesicles. However, this is not expected to

influence the RP behaviour, or MFEs, as the ratio of concentrations of probe molecules to amphiphilic molecules is approximately constant in both micelles and vesicles, and so the total hydrophobic volume per probe molecule should be of the same order of magnitude in both types of structure.

3: METHODS AND MATERIALS

As described in chapter one, the investigation of magnetic field effects requires a system in which either the rate of spin mixing or the concentration of one or more of the products can be quantitatively measured. It is technically very difficult to observe the rate of spin mixing directly, and the most common approach is to determine either the radical concentration, or the ratio of product concentrations when geminate and escape reactions give different products. The work in this thesis is focused on the study of neutral radical pairs, and the method of observation utilised is optical absorption of the transient radical species. As opposed to fluorescence measurements, absorption is not a zero background technique, which makes the observation of small changes in the concentration of the radicals more complicated. The radicals are generated using a short laser pulse, and a second, continuous, light source is employed to determine the absorption of one of the radical species, and hence give a time resolved measure of the radical concentration. This technique is known as laser flash photolysis (LFP).

Absorbance methods have been extensively used in the investigation of magnetic field effects on neutral RP reactions. The initial experiments were concerned with the effects of magnetic fields stronger than the average hyperfine coupling of the RPs and were performed on radical pairs derived from benzophenone (BP) or dibenzylketone (DBK) in SDS micelles [1, 2]. These showed that the rate constant for the geminate recombination reaction of the RP decreased with increasing magnetic field strength. A significant number of MFE studies have been carried out using LFP in micellar solution and can be subdivided into two classes; photoreduction reactions, and photodissociation reactions. In photoreduction reactions the laser flash induces

hydrogen abstraction by a probe molecule (usually BP, naphthoquinone, or a derivative of one of the two) from either a micelle monomer, or an additional hydrogen donor [3-9]. Photodissociation reactions form a RP from a single precursor; the laser flash causes the probe molecule inside the micelle to undergo homolysis to form the neutral RP. The most common studies have involved DBK, or deoxybenzoin, and their derivatives [10-13].

The effects of weak magnetic fields on neutral radical pairs have been studied to a much smaller extent, with only a few observations of the LFE made by flash photolysis methods. Shkrob et al. [14] observed the LFE for RPs formed from photodissociation of derivatives of deoxybenzoin in SDS micelles. Tarasov et al. [15] also observed the LFE with RPs derived from the photodissociation of deoxybenzoin in alkyl sulfate micelles of varying chain lengths. Eveson et al. [16] again investigated the effect of chain length of a series of alkyl sulfate micelles at weak magnetic fields, but using RPs formed from the photoreduction of BP.

The work presented in this thesis is concerned with the photoreduction of BP (or a BP derivative) contained in either micelles or vesicles. The reaction scheme was shown in figure 1.5, and depicts the generation of the RP. The ground state BP molecule is excited by the laser pulse to an excited singlet state, which subsequently undergoes rapid ISC to an excited triplet state. This triplet state BP abstracts a hydrogen atom from a suitable donor, either a monomer from the micelle or vesicle, or any additional hydrogen donor that may have been introduced into the system. The hydrogen abstraction step forms the triplet RP, consisting of the $BPH^{\bullet}$ ketyl radical, and the radical formed by the molecule that underwent hydrogen abstraction.

3.1 Concentration and Extinction Coefficient

Radicals can undergo transitions between their electronic states when exposed to light in the UV or visible region of the spectrum. The intensity of light which is absorbed by a solution can be used to calculate the concentration of the species in the solution. The Beer-Lambert law shows this relationship:

$$I = I_0 \, 10^{-(\varepsilon c l)} \qquad (3.1)$$

where I is the transmitted light intensity, I_0 is the incident light intensity, ε is the molar absorption coefficient, c is the concentration of the sample, and l is the length of the analysis beam through the sample. The product of the last three values, A, is the absorbance of the sample.

$$A = \varepsilon \, c \, l = \log (I_0 / I) \qquad (3.2)$$

The absorbance is calculated from the light intensity that is absorbed as the light passes through a solution containing the radicals, and as it is proportional to the radical concentration it provides a way of assessing the radical concentration, and any changes in this parameter which may be caused by a magnetic field.

3.2 Experimental Apparatus

Figure 3.1 shows a flow diagram of the experimental apparatus and is described in more detail in the section below.

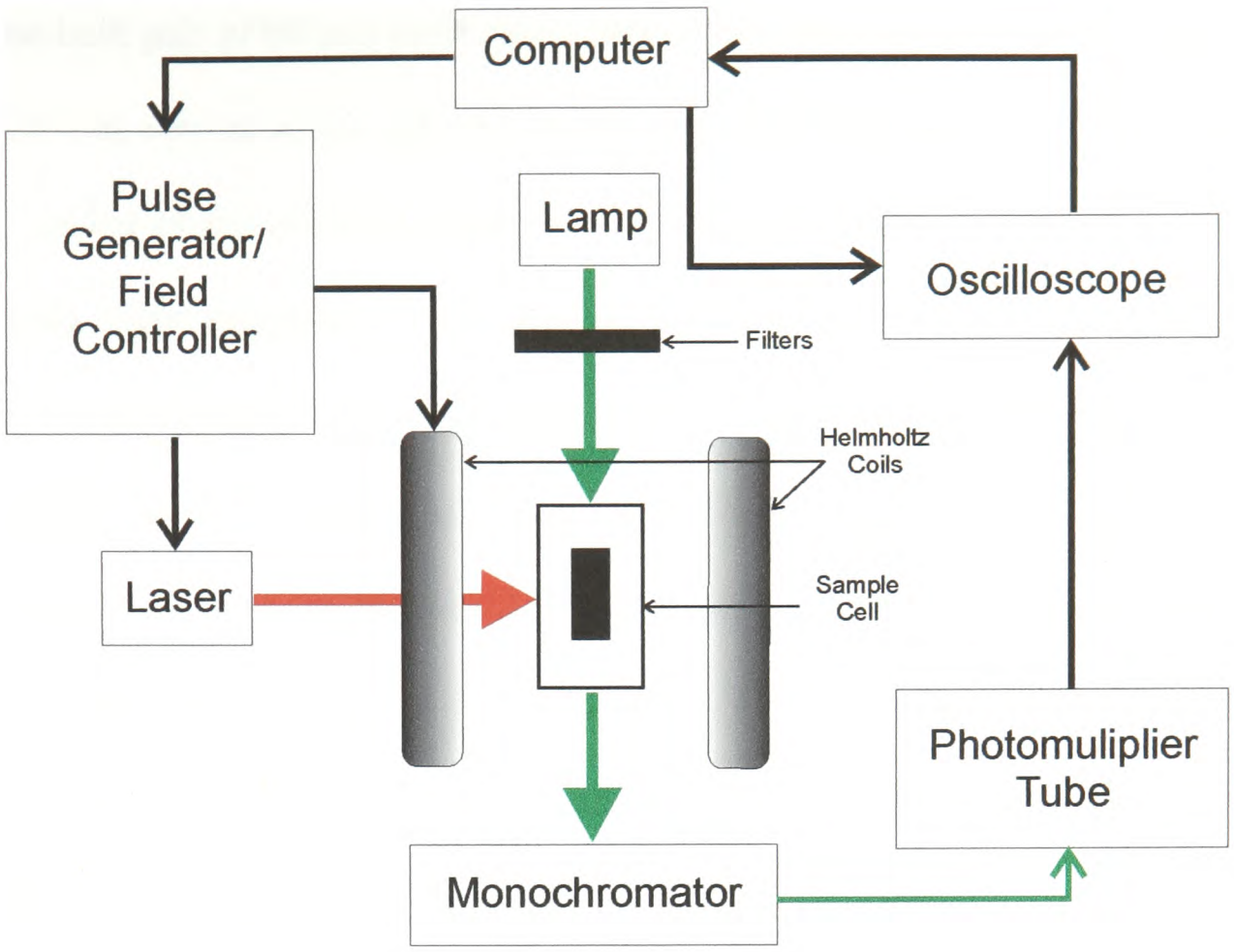


Figure 3.1: Flow diagram of experimental apparatus

Radicals were created using pulses from a Lambda Physik COMPex 102 XeCl excimer laser at a wavelength of 308 nm, pulse energy of 80 mJ, and pulse width of 20 ns, or a Spectra-Physics Quanta Ray GCR-130 Nd:YAG laser at a wavelength of 355 nm, pulse energy of 70 mJ, and pulse width of 5 ns. The repetition rate was approximately 1.5 Hz for both lasers. The sample solution was flowed through a silica cuvette of 565 mm^3 volume, and analysis light path length of 45 mm (see section 3.6.1) where it was irradiated by the laser light. Light from a 1000 W Oriel Xe arc lamp was passed through the cell perpendicular to the laser beam, and then entered a monochromator in series with a Hammamatsu R1913 fast photomultiplier tube (PMT). The PMT output was fed to a Tektronix 500 MHz two channel digital oscilloscope that stored and averaged a user defined number of traces before sending the results to a personal computer.

A home-built pair of 80 mm radius Helmholtz coils provided a magnetic field of up to ~18 mT. The current to the coils was supplied by the pulse generator / field controller under control of the personal computer. The magnetic field was pulsed at the same rate as the laser, typically 1.5 Hz, with an "on" time of 150 μs. This pulsing of the magnetic field prevents ohmic heating of the coils at the higher current levels needed to generate the larger magnetic fields. The whole timing of the experiment was controlled by the pulse generator / field controller with the laser pulse timed to occur after the magnetic field had reached a constant value, as is shown in figure 3.2. Note that the laser pulse itself is only 20 ns long, and it is the signal from the pulse generator (indicated in red in figure 3.2) that triggers the laser.

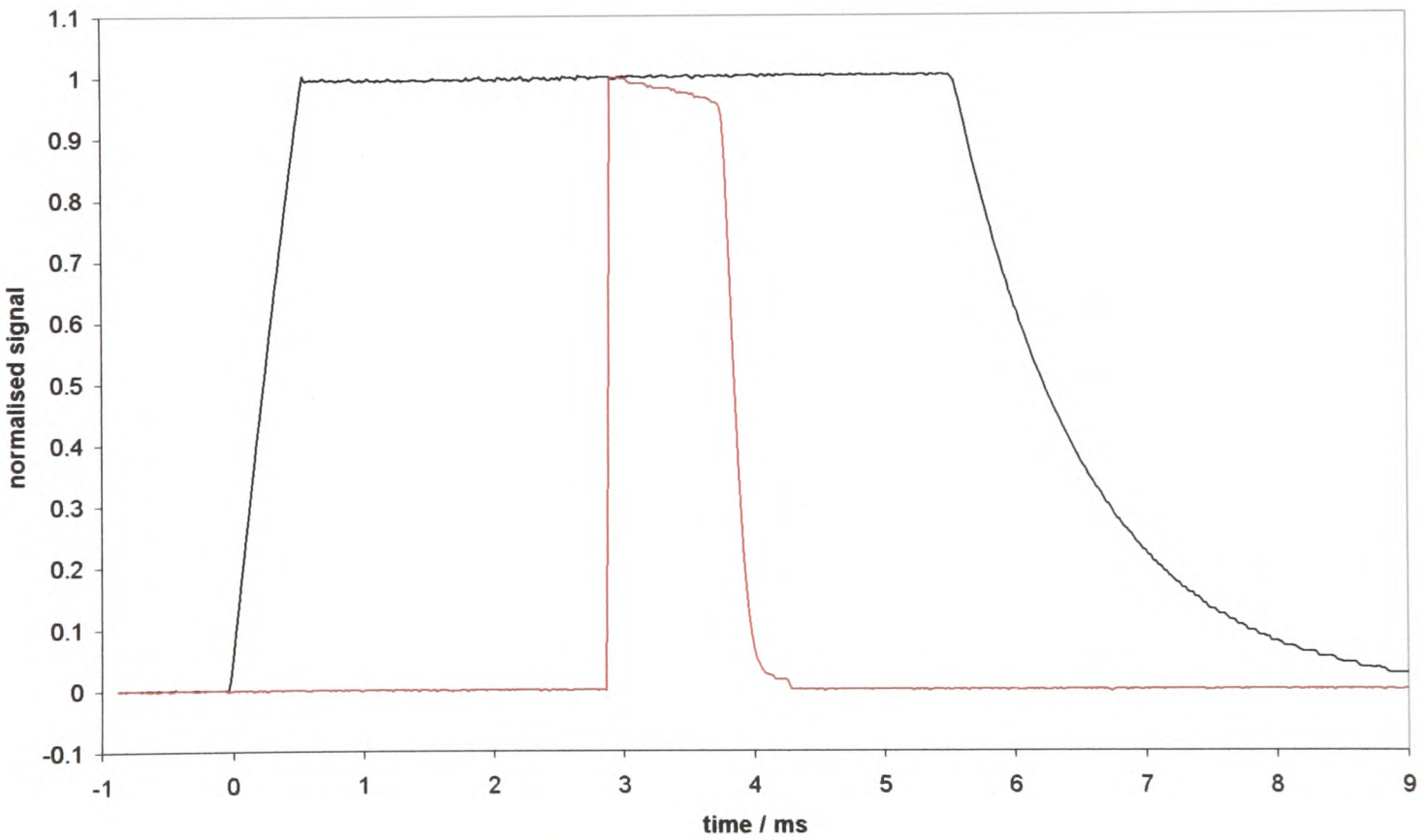


Figure 3.2: The timing of the (•) magnetic field (as measured by Hall probe), and (•) laser trigger signal from pulse generator

A dedicated PC running custom written software written in National Instruments LabVIEW controls the experiment. This software regulates the type of measurements

taken (as discussed in section 3.5), the number of averages recorded, and the magnetic field strength applied to the sample.

3.3 Solution Preparation

All chemical systems used were composed of a hydrogen abstractor probe molecule inside a confined structure such as a micelle or vesicle comprised of amphiphilic molecules. A variety of amphiphile and hydrogen abstractor probe molecules were studied in the course of this work, and their properties and characteristics will be described in detail in the corresponding chapters and sections. Solutions were prepared by weighing out the required amount of hydrogen abstractor and amphiphile and adding approximately 90% of the distilled water needed to make the total volume of solution. The resulting solution was prepared by sonication in an Ultrawave ultrasonic bath for at least one hour. The water in the ultrasonic bath was maintained at constant temperature by circulation through a thermostatted system external to the bath. Sonication was carried out at room temperature for the micellar solutions, and at higher temperatures for vesicle solutions. When hydrogen donors other than the amphiphile molecules were present they were added to the solution for the last hour of sonication. After sonication the solution was cooled to room temperature and the remainder of the distilled water was added to the solution to achieve the correct volume. In most cases this was 250 ml, but for experiments with a limited supply of reagents, 100 ml solutions were used.

3.4 ABSORPTION SPECIFICITY

One of the problems with radical detection using light absorption is that excited triplet states often have electronic absorption bands very close in frequency to the radicals that they produce, the hydrogen abstractor molecules used in this thesis are no exception. This is inconvenient because long lived molecular triplet states will also absorb the analysis light, and add to the absorption signal given by the radical species at a given wavelength. This scenario is demonstrated here for the case of BP. The excited BP triplet molecule has an absorption peak centred at 525 nm, with an extinction coefficient of 1.03×10^4 M^{-1} cm^{-1} (measured in hexane, [17]), while the $BPH^{\bullet}$ ketyl radical has an absorption peak centred at 545 nm, with an extinction coefficient of 7.9×10^3 M^{-1} cm^{-1} (also measured in hexane, [17]). The BP excited triplet lifetime is significantly shorter than that of the ketyl radical, but it is important to minimise the contribution of the former to the signal produced by the latter by choosing an appropriate wavelength to discriminate in favour of radical detection. The lifetime of the excited triplet state of BP is 6.9 μs in benzene [18], but this shortens to 320 ns in an SDS solution [4] where ketyl formation can take place. In SDS solution the lifetime of the BP ketyl radical is one to two orders of magnitude greater than the lifetime of the excited triplet state, as can be seen from the time curves in chapter four.

To illustrate the problem of absorption specificity further, and to show the overlap of the two spectra, figure 3.3 shows the transient absorption spectra for a derivative of BP, 4-benzoylbenzoic acid (BP-COOH) another photoactive compound used during the course of this work. The black curve is BP-COOH in acetonitrile (MeCN), an aprotic solvent that does not undergo hydrogen abstraction. The red curve is

BP-COOH in an aqueous SDS micellar solution. It should be noted that although there is no ketyl radical formed in the reaction of BP-COOH in MeCN the converse is not true for the reaction of BP-COOH in the micellar solution. As the excited triplet state is the precursor for the radical, it is impossible to form the radical in the absence of the excited triplet state. However, the spectra shown in figure 3.3 show the absorbance 500 ns after the laser flash, so by this time all the triplet BP-COOH should have reacted in the micellar solution to form the radical species. The purpose of taking the spectra in the two environments is to determine a wavelength that minimises the contribution of the excited triplet state, whilst maximising the contribution from the radical.

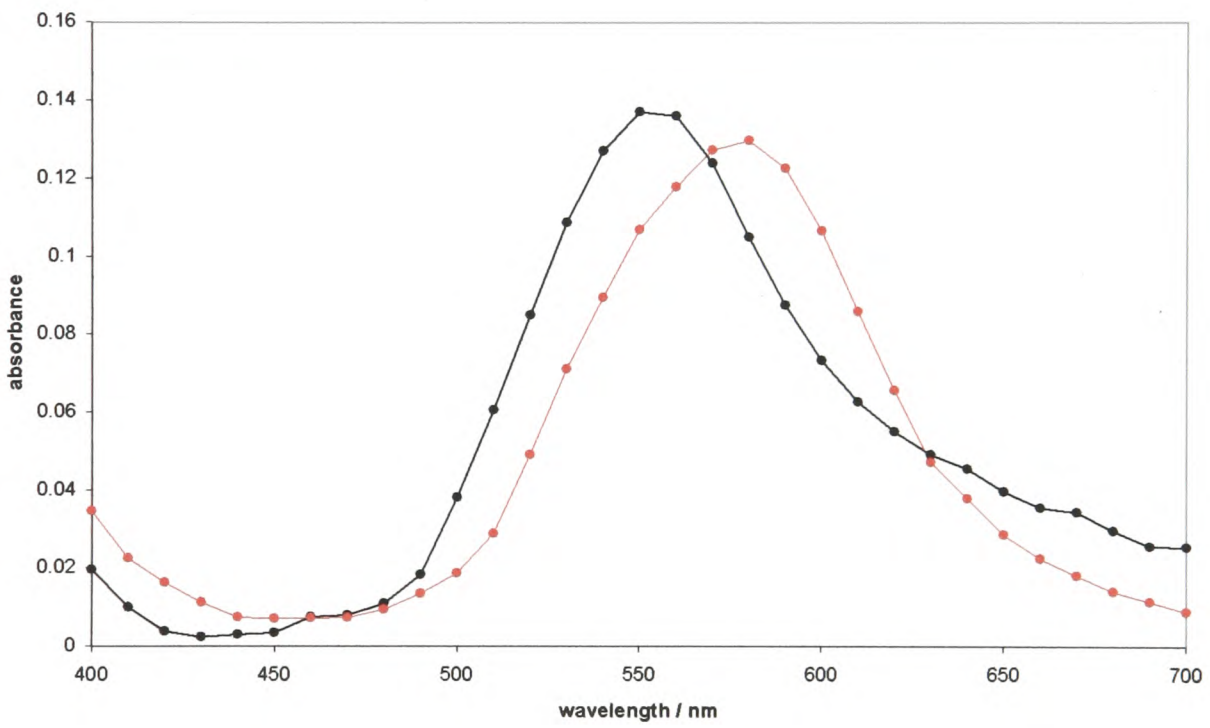


Figure 3.3: Transient absorption spectra of (●) BP-COOH/MeCN, and (●) SDS/BP-COOH 500 ns after laser flash

In further experiments using BP-COOH it was decided to use analysis light at a wavelength of 580 nm as this gave the largest difference between the triplet and radical signals, whilst still having a large enough absorption value to investigate MFEs.

A further possible method for detecting the influence of excited triplet to the absorption of the analysis light is outlined in [4]. Here it is suggested that if two wavelengths can be found in which the ratio of extinction coefficients for the two species differ considerably then the signals from the two species can be deconvoluted. This approach however has not been attempted in this thesis.

All the methods described so far in this section involve detection of the $BPH^{\bullet}$ radical. This is understandable as the BP molecule is chosen for its optical properties, however its main drawback is the problems with the absorption of the excited triplet BP. A way to circumvent this completely would be to detect the counter radical formed, rather than the $BPH^{\bullet}$ radical. The counter radical is formed when the excited BP abstracts a hydrogen atom from a suitable donor molecule. In most of the thesis this is either a micelle or vesicle molecule, or a specific hydrogen donor that has been added to the solution. As the donor molecule is in the ground state when the hydrogen is abstracted there are no problems with absorption specificity, unless the ground state molecule happens to absorb in the same region of the spectrum. The drawback with detecting the counter radical is that none of the counter radicals used in this work absorb strongly enough in the visible region for useful data to be obtained. For example the radical formed by hydrogen abstraction from 1,4-cyclohexadiene (see section 4.2, etc.) has an absorption peak in the UV region at around 315 nm [18A], which is too close to the frequency of the excimer laser for detection. It also has a second peak in the visible region, but this is much weaker, and too small to be useful for detecting MFEs.

3.5 Typical Measurements and Results

As discussed above the experimental apparatus is used to measure the amount of light absorbed by radical species as a function of time. This data can be used in two ways, either to calculate the absorbance (as defined in equation 3.2) as a function of time, or to find the MFE at a certain value of the applied magnetic field strength. The signal from the PMT was recorded for 10 μs by the oscilloscope, and averaged, before being sent to the personal computer. Before the experimental run commenced a measurement was taken of the intensity of analysis light that passes through the solution in the absence of any preceding laser firing, this is the transmitted light I_0, measured in volts by the PMT. The I_0 value was recorded again at the end of the experimental run to check for consistency.

A typical time curve showing the absorbance of the benzophenone ketyl radical in micellar solution is shown in figure 3.4. There are two distinct regions in the time curve shown in figure 3.4 (marked A and B). These are approximately the geminate (A), and F pair (B) periods, although there is some overlap. The negative spike immediately preceding the initial absorption peak corresponds to a short period of light emission. This is thought to be due to fluorescence from the cell caused by the laser flash. The spike is present at all wavelengths, so is not a reflection of the laser light itself.

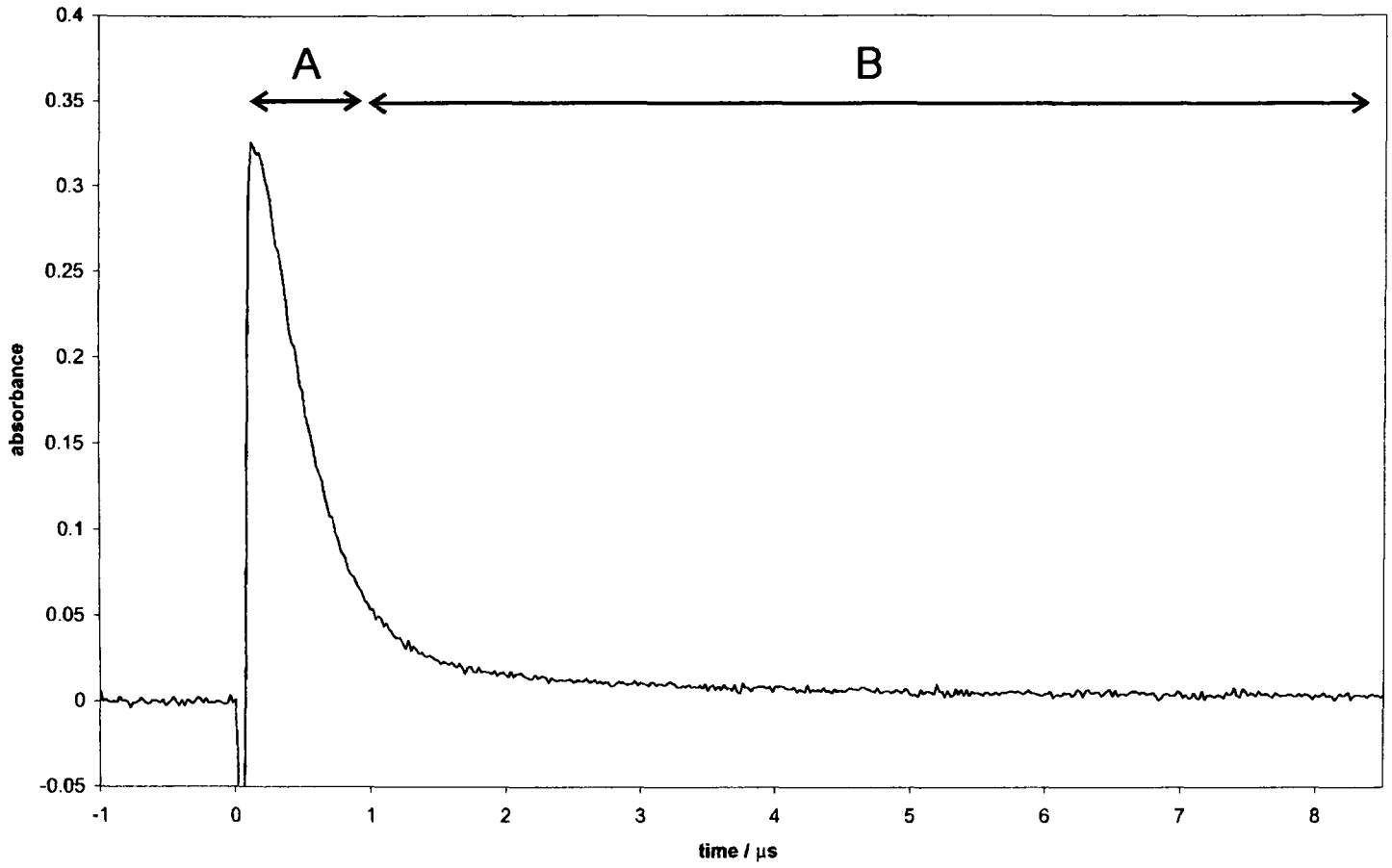


Figure 3.4: Typical time curve showing the two regions of radical recombination ([SDS] = 100 mM, [BP] = 3 mM) A – approximate geminate period, B – approximate F pair period

After the laser flash and initial absorbance peak the trace shows a fast decay while the geminate reaction occurs (plus escape of either member of the RP from the micelle or vesicle), this is the region marked A in figure 3.4. During this time (about 1 μs in this case) the majority of the radical pairs have either recombined inside the micelle or vesicle, or one or both of the radicals have escaped from the geminate RP. The remainder of the signal decay is due to F pair recombination, and this is the period marked B. The kinetics of these processes can be modelled via rate equations, and this is discussed in section 3.8.

The second type of measurement is undertaken to quantify the size of any magnetic field effects that may be present. As discussed earlier, a magnetic field might change the rate of spin mixing between singlet and triplet states, and hence the rate of radical recombination. This effect can be seen in the time curves; at magnetic field strengths exceeding the typical average hyperfine coupling in the RP the extent of

singlet - triplet mixing will be smaller than that at zero magnetic field, due to the Zeeman splitting. For triplet born radical pairs, which this thesis studies exclusively, this means a slower rate of radical recombination so the radical concentration (and hence the absorbance) will decay at a slower rate at high magnetic field strengths compared to zero field, giving a way of measuring the effect of the magnetic field. In the experiments presented here the MFE is defined as the percentage difference between the areas under the time curves in the presence and absence of applied magnetic fields, *i.e.*:

$$\mathrm{MFE} = \frac{\int_{t_1}^{t_2} A(t)^{B\neq 0}\,dt - \int_{t_1}^{t_2} A(t)^{B=0}\,dt}{\int_{t_1}^{t_2} A(t)^{B=0}\,dt} \times 100. \qquad (3.3)$$

When the singlet – triplet mixing rate is slower than at zero magnetic field this gives a positive MFE, and when the mixing rate is faster than at zero magnetic field (*e.g.* the LFE) the MFE is negative. Figure 3.5 shows graphically how the MFE is defined.

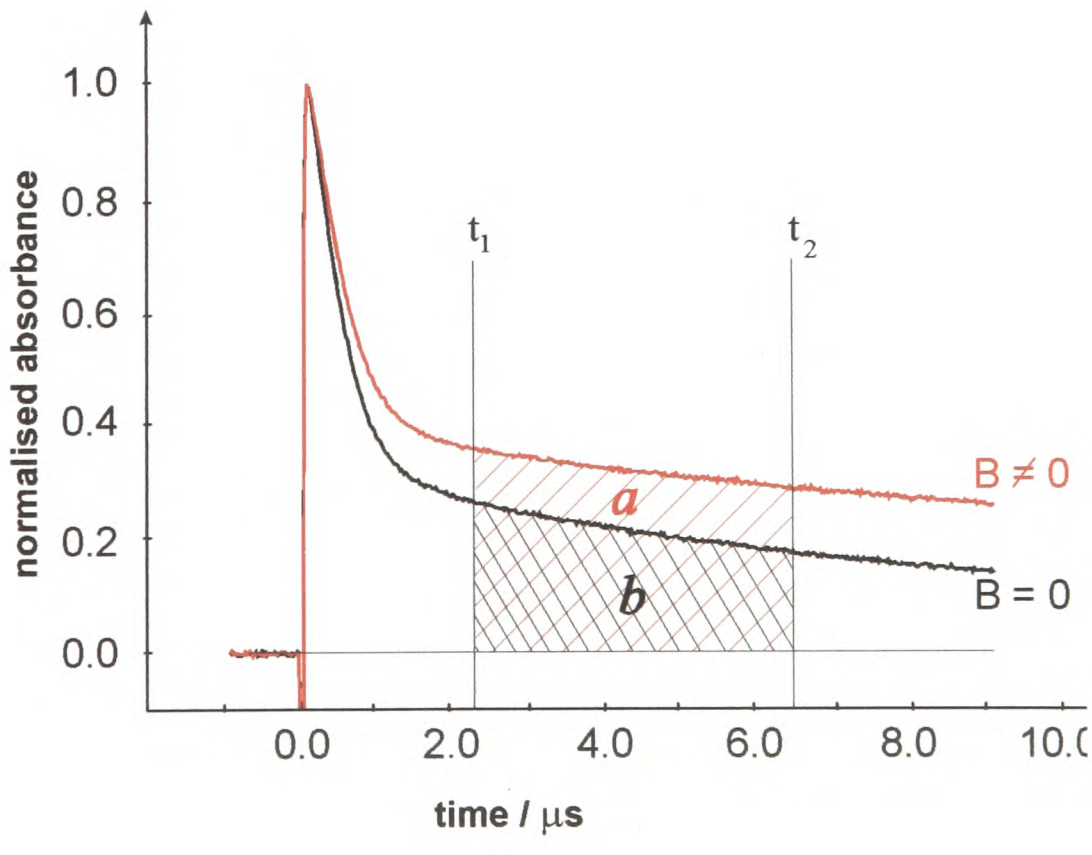


Figure 3.5: Time curves at zero and non-zero magnetic field showing how MFE is calculated

Using the areas shown in the diagram above the MFE can also be described as:

$$\text{MFE} = \frac{a-b}{b} \times 100 \qquad (3.4)$$

In every case in this thesis the MFEs were calculated over the entire range of the time curves measured, *i.e.* in figure 3.5 this would mean $t_1 = 0$ μs and $t_2 = 10$ μs.

MFEs can be calculated for any magnetic field value provided by the Helmholtz coils, when a graph is drawn of MFE vs. magnetic field strength a MARY curve results, where MARY stands for MAgnetic field effects on Reaction Yields. A typical MARY curve is shown in figure 3.6.

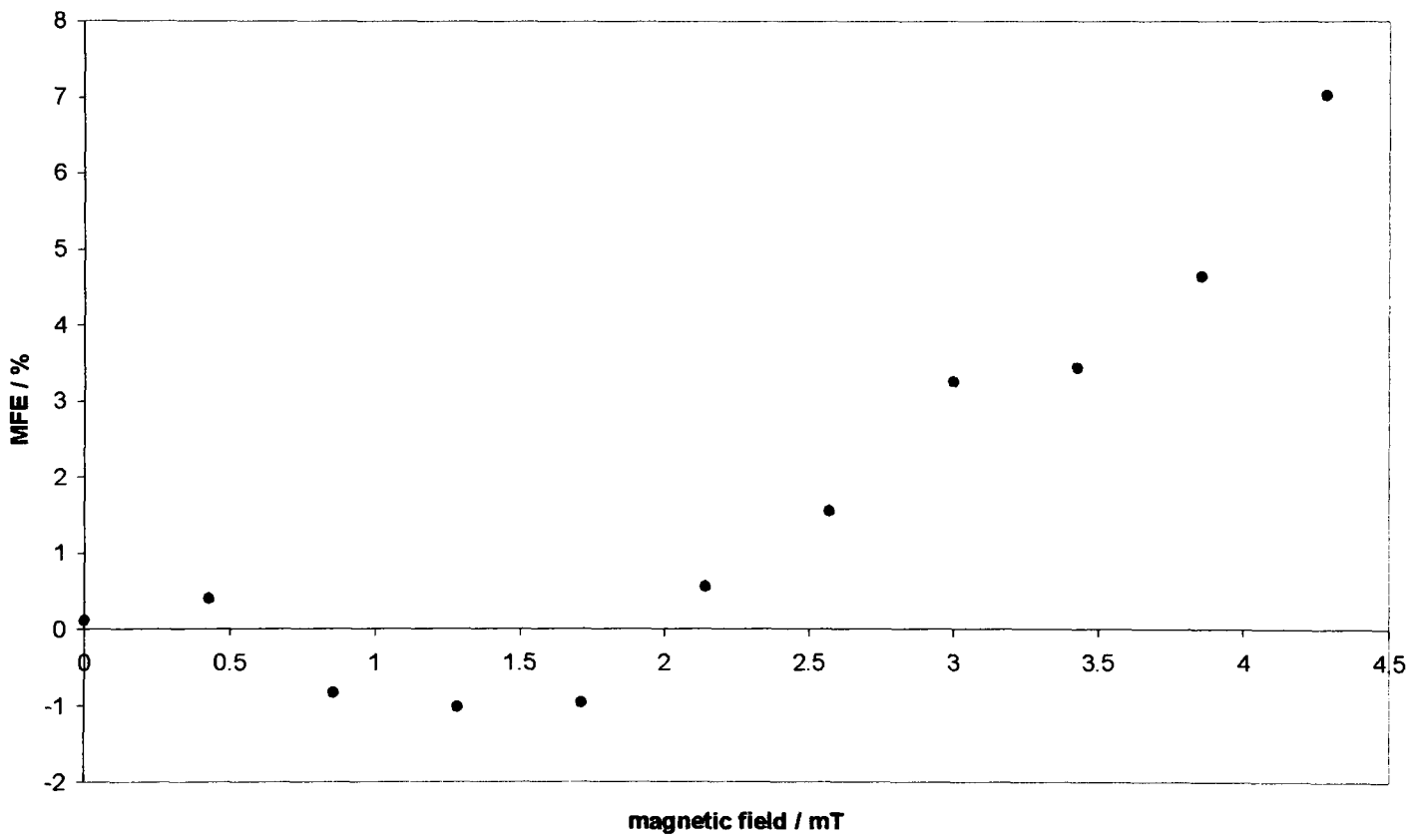


Figure 3.6: Typical MARY curve (actual system: SDS/BP)

The methods described above are not the only techniques used for obtaining MARY spectra. The general form of the spectra is the same in every case, with MFE plotted against magnetic field strength, but the manner of determining the MFE can vary. For

example, in experiments where the RP under investigation is a radical ion pair detected by fluorescence, and the magnetic field is modulated to improve the signal to noise ratio. The MFE is then measured as the change in fluorescence between an applied magnetic field and zero applied magnetic field [19, 20]. Differences in the method of measuring MFEs can lead to different values being recorded. For example the method used in this thesis can be affected by factors which change the size of the absorbance, such as any products formed which absorb at the monitoring wavelength. These would contribute to the absorbance at longer timescales, distorting the size of any MFEs measured. Another issue is that only the absorbance in the measurement window is used in the MFE calculation, any difference in absorbance at timescales longer than *e.g.* 10 μs (in the case of figure 3.5, and the majority of systems used in this thesis) is not included in the MFE calculation. The changes in absorbance due to the application of a magnetic field can persist for different lengths of time in different systems (*e.g.* see figure 5.3) and the time period chosen for integration will affect the relative sizes of the MFEs recorded. This is an unavoidable problem, but to minimise its effect the integration period for all systems in this thesis has been fixed at 10 μs, unless stated otherwise.

3.5.1 Manually Calculated MFEs

The MFEs described in the previous section, and those seen in the MARY curve in figure 3.6, were all calculated by the LabVIEW software program controlling the experiment. Averaged time curves were taken from the oscilloscope, the areas underneath the curves determined, and the MFE calculated using the formulae in equations 3.3 and 3.4. In the following chapters the phrase 'manually calculated

MFEs' is also used. This refers to MFE values that have been calculated not as described above, but by using time curves recorded at various magnetic field strengths, and a corresponding time curve recorded at zero applied magnetic field. The areas underneath these time curves are then calculated by summing the absorbance at every time point (assigning each time point a width of unity to give an area) and using these summed areas in equation 3.4 to calculate the MFEs. The advantage of the manual calculation is that the time curves used to calculate the MFEs can be seen and compared by eye, whereas when the LabVIEW software calculates MFEs, the time curves are not recorded for later inspection. It is beneficial to have time curves recorded at various magnetic field strengths in order to assess the effect of the magnetic field, and to use these time curves to calculate MFEs, rather than obtaining separate MFE values using the LabVIEW software. This means that more averages could be obtained in the limited time provided by the volume of the solution used.

Unless stated otherwise, all manually calculated MFEs were calculated using the entire time curve from the oscilloscope (*i.e.* an integration period of 10 μs).

3.6 Evolution of the Experiment

In order to improve the quality of data obtained, and to facilitate the study of new systems, a number of components of the experimental apparatus outlined in section 3.2 were redesigned.

3.6.1 The Cell

During the course of this research two different cell designs have been used. The first was an ordinary Hellma quartz flow cuvette measuring 10 mm x 10 mm x 40 mm. The cell was held in a custom designed aluminium block, constructed in the laboratory workshop, which contained mirrors to give multiple reflections of the analysis light inside the cell and hence a longer path length, as shown in figure 3.7. The total path length of the analysis light through the cell was 36 mm.

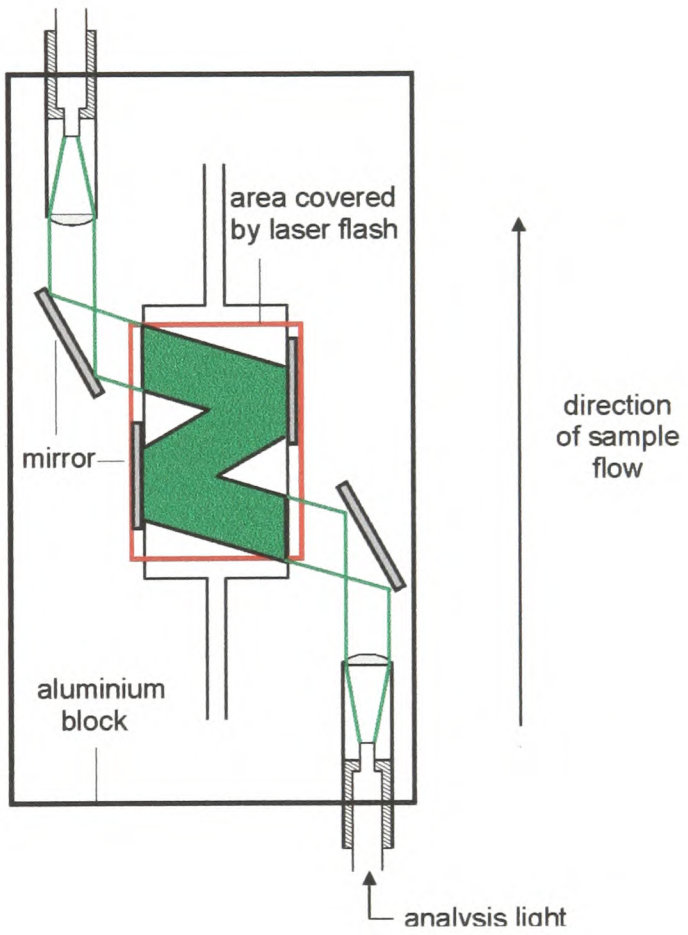


Figure 3.7: Cross-section of original cell design

The analysis light from the Xe lamp passed through a water bath to filter out the IR wavelengths and then through a 545 nm band pass filter to cut out UV light. The UV light is removed from the analysis light to prevent photolysis of the sample by light other than the laser light. The analysis light was carried to the cell by liquid filled light guides, the ends of which were rigidly held in place by the aluminium block that housed the cell.

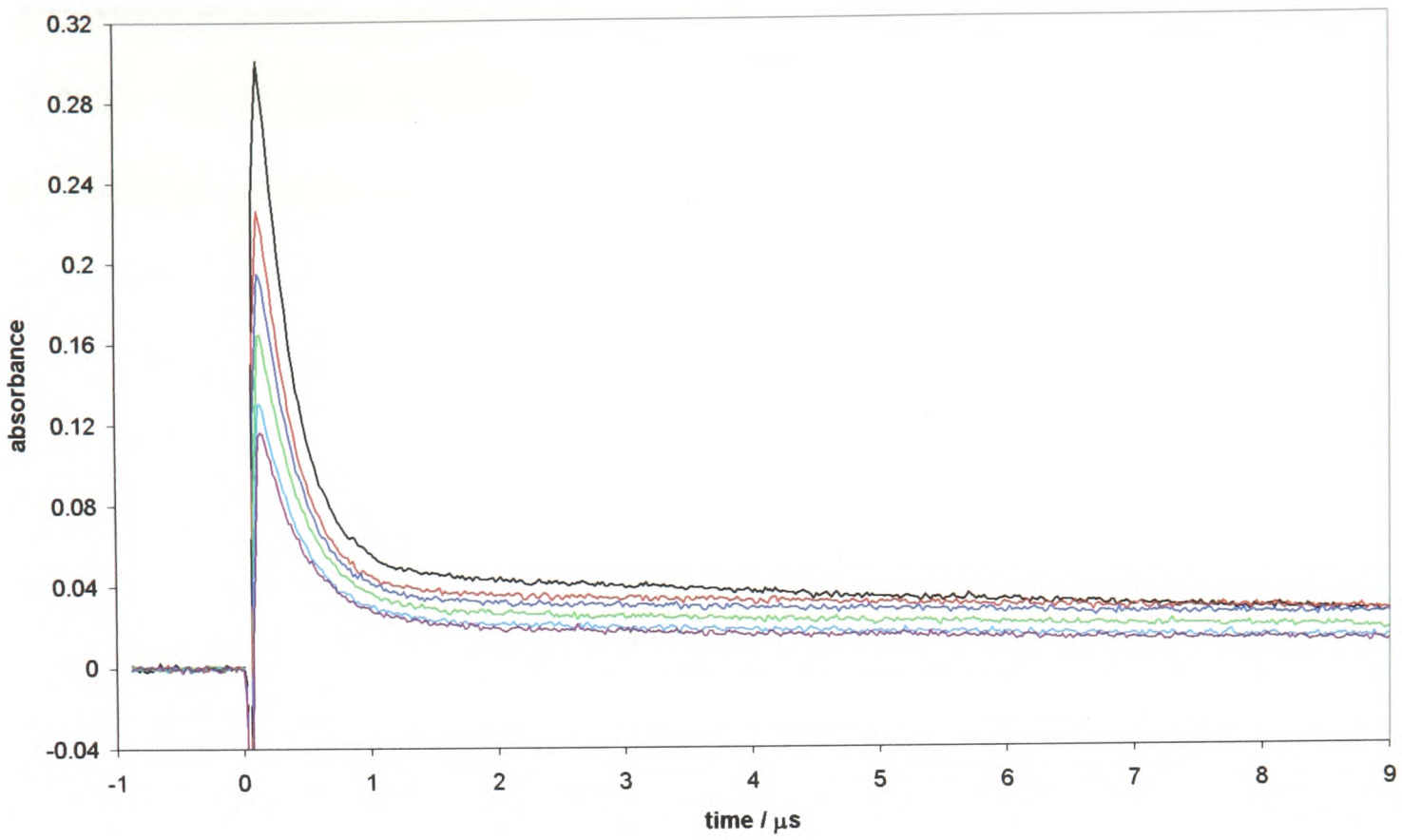


Figure 3.8: Depletion of signal during the course of an experiment. Zero field time curves of DTAC/BP at (●) 5, (●) 15, (●) 30, (●) 60, (●) 90, and (●) 120 minutes after start of experiment

The relatively large cuvette volume of 4000 mm^3, and the fact that the recombination products of the RP reaction are different from the starting materials means that if the solution in the cell is to be replaced between each laser pulse, large flow rates must be used. This in turn leads to a large volume of solution being required for each experimental run. To limit the amount of chemicals needed the solution has to be recycled several times for a typical experiment. Recycling creates further difficulties in that the previously photolysed sample is reintroduced to the cuvette where depletion occurs, and this causes a gradual decay in signal size during the course of an experimental run. This can be seen from figure 3.8, which shows zero field time curves taken over a 120 minute experimental run. The volume of the cell and the speed of the pump used to flow the solution meant that the entire 250 ml sample flowed through the cell approximately once every eight minutes.

To overcome this problem a new cell was designed with significantly smaller volume (565 mm^3, with an internal diameter of 3 mm). This allowed slower flow rates to be used, and eliminated the need to recycle the solution.

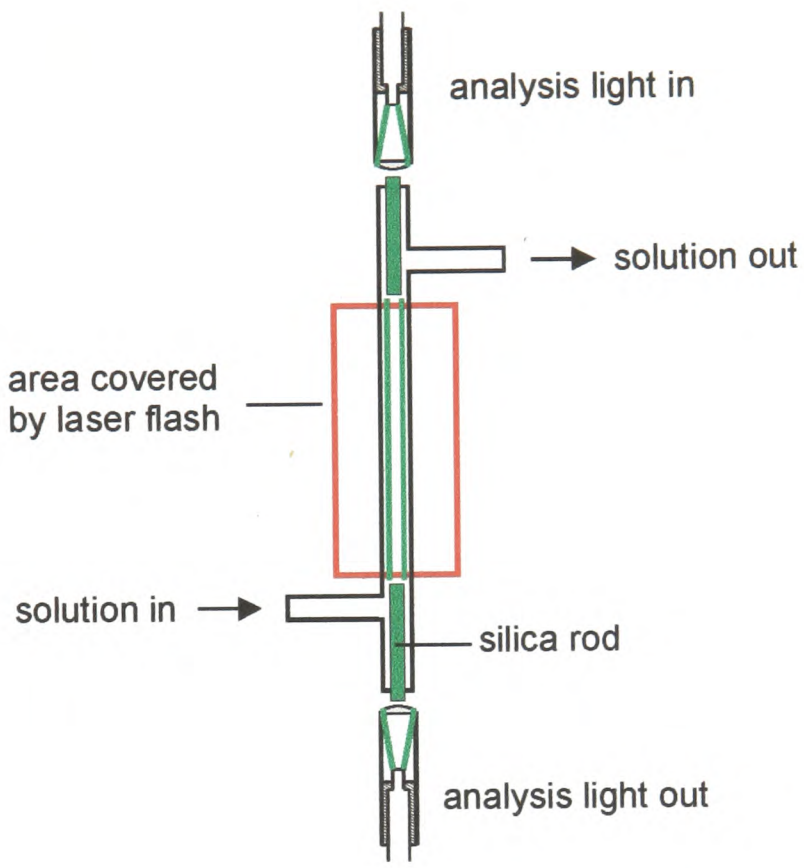


Figure 3.9: Cross-section of new cell design

The reduced volume cell was designed to have the analysis light perpendicular to the laser light, as with the original cell. However, passing the light along the cell axis, and increasing the path length over the original design (from 36 mm to 45 mm) removed the need for reflection of the analysis light. The cell is fixed in a plastic stand that also holds the ends of the light pipes to keep the geometry rigid. Silica rods take the light from the end of the light pipes to the sample volume of the cell.

For all results shown in the following chapters (except those in section 5.4) the new cell was used as part of the experimental apparatus.

3.6.2 The Lamp

In the original experimental apparatus a 200 W Spiers Robertson mercury lamp provided the analysis light. This was replaced with the 1000 W Xe lamp to increase the amount of light that passed through the solution, and hence give a larger absorption signal. The light from the lamp is passed through a water bath and a band pass UV filter before being focussed onto the end of the liquid filled light guide by a lens. The light exits the other end of the light guide and another lens focuses it onto the silica rod of the cell seen in figure 3.9.

3.7 Experimental Uncertainties

Every effort was made to minimise experimental uncertainties during the course of the experiment. The errors in the size of the MFEs can be calculated from consideration of equation of 3.4, a description of the size of the MFE. This equation can be rewritten to put it in the form shown in equation 3.5.

$$\mathrm{MFE} = \left(\frac{a}{b} - 1\right) \times 100 \qquad (3.5)$$

Assuming that the errors in a and b are independent, the formula for the fractional error in the MFE is given by:

$$\frac{\Delta \mathrm{MFE}}{\mathrm{MFE}} = \sqrt{\left(\frac{\Delta a}{a}\right)^2 + \left(\frac{\Delta b}{b}\right)^2} \,. \qquad (3.6)$$

If it is furthermore assumed that the errors in the areas of the time curves are the same in zero and applied magnetic field, the error in the MFE becomes:

$$EE = \frac{\Delta MFE}{MFE} = \sqrt{2}\frac{\Delta a}{a} \qquad (3.7)$$

where Δa is the standard deviation of the areas under the zero field time curves and a is the mean value of the areas under the zero field time curves. The fractional error in the MFE is labelled the error estimation (EE). As mentioned in section 3.5.1 the computer does not store the time curves it uses to calculate the MARY curves, so to estimate the error for any particular experiment the first twelve zero field time curves were used to calculate EEs on the MARY curves. The EE values for each system are displayed as percentages in the figure captions of the MARY curves in the subsequent chapters.

As its name suggest the EE only gives an estimation of the errors in the MFE values, but it provides a quick and easy comparison of the data quality of different experiments.

3.8 Kinetic Analysis

One of the main advantages of flash photolysis and optical absorption is that the kinetics of the RP process can be studied directly. In experiments where the radicals are generated by continuous illumination a steady state radical concentration is obtained, and so the lifetime of the RP cannot be studied. With the flash photolysis experiment the laser flash generates a concentration of radicals and the rate of radical recombination can be studied by following the absorbance decay as a function of time.

The effect of magnetic fields on RPs formed by hydrogen abstraction inside micelles has been thoroughly investigated, and several methods of kinetic analysis have been employed to quantify the size of the effects. Scaiano et al. [4] proposed a kinetic model that ignores F pair recombination and uses the difference in absorption at the initial absorption peak and after the geminate period of the decay to calculate an observed decay rate, k_{exptl}, that is the sum of the escape and geminate recombination rate constants. Aside from the fact that this scheme disregards the recombination outside the micelles, it is often hard to assign a time when the geminate recombination is complete to obtain a value for the absorption at this time. The advantage of this technique is that the differential equations given by this kinetic scheme are fairly straightforward to solve, and hence fit to the experimental data. A second method, shown by Sakaguchi et al. [3], is to fit a first order exponential to the fast, geminate part of the decay curve and use the rate constant given by this exponential fit to compare between different magnetic field strengths and different chemical systems. The advantage of this method is again that it is relatively straightforward to apply, but it has the disadvantage that the selection of the section of the decay curve on which the fitting is carried out can be arbitrary, in that the end of the geminate period is hard to accurately define, and choosing different periods to fit to leads to different rate constants for the same decay curve. The most comprehensive treatment of the kinetics of a radical pair inside a micelle has been shown by Woodward and Sakaguchi [9, 21] where three separate experimental techniques (B_0 field sweep, single pulse response, and pulse shift spectra) utilising LFP, magnetic fields, and microwave pulses are used to obtain rate constants, including the singlet state recombination rate constant. The advantages of this approach are obviously the increased amount of data obtained, but it is technically more difficult to perform, and also must be carried out at magnetic

field strengths of around 300 mT for the SDS/BP system, so that optimum microwave pulses may be applied to the system. The approach described below, and applied in this thesis falls between the methods described above. It is not as comprehensive as the third method, but as will become obvious in later chapters, for the systems investigated in this work, F pair recombination cannot be ignored as it strongly influences the time dependence of the absorption signal. Hence the whole of the measured decay curve is used without having to arbitrarily decide when the geminate period has come to an end.

The reaction scheme for BP with a hydrogen donor was shown in figure 1.5. However, the kinetic scheme used to analyse the time curves is based on a simplified version to reduce the number of unknowns and facilitate analysis. This is shown in figure 3.10.

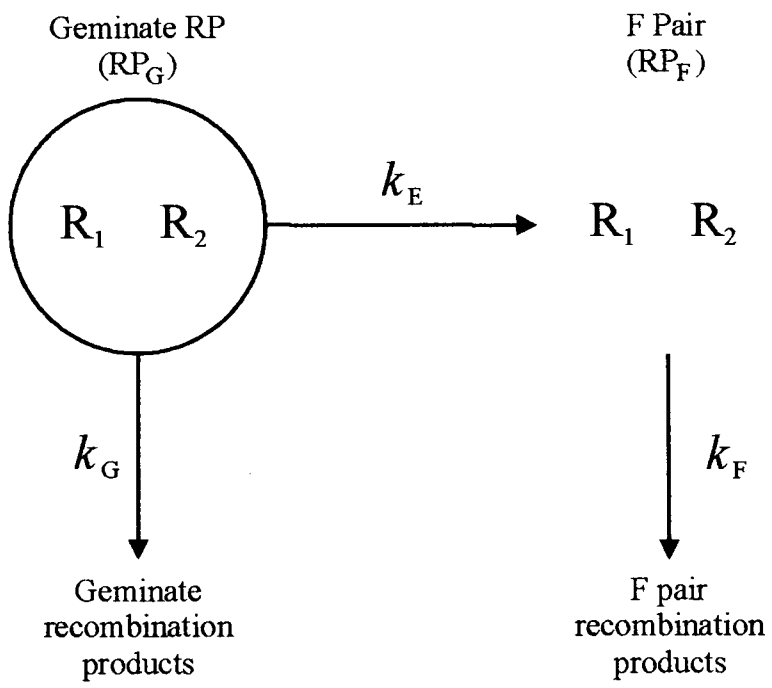


Figure 3.10: Reaction scheme for kinetic analysis

The geminate RP can either undergo geminate recombination, with a rate constant k_G, from the singlet state only, or escape from the geminate cage in either spin state of the RP, with a rate constant k_E. The radicals that escape the geminate RP can recombine

as F pairs, with a rate constant of k_F. The model assumes that the geminate RP is formed instantly at zero time, *i.e.* an infinitely fast rate of hydrogen abstraction. The hydrogen abstraction rate by BP from SDS micelles has been measured to be 3.48×10^6 s^{-1} [9], which is comparable to the other rate constants in the fitting routine, however the assumption of infinitely fast hydrogen abstraction was made to simplify the kinetic scheme, and reduce the number of parameters that have to be obtained from fitting to the time curves.

The geminate recombination product is R_1R_2, whereas the F pair recombination products include R_1R_2, but can also be R_1R_1 or R_2R_2.

The rate of spin mixing of the RP is included in the geminate rate constant, k_G. Hence no term is required to describe the spin state of the RP in this kinetic model. The geminate RP is formed in a triplet state, and hence, in order to form the geminate recombination products any triplet RP must first undergo a change of spin state to the singlet state. The effect of the magnetic field in the model is to change the rate of k_G and hence the proportion of radicals that form geminate recombination products.

The rate equations for this model are then set up as follows; the rate equation for the concentration of geminate RP is:

$$\frac{d[RP_G]}{dt} = -(k_G + k_E)\,[RP_G] \qquad (3.8)$$

where $[RP_G]$ is the concentration of the geminate RP. The rate equation for the concentration of F pairs is given by:

$$\frac{d[RP_F]}{dt} = k_E[RP_G] - k_F[R_1][R_2] \qquad (3.9)$$

where $[RP_F]$ is the F pair concentration, and $[R_1]$ and $[R_2]$ are the concentrations of the individual radicals outside the geminate RP. Equations 3.8 and 3.9 are the same as those from Eveson et al. [16], with the addition of a term to account for the F pair recombination in equation 3.9. For the data obtained in this work there is no obvious cut-off point between the geminate and F pair periods, especially for the experiments using vesicles (*e.g.* see figures 6.1 and 8.1), and hence the F pair recombination has to be included in the kinetic model.

The assumption is made that the concentrations of R_1 and R_2 are equal, and so can be replaced by the concentration of RP_F instead. Equation 3.9 then becomes:

$$\frac{d[RP_F]}{dt} = k_E[RP_G] - k_F[RP_F]^2. \qquad (3.10)$$

These coupled kinetic equations (3.8 and 3.10) can be solved analytically, but the analytical solution offers no advantage over numerical solution in respect of model fitting. A program was written in Mathworks Matlab to provide numerical solutions to the differential equations for a given set of rate constants. The program used the ode45.m function in Matlab, which employs a Runge-Kutta formula to solve the equations.

A separate fitting program was written using Matlab to utilise a least squares curve fitting routine (lsqcurvefit.m) to generate values of the three rate constants which most closely reproduce a given experimental time curve. This program takes lower and

upper limits for the three rate constants and calculates ten values for each, on a logarithmic scale, to provide 1000 sets of initial values. The least squares curve fitting program uses each of the 1000 initial values to fit the experimental data. Out of the resulting 1000 data sets, those which converged were examined in an attempt to determine if a global minimum was reached, and to give error bounds for the rate constants. The maximum and minimum values for each rate constant were listed for the curves that converged, a small difference between the maximum and minimum indicates that a global minimum was reached, and visual inspection showed how good the fits were compared to the experimental curves. For those curves where kinetic fitting was not possible it is thought that it is due to the faults of the assumptions and simplifications of the model rather than inadequate numerical optimisation. All program listings are provided in appendix 1.

To fit the time curves the experimental curves were normalised to an initial absorbance value of unity, and the fitting performed on these normalised curves. If the decay curves were assumed to be first order the initial radical concentration would not be important, but as the F pair recombination is assumed to be second order the initial concentration of the radical pairs becomes important. As the time curves were normalised prior to fitting this assumes an initial radical concentration of 1.0 M. The actual value of the initial radical concentration is hard to measure experimentally, especially with the presence of the fluorescence spike described in section 3.5. A calculation of the initial radical concentration could be performed by measuring the amount of laser light that is absorbed by the sample, and using the quantum yield of the probe molecule, but accurate measurement of the amount of laser light absorbed using the current apparatus would be technically difficult. The assumption of an initial

radical concentration of 1.0 M therefore means that all k_F values provided by the curve fitting are in error by a factor equal to the (unknown) initial concentration. However, for systems which would be assumed to have similar initial concentrations the relative sizes of the k_F values can be compared.

3.8.1 Effects of Rate Constants

As well as fitting to experimental time curves the fitting program can also be used to investigate the radical concentrations as a function of the rate constants. Figure 3.11 shows a simulated time curve with values of the rate constants of $k_G = 10^6\ s^{-1}$, $k_E = 10^6\ s^{-1}$, and $k_F = 10^7\ s^{-1}\ M^{-1}$. These values were chosen as they are the order of magnitude results obtained from fitting the zero field time curves of BP in SDS micelles.

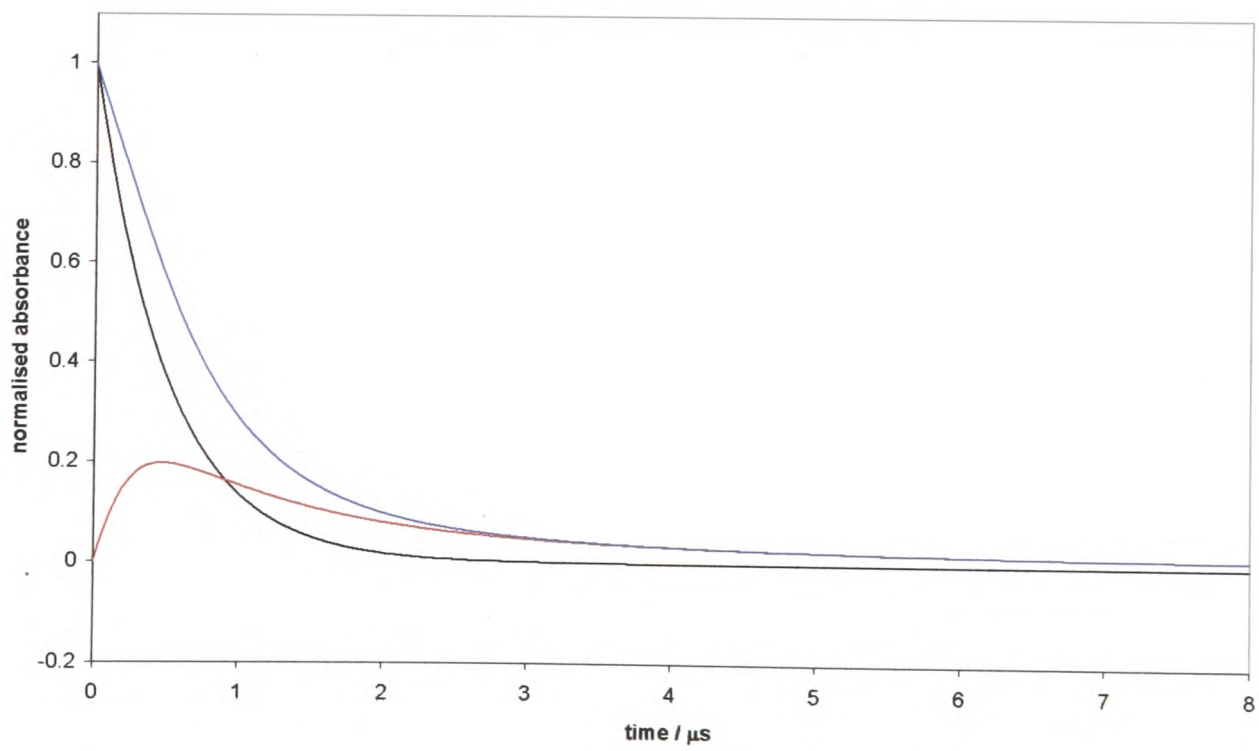


Figure 3.11: Simulated time curves with fixed rate constants showing (●) RP_G, (●) RP_F, and (●) $RP_G + RP_F$

To show the effect of the individual rate constants figure 3.12 depicts the total RP concentration for the values seen in figure 3.11 along with the total RP concentration when each of the three rate constants are doubled in turn.

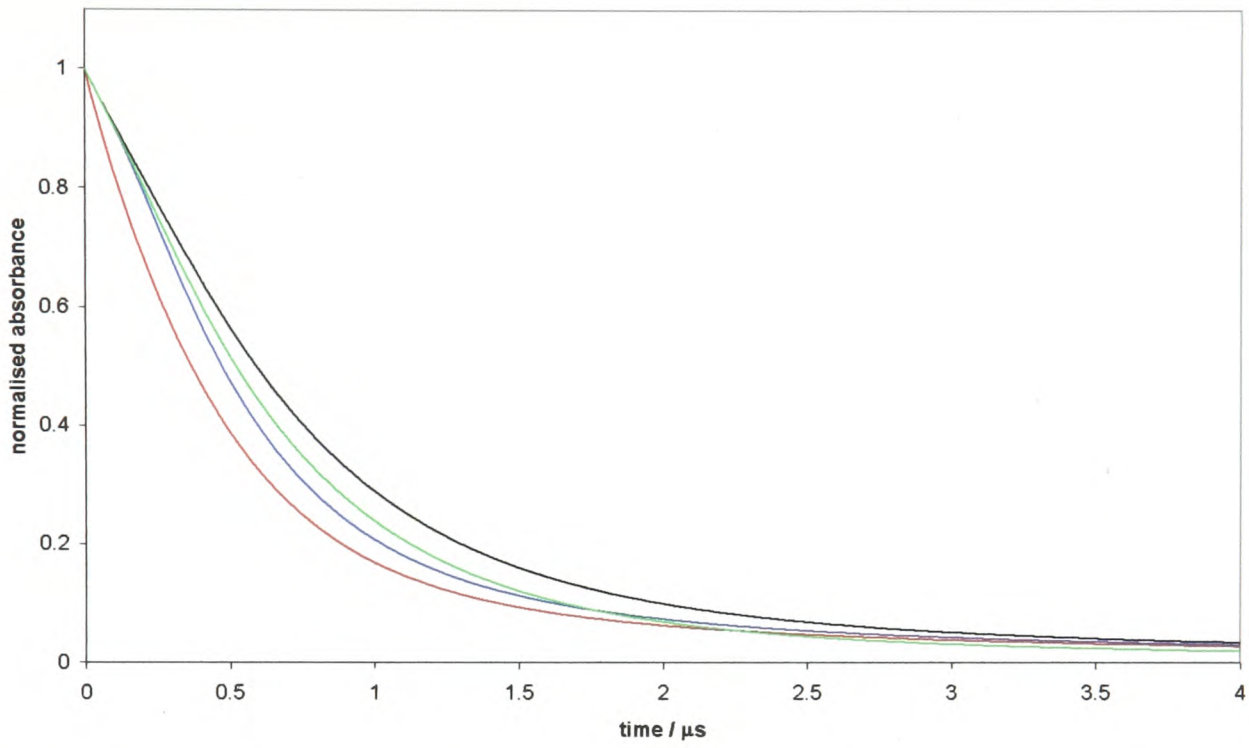


Figure 3.12: Simulated time curves showing effect of changing individual rate constants, with k_G / 10^6 s^{-1}, k_E / 10^6 s^{-1}, k_F / 10^7 s^{-1} M^{-1} (●) 1, 1, 1, (●) 2, 1, 1, (●) 1, 2, 1, and (●) 1, 1, 2

As would be expected increasing any of the rate constants results in an increased decay rate for the radical concentration. Doubling k_G has the largest effect at early timescales, followed by k_E and then k_F. This is not a surprising result, as increasing k_G has an immediate effect on the RP concentration, the more k_G is increased the quicker the geminate RPs recombine, and the faster the signal decays. Increasing k_E does not lead directly to faster recombination, as the radical absorbs the same intensity of light independent of whether or not it is part of a geminate RP. However, in this model, the rate of F pair recombination depends on the square of the F pair concentration, and hence increasing the concentration of F pairs, which is the consequence of increasing k_E, results in a faster decay. Increasing k_F has the smallest effect at early timescales because the radicals must escape from the geminate RP before any F pair

recombination can take place. If figure 3.12 is studied closely the radical concentration at 4 μs is smallest for the green curve, implying that over this timescale doubling the value of k_F has the largest effect of doubling any of the three rate constants.

The expected change in the magnitude of the rate constants with magnetic field obviously depends on the size of the applied magnetic field. Sakaguchi et al. [5] investigated the change in the initial, geminate portion of the decay of BP in SDS micelles using a single exponential decay, and found that this rate halved in size between zero applied field and 70 mT.

3.8.2 Fractional Lifetimes

A second method of quantitatively comparing between different time curves has also been used in this work. It is a simpler method than the curve fitting introduced in section 3.8, but works on all time curves, including those that produce inconclusive results using the fitting program. To compare between time curves three time periods are used; $T_{3/4}$, $T_{1/2}$, and $T_{1/4}$, which are defined as the time taken for the time curves to reach 75%, 50%, and 25% respectively of the initial absorption maximum. These fractional lifetimes are used to give an indication of the speed of decay of the absorption signal, and how it varies between different systems. To show an example of this, table 3.1 gives the fractional lifetimes for the simulated time curves in figure 3.11.

Curve – k_G / 10^6 s^{-1}, k_E / 10^6 s^{-1}, k_F / 10^7 s^{-1} M^{-1}	**$T_{3/4}$ / μs**	**$T_{1/2}$ / μs**	**$T_{1/4}$ / μs**
1,1,1 (•)	0.28	0.60	1.12
2,1,1 (•)	0.16	0.38	0.76

1,2,1 (•)	0.24	0.48	0.88
1,1,2 (•)	0.26	0.54	0.98

Table 3.1: Fractional lifetimes of simulated time curves

The fractional lifetimes reiterate the discussion following figure 3.11, showing that doubling k_G has the largest effect, followed by k_E, and then k_F, at all three stages of the decay.

Due to the complex nature of the kinetics involved full kinetic analysis is not carried out for all systems studied, especially since the time curves vary greatly as additives are added to solutions, or as vesicular systems are compared to micellar ones. However, as table 3.1 shows, comparing the fractional lifetimes of the time curves provides a short, simple, but effective method of comparing systems of different structure and chemical nature with respect to some of their general radical pair kinetics.

4: SYNTHETIC MICELLES – NEGATIVELY CHARGED HEAD GROUPS

The aim of this thesis is to investigate magnetic field effects in confined systems, with the eventual objective of discussing their significance and the likelihood of their presence in biologically relevant microenvironments. However, before studying complex biological systems it was considered prudent to investigate radical pairs in well characterised structures whilst systematically introducing minor alterations, such as additional molecules inside the micelle or small changes to the micelle structure. The latter is covered in chapter five, but this chapter reports on the work undertaken in sodium dodecyl sulfate (SDS) micelles, and can be broken up into main three sections. The first is a study reporting on the effect the addition of hydrogen donor molecules into SDS micelles exerts on both the radical pair lifetime and the MARY curves. The second part explores the consequence of deuterating one or both of the components in the radical pair, and the third is an investigation of a theoretical prediction [1] that there should be a significant difference in radical recombination rate between true zero magnetic field and very small non-zero magnetic field strengths. As mentioned in chapter two, SDS is the most commonly employed molecule for MFE studies in micellar systems, and hence forms a good basis for further investigations such as those outlined above.

4.1 EXPERIMENTAL SECTION

All experiments were performed with concentrations of 100 mM SDS, 3 mM BP and 60 mM hydrogen donor at 25 °C. Solutions were sonicated for 59 minutes at 25 °C

prior to the experiment, and the experiment started within at least one hour after completion of sonication.

For all time curves shown there are 96 averages per curve and each is the average of two sets of acquisitions, unless stated otherwise. All time curves shown were recorded at zero applied magnetic field unless stated otherwise.

4.1.1 Abbreviations Used in this Chapter

Several different hydrogen donors were used in the experiments discussed in this chapter, and all have been abbreviated for clarity. Table 4.1 shows the hydrogen donors that are discussed in this chapter, and the abbreviations that have been used.

Hydrogen donor	Abbreviation
cyclohexene	CH
1,4-cyclohexadiene	CHD
2-propanol	PrOH
tetrahydrofuran	THF
triethylamine	TEA

Table 4.1: Abbreviations for hydrogen donors used

4.2 Hydrogen Donors

Adding another chemical inside the micelle to act as a hydrogen donor, in preference to SDS, changes the rate of hydrogen abstraction to form the RP [2]. The purpose of these experiments was to investigate the consequence to both the time curves and the magnetic field effects upon the addition of these hydrogen donors, with a view to further maximise the MFEs that are known to be present in the SDS/BP system. The

rate of hydrogen abstraction by BP, in benzene is shown in table 4.2 for the hydrogen donor molecules investigated.

Donor	Rate / $M^{-1} s^{-1}$	Pseudo 1st Order Rate / s^{-1}	Percentage of RPs
CH	1.7×10^7 [3]	5.2×10^7	94
CHD	2.73×10^8 [3]	8.4×10^8	99.6
PrOH	1.1×10^6 [4]	3.4×10^6	49
THF	9.6×10^6 [5]	3.0×10^7	90
TEA	4.1×10^9 [6]	1.3×10^{10}	99.9

Table 4.2: Rate of H abstraction by BP in benzene from various donors

It is impossible to directly compare the rate of hydrogen abstraction by BP from hydrogen donors, such as those in table 4.2, and the rate of hydrogen abstraction by BP from the SDS micelle. The rate constants shown in table 4.2 are second order and bimolecular, for the reaction of excited ^{3}BP with the hydrogen donor in a homogeneous benzene solution. In a micelle the hydrogen abstraction reaction from the surfactant is also bimolecular, but follows first order kinetics. The BP molecule is confined inside the micelle, which means that the local concentration of SDS is much greater than the average SDS concentration over the entire solution, and hence the reaction is pseudo first order and will follow first order kinetics. Values for this first order hydrogen abstraction reaction of ^{3}BP from an SDS molecule inside the micelle are given in the literature and are generally around 3.5×10^6 s^{-1} (3.0×10^6 s^{-1} [7], 3.48×10^6 s^{-1} [8], 4.1×10^6 s^{-1} [9]). The hydrogen abstraction rates were measured using a short resonant microwave pulse in conjunction with the flash photolysis experiment to alter the relative populations of the singlet and triplet states. By varying the timing of the microwave pulse with respect to the laser flash, the hydrogen abstraction rate (and other kinetic information) can be extracted. The rate constants for the hydrogen donors listed in table 4.2 could also be measured this way inside SDS micelles, but no

values are available in the literature. However, a rough estimate of the pseudo first order hydrogen abstraction can be made from the rate constants in benzene and a consideration of the concentration of the hydrogen donors in the interior of the SDS micelles. The micelle radius in table 2.1 was used to calculate the percentage of the solution volume occupied by the micelles, at a concentration of 100 mM SDS. Assuming that all the hydrogen donors are contained in the interior of the micelles an effective micellar concentration of hydrogen donor could be calculated. This value was used with the hydrogen donor rates in benzene given in the second column of table 4.2 to calculate a pseudo first order rate constant for the five hydrogen donor molecules, and the results are shown in the third column of table 4.2. All of these pseudo first order rate constants except for PrOH are larger than that of SDS as quoted above.

Also shown in table 4.2 is the percentage of RPs, this is a value that compares the pseudo first order hydrogen abstraction rate given in the third column to that of SDS, and is calculated using equation 4.1, below:

$$\text{Percentage RP} = \frac{k_H(\text{donor})}{k_H(\text{donor}) + k_H(\text{SDS})} \times 100 \qquad (4.1)$$

where k_H(donor) is the pseudo first order hydrogen abstraction rate constant for the additional hydrogen donor and k_H(SDS) is the hydrogen abstraction rate constant for SDS (which is taken to be 3.5×10^6 s^{-1}). These values show that for all the donors except PrOH the RP can be assumed to consist of a BP ketyl radical and a radical derived from the hydrogen donor. In the case of PrOH approximately half the radical pairs would be expected to contain radicals derived from PrOH, with the other half containing radicals derived from SDS.

Figure 4.1 shows the zero field time curves for the five hydrogen donors and also for SDS/BP with no additional donor. The most obvious aspect is how different SDS/BP/TEA is from the other systems. The size of the absorbance is much greater than any of the other systems, and the lifetime is also much longer. In fact, as

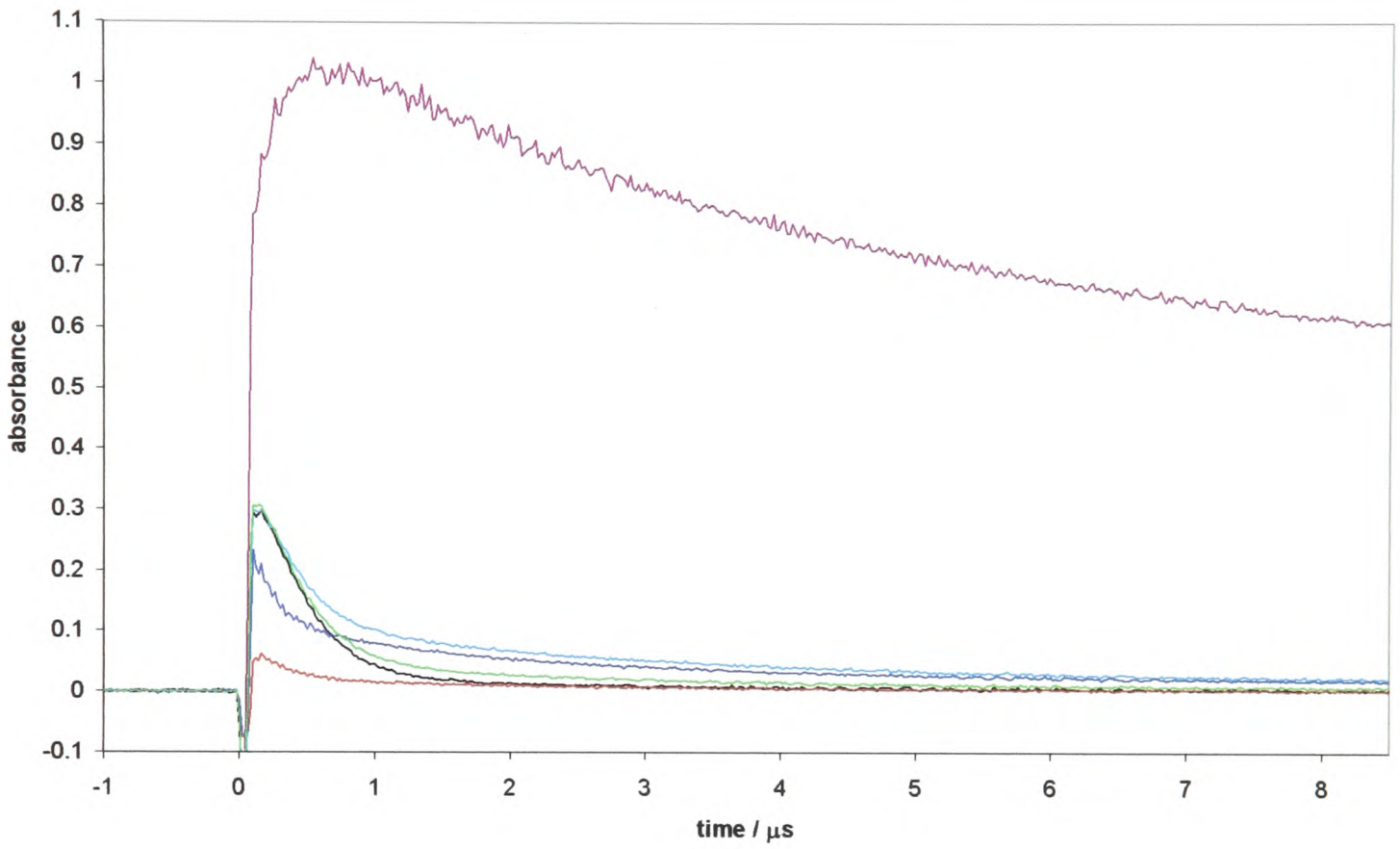


Figure 4.1: Zero field time curves of (•) SDS/BP, (•) SDS/BP/CH, (•) SDS/BP/CHD, (•) SDS/BP/PrOH, (•) SDS/BP/THF, and (•) SDS/BP/TEA

figure 4.2 shows, the signal for SDS/BP/TEA looks even more anomalous when longer time scales are examined. The absorption part of the signal lasts for about 1 ms after the laser flash, and then the signal becomes emissive. This strongly suggests that either a different product is being formed and its absorbance detected at 555 nm, or that a different mechanism is taking place for the creation and fate of the RP. It has been noted in the literature that the photoreduction of BP by amines proceeds by a different mechanism than the reduction by alcohols [10]. It has been proposed that ketone photoreduction by amines occurs via a charge transfer complex [11], and that

in favourable conditions, *i.e.* in polar solvents, complete electron transfer can compete with hydrogen abstraction. It has also been reported that the neutral TEA radical reacts with ground state BP to produce the $BPH^{\bullet}$ ketyl radical [10], which will increase the size of the absorption signal. Due to the atypical kinetics of the SDS/BP/TEA system it was not investigated any further.

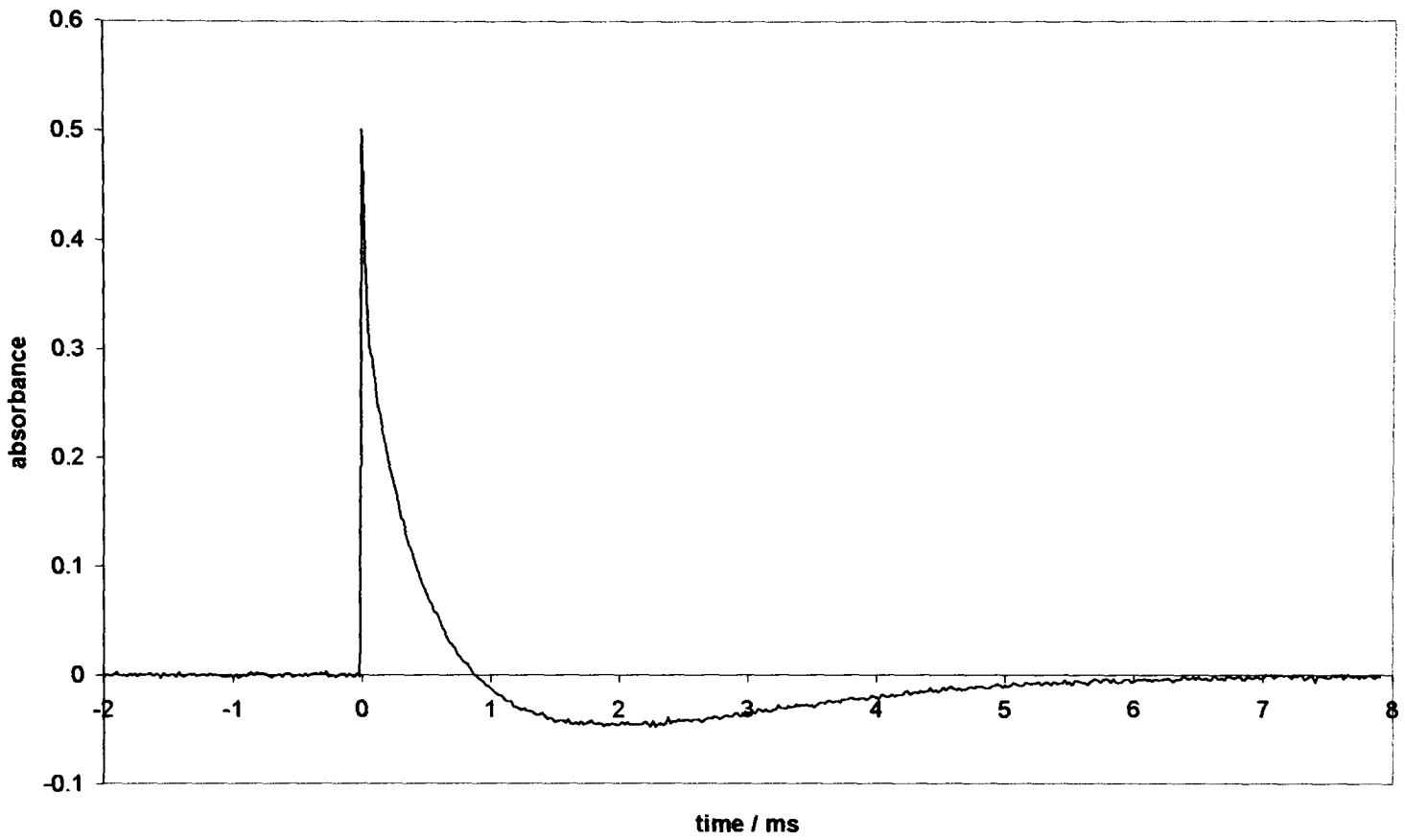


Figure 4.2: Zero field time curve of SDS/BP/TEA at longer timescales

When the SDS/BP/TEA time curve is removed from the graph and the other five systems are studied in more detail (figure 4.3) some trends become apparent. Firstly that despite the difference in hydrogen abstraction rates shown in table 4.2 no difference can be seen in the 'rise time' of the signal in figure 4.3, which is approximately 80 ns for all five systems. The lack of any observable difference is partly because the rate of radical formation is fast compared to the measurement period needed to observe the absorbance signal, and partly because the absorption immediately following the laser flash is masked by the emissive spike, as discussed in

section 3.4. Secondly, consider the size of the initial absorption peaks; the smallest by far is that of SDS/BP/CH. This is due to quenching of the ^{3}BP* by the double bond in CH, as described in [3], which states that for CH in benzene with BP, hydrogen abstraction accounts for 23% of the quenching events of the ^{3}BP*. The remainder of the quenching results in reaction back to the ground state BP molecule.

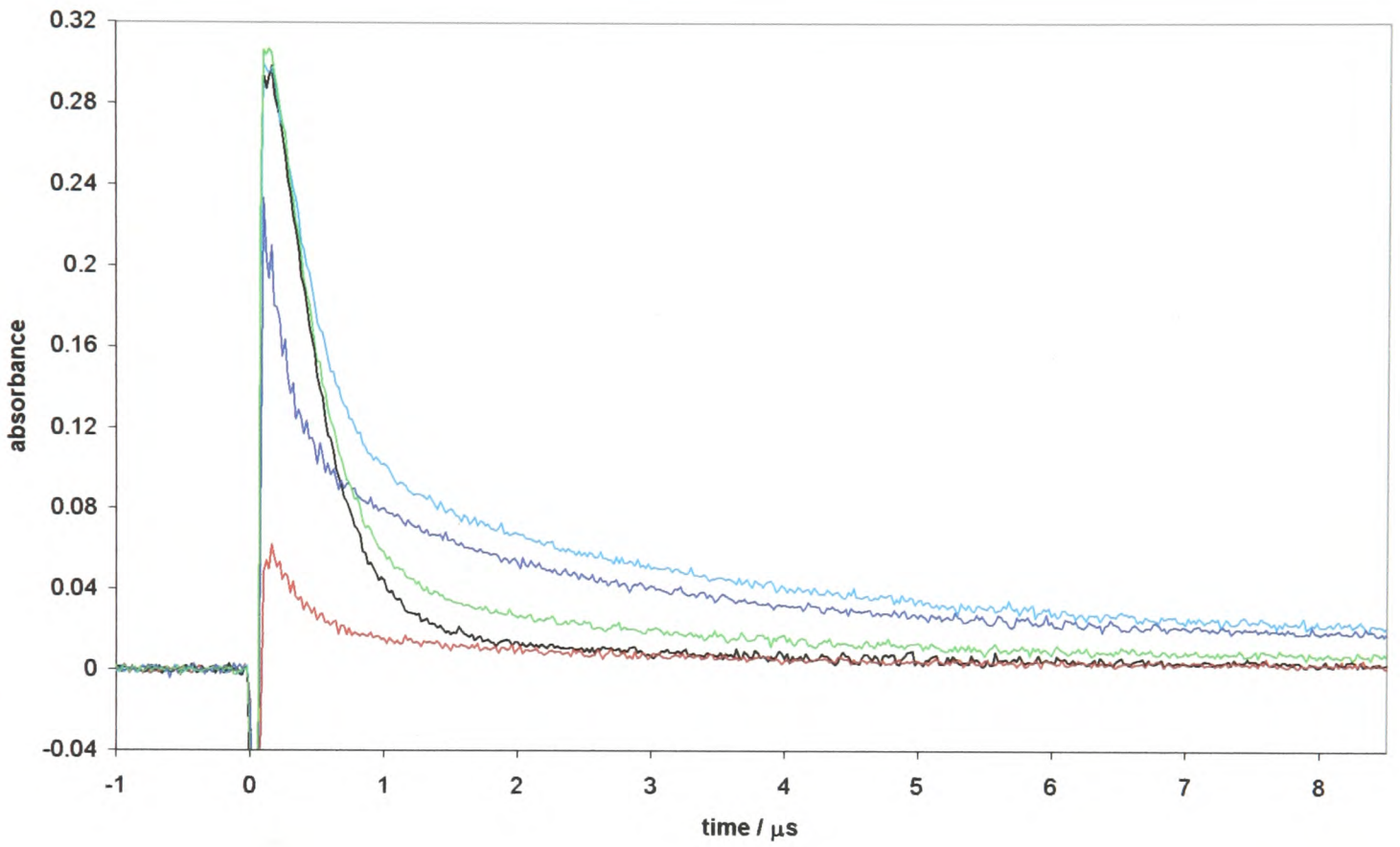


Figure 4.3: Zero field time curves of (•) SDS/BP, (•) SDS/BP/CH, (•) SDS/BP/CHD, (•) SDS/BP/PrOH, and (•) SDS/BP/THF

This could also explain why SDS/BP/CHD has a smaller signal than the remaining three systems for the early time period after radical formation. SDS/BP, SDS/BP/THF and SDS/BP/PrOH have almost identical initial peak heights, but the signals decay at different rates with SDS/BP > SDS/BP/PrOH > SDS/BP/THF. When the zero field time curves are normalised (figure 4.4) the five curves fall in to three groups for the initial decay rates. The fastest is for SDS/BP/CH and SDS/BP/CHD, the next for SDS/BP and SDS/BP/PrOH and the slowest for SDS/BP/THF. However the SDS/BP/CH and SDS/BP/CHD curve shapes are different from the others with the

SDS/BP/CHD signal approaching the size of the SDS/BP/THF signal towards the end of the measurement period. The curve shapes are analysed more quantitatively by examining the fractional lifetimes quoted in table 4.3.

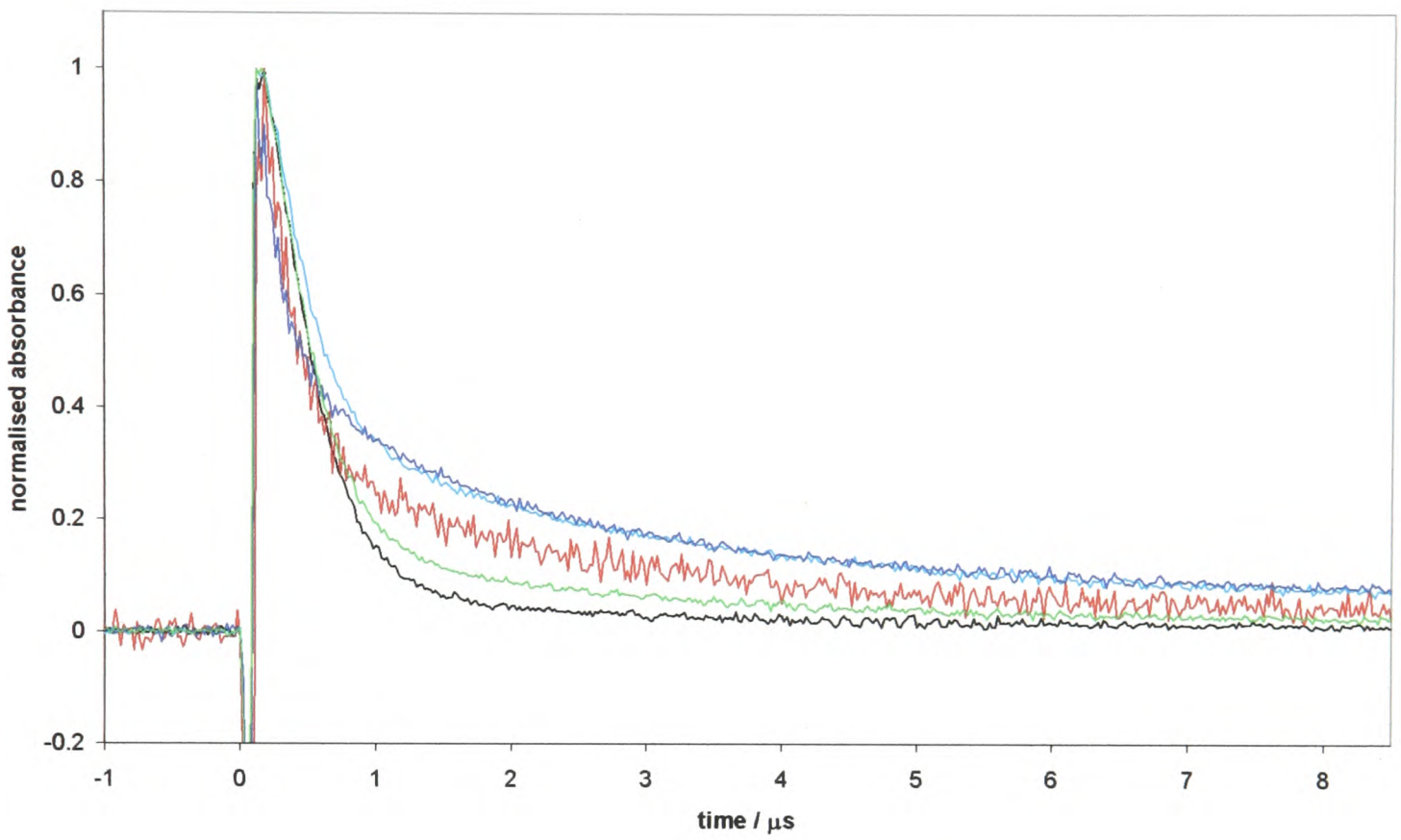


Figure 4.4: Normalised zero field time curves of (•) SDS/BP, (•) SDS/BP/CH, (•) SDS/BP/CHD, (•) SDS/BP/PrOH, and (•) SDS/BP/THF

System	$T_{3/4}$ / μs	$T_{1/2}$ / μs	$T_{1/4}$ / μs
SDS/BP	0.16	0.34	0.62
SDS/BP/CH	0.12	0.26	0.84
SDS/BP/CHD	0.12	0.36	1.72
SDS/BP/PrOH	0.2	0.38	0.7
SDS/BP/THF	0.22	0.44	1.3

Table 4.3: Fractional lifetimes for SDS/BP with various additional hydrogen donors

The fractional lifetimes for the five systems show these trends in a slightly different way. The $T_{3/4}$ times show that the fastest initial recombination occurs with SDS/BP/CH and SDS/BP/CHD, with SDS/BP/THF the slowest. However by the $T_{1/4}$ times the SDS/BP/CHD has the largest value. This means that it takes the longest of

the five systems to reach a quarter of the initial signal size, due to a smaller proportion of the radical recombination occurring in the geminate period than for the other systems.

Kinetic analysis (as described in section 3.7) was performed on the zero field time curves shown in figure 4.4, and the results are shown in table 4.4.

System	k_G / 10^6 s^{-1} (st. dev.)	k_E / 10^6 s^{-1} (st. dev.)	k_F / 10^6 s^{-1} M^{-1} (st. dev.)
SDS/BP	1.42 (4.0×10^3)	2.77 (8.8×10^3)	16.2 (1.7×10^4)
SDS/BP/CH	3.45 (2.9×10^3)	2.13 (6.1×10^3)	2.52 (1.26×10^3)
SDS/BP/CHD	3.38 (5.1×10^3)	3.16 (1.0×10^4)	1.38 ($5.3\ 10^2$)
SDS/BP/PrOH	0.95 (5.8×10^3)	6.01 (1.8×10^4)	6.33 (2.6×10^3)
SDS/BP/THF	1.53 (7.9×10^2)	0.62 (1.3×10^3)	1.26 (1.1×10^3)

Table 4.4: Rate constants (with standard deviation) from kinetic analysis of time curves

The rate constants shown in table 4.4 confirm that the addition of hydrogen donors has a far greater effect than just changing the hydrogen abstraction rate. With the exception of PrOH the addition of hydrogen donors leads to an increased geminate recombination rate over SDS/BP without any additional donor. As described in section 1.2.4 the probability of geminate reaction is dependent on both the rate of spin mixing, and the rate of diffusion inside the micelle. The order of k_G is SDS/BP/CH ~ SDS/BP/CHD > SDS/BP/THF > SDS/BP/PrOH, which agrees quite well with the order of hydrogen abstraction shown in table 4.2. However, there are many other factors to consider, and an alternative explanation for the trend in the size of k_G is discussed below.

The effect on the escape rate is dependent on the hydrogen donor. PrOH and CHD cause an increase in the escape rate, whilst CH and THF show a decrease in escape rate. It might be thought that the size of the escape rate would correlate with the affinity of the radical for being in the bulk aqueous solution, in comparison with the affinity for the hydrophobic interior of the micelle. Table 4.5 shows the logarithm of the partition coefficients between octanol and water (log P_{ow}) for the neutral forms of the four hydrogen donor molecules, and for benzophenone. The partition coefficient of a substance, between octanol and water is defined as the ratio of the concentration of the substance in the octanol phase to the concentration of the substance in the aqueous phase of a two-phase octanol/water system.

Molecule	**log P_{ow}**
CH	2.90
CHD	2.30
PrOH	0.16
THF	0.33
BP	3.18

Table 4.5: Logarithmic value of the partition coefficient between octanol and water [12]

Table 4.5 shows data for the neutral forms of the molecules, rather than the radicals, but the relative values for the five compounds should not change dramatically from the molecular form to the radical. The table also shows that there is no relationship between the partition coefficients and the value of k_E in SDS micelles. However, table 4.5 could shed some light on the variation in k_G shown in table 4.4. For the four systems with additional hydrogen donors the two with the lowest values of k_G also have the lowest values of P_{ow}. The relative affinity for the hydrogen donors between the micelle interior and the bulk aqueous solution could influence the position of the radical inside the micelle. The BP molecule has the largest value of P_{ow} of the five substances shown in table 4.5, so could be expected to be in the interior of the micelle.

If molecules like PrOH and THF have a greater affinity for water then they could, on average be expected to be closer towards the edge of the micelle than molecules like CH and CHD. This could mean a smaller average inter-radical distance for CH and CHD, and hence a faster rate of geminate recombination. The lower values of P_{ow} for THF and PrOH also imply that the concentration of these molecules inside the micelle is going to be lower than that of CH and CHD, however the large excess of hydrogen donor molecules over BP should ensure that this does not affect the identity of the RP formed.

As discussed in section 3.8, other groups have proposed kinetic analysis schemes to analyse data from flash photolysis experiments, and these schemes have been applied to the SDS/BP system. Scaiano et al. [2] investigated both SDS/BP and SDS/BP/CHD and calculated escape rates of 2×10^5 s^{-1} and 4.4×10^6 s^{-1} for SDS/BP and SDS/BP/CHD respectively. Eveson et al. [13] used a similar method to calculate the geminate recombination and escape rate constants for the SDS/BP system, and determined values of 1.6×10^6 s^{-1} and 2×10^5 s^{-1} for k_G and k_E respectively. Both these reports were measured at zero applied magnetic field. In 2003 Sakaguchi and Woodward [14] also investigated the SDS/BP and SDS/BP/CHD systems using a combination of three techniques, as described in section 3.8. Values of the escape rate constant were given as 2.1×10^5 s^{-1} and 2.0×10^6 s^{-1} for SDS/BP and SDS/BP/CHD respectively. These data were recorded at approximately 330 mT, but the escape rate should be independent of magnetic field strength. The rate constants from these three sources do not agree very well with those given in table 4.4, the value of k_E for SDS/BP is approximately ten times larger than the literature values. However, the value of k_G for SDS/BP of 1.4×10^6 s^{-1} is close to the value given in [13], and the

value of k_E for SDS/BP/CHD falls between the values quoted in [2] and [14]. There are two main reasons for the lack of agreement between the values in table 4.4 and the literature values. The first is that (as described in section 3.8) the kinetic schemes of [2] and [13] take no account of the F pair recombination, and only use the slope of the fast, geminate decay to calculate the rate constants. The second reason for the discrepancies is that the fitting of three rate constants to one decay curve (as is the case with the kinetic scheme used in this thesis) is somewhat dangerous, despite the precaution of taking a wide range of initial guesses and checking the convergence for the three rate constants for each fitting routine.

Figure 4.5 shows MARY curves for the five systems (*i.e.*, not including SDS/BP/TEA). Each curve has 144 averages per point and is the average of three different MARY curves. The curves for the five systems are fairly similar, but at higher magnetic field strengths there is a definite trend in the order of the magnitude of the magnetic field effects, with SDS/BP/CHD > SDS/BP/CH > SDS/BP > SDS/BP/PrOH > SDS/BP/THF. Despite extensive signal averaging the presence of any LFEs is not resolved within the noise of the experiment, and therefore trends between the size of any LFEs cannot be determined. However, it is valid to say from figure 4.5 that the LFEs of the hydrogen donor systems are not significantly larger than those of SDS/BP in the absence of any additional hydrogen donor.

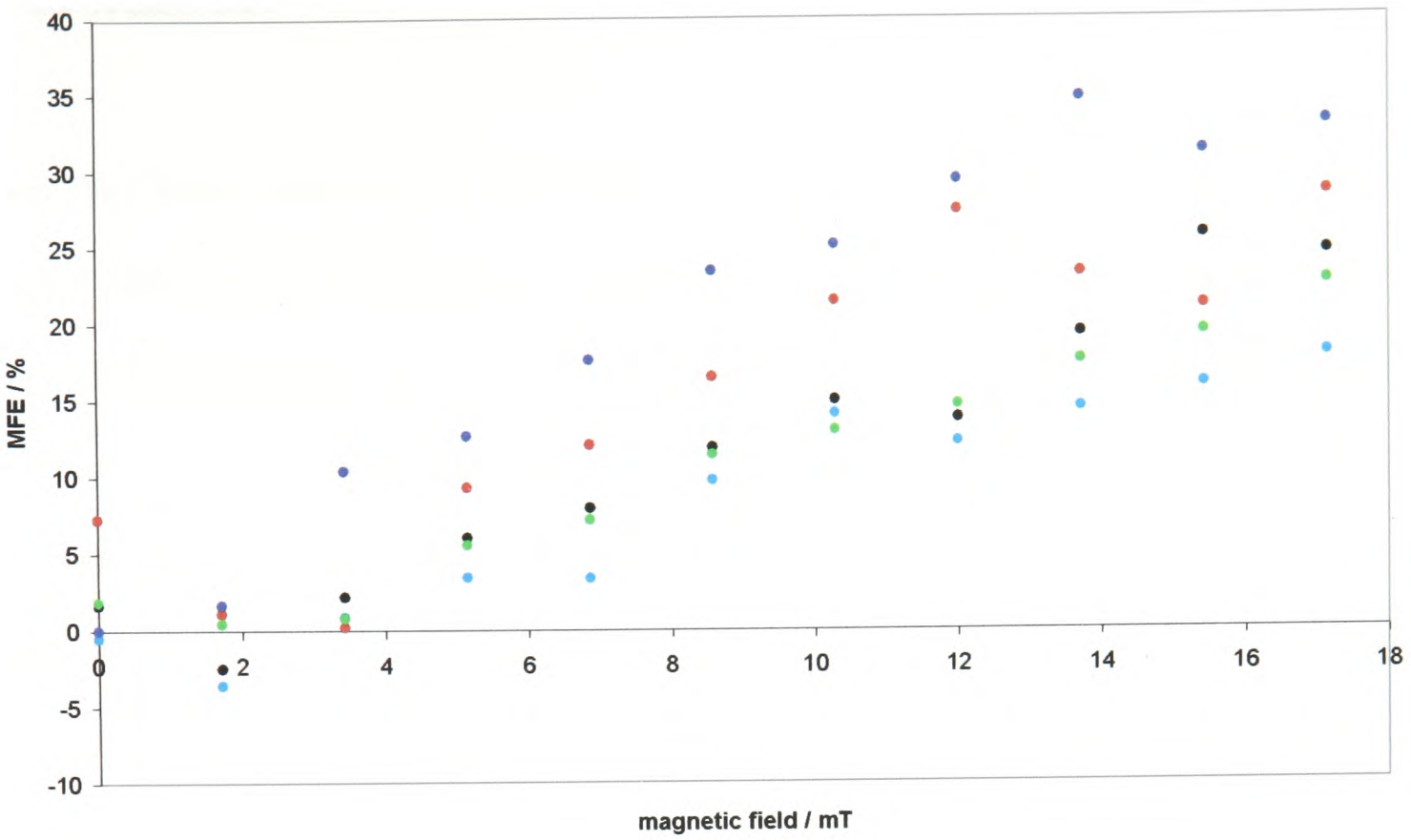


Figure 4.5: MARY curves of (•) SDS/BP (1.7), (•) SDS/BP/CH (7.0), (•) SDS/BP/CHD (3.0), (•) SDS/BP/PrOH (1.9), and (•) SDS/BP/THF (3.0) (figures in brackets show EE / %)

In 2000 Eveson et al. [13] also discussed the relationship between the relative sizes of k_G and k_E and the size of the MFE. From consideration of a simple kinetic model they calculate that the optimum MFE should be seen for systems where k_E / k_G ~ 1. If the rate constants from table 4.4 are used to calculate k_E / k_G (or k_G / k_E when $k_E > k_G$) the order for the five systems is SDS/BP/CHD (0.94) > SDS/BP/CH (0.62) > SDS/BP (0.51) > SDS/BP/THF (0.41) > SDS/BP/PrOH (0.16), which gives qualitative agreement with the MARY curves in figure 4.5.

It is also worth noting that the size of the $T_{3/4}$ fractional lifetimes agree qualitatively with the size of the MFEs of the five systems, with those systems with the shortest $T_{3/4}$ times having the largest MFEs.

4.3 DEUTERATION

There has been discussion in the literature as to how the LFE is affected by the number and size of the hyperfine couplings of the RP. One suggestion is that a large LFE is only seen when one radical has a few, small hyperfine couplings and the other has much larger hyperfine couplings [15-17]. Theoretical calculations have shown however that the magnitude of the LFE should be independent of the number and arrangement of magnetic nuclei on the radicals [18]. Deuterating one, or both, of the radicals in a pair allows the size of the hyperfine couplings to be changed whilst keeping almost all other factors constant. The normal MFE is also affected by a change in the hyperfine couplings of the RP. As discussed in section 1.3.1 it is the hyperfine couplings on the radicals that drive the coherent spin mixing between the triplet and singlet states of the RP in the weak magnetic field region. When hydrogen atoms on either radical are replaced with deuterium atoms this changes the size of the hyperfine couplings and the spin quantum number, I, and hence changes the rate of spin mixing, leading to magnetic isotope effects. It has been shown for radical ion pairs [19] that the position of the maximum of the hyperfine mixing dominated magnetic field effect can be related to the average hyperfine coupling on the two radicals by equation 4.2:

$$B_{1/2} = \frac{2(<a_1>^2 + <a_2>^2)}{<a_1> + <a_2>} \qquad (4.2)$$

where $B_{1/2}$ is the magnetic field strength at half the saturation value of the MFE (as seen in figure 1.6), *i.e.* for a saturating MFE of X% $B_{1/2}$ is the magnetic field strength

when the MFE is $^{X}/_{2}$%. $\langle a_1 \rangle$ and $\langle a_2 \rangle$ are the average hyperfine couplings on the two radicals as defined by equation 4.3:

$$\langle a_k \rangle = \sqrt{\sum_i a_i^2 I_i (I_i + 1)} \,. \qquad (4.3)$$

For the chemical systems used in this work the saturation value of the magnetic field strength is not reached at the maximum magnetic field strengths used, for SDS/BP this saturation value of magnetic field strength is reported to be approximately 2 T [20], but this is due to a combination of the hyperfine coupling mechanism and the relaxation mechanism [21]. However, equation 4.2 can be used as an indicator of the predicted relative positions of the MFEs in systems of known hyperfine couplings.

There are further complications in the SDS/BP system in that to form the RP a hydrogen atom is abstracted by BP from a hydrogen donor, as shown in the reaction scheme in section 1.2.5. If this hydrogen is changed to a deuterium atom the rate of abstraction may be changed due to the kinetic isotope effect, and this could also affect the kinetics of the RP. Tominaga et al. [22] have investigated the effect of deuteration on the hydrogen abstraction reaction by acetone from PrOH and $PrOH_{d8}$. They found that the ratio of the hydrogen abstraction rates from the protonated and deuterated forms of PrOH (k_H/k_D) was 4.1 ± 0.8 at 19 °C.

Deuterated BP is available commercially, but deuterated SDS is prohibitively expensive for sufficient data to be obtained. This means that for more than one member of the RP to be deuterated an alternative hydrogen donor needs to be found. Of the hydrogen donors used in section 4.2 fully deuterated THF and PrOH were the

only economically viable donors available, and their effects on both the time curves and MARY curves were investigated, as discussed in the following sections.

4.3.1 SDS/BP

The first system to be investigated was SDS/BP, to see if fully deuterating the BP (to form BP_{d10}) impacts on either the time or the MARY curves. Full deuteration of BP does not give a fully deuterated radical, as to form the radical pair a hydrogen is abstracted from a suitable donor as mentioned above. In the case of SDS/BP the donor is one of the SDS molecules that makes up the micelle. Table 4.6 lists the hyperfine couplings on the $BPH^{\bullet}$ radical, and as it shows the hyperfine coupling to the abstracted hydrogen molecule is not the largest in the radical, but it is of significant size, so deuterating the other hydrogen atoms on BP may not show the large isotope differences which have been shown in other RP systems [23,24]. Table 4.6 also shows the average hyperfine coupling in the $BPH^{\bullet}$ and $BPH_{d10}^{\bullet}$ radicals, $\langle a_{BPH} \rangle$ and $\langle a_{BPH\ d10} \rangle$, which are calculated using equation 4.3.

Hydrogen on BPH radical	Hyperfine coupling / mT
4H(o)	0.323
4H(m)	0.123
2H(p)	0.364
H(OH)	0.291
$\langle a_{BPH} \rangle$	0.787
$\langle a_{BPH\text{-}d10} \rangle$	0.314

Table 4.6: Hyperfine couplings on the BPH radical [25]

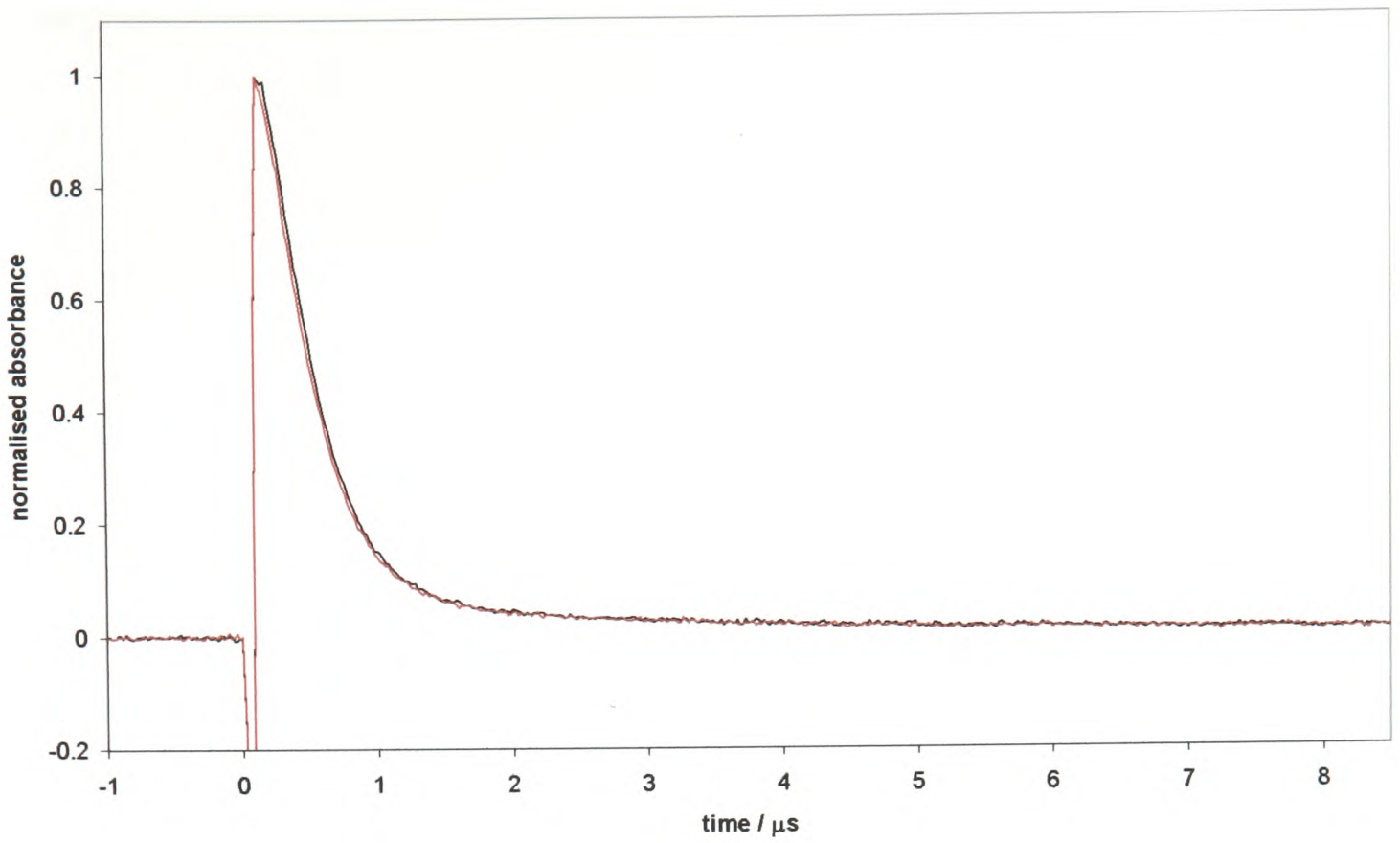


Figure 4.6: Normalised zero field time curves of (•) SDS/BP, and (•) SDS/BP_{d10}

Figure 4.6 shows normalised zero field time curves of both SDS/BP and SDS/BP_{d10}, and the fact that the curves are almost identical. The rate of decay of the signal is the same regardless of whether the BP is protonated or deuterated. This agrees with results which have been reported previously for BP in SDS micelles [26,27] which give identical decay rate constants for SDS/BP and SDS/BP_{d10}.

Figure 4.7 shows MARY curves for both protonated and deuterated BP in SDS. Each MARY curve is made up of an average of twelve MARY curves, and in total there are 576 averages per point. It is hard to see any real difference over the whole magnetic field range, although SDS/BP_{d10} seems to have smaller MFE at higher strength magnetic fields. Again this agrees with reported results [26,27], which show that although the decay rate constant decreases with increasing magnetic field for both SDS/BP and SDS/BP_{d10}, the difference between the two isotopes is negligible, even at magnetic fields up to 70 mT.

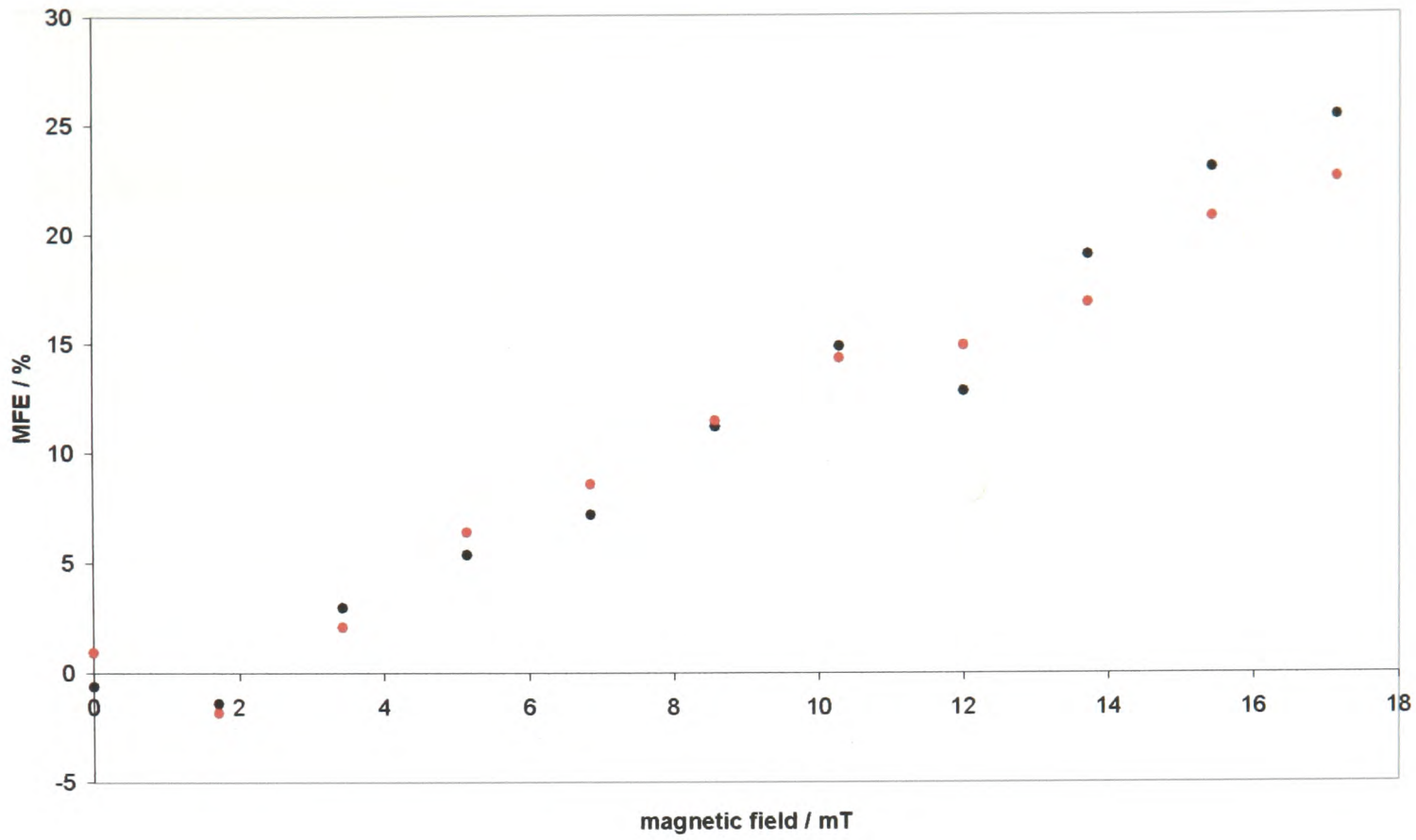


Figure 4.7: MARY curves of (•) SDS/BP (2.2), and (•) SDS/BP_{d10} (2.3) (EE / %)

The average hyperfine coupling in the SDS derived radical is calculated to be 4.79 mT using equation 4.3 and hyperfine couplings taken from [28]. This gives $B_{1/2}$ values of 8.5 mT and 9.0 mT for SDS/BP and SDS/BP_{d10} respectively using equation 4.2, which again suggests a very small difference between the two systems.

Figure 4.7 also shows that the $B_{1/2}$ values predicted by equation 4.2 do not give a quantitative forecast of the saturation value of the SDS/BP system. A $B_{1/2}$ value of 8.5 mT means that from figure 4.7 the MARY curve of SDS/BP should level off at a MFE value of around 20%. However, by the largest magnetic field strengths reached by the Helmholtz coils the MFE is approximately 25%, with no sign of reaching its saturation value.

4.3.2 SDS/BP/THF

As the deuterated versions of both BP and THF are available there are four different permutations possible within this system. Figure 4.8 shows normalised zero field time curves of each of the different combinations of isomers. As with the previous section deuterating the BP makes very little difference to the absorption. However deuterating the THF does change the decay rate from around 0.5 μs after the initial peak, with the two THF_{d8} curves showing a smaller absorption, and hence faster radical recombination than the curves with protonated THF.

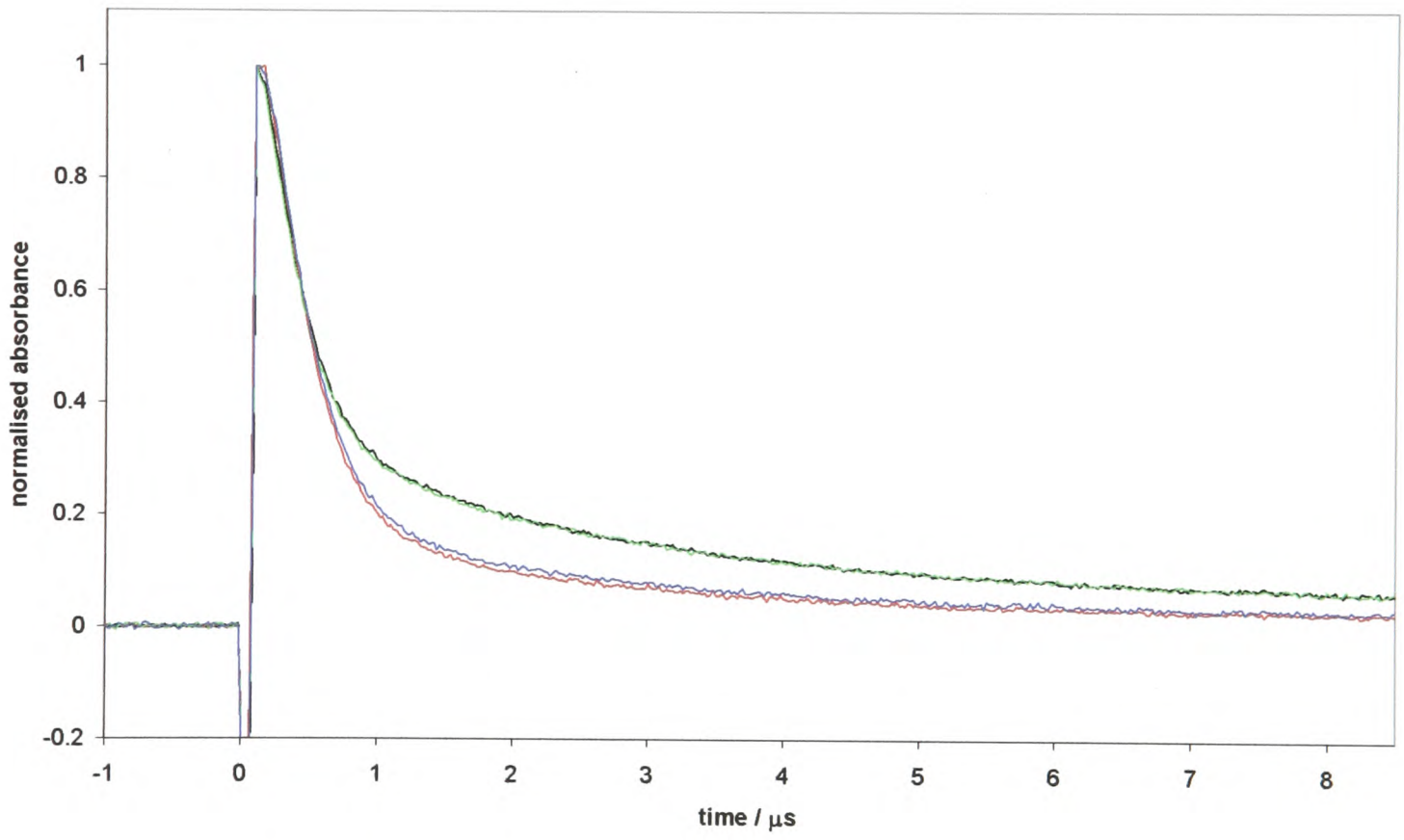


Figure 4.8: Normalised zero field time curves of (•) SDS/BP/THF, (•) SDS/BP/THF_{d8}, (•) SDS/BP_{d10}/THF, and (•) SDS/BP_{d10}/THF_{d8}

Table 4.7 gives the fractional lifetimes of the four systems, calculated from the data in figure 4.8. It can be seen that the difference in recombination rates does not become visible until after the signal has fallen to half its initial size.

BP	THF	$T_{3/4}$ / μs	$T_{1/2}$ / μs	$T_{1/4}$ / μs
p	p	0.22	0.44	1.3
p	d	0.24	0.42	0.78
d	p	0.22	0.44	1.26
d	d	0.24	0.44	0.8

Table 4.7: Fractional lifetimes for the four combinations of isotopes in the SDS/BP/THF system. p indicates protonated, and d indicates deuterated

Another factor that could be influencing the appearance of the zero field time curves is the kinetic isotope effect, discussed above. The rate of hydrogen abstraction is expected to be slower from deuterated THF than from protonated THF. As there is a competition between the THF and SDS molecules to donate a hydrogen atom a decrease in the hydrogen abstraction rate would lead to an increase in the proportion of RPs that are formed from SDS monomers. Using equation 4.1, and assuming that the rate of hydrogen abstraction from THF drops by a factor of four upon deuteration (as it does with abstraction by acetone from PrOH [22]) then upon deuteration the proportion of RPs that contain a THF derived radical drops from 90% to 71%. Hence the kinetic isotope effect cannot be observed in a difference in hydrogen abstraction and radical formation, but is rather observed in a difference in the decay kinetics due to an alteration of the proportion of RPs that are derived from the THF molecule, with a decrease in the proportion of THF derived radicals in the solutions that contain deuterated THF. The observed signal is due to the ketyl radical in both cases, but the identity of the counter radical determines the rate of signal decay.

If figure 4.4 and table 4.3 are examined it can be seen that the SDS/BP/THF system shows a slower rate of signal loss than the SDS/BP system, with all three fractional lifetimes of SDS/BP/THF being greater than the corresponding fractional lifetimes of SDS/BP. This trend is not repeated upon deuteration of THF, but it could partially explain why the zero field time curves with the deuterated THF have a faster overall rate of signal loss than those with deuterated THF in figure 4.8.

It is not known from which position BP abstracts a hydrogen (or deuterium) atom from THF, but hyperfine couplings are available in the literature for both positions and they are shown below in table 4.8, with the average hyperfine coupling for both radicals. The average hyperfine coupling for the deuterated forms of the THF radicals is also shown for comparison.

Abstraction α to oxygen		**Abstraction β to oxygen**	
Hydrogen on THF radical	**Hyperfine coupling / mT**	**Hydrogen on THF radical**	**Hyperfine coupling / mT**
H(α)	1.229	H(α)	2.12
2H(β)	2.857	4H(β)	3.55
$2H(\gamma_1)$	0.082		
$2H(\gamma_2)$	0.164		
$\langle a_{THF\alpha} \rangle$	3.66	$\langle a_{THF\beta} \rangle$	6.42
$\langle a_{THF\alpha\text{-}d8} \rangle$	0.921	$\langle a_{THF\beta\text{-}d8} \rangle$	1.61

4.8: Hyperfine couplings for radicals formed by hydrogen abstraction from the two different positions of THF [29]

Not only are the hyperfine couplings in the THF radicals bigger than those in $BPH^{\bullet}$, but, as stated in section 4.2.1, when the $BPH^{\bullet}$ radical is formed from BP the hydrogen that is abstracted comes from the hydrogen donor molecule. Hence, reducing the hyperfine couplings by deuterating the hydrogen donor has the added effect of reducing one of the hyperfine couplings on the ketyl radical by changing the abstracted atom from hydrogen to deuterium. Both these reasons explain why deuterating THF makes a larger difference to the zero field time curves than deuterating BP in terms of the hyperfine couplings. Table 4.9 summarises the average hyperfine couplings in the four different isomeric permutations of the SDS/BP/THF system. For the THF derived radical values are given for hydrogen abstraction from positions both α– and β– to the oxygen. The table also shows the $B_{1/2}$ values calculated from equation 4.2.

BP/THF	average coupling on ketyl radical / mT	average hyperfine coupling on THF radical / mT		$B_{1/2}$ / mT	
		THFα	THFβ	THFα	THFβ
p/p	0.785	3.66	6.42	6.3	11.6
p/d	0.749	0.921	1.61	1.7	2.7
d/p	0.314	3.66	6.42	6.8	12.3
d/d	0.198	0.921	1.61	1.6	2.9

Table 4.9: Average hyperfine couplings and $B_{1/2}$ values in the SDS/BP/THF system. p indicates protonated, and d indicates deuterated

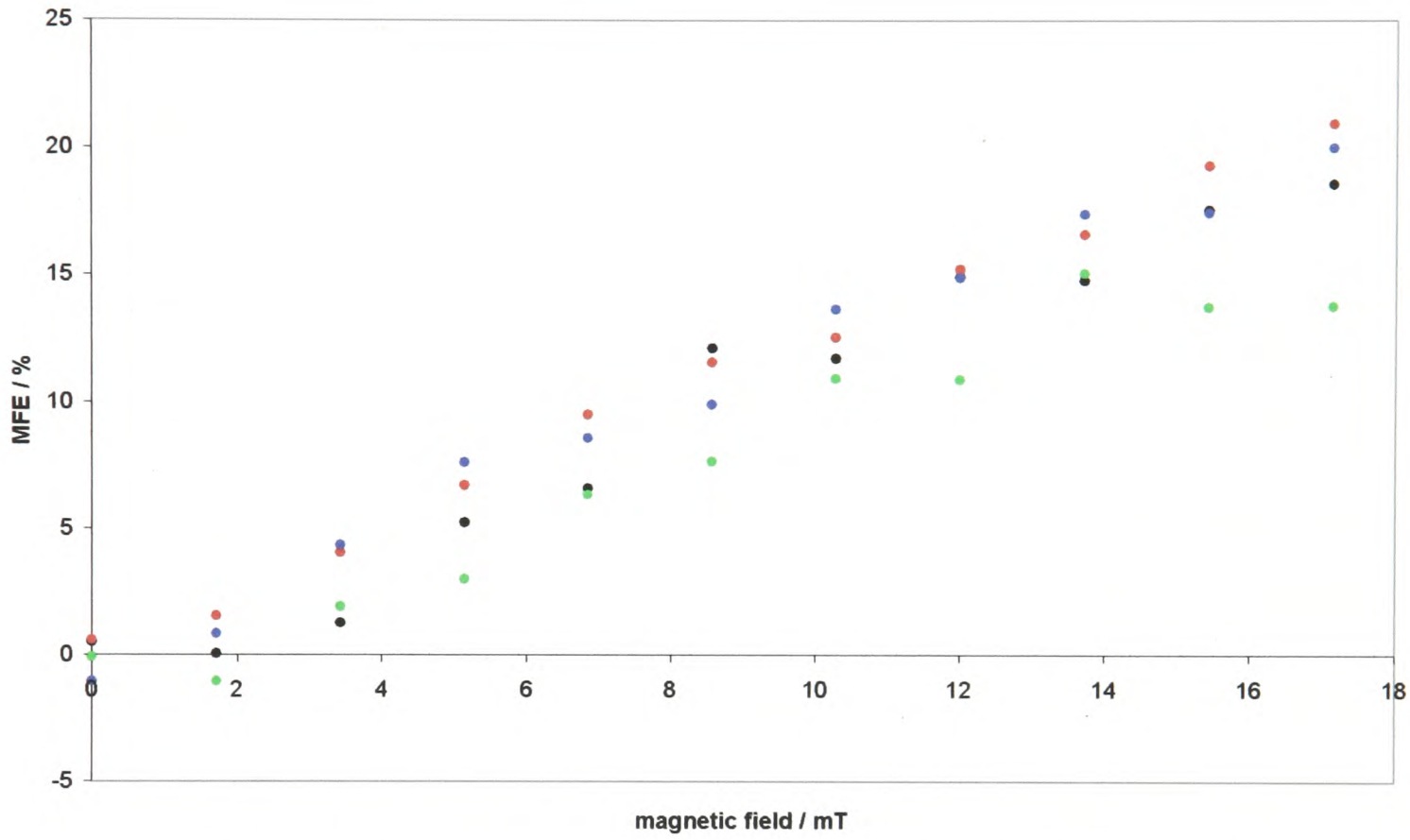


Figure 4.9: MARY curves of (•) SDS/BP/THF (2.6), (•) SDS/BP/THF_{d8} (1.8) (•) SDS/BP_{d10}/THF (2.7), and (•) SDS/BP_{d10}/THF_{d8} (2.5) (EE / %)

The MARY curves of the four systems, shown in figure 4.9, do not show differences as obvious as those in the zero field time curves. In general SDS/BP_{d10}/THF has the smallest magnetic field effects and SDS/BP/THF_{d8} the largest, but the differences between the sizes of the MFEs are very small. The curves have different numbers of averages, but this will not affect their shape, or ordering. The SDS/BP_{d10}/THF MARY curve is made up of eight separate MARY curves, each of 48 averages per point. SDS/BP/THF and SDS/BP_{d10}/THF_{d8} are averages of nine MARY curves, again of 48 averages per point and SDS/BP/THF_{d8} is made from 18 separate MARY curves.

From the $B_{1/2}$ values in table 4.9 the MARY curves with deuterated THF would be expected to reach the saturation value of MFEs before those with protonated THF, but as was the case with SDS/BP no indication of this is given in figure 4.9.

The largest suggestion of a LFE from figure 4.9 (within experimental error) is from SDS/BP_{d10}/THF, and from table 4.8 it can be seen that it is this system that has the largest difference in average hyperfine couplings between the two radicals in the RP.

4.3.3 SDS/BP/PrOH

With this system only the PrOH was deuterated to provide a comparison with the SDS/BP/THF system, where it was only the deuteration of THF that made an obvious difference to the zero field time curves. Figure 4.10 shows the zero field time curves for the protonated and deuterated versions of PrOH with SDS and BP. As with the SDS/BP/THF system it is the deuterated form of the hydrogen (deuterium) donor which has the smaller absorption, *i.e.* the rate of loss of the ketyl radical is greater with the deuterated version. The difference between the zero field time curves of the deuterated and protonated forms is greater in the THF system than in PrOH. As with the THF results the differences in the zero field time curves caused by deuteration are not seen until almost the end of the fast decay portion of the curves.

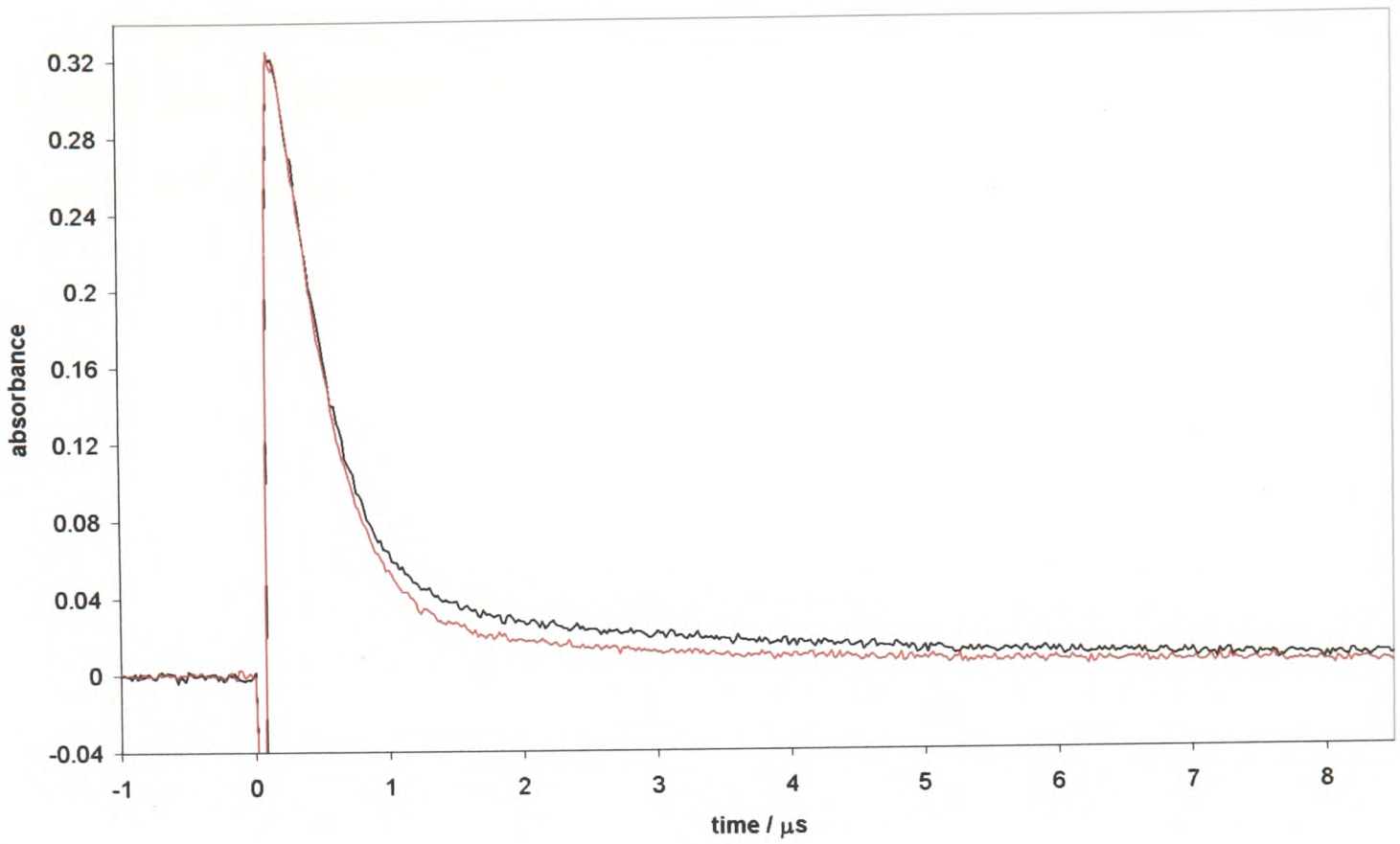


Figure 4.10: Zero field time curves of (•) SDS/BP/PrOH, and (•) SDS/BP/PrOH$_{d8}$

As with THF, the kinetic isotope effect on the RP forming hydrogen abstraction reaction is most likely to be the major factor in the differences in the zero field time curves. Using equation 4.1 and assuming the hydrogen abstraction rate falls by a factor of four upon deuteration the proportion of RPs that contain a PrOH derived radical drops from 49% to 20%. Figure 4.4 and table 4.3 showed that of the five hydrogen donor systems investigated the SDS/BP/PrOH system was closest to the SDS/BP in terms of both appearance of the zero field time curves and size of the fractional lifetimes, and table 4.2 showed that PrOH had the lowest proportion of hydrogen donor derived radical in the RP of the five systems. Both these facts could account for the small change in the zero field time curves of SDS/BP/PrOH upon deuteration.

Table 4.10 gives the average hyperfine couplings and the $B_{1/2}$ values for the RPs with protonated and deuterated PrOH. The average hyperfine coupling for the radical derived from PrOH was calculated from hyperfine coupling values published in [30].

PrOH	average coupling on ketyl radical / mT	average coupling on PrOH radical / mT	$B_{1/2}$ / mT
protonated	0.785	4.20	7.3
deuterated	0.749	1.06	1.9

Table 4.10: Average hyperfine couplings and $B_{1/2}$ values in the SDS/BP/PrOH system

The MARY curves for the SDS/BP/PrOH system are shown in figure 4.11 and it can be seen that deuterating the PrOH makes no difference at all to the magnetic field effects. This agrees with the results seen in section 4.2.2 with THF, where the difference in the zero field time curves is not reflected in the MARY curves.

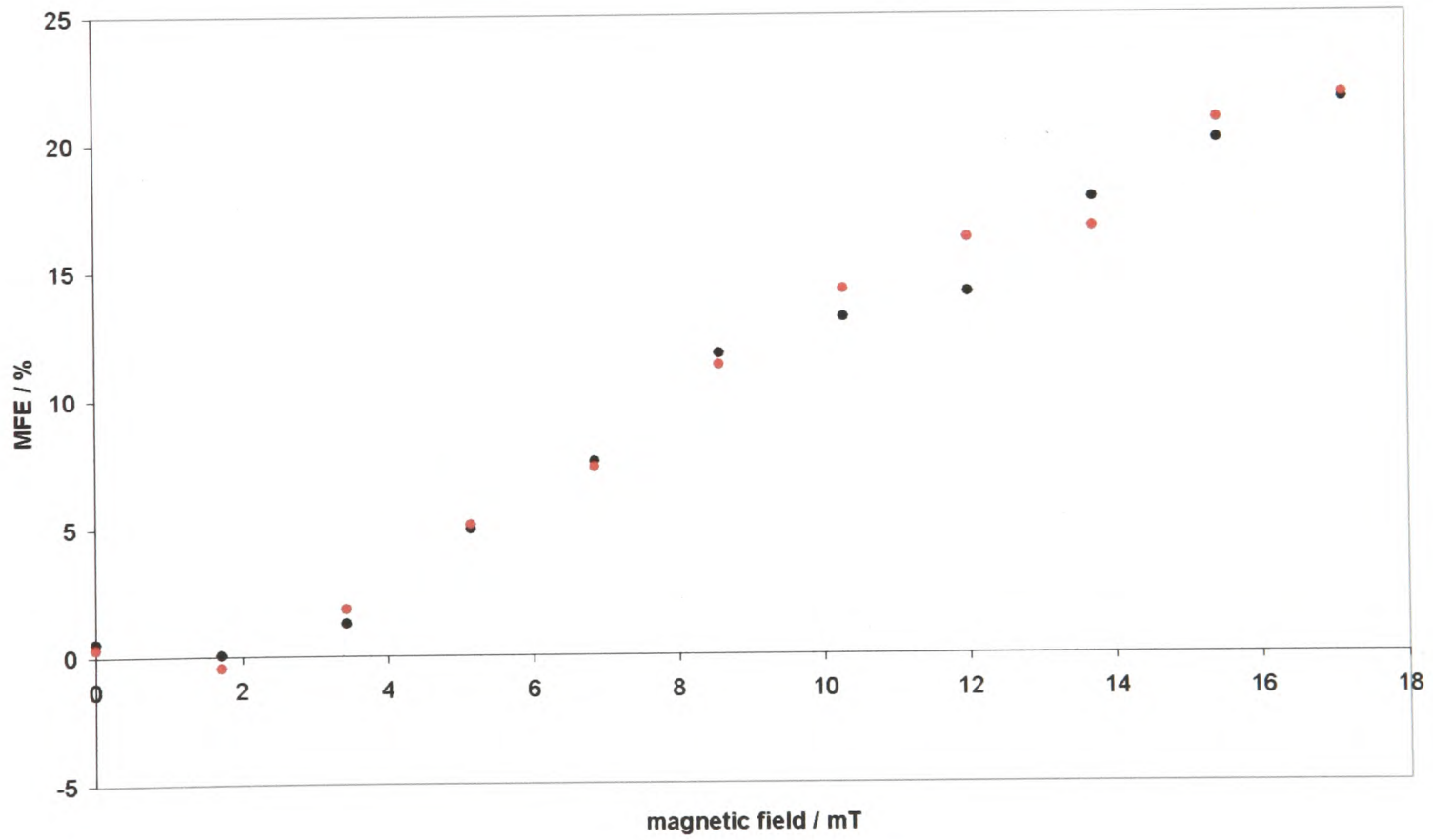


Figure 4.11: MARY curves of (•) SDS/BP/PrOH (1.9), and (•) SDS/BP/$PrOH_{d8}$ (2.5) (EE / %)

Overall the deuteration work has proved somewhat inconclusive. The large differences in the size of the MFEs predicted by the $B_{1/2}$ formula have not been seen

in any of the three systems, despite deuteration of the hydrogen donor molecule having a visible effect on the zero field time curves of the two systems investigated. One possible explanation could be the actual identity of the RP formed. In all cases where a hydrogen donor molecule is present inside the micelle hydrogen abstraction by the excited BP triplet could occur from both the hydrogen donor and SDS molecules, and estimates for the proportion of RPs that contain hydrogen donor derived radicals have been made. Hence the kinetic isotope effect of deuterating the hydrogen donor could lead to a larger proportion of hydrogen abstraction from SDS in comparison to the protonated form of the hydrogen donor. To investigate this further detailed product studies would have to be carried out to identify the recombination products, or EPR spectroscopy could be used to detect the nature of the RP formed in each case.

4.4 True Zero Magnetic Field

The largest LFEs seen using the flash photolysis equipment described in chapter three are of the order of 3%, and were seen for the DTAC/BP system at 50 °C. Experiments undertaken by other research groups using the same techniques, but using other chemical systems have seen LFEs of the order of 10%, for example Maeda et al. [31] using diphenyl (2,4,6-trimethyl-benzoyl) phosphineoxide (TMPDO) in SDS micelles have seen LFEs of this magnitude. In one theoretical investigation by Curtis [1] very large changes in the size of the MFE were predicted when moving from true zero magnetic field to very small magnetic fields of the order of 0.1 mT, for a radical pair with hyperfine couplings of the order of 1 mT. A magnetic field strength of 0.1 mT is approximately twice that of the Earth's magnetic field. Hence, in order to investigate

the theoretical predictions experimentally modifications to the apparatus had to be made.

4.4.1 Theoretical Model

The theoretical model is based on a spin correlated radical pair with a single spin ½ nucleus on one of the radicals, the one proton radical pair as introduced in section 1.2.1b. The electron and nuclear spins on the radicals interact with one another through hyperfine and exchange interactions, and with the magnetic field by Zeeman interactions. Only one single hyperfine interaction is included in the simulation and provides the sole mechanism of mixing between the singlet and triplet states.

One of the radicals is considered to be stationary and fixed at the centre of the micelle, and the other radical is free to diffuse around the micelle and either to recombine with the radical in the centre, or to escape from the surface of the micelle.

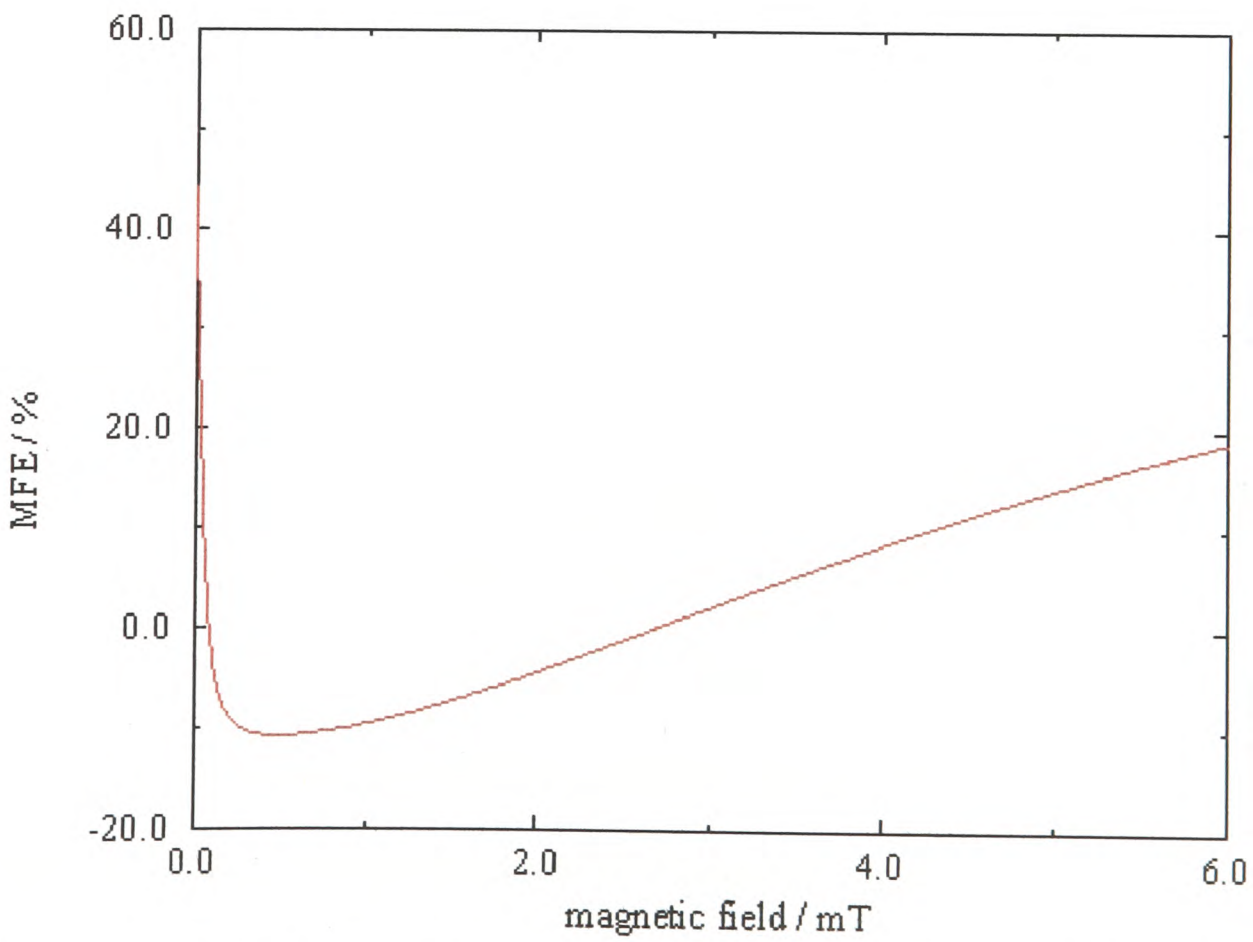


Figure 4.12: Simulation for one proton radical pair showing large change in MFE between zero and very small magnetic fields (adapted from Curtis [1])

The model only allows two fates of the RP, either geminate recombination inside the micelle, or escape of the mobile radical; no F pair recombination is considered.

The time evolution of the model is provided by solving the stochastic Liouville equation (SLE) [32], which allows both spin evolution and radical diffusion to be considered simultaneously. Figure 4.12 shows a typical simulated MARY curve, and the very large difference in MFE between true zero field and very low magnetic field strengths.

The results obtained in [1] by varying the various parameters such as the size of the exchange interaction, the rate constants, and the various diffusion parameters could be changed to fit either the experimental time curves, or the experimental MARY curves, but never both with the same set of parameters. When the theoretical model gave a good fit to the experimental time curves the MARY curve shown in figure 4.12 was produced, and it was for this reason that it was thought that the large change in MFE size between true zero and very small magnetic field strengths could be present.

4.4.2 Experimental Results

To investigate these theoretical predictions experimentally a method of shielding the cell from the Earth's magnetic field was designed. A mu-metal box was employed to enclose the cell, with small windows cut into it to allow the laser light to reach the cell, and to allow the analysis light to pass through from the lamp to the monochromator. Measurements of the magnetic field strength at the cell, inside the mu-metal box, with a Hall probe showed a reduction in magnetic field strength of

between 10 and 20 times that without the mu-metal box present, giving a magnetic field of the order of 5 μT.

To provide a very small magnetic field inside the mu metal box a pair of Helmholtz coils of radius 50 mm were wound, and connected to a DC power supply providing a steady current of 0.6 A. The magnetic field strength measured with a Hall probe, at this current, at the cell was between 0.23 and 0.26 mT. Time curves were obtained with the DC power supply turned off, and with the power supply turned on in turn over a period of around 90 minutes with time resolutions of both 10 μs and 2 μs.

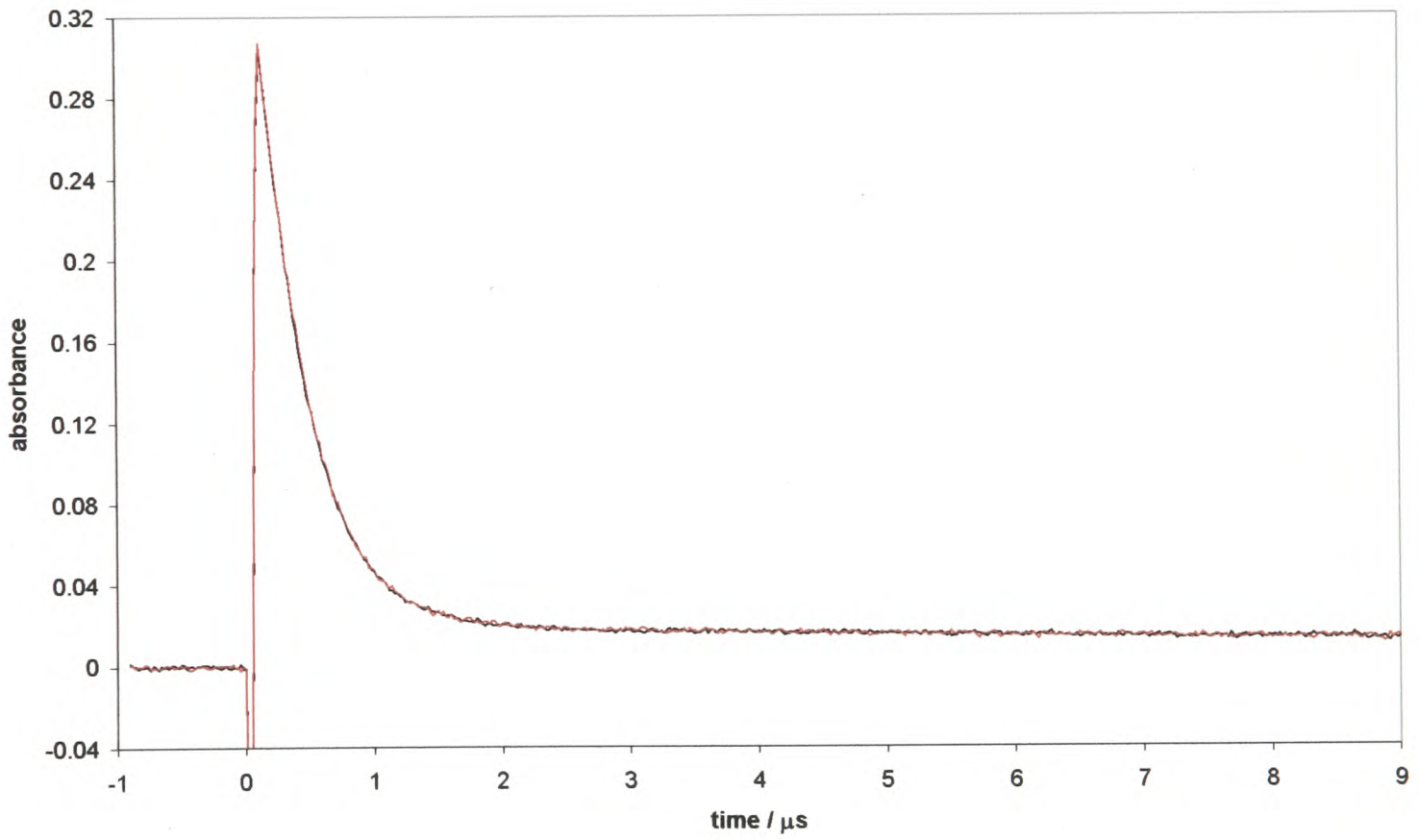


Figure 4.13: Time curves of SDS/BP inside mu metal box with (●) DC power supply turned off, and (●) DC power supply turned on

These investigations were carried out using the 4 ml, multiple reflection cell described in section 3.5.1, and the solution used was SDS/BP with concentrations as described in section 4.1.

Figure 4.13 shows time curves obtained over 10 μs, using this apparatus in both the presence and absence of the magnetic field provided by the Helmholtz coils inside the mu-metal box. Each curve shown is the average of four time curves, each of 30 averages. The curves were recorded in batches of two curves, with the DC power supply switched on or off between each batch, *i.e.* off off, on on, off off, on on, with all the off curves averaged and all the on curves averaged. No difference can be seen in the size of the two time curves in figure 4.13.

These results do not conclusively prove that the effect predicted in [1] does not exist, but indicate that if it is present then it is at a much reduced size to that predicted. The simulations are based on the one proton radical pair, with a hyperfine coupling of 1 mT on one of the radicals. The experimental system has hyperfine couplings on both radicals, with an average hyperfine coupling of 0.787 mT on the $BPH^{\bullet}$ radical, and 4.79 mT on the SDS derived radical. However, simulations carried out in [1] show that increasing the size of the hyperfine coupling in the one proton RP increases the size of the LFE.

Theoretical simulations of the LFE were discussed in section 1.3.2b and it was stated that in investigations by Till et al. [33] the lifetime of the radical pair needs to be long for large LFEs to be observed (specifically that $\tau^{-1} >> a$, as described in section 1.3.2b) The simulations in [1] define the magnetic field effect as:

$$\mathrm{LFE} = \frac{\Phi_S(0) - \Phi_S(B)}{\Phi_S(0)} \times 100 \qquad (4.4)$$

where $\Phi_S(0)$ is the singlet yield at zero magnetic field, and $\Phi_S(B)$ is the singlet yield at a magnetic field strength of B. The singlet yield is defined as the proportion of the

initial RPs which have formed the singlet recombination product at infinite time. In the experimental system all the radicals have recombined within around 10 μs of RP formation, and so any effects that require a longer RP lifetime, and especially a longer geminate lifetime will not be seen.

4.5 Conclusions

This chapter has investigated three different methods which were believed to affect the magnitude and characteristics of both the LFE and the normal MFE, in the SDS/BP system. The first was based on the introduction of additional, more efficient hydrogen donors to the micelle. Further experiments tested for the effect of changing the hyperfine couplings within the radical pair, and, in the final portion of the chapter very low strength magnetic fields were studied with respect to their influence on the RP recombination efficiency following the theoretical hypothesis that had indicated a large MFE. Whilst the first two methods showed distinct changes to the zero field time curves, interestingly none of the three investigations showed a dramatic effect on either the LFE or the normal MFE. However, this chapter has demonstrated that excellent signal to noise ratios can be obtained with the SDS/BP system, which makes it an ideal candidate as a 'default' system for further MFE studies, and for comparison with other 'microstructure' environments.

5: Synthetic Micelles – Positively Charged Head Groups

During the experiments presented in this chapter the radical pair is again formed within a micelle, but in contrast to the previous chapter the amphiphilic molecules used to make the micelles have cationic head groups. The effects on RP behaviour of changing the length of the hydrophobic tail, and the consequence of the addition of some of the hydrogen donors used in chapter four are investigated. The overall charge of the micelle also influences its interactions with chemicals in the bulk solution, exterior to the micelles, and the consequences of this are explored briefly with the addition of paramagnetic and diamagnetic cations.

5.1 Experimental Section

All experiments were performed with 2 mM BP and 40 mM hydrogen donor at 25 °C. The concentration of surfactant varied as described below. Solutions were sonicated for 59 minutes at 25 °C prior to the experiment, and the experiment started within at least one hour after completion of sonication.

For all time curves shown there are 96 averages per curve, and each is the average two sets of acquisitions, unless stated otherwise. All time curves shown were recorded at zero applied magnetic field unless stated otherwise.

5.2 CARBON CHAIN LENGTH

As mentioned in chapter two the four different surfactants investigated in this section differ from each other only in the number of CH_2 units in the hydrophobic 'tail' of the molecule. They have the general formula $CH_3(CH_2)_{n-2}CH_2NMe_3Cl$, where n = 12 (DTAC), n = 14 (TTAC), n = 16 (CTAC), and n = 18 (OTAC). The difference in chain length affects the micelle properties in a number of ways. Increasing the length of the hydrophobic tail of the molecule decreases its solubility in water, and consequently the CMCs of the surfactants, which decrease from DTAC to OTAC, as listed in table 2.1. Listed in the same table are the aggregation numbers and it can be seen that the N_{agg} of the cationic micelles increases with increasing chain length. Both these effects were taken into account when calculating the concentration of surfactant needed for each experiment, to ensure that the BP:micelle ratio was kept constant in all four systems. The actual amphiphile concentrations used in the experiments were [DTAC] = 69 mM, [TTAC] = 70 mM, [CTAC] = 90 mM, and [OTAC] = 116 mM. These values were calculated to give an average of 1.5 BP molecules per micelle.

5.2.1 Zero Field Results

Figure 5.1 shows zero field time curves of all four cationic micelle systems, each curve is an average of 288 separate acquisitions at zero applied magnetic field. The curves have been normalised to give an absorbance of unity at the absorption peak, which allows a direct comparison between the kinetics of the four systems. The main differences that can be seen are in the gradient of the initial decay and in the time taken for each signal to decay to zero.

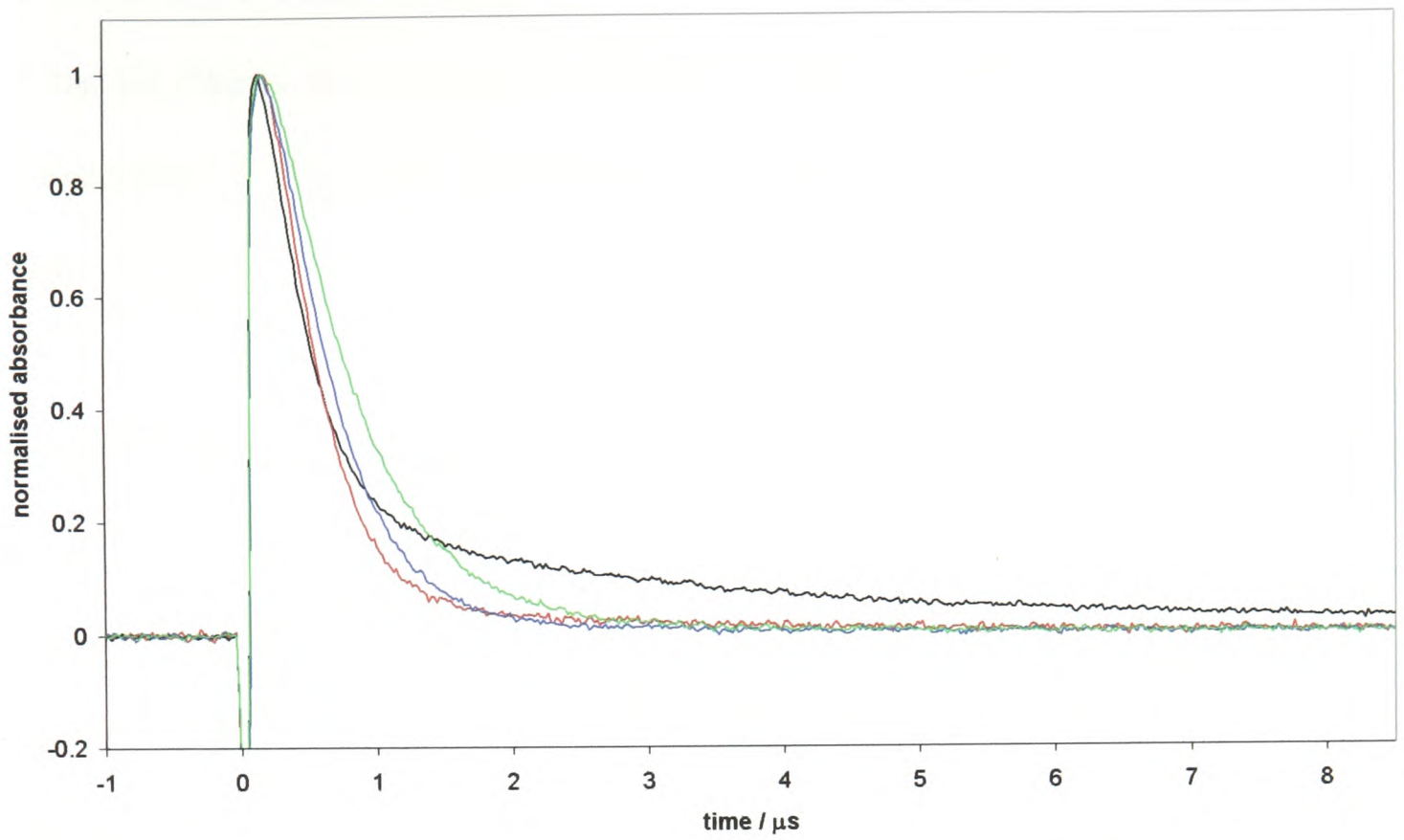


Figure 5.1: Normalised zero field time curves of BP in (•) DTAC, (•) TTAC, (•) CTAC, and (•) OTAC micelles

The initial decay of the signal is fastest for DTAC, with the other curves following in the order of their chain length. However, this is only true for approximately the first 0.6 μs after the laser flash, as at this point the DTAC curve crosses the TTAC curve and decays at a much slower rate. It is not as obvious, but the same behaviour is observed for the TTAC curve at approximately 1.8 μs post flash. It crosses the CTAC curve, and decays to zero at a later time than the CTAC curve. To show the difference in lifetimes and the shape of the curves table 5.1 shows the time taken for each curve to reach ¾, ½, and ¼ of the initial peak height.

System	$T_{3/4}$ / μs	$T_{1/2}$ / μs	$T_{1/4}$ / μs
DTAC/BP	0.20	0.40	0.82
TTAC/BP	0.22	0.38	0.66
CTAC/BP	0.28	0.48	0.78
OTAC/BP	0.30	0.58	1.02

Table 5.1: Fractional times for BP in alkyltrimethylammonium micelles

The $T_{3/4}$ time shows the difference in the fast, initial decay between the four systems, and that the shorter the carbon chain length the quicker the decay of the signal. With the exception of DTAC/BP the fractional lifetimes increase with increasing chain length.

The effect of micelle size on radical pair reactions has been studied for other systems, and conflicting results have been reported depending on the identity of the RP under investigation. In 1992 Tarasov et al. [1] investigated the reaction of geminate radical pairs derived from methyldeoxybenzoin (MDB) and from diastereomerically pure 2,4-diphenylpentan-3-one (DPP). The probability of geminate recombination of the primary radical pairs (labelled P_r), in alkyl sulfate micelles of different sizes, was measured by monitoring the extent of isomerization in the product ketones as a function of conversion. It was found for alkyl sulfate micelles of chain length eight carbons to twelve carbons that P_r for MDB increases as micelle size increases, but P_r for DPP decreases as micelle size increases. Increasing the number of carbons in the hydrophobic chain of the micelle increases both the size of the micelle, and the viscosity inside the micelle, and this has the effect of decreasing the re-encounter probability of the RP and also decreasing the escape rate of the radicals from the micelle. This example illustrates that changing even a simple parameter like the chain length of a micelle monomer can have complex effects on RP behaviour, and demonstrates the delicate balance between the processes that occur such as recombination and escape. In 2000 Eveson et al. [2] investigated the effect of chain length on the MFEs of BP in a series of alkyl sulfate micelles of chain lengths from eight carbons to fourteen carbons. From the results presented in this paper the

fractional lifetimes were calculated for the four different chain lengths, and are displayed in table 5.2.

No. of carbon atoms in 'tail'	$T_{3/4}$ / μs	$T_{1/2}$ / μs	$T_{1/4}$ / μs
8	0.25	0.51	9.1
10	0.31	0.67	2.5
12	0.36	0.64	1.1
14	0.36	0.59	0.92

Table 5.2: Fractional lifetimes for BP in sodium alkyl sulfate micelles from results presented by Eveson et al. [2]

The $T_{3/4}$ follow the same trends with chain length as those for the cationic micelles from table 5.1, namely that the $T_{3/4}$ value increases with increasing chain length. The $T_{1/2}$ values show opposite trends with the anionic and cationic micelles. Table 5.1 showed that the $T_{1/2}$ times for the cationic micelles reached a minimum with TTAC/BP (n = 14), and then increased with increasing chain length. The sulfate micelles show a maximum in $T_{1/2}$ times for n = 10, and then decrease with increasing chain length. The $T_{1/4}$ lifetimes also show opposite trends between the cationic and anionic micelles, those for cationic micelles show a minimum with TTAC/BP and then increase with increasing chain length. The $T_{1/4}$ lifetimes for the sulfate micelles decrease dramatically from n = 8 to n = 10, and then continue to decrease with increasing chain length, but at a slower rate. However, it is important to note that the two series of micelles are not completely analogous. The anionic, sulfate micelles studied in [2] range from a chain length of eight carbons to fourteen carbons, and the cationic micelles range from chain lengths of twelve to eighteen. From table 2.1 in the structures chapter it can be seen that SDS (the n = 12 sulfate micelle) has properties most similar to DTAC (the n = 12 cationic micelle) in terms of micelle radius and microviscosity. If it is assumed that the n = 14 sulfate micelle is similar to TTAC in its

properties then it can be seen that the trends in all three of the fractional lifetimes for the n = 12 and n = 14 micelles are the same for both cationic and anionic micelles.

Cationic micelles with chain lengths of n = 8 and n = 10 were not commercially available with a chloride counter ion, and hence a direct comparison between the anionic and cationic micelles for these chain lengths could not be undertaken.

Attempts to use the model described in section 3.8 to fit the time curves for the cationic micelles did not give satisfactory results, with values of k_G for all the systems except DTAC/BP calculated to be of the order of 10^2 s^{-1}. The failure of the fitting is thought to be due to shortcomings in the model such as the problem with the initial radical concentration, and the difficulties of fitting three rate constants to one curve as described in sections 3.8 and 4.2. For any future attempts at fitting the time curves it is suggested that the hydrogen abstraction rate, and hence the triplet contribution to the absorption signal, is also included in a revised model as this may give a more satisfactory fit to the curves.

5.2.2 Magnetic Field Effects

The MARY curves for the four systems are shown in figure 5.2, and they follow the pattern set in the zero field time curves in figure 5.1 with a small change with chain length for OTAC, CTAC, and TTAC, but a larger difference between TTAC and DTAC.

The DTAC/BP system gives the largest MFEs by a big margin, with the MFE at the largest magnetic field strength being almost twice that of the MFEs of the other three systems. It is harder to assign an order to the other three, but from the graph it can be

seen that OTAC generally gives the smallest MFEs, and it is possible to argue that in general the MFEs for TTAC are larger than those of CTAC.

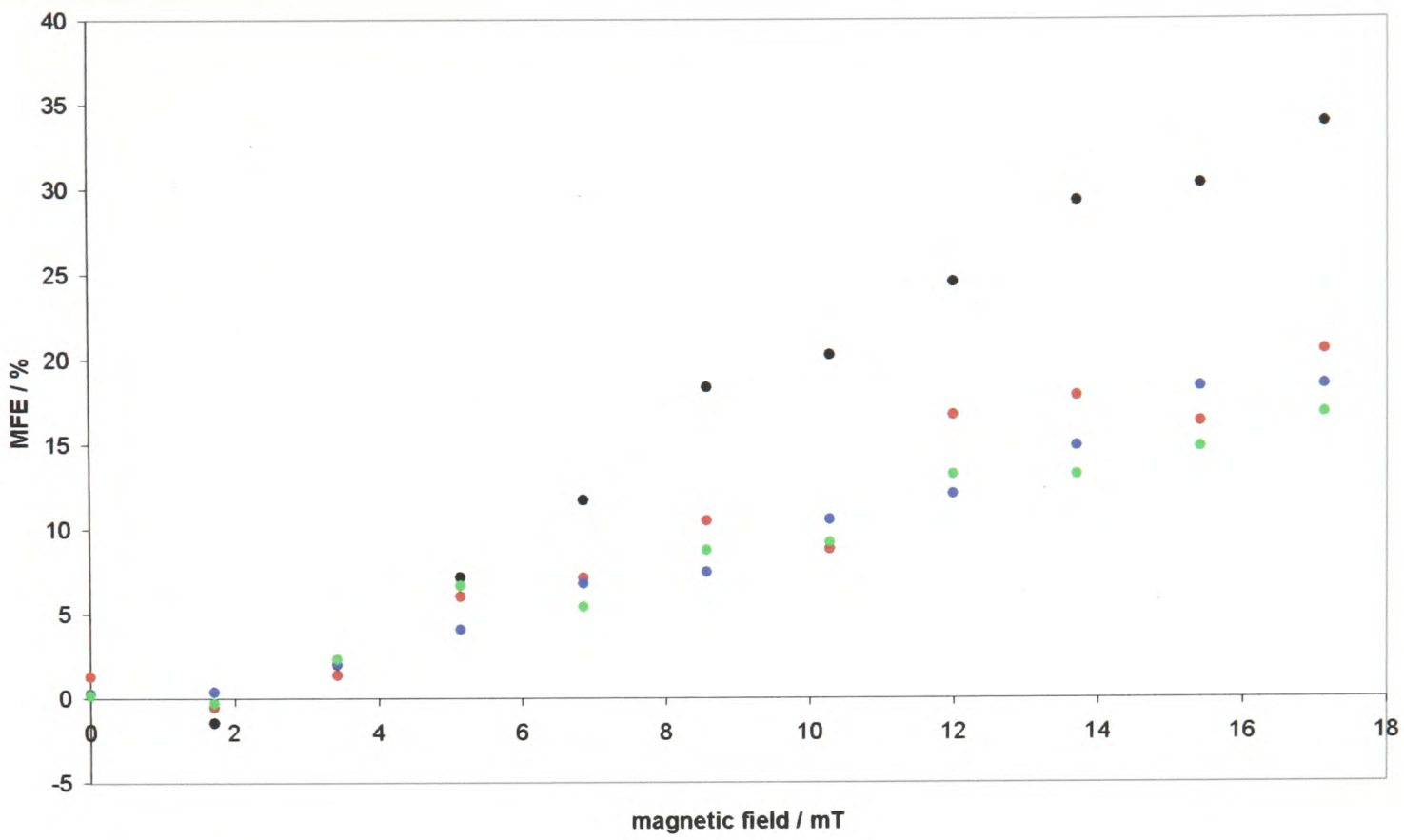


Figure 5.2: MARY curves of BP in (•) DTAC (3.9), (•) TTAC (4.3), (•) CTAC (1.6), and (•) OTAC (4.3) micelles (figures in brackets show EE / %)

Table 5.3 shows the manually calculated MFEs (as described in section 3.5.1) for the four systems at 8.6 and 17.1 mT. These data were calculated from time curves with 288 averages per curve.

System	MFE at 8.6 mT / %	MFE at 17.1 mT / %
DTAC/BP	20.5	45.0
TTAC/BP	14.7	27.5
CTAC/BP	10.6	20.4
OTAC/BP	7.78	18.9

Table 5.3: Manually calculated MFEs in cationic micelles

The manually calculated MFEs in table 5.3 were calculated from time curves, using the absorption values between 0.1 μs and 8.5 μs after the laser flash. The reason for changing the integration period is that it highlights the trends between the different chain length micelles to a greater extent than that seen from the MARY curves in

figure 5.2. Changing the time limits for the integration (as described in section 3.5) is one of the advantages of the manually calculated field effects over those given by the LabVIEW software, which uses the entire time curve in all cases.

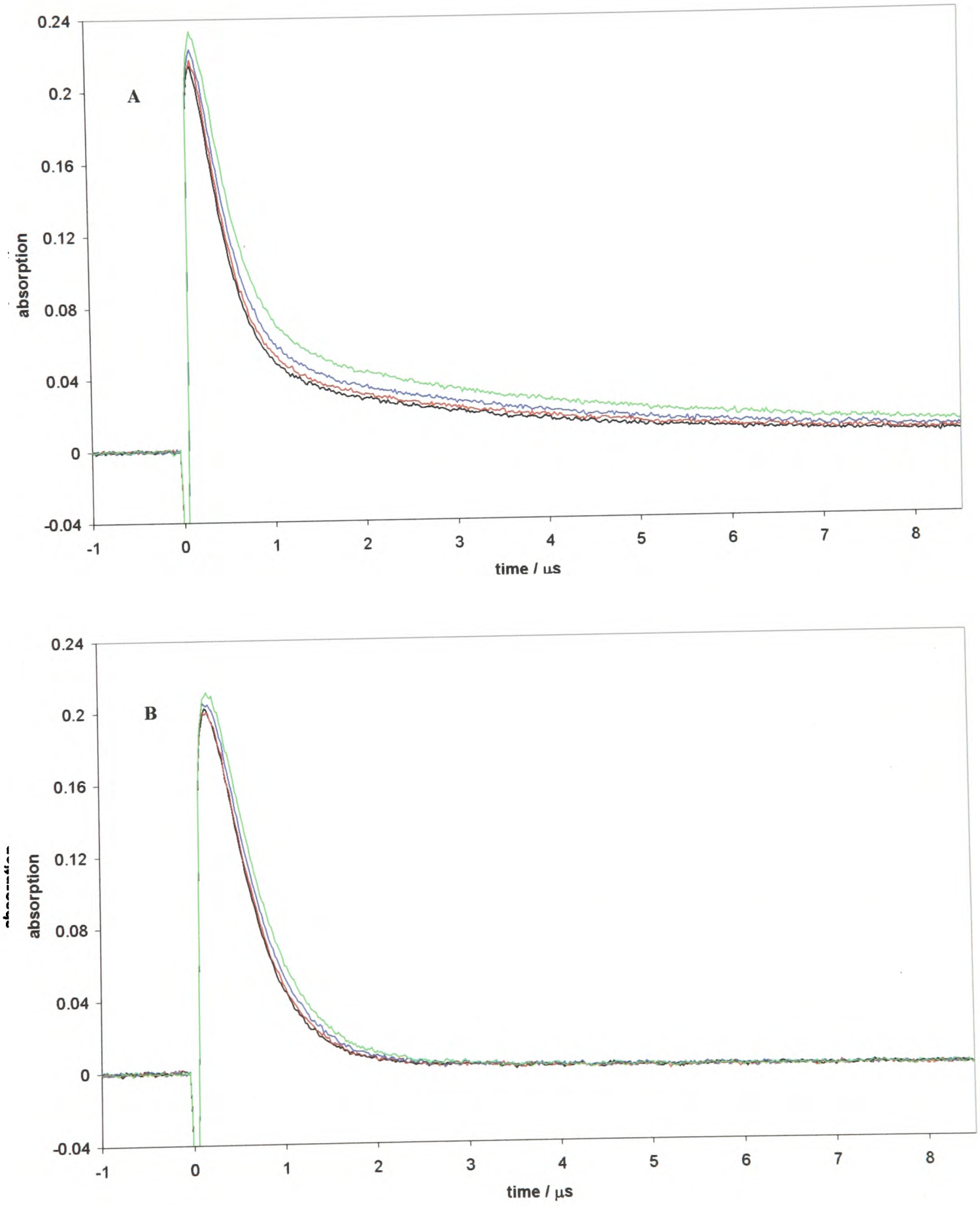


Figure 5.3: Time curves of A) DTAC/BP, and B) CTAC/BP at (•) 0 mT, (•) 4.3 mT, (•) 8.6 mT, and (•) 17.1 mT

Figure 5.3 shows time curves for both DTAC/BP and CTAC/BP at four magnetic field strengths, and highlights the difference between DTAC/BP and the other three cationic micelle systems. For DTAC/BP (as shown in figure 5.3A) the difference between the size of the absorption at the four magnetic field strengths is clear, and can be seen over the whole time range from the initial peak after the laser flash until the end of the measurement period. However, in the case of CTAC/BP (figure 5.3B), TTAC/BP, and OTAC/BP (not shown) the difference in absorption at different magnetic field strengths can only be seen from the initial peak until around 3 μs later. By this point the differences in concentration have essentially become zero, while the absorption signal remains marginally above zero.

In the work of Eveson et al. [2] the sizes of the MFEs were also compared between the different chain length micelles, and it was found that the largest MFEs at a magnetic field strength of 6 mT were in micelles with a carbon chain length of ten. This was ascribed to a balance between the recombination rate and the escape rate of the RP. The results for the cationic micelles reported in this section show that decreasing the chain length increases the size of the MFEs. However, it is only true for the chain lengths investigated, and if shorter chain lengths were studied it is probable that a maximum in the size of the MFEs would be reached. However, as mentioned previously these shorter chain length cationic micelles were not commercially available.

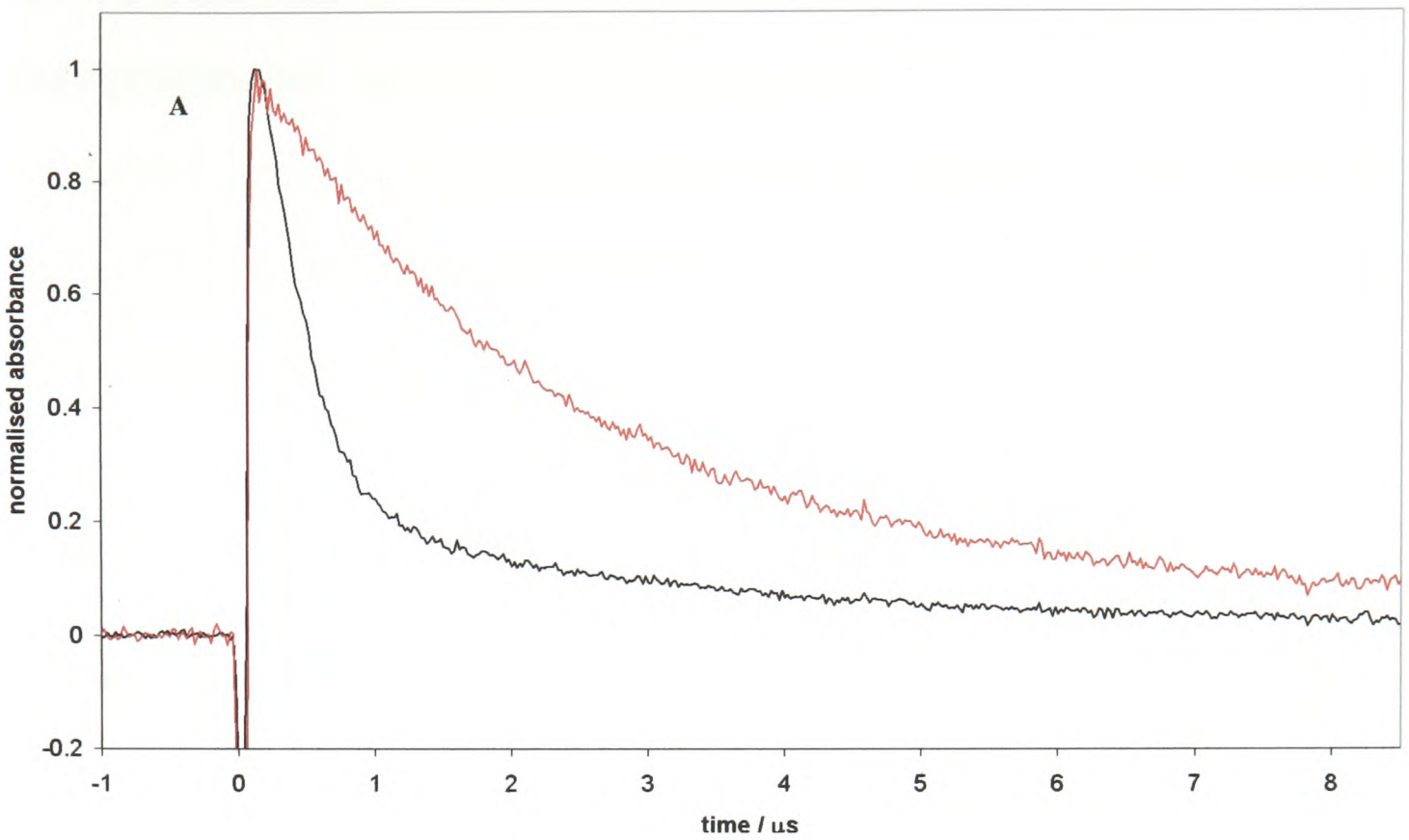
Investigation of LFEs in the cationic micelle systems showed no coherent trend between the different chain lengths (results presented in [3]), further investigation will require better resolution of the MFEs at magnetic field strengths below ~3 mT if trends are to be discovered.

5.3 HYDROGEN DONORS

The effect of added hydrogen donors in SDS micelles was investigated in chapter four, where it was found that the hydrogen donors studied affected the rate of radical recombination, the rate of escape from the micelle, and also the size of the MFEs. Three different systems have been investigated where hydrogen donors have been added to cationic micelles. CHD has been added to the DTAC/BP system, and both CHD and THF have been added to the CTAC/BP system. The concentration of added hydrogen donor was 40 mM in all cases, as stated in section 5.1. This concentration was chosen to keep the BP:CHD concentration ratio the same as in the experiments with SDS micelles.

5.3.1 Hydrogen Donors with DTAC/BP

When comparing the four systems containing cationic micelles of different chain lengths DTAC showed marked differences from the other three surfactants, in both the shape of the time curves and the size of its magnetic field effects. As in section 4.2, the purpose of adding CHD is to change both the identity and character of the RP to maximise the magnetic field effect as observed in both the time curves and MARY curves.



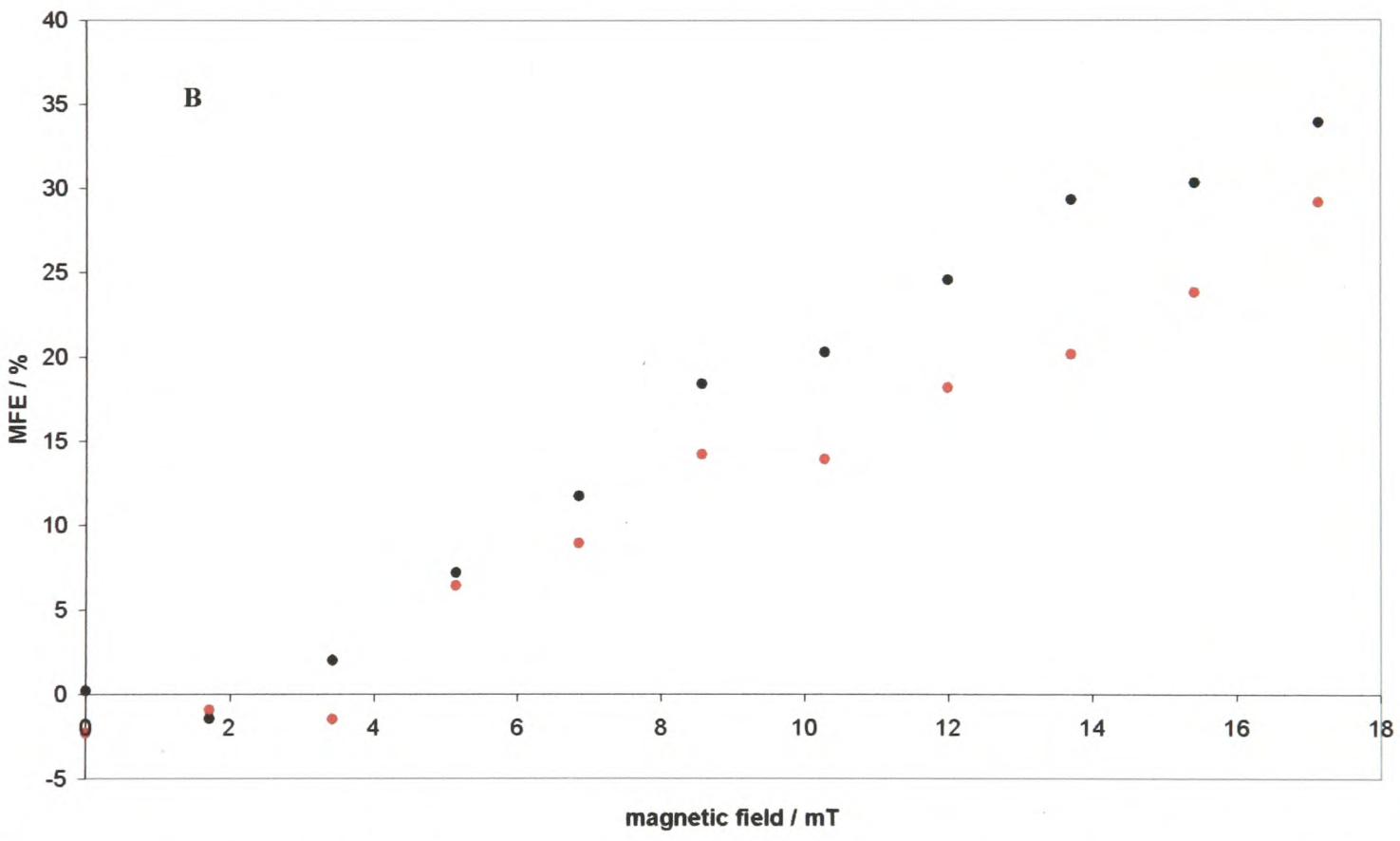


Figure 5.4: A) Zero field time curves, and B) MARY curves of DTAC/BP (•) without CHD (3.9), and (•) with CHD (3.0) (EE / %)

Figure 5.4A shows normalised zero field time curves for DTAC/BP in the presence and absence of CHD. The CHD makes a very large difference to the appearance of the time curves, with a much slower rate of signal decay than DTAC/BP in the absence of a hydrogen donor. The shape of the curve changes from a biphasic decay in DTAC/BP

with visible fast and slow components of the decay, to a monophasic decay with DTAC/BP/CHD. The implications of this change are discussed more fully in section 5.3.3. Table 5.4 shows the fractional lifetimes and also the manually calculated MFE for both DTAC/BP and DTAC/BP/CHD. These data were calculated from time curves with 288 averages per curve.

System	Lifetimes / μs			MFE / %		
	$T_{3/4}$	$T_{1/2}$	$T_{1/4}$	4.3 mT	8.6 mT	17.1 mT
DTAC/BP	0.20	0.40	0.82	7.86	20.6	45.3
DTAC/BP/CHD	0.70	1.78	3.76	4.21	13.5	32.8

Table 5.4: Fractional lifetimes and MFE for DTAC/BP and DTAC/BP/CHD

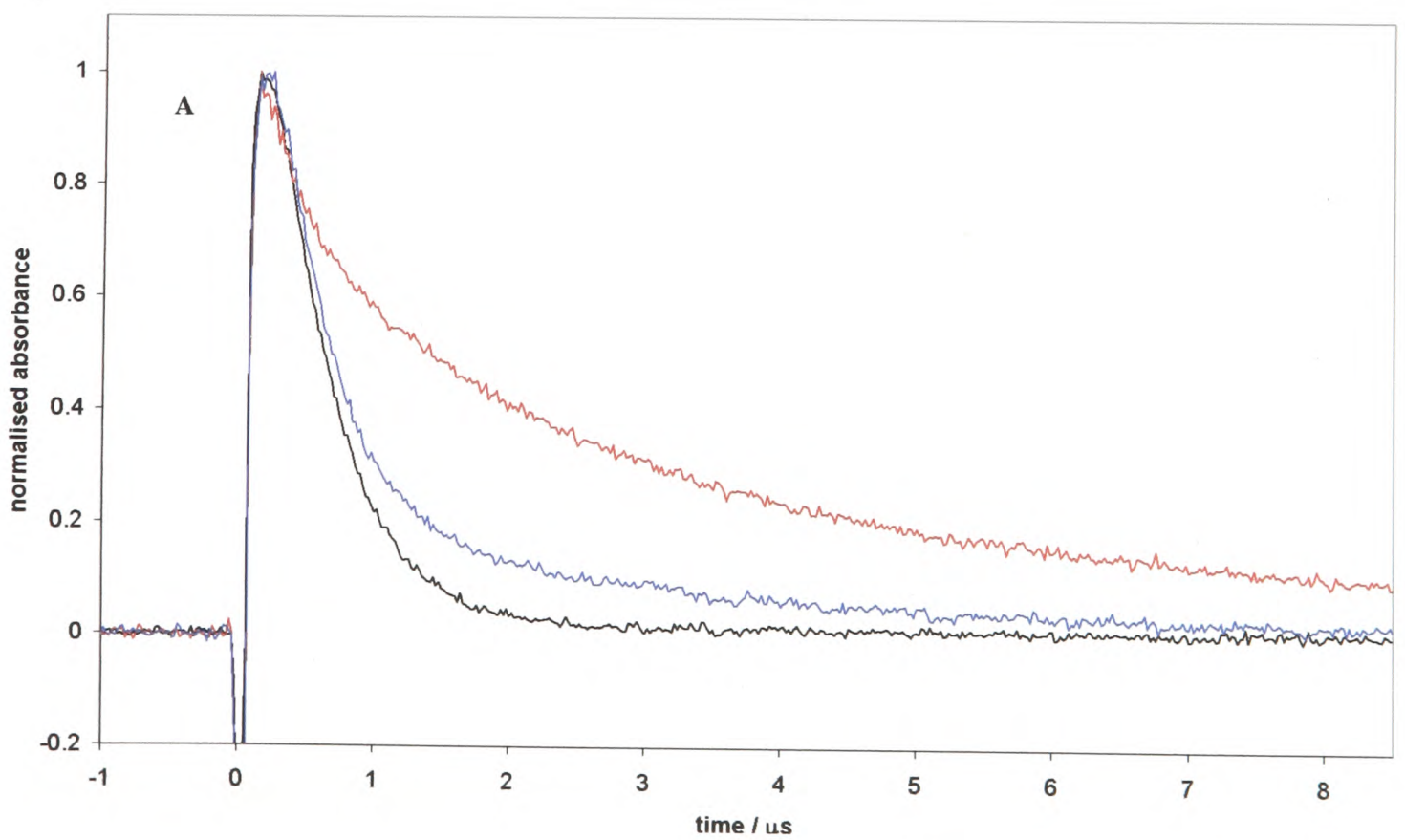
In SDS/BP the addition of CHD increased both the rate of geminate recombination and the escape rate of the radical pair compared to SDS/BP with no additives. The time curve for DTAC/BP/CHD in figure 5.4A has no fast decaying component at short timescales implying that a very large proportion of the RPs escape the micelle to undergo slower F pair recombination. Despite the similarities in the size and microviscosities of SDS and DTAC shown in table 2.1 the behaviour on addition of CHD to the system shows very large differences. The aggregation number for SDS from table 2.1 is 65, whilst that for DTAC is 51, and this could explain the much faster escape in DTAC seen on addition of CHD. If there are fewer molecules per micelle in DTAC the stability of the micelle is lower and the escape rate of the radicals from the micelle is increased.

Figure 5.4B shows the effect on the MARY curves of adding CHD to the DTAC/BP system. In a reversal to the effect seen with SDS micelles, adding CHD causes an, albeit small, decrease in the size of the MFE in this system. This is also shown in table 5.4 where at all three magnetic field strengths the MFE is smaller in DTAC/BP/CHD.

However, even though the size of the MFEs is reduced on addition of CHD the MFEs are still present, and of a substantial size. This result is surprising as the kinetics of the two systems are so very different, as seen in figure 5.4A. This behaviour was also seen in chapter four with both the hydrogen donor and deuteration results where a large change in the time curves led to a comparatively small change in the MFEs observed.

5.3.2 Hydrogen Donors with CTAC/BP

Two different hydrogen donors were investigated with the CTAC/BP system, CHD and THF. The results with SDS/BP in chapter four showed that the addition of CHD resulted in an increase in both k_G and k_E, plus an increase in the size of the MFEs. The addition of THF to SDS/BP also resulted in an increased value for k_G, but reduced the value of k_E and gave smaller MFEs than those seen in the absence of any hydrogen donor. Figure 5.5 shows the effect of adding both of these hydrogen donors to the CTAC/BP system.



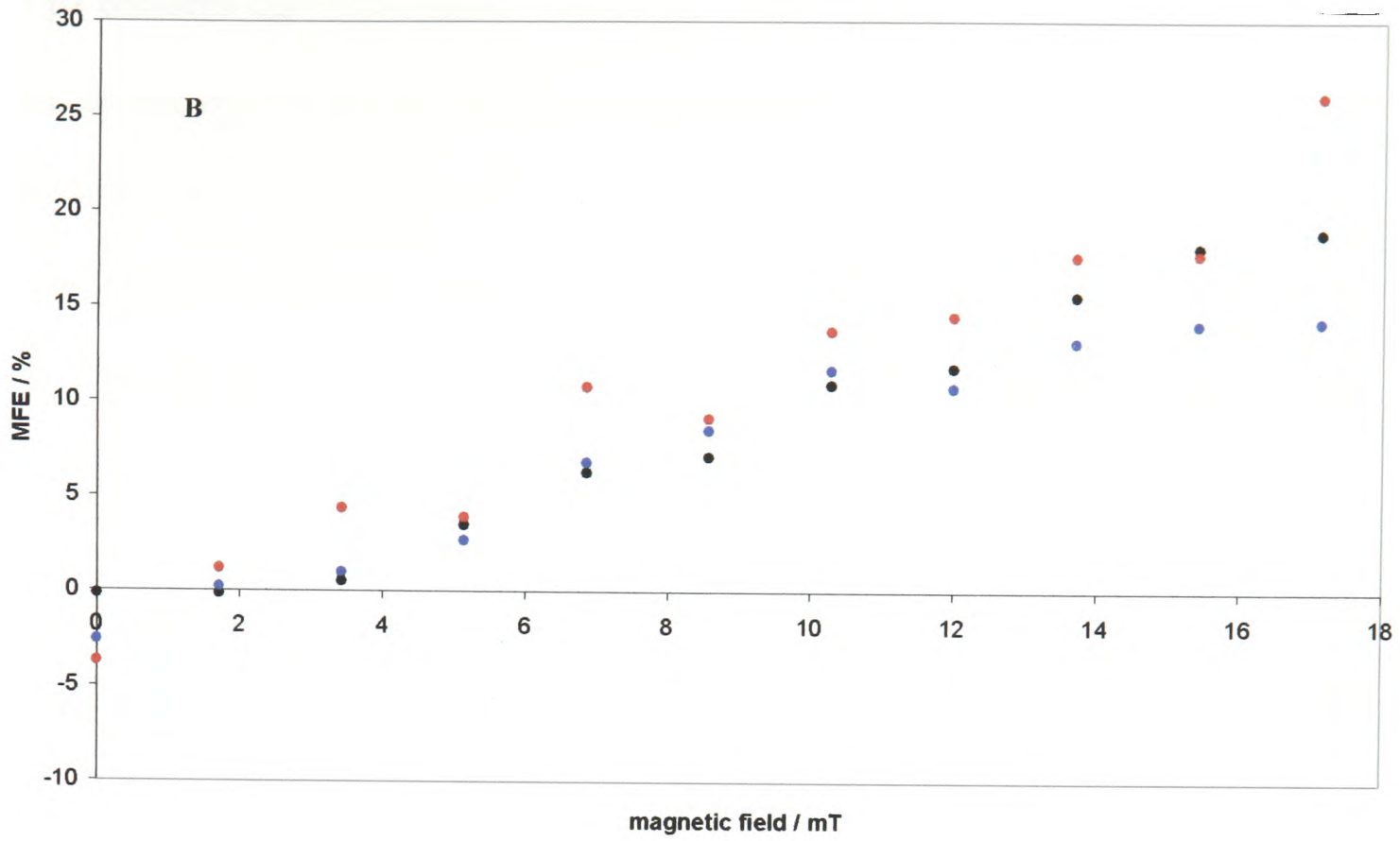


Figure 5.5: A) Zero field time curves, and B) MARY curves of CTAC/BP (•) without any additional hydrogen donor (2.0), (•) with CHD (2.4), and (•) with THF (3.8) (EE / %)

Figure 5.5A shows normalised zero field time curves for the three systems, and, as with the DTAC, adding CHD causes a large change in the appearance of the time curves. However, in contrast to the DTAC results the CTAC/BP/CHD curve does not fit well to a mono-exponential curve, it remains a bi-phasic shape, albeit a very different one to CTAC/BP and CTAC/BP/CHD. Adding THF also causes an increase in lifetime of the ketyl radical, but to a lesser extent than CHD.

Table 5.5 gives the fractional lifetimes for the three systems, and at all three fractional concentrations the lifetimes are in the order CTAC/BP < CTAC/BP/THF < CTAC/BP/CHD. This contrasts with the results in SDS/BP where addition of CHD caused $T_{3/4}$ to be smaller for SDS/BP/CHD than for SDS/BP. In SDS the addition of CHD resulted in an increase in both k_G and k_E, and this would also be expected to be the case for CTAC. On inspection of figure 5.5A it can be seen that for the first 0.3 μs following the initial absorption peak the CHD signal decays at a faster rate than the other two systems, suggesting increased geminate recombination rates. However, at

0.3 μs onwards the CHD signal crosses that of the other two systems, and from that point on decays at a slower rate, as would be expected from a faster escape rate with relatively slow F pair recombination. From this argument the addition of CHD causes an increase in k_G and k_E in both SDS and CTAC micelles, but this manifests itself differently in the two systems depending whether the increase in the geminate recombination or the escape dominates.

The behaviour upon addition of THF is the same in CTAC as that seen with SDS, with a slower rate of signal decay, and larger absorbance at all times after the initial absorbance peak.

System	Lifetimes / μs			MFE / %		
	$T_{3/4}$	$T_{1/2}$	$T_{1/4}$	4.3 mT	8.6 mT	17.1 mT
CTAC/BP	0.28	0.48	0.78	4.14	10.8	20.7
CTAC/BP/THF	0.30	0.54	1.06	3.41	9.30	17.2
CTAC/BP/CHD	0.34	1.22	3.46	5.03	13.0	24.6

Table 5.5: Fractional lifetimes and MFE for CTAC/BP, CTAC/BP/THF, and CTAC/BP/CHD calculated from time curves with 288 averages per curve

Figure 5.5B shows MARY curves for the three different CTAC systems, but the difference between the sizes of the magnetic field effects is small. Table 5.5 gives the manually calculated MFE at three magnetic field strengths for the three systems, and the differences here are slightly larger. For all three magnetic field strengths the order of the MFE is CTAC/BP/THF < CTAC/BP < CTAC/BP/CHD. Not only is this order different to the lifetimes of the ketyl radical in the three systems, but also the effect of adding CHD is different to that seen with DTAC/BP, where the addition of CHD led to smaller MFEs.

This illustrates the complexity of the kinetics in these systems, and that no one constraint holds the key to the size of the MFEs. The addition of CHD with DTAC/BP leads to a decrease in the size of the MFEs, whereas the addition of CHD to the

CTAC/BP system leads to an increase in the size of the MFEs. In SDS/BP the addition of CHD also lead to an increase in the size of the MFEs, but had a different effect on the initial signal decay. In SDS/BP the addition of CHD caused a decrease in the $T_{3/4}$ time, whereas in CTAC/BP the addition of CHD leads to an increase in $T_{3/4}$. The data in figure 5.5 and in table 5.5 also show that there is no simple relationship between the lifetime of the signal and the size of the MFEs, with both THF and CHD causing an increase in the fractional lifetimes over CTAC/BP, but CHD causing an increase, and THF causing a decrease in the size of the MFEs.

In section 5.2.2 figure 5.3B showed time curves for CTAC/BP at four different magnetic field strengths, and that the difference in concentration caused by the magnetic field only lasted for about 3 μs after the laser flash. With both CHD and THF the difference in concentrations between the four magnetic field strengths can be observed all the way to the end of the measurement period, although this is more obvious with CHD, as can be seen in figure 5.6.

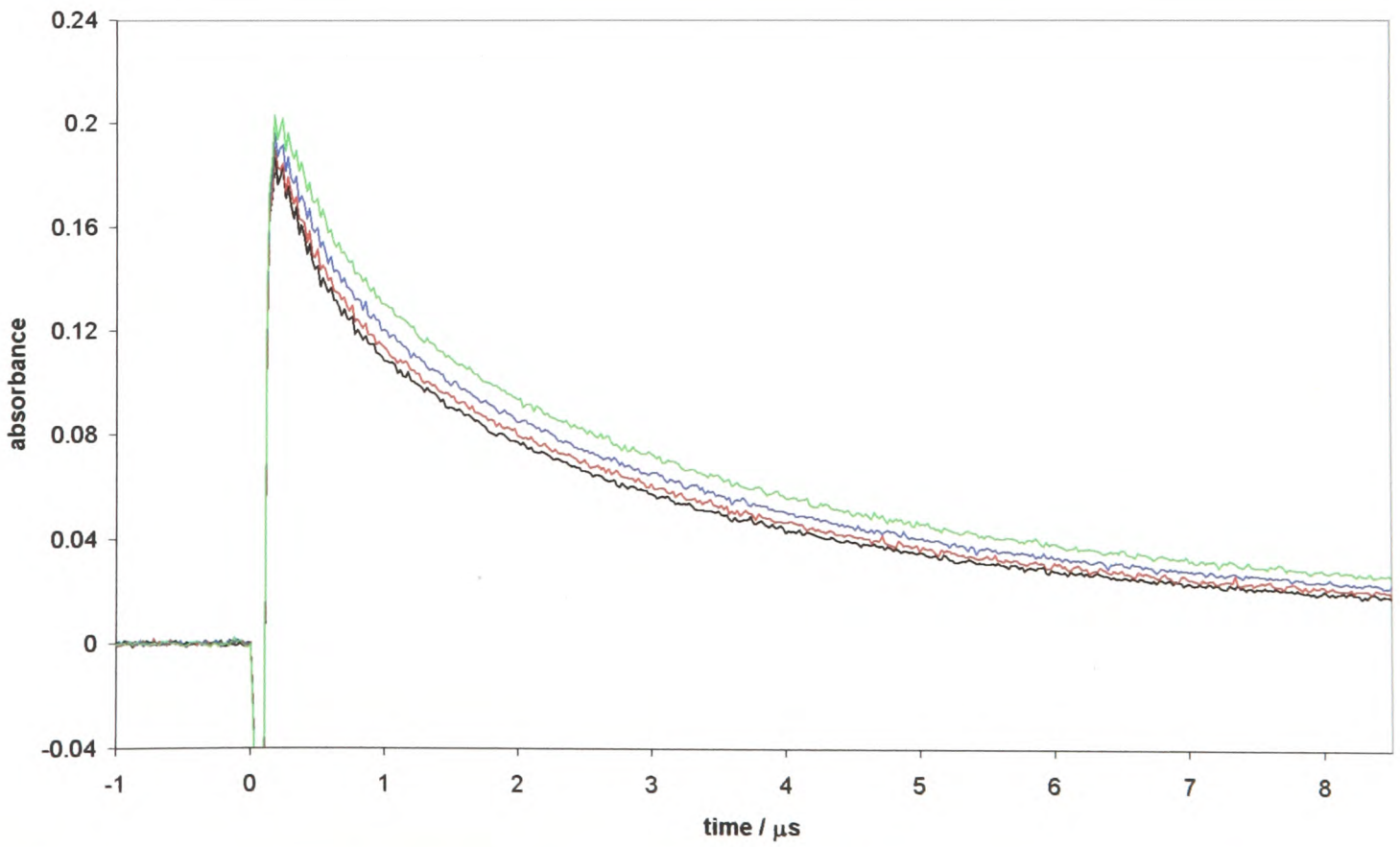


Figure 5.6: Time curves of CTAC/BP/CHD at (•) 0 mT, (•) 4.3 mT, (•) 8.6 mT, and (•) 17.1 mT

5.3.3 Comparing Chain Length Effects in the Presence of CHD

In section 5.2.1 it was seen that DTAC/BP had the fastest initial decay, but also the longest lifetime of the four different chain length micelles. Figure 5.7 shows that upon addition of CHD the DTAC/BP/CHD zero field time curve shows longer fractional lifetimes than CTAC/BP/CHD, and a slower initial decay. The most likely explanation for this is that CHD has a larger effect on the escape rate of the RP from DTAC micelles than from CTAC micelles. DTAC micelles have a lower aggregation number and a smaller size than the CTAC micelles, so if adding CHD causes an increase in the mobility of the RP then this effect will be larger in DTAC micelles than in CTAC micelles.

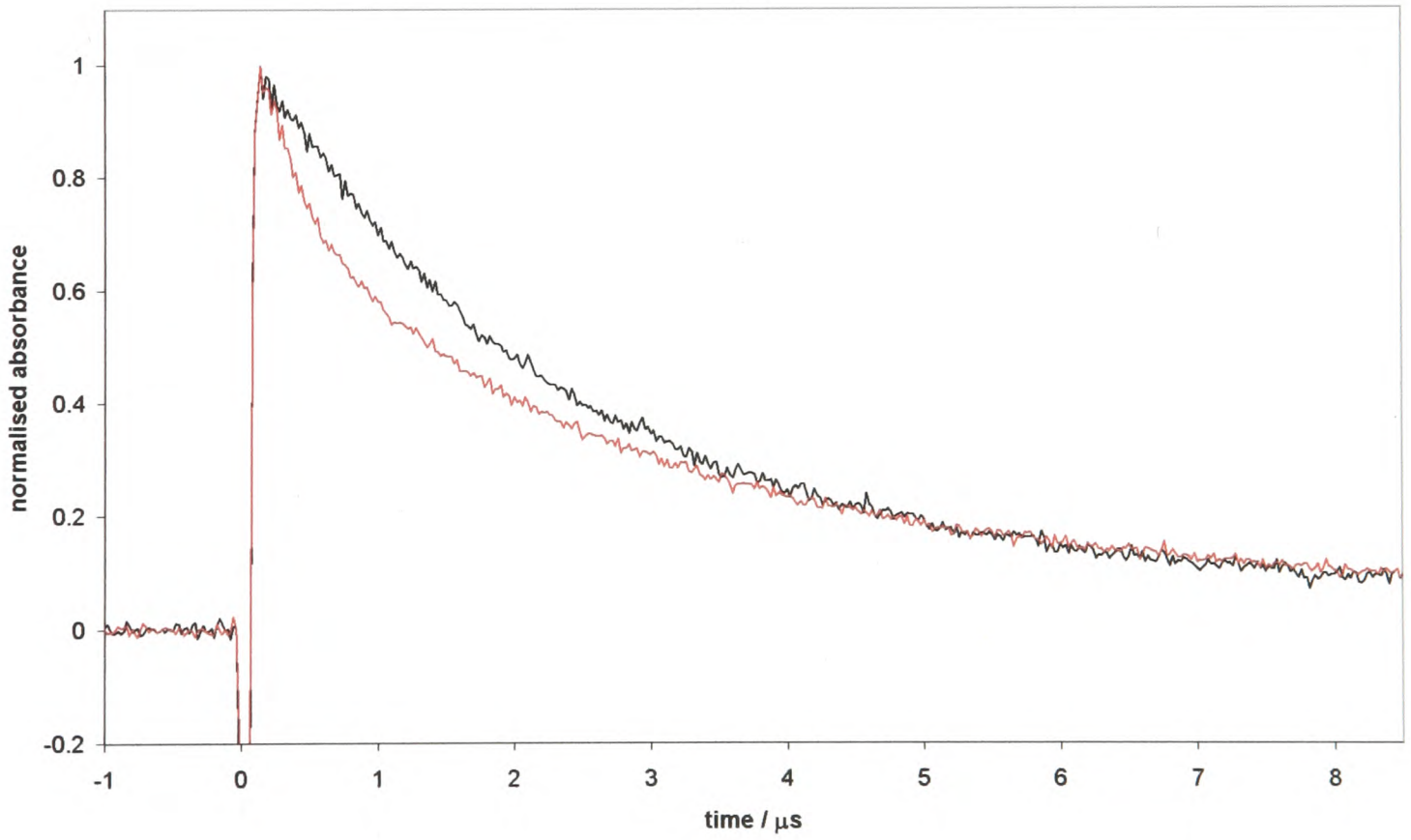


Figure 5.7: Zero field time curves of BP/CHD in (•) DTAC, and (•) CTAC micelles

From figure 5.7 the differences in the shapes of the two curves can also be seen, with DTAC undergoing a mono-phasic decay and CTAC undergoing a bi-phasic decay.

The shape of the DTAC curve implies that only one process is occurring in this system, and the slow rate of signal decay would imply that only F pair recombination can be observed. This would be consistent with the fact that the decay rate of both curves is very similar for the last 4 μs of the measurement period, when all geminate recombination would be expected to be completed. However, MFEs are still observed for the DTAC/BP/CHD system as can be seen from figure 5.4. This implies that the MFEs are either due to a MFE on the F pair recombination, or there is a small amount of geminate recombination that cannot be observed from the zero field time curves, but is still large enough to cause the MFEs. Magnetic field effects on F pair recombination have been reported for the case where the geminate and F pairs have a different identity due to the escaped radical undergoing a subsequent reaction before recombining [4]. However, in the case of DTAC/BP/CHD it is not possible to differentiate between the geminate and F pairs by optical absorption techniques. The fact that addition of CHD to the DTAC system causes a reduction of the size of the MFEs could indicate that a smaller, but non-negligible, proportion of radical pairs are undergoing geminate recombination and causing the magnetic field effects.

The fractional lifetimes for DTAC and CTAC both in the presence, and absence, of CHD are collected from tables 5.4 and 5.5, and are presented together in table 5.6, below.

System	$T_{3/4}$ / μs	$T_{1/2}$ / μs	$T_{1/4}$ / μs
DTAC/BP	0.20	0.40	0.82
CTAC/BP	0.28	0.48	0.78
DTAC/BP/CHD	0.70	1.78	3.76
CTAC/BP/CHD	0.34	1.22	3.46

Table 5.6: Fractional lifetimes of DTAC/BP and CTAC/BP in presence and absence of CHD

Whilst it can be seen that the addition of CHD to both systems causes an increase in all three fractional lifetimes the effect is larger in DTAC than in CTAC, meaning that the trend of increasing fractional lifetimes with increasing chain length in the absence of CHD is reversed in the presence of CHD.

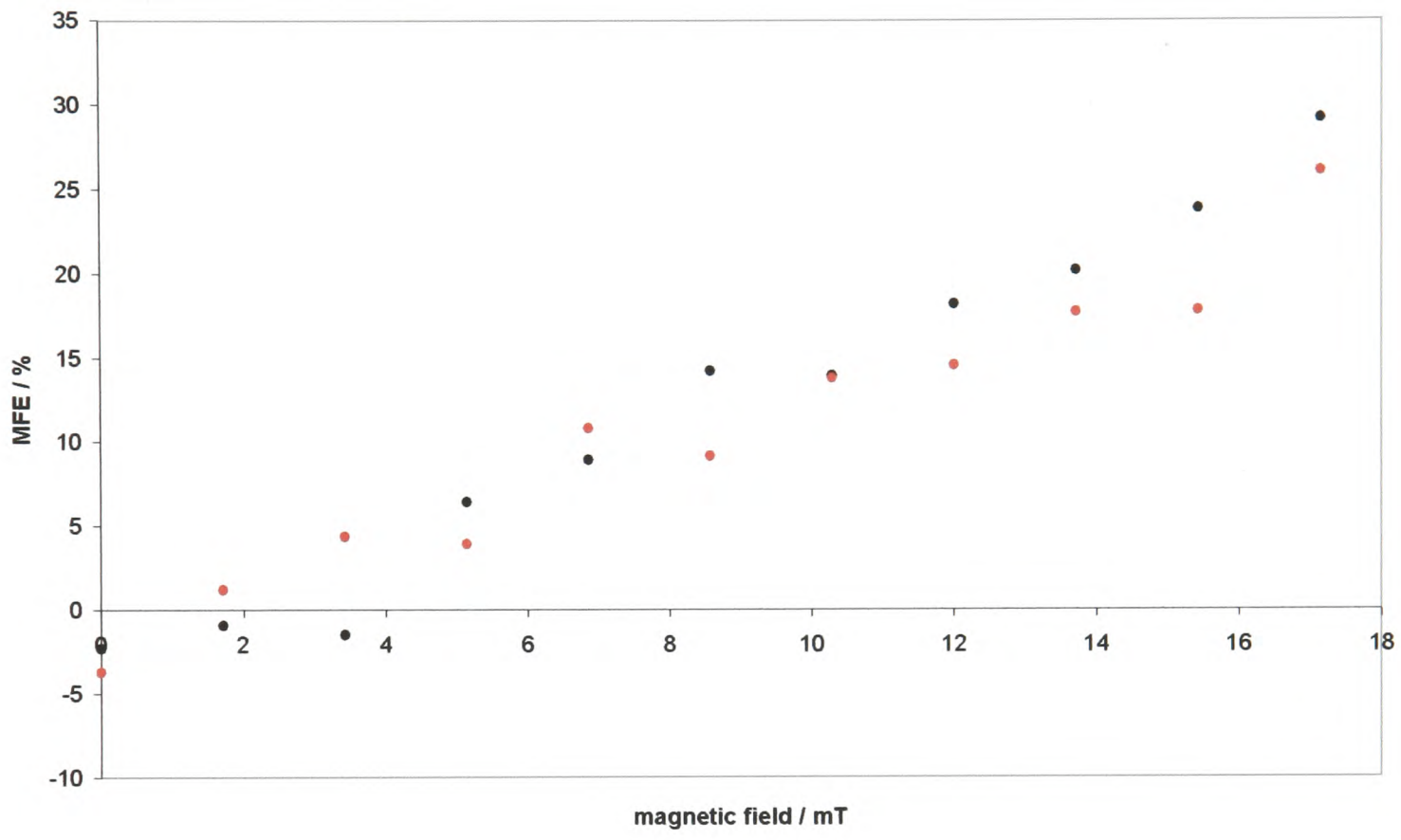


Figure 5.8: MARY curves of BP/CHD in (•) DTAC (3.0), and (•) CTAC micelles (2.4) (EE / %)

In section 5.2.2 it was seen that, for the four cationic micelles investigated, the size of the MFEs increased with a decrease in hydrophobic chain length. This trend is repeated in DTAC/BP/CHD and CTAC/BP/CHD albeit to a smaller extent The MARY curves in figure 5.8 look very similar at lower magnetic field strengths, but from around 8 mT DTAC has the larger MFE. This is the same with the manually calculated MFE from tables 5.4 and 5.5. At 4.3 mT and 8.6 mT the two systems have very similar MFE, but at 17.1 mT DTAC clearly has the larger MFE.

5.4 Radical Quenchers

It is known that when paramagnetic ions are added to micellar solutions containing radical pairs the ions can quench any magnetic field effects that may be present by spin relaxation [5-7]. The paramagnetic ions interact with the RP to destroy any correlation between the RP spins, and hence nullify any change of spin mixing rate that may be due to an applied magnetic field. The paramagnetic ions do not enter into the interior of the micelle, but their presence in the Stern layer is enough to cause relaxation of the RP.

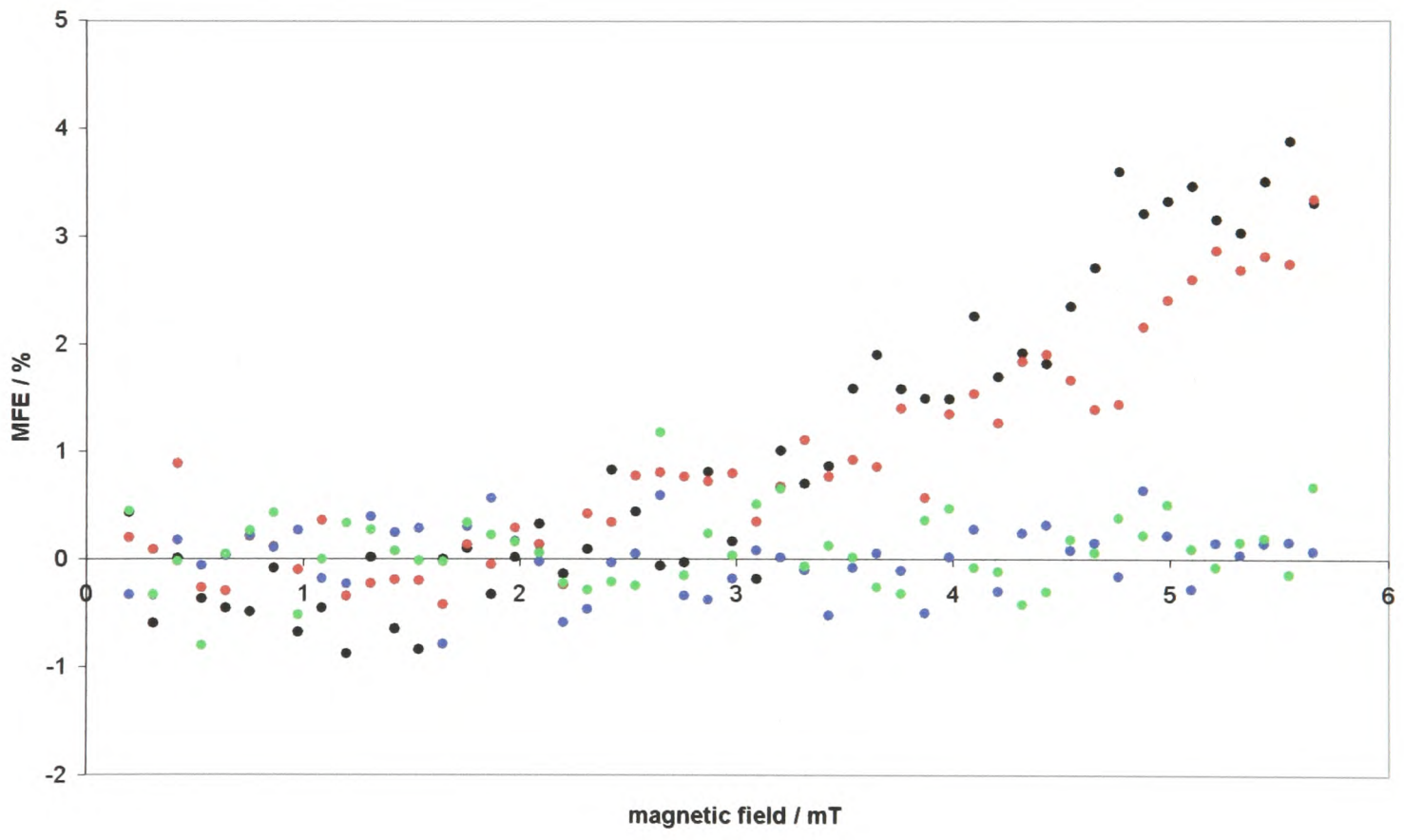


Figure 5.9: MARY curves of SDS/BP in the presence of (•) no additional ions, (•) $CaCl_2$, (•) $CuCl_2$, and (•) $MnCl_2$

Three divalent metal salts were added to SDS/BP solutions, two of which contained paramagnetic ions, and one which contained diamagnetic ions. The effect on the MARY curves can be seen in figure 5.9. The addition of both $CuCl_2$ and $MnCl_2$

causes complete quenching of the MFEs over the magnetic field range studied, but the $CaCl_2$ has no effect on the MFEs. From a similar investigation by Sakaguchi and Hayashi [7] it was found that the magnetic moment of the paramagnetic ion does not affect the quenching rate, with all paramagnetic ions investigated having a rate that was independent of the number of unpaired electrons in the ion. This result rules out a dipole-dipole mechanism for interaction between the ions and the RP, and hence a mechanism based on the exchange interaction was proposed by the authors.

When the same salts were added to DTAC/BP solutions no quenching of the MFEs was observed, as is shown in figure 5.10. The lack of quenching in CTAC, and the difference from the effect in SDS, is due to the sign of the charge on the head groups of the micelles. The positively charged paramagnetic ions are repelled by the positively charged head groups of the CTAC micelles, and hence do not get close enough to the geminate RPs to cause relaxation. However, the negatively charged SDS micelles attract the cationic ions and relaxation occurs. As can be seen from table 2.1 the micelle radii for SDS and DTAC are very similar (17.5 Å and 17 Å, respectively), hence the distance from the RP to the edge of the micelle should be the same in both cases, indicating it is the distance of the paramagnetic ions from the micelle that is the important factor in these two systems.

This result has important implications for MFEs in biological systems, where many paramagnetic ions play crucial roles in the processes that occur. The results in SDS and DTAC micelles demonstrate that the distance between the RP and any paramagnetic ions (or paramagnetic species such as molecular oxygen) that are present is a crucial factor in determining whether any quenching of MFEs could

transpire. Figure 5.10 also proves that the presence of paramagnetic ions in a solution does not guarantee the absence of MFEs, as long as microenvironments such as micelles keep the RP at sufficient distance from the paramagnetic species. From figure 5.10 there is a suggestion that the addition of $CuCl_2$ leads to an increased LFE and MFE over the other three solutions. Further detailed experiments would have to be undertaken to investigate if this is true.

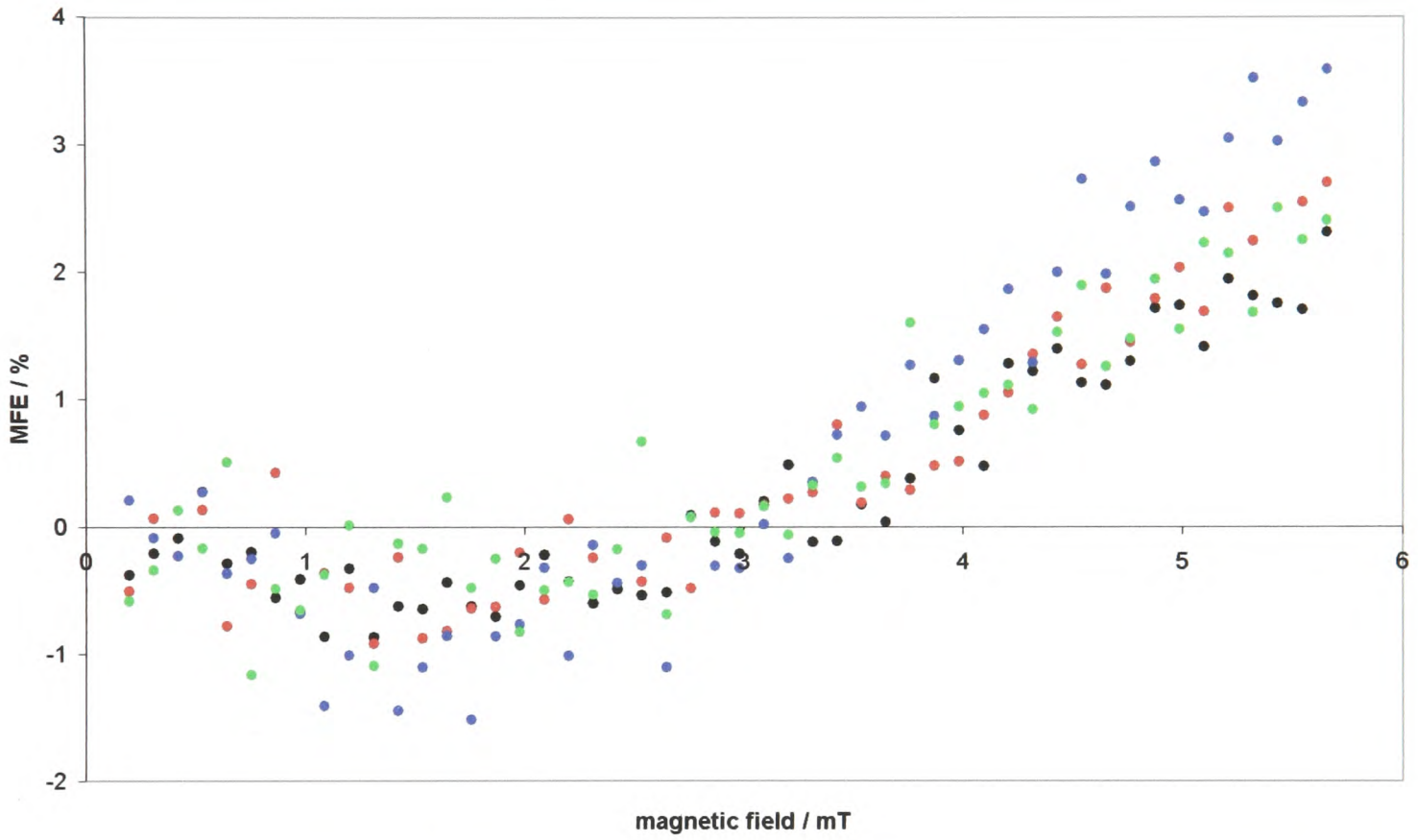


Figure 5.10: MARY curves of DTAC/BP in the presence of (•) no additional ions, (•) $CaCl_2$, (•) $CuCl_2$, and (•) $MnCl_2$

The MARY curves shown in figures 5.9 and 5.10 were obtained using the 4 ml, multiple reflection cell described in section 3.6.1, and hence solution recycling which allows for longer periods of data acquisition and a higher number of points per MARY curve. This also permits many points to be obtained in the LFE region of the magnetic field, however, the recycling of the solution leads to a decrease in the size of the absorbance signal over the course of the experiment and this results in MFEs that can also vary in size. Hence the introduction of the new, smaller cell, described in section 3.6.1, that eliminates the need for recycling of the solution.

5.5 CONCLUSIONS

This chapter investigated radical reactions inside cationic micelles of varying chain lengths, contrasted these with anionic micelles of varying chain lengths, and investigated the effect of hydrogen donors and divalent ions on the cationic micelle systems. Increasing the chain length in the cationic micelles (from n = 12 to n = 18) leads to slower initial recombination rates and smaller MFEs. It was noted that this was also the case for anionic micelles, as investigated in [2], but in this case a maximum in the MFEs was seen for a chain length of ten carbon atoms.

Addition of CHD to the cationic micelles caused the opposite effect to that seen in SDS micelles in the previous chapter in terms of the lifetime of the signal, with addition of CHD to both DTAC/BP and CTAC/BP leading to an increase in the signal lifetime. The effect of CHD on the size of the MFEs is dependent on the micelle; addition of CHD to DTAC/BP leads to decreased MFEs compared to no additional CHD. However the addition of CHD to CTAC/BP leads to an increase in the MFEs, as was seen with SDS micelles. The shapes of the zero field time curves vary in DTAC/BP/CHD and CTAC/BP/CHD, with the DTAC curve showing a mono-phasic decay, with no visible geminate recombination period. This was held to be the reason for the decrease in MFE size upon addition of CHD.

The effect of the positive charge of the head group of the cationic micelles was seen upon addition of paramagnetic ions to the micellar solutions. In solutions containing anionic SDS micelles the addition of paramagnetic ions led to quenching of the MFEs, but this behaviour was not seen with the cationic DTAC micelles due to the electrostatic repulsion between the head groups and the cationic paramagnetic ions. This last result highlights the fact that although the behaviour of the RPs inside the

micelles may not change a great deal between cationic and anionic micelles the interaction of the micelles themselves with other components of the solutions can play a part in the behaviour of the system as a whole.

6: SYNTHETIC VESICLES – DODAC

The previous two chapters have investigated radical pair reactions inside micelles, structures which have been thoroughly utilised by many researchers for MFE studies, as discussed in chapters one and two. This chapter focuses on RP reactions inside slightly more complex structures than micelles. In chapter two it was said that not all amphiphilic molecules aggregate to from micellar structures, those with a molecular structure that precludes micelle formation can form double layer structures such as vesicles. DODAC (whose structure was shown in figure 2.6) is one such molecule. Preliminary experiments focussed on obtaining a reproducible signal from the DODAC/BP system, and following this investigations were performed into the effect of changing both the DODAC and BP concentration, the addition of CHD to the system, and increasing the temperature of the solution above the phase transition temperature of DODAC (as discussed in section 2.3.1).

6.1 EXPERIMENTAL SECTION

Experiments were performed with DODAC concentration ranging from 25 mM to 40 mM and two concentrations of BP, 2 mM and 2.5 mM.

For all time curves shown there are 96 averages per curve and each is the average of two sets of acquisitions, unless stated otherwise. All time curves shown were recorded at zero applied magnetic field unless stated otherwise.

6.1.1 Solution Preparation

When DODAC/BP was first used the solutions were sonicated in periods of twenty minutes with five minutes rest before the next session of sonication (following the procedure in [1]). This was carried out above the phase transition temperature, at 60 °C to aid dissolution following the procedure of [1-3]. To see how long the solution needed in the ultrasound an experiment was carried out where a normal solution was made up and sonicated until all the solids had dissolved. 50 ml aliquots of this solution were taken and zero field time curves obtained, while the remainder of the solution was put back into the sonic bath for a further twenty minutes. As the sonication was at 60 °C the experiment also had to be performed at this temperature to prevent time being wasted by heating and cooling of the water bath and solution. From these results it was decided that each solution would need four hours of sonication at 60 °C, as this gave reproducible signals. It was also found that the five minutes rest period made no difference to the appearance of the decay curves, so the four hours of sonication could be continuous.

As discussed in section 2.3 increasing the sonication time of DODAC solutions results in a decrease in the viscosity and turbidity of the solution, down to a point where further sonication has no appreciable effect. This point is considered to correspond to the appearance of single compartment, unilamellar vesicles [2]. Hence, the DODAC/BP solutions prepared as described above are assumed to contain unilamellar vesicles as they were sonicated until no change was seen in either solution appearance, or the time curves which were produced.

6.1.2 Reproducibility

In the initial experiments with DODAC/BP there were problems with the reproducibility of the signal during the course of the experiment. The size of the zero field time curves reduced during the experiment, as is shown in figure 6.1.

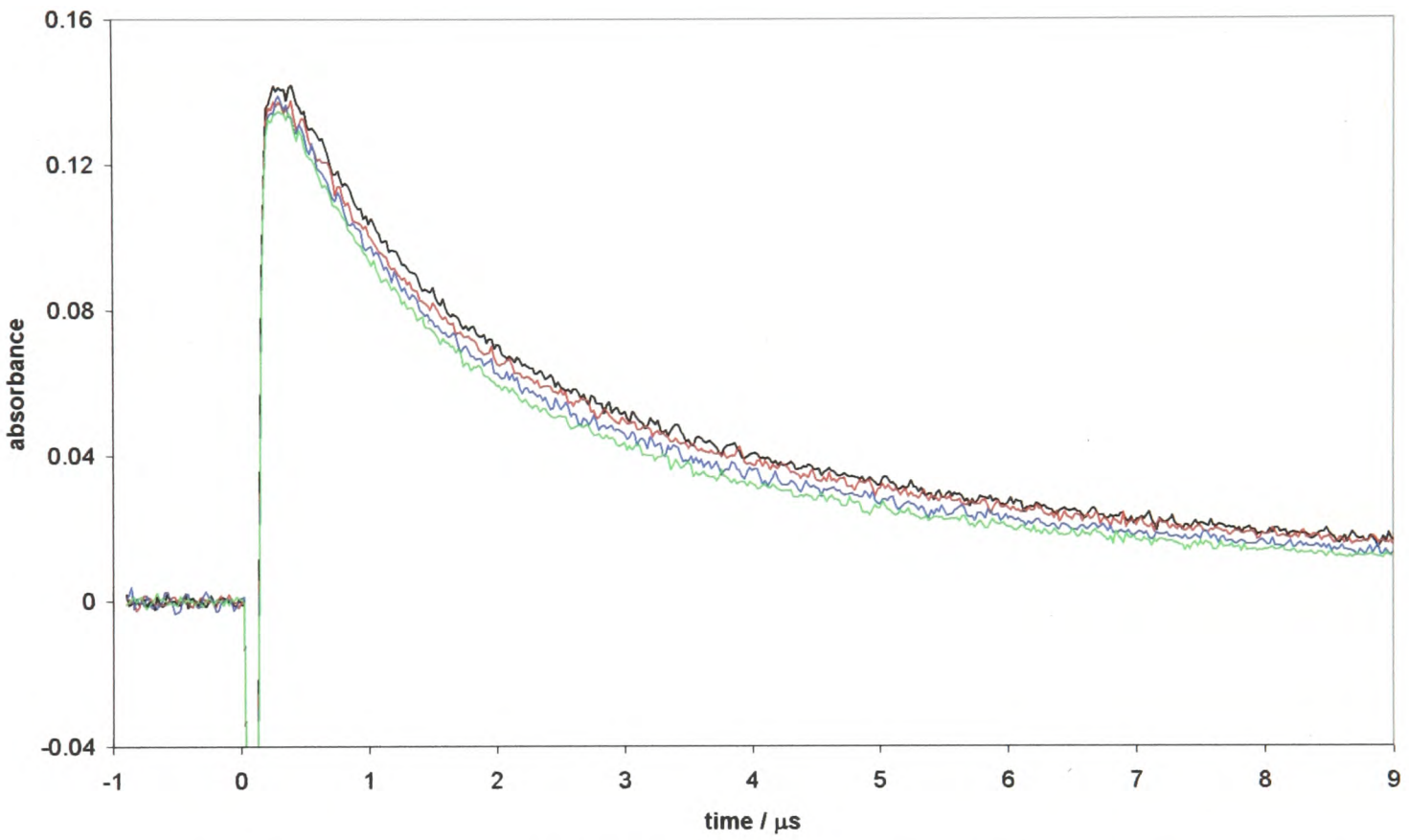


Figure 6.1: Zero field time curves of DODAC/BP at (•) 2, (•) 30, (•) 58, and (•) 80 minutes after start of experiment

The change in size is small, the initial peak height drops by about 5% during the ninety minute duration of the experiment, but the time curves also change in shape. This is shown in figure 6.2 which depicts the first and last curves from figure 6.1 with their initial peak heights normalised to unity.

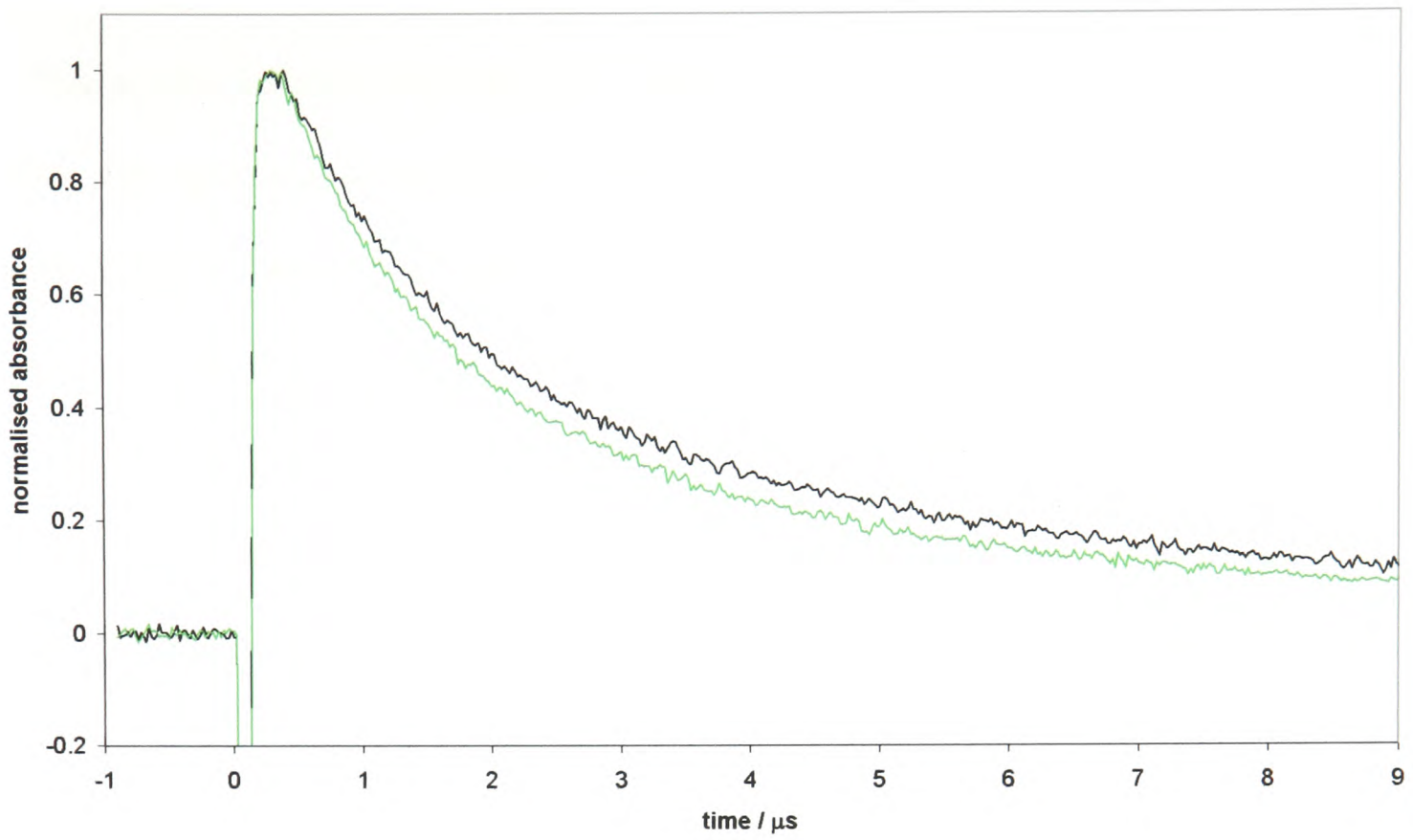


Figure 6.2: Normalised zero field time curves of DODAC/BP at (•) 2, and (•) 80 minutes after start of experiment

The green curve, which was the final time curve of the day taken eighty minutes after the start of the experiment, shows a faster decay in the signal than the black curve which was the first time curve taken. This is more serious than a reduction in size of signal as it indicates the kinetics are changing throughout the experiment, and so will make any changes in kinetics due to the magnetic field harder to identify and characterise. Several factors such as temperature, laser power, and lamp power were tested at the beginning and end of the experiment and were all found to be constant. This left the solution itself as the only variable. The solution is only flowed through the tubing and cell once during the experiment, and it was suggested that the DODAC could be absorbing onto the tubing and cell during the experiment and hence change the concentration of the solution and also the absorption and scatter of the excitation light on the cell surface. To test for this a solution was made up in the usual way and then split up into four samples. Each sample was flowed through the apparatus and zero field time curves obtained with no cleaning or washing out of the cell and tubing

between samples. Figure 6.3 shows the time curves for this experiment, and the effect of flowing the solutions through the tubing and cell. The signal size decreases as before, but reaches a constant size with no reduction in signal between the third and fourth samples. To see what effect this had on the reproducibility of the time curves during an experiment a solution was made as usual and then flowed around the tubing and cell several times before starting to fire the laser or take any measurements. From the results shown in figure 6.3 it was decided to flow the solution around four times before starting to collect data. When the zero field time curves from this experiment were examined it was found that they were completely reproducible hence, for all subsequent DODAC experiments the solution was flowed around the cell and tubing four times prior to the start of the data collection.

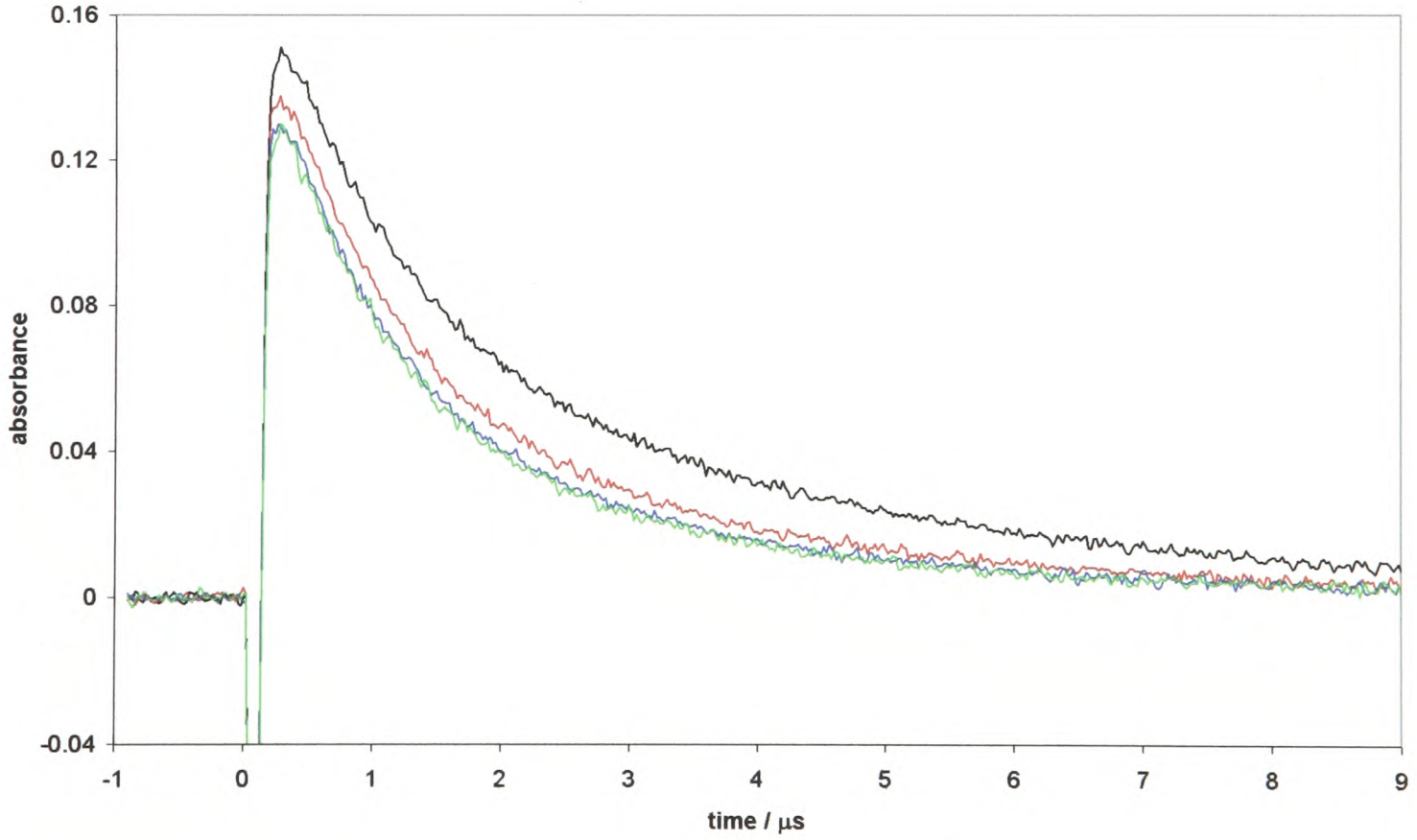


Figure 6.3: Zero field time curves showing effect of flowing sample through apparatus (•) zero, (•) once, (•) twice, and (•) three times before obtaining time curves

6.2 Concentration Studies

The concentration of both DODAC and BP was varied to investigate the consequences on both the time curves and MARY curves, and to try and maximise any MFEs in this system. Four different concentrations of DODAC were used, between 25 mM and 40 mM, and two concentrations of BP, 2 mM and 2.5 mM.

6.2.1 Time Curves

With the BP at a concentration fixed at 2 mM experiments were carried out with the DODAC at concentrations of 25 mM, 30 mM, 35 mM, and 40 mM. Figure 6.4 shows zero field time curves for these four concentrations.

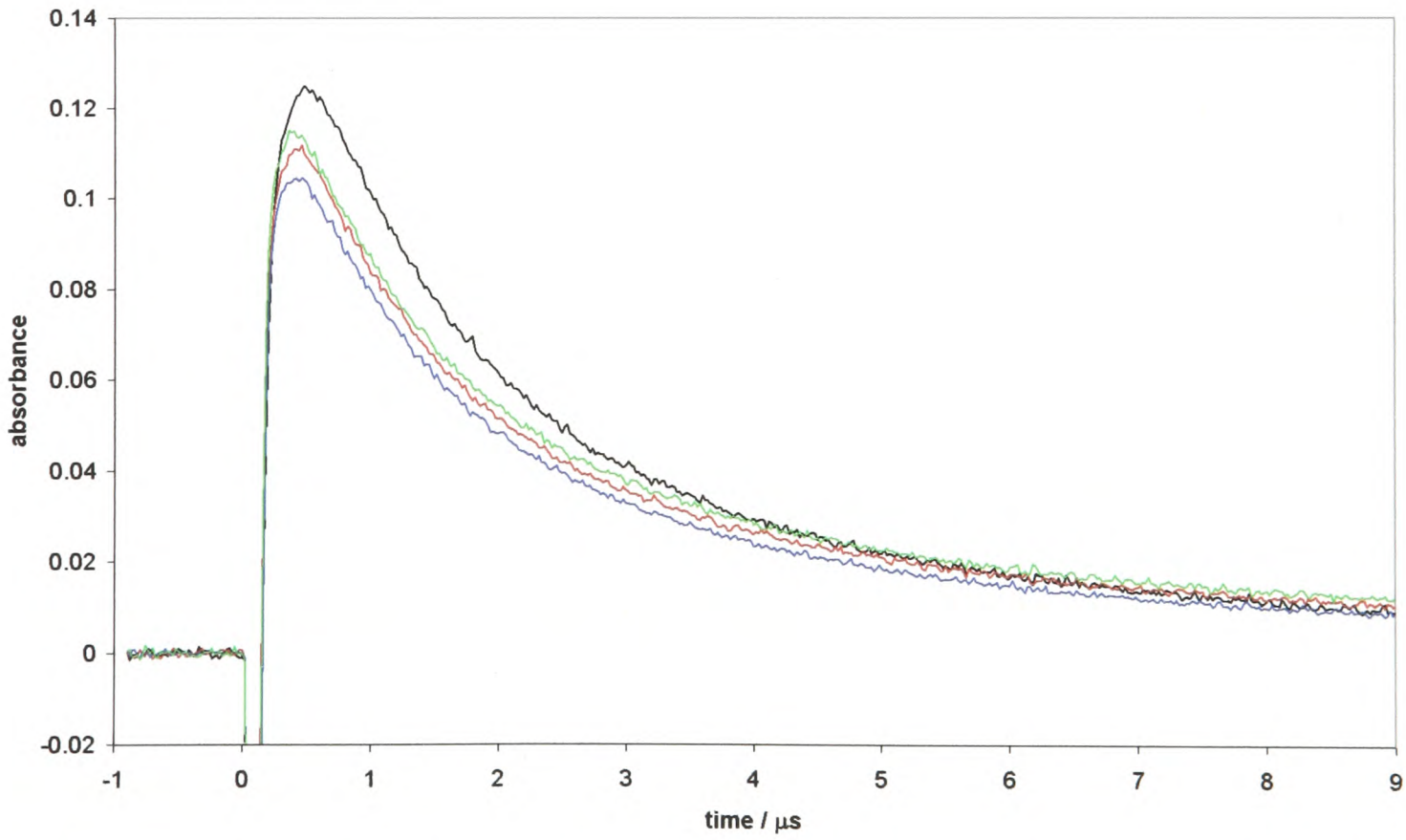


Figure 6.4: Zero field time curves of 2 mM BP and DODAC concentrations of (•) 25, (•) 30, (•) 35, and (•) 40 mM

Each curve is the average of three time curves, each of one hundred averages per curve, so a total of three hundred averages per curve. There is no clear trend in the size of the absorption peaks. The 25 mM curve has the largest peak, but the 40 mM curve has the second largest. However it is the shapes of the curves which give more information, and these are shown in the normalised versions of these curves in figure 6.5. From this it can be seen that there are also no clear trends between the different concentrations. The slowest recombination is in the 40 mM curve, but there is very little difference between the absorbance of the four time curves at the end of the measurement period.

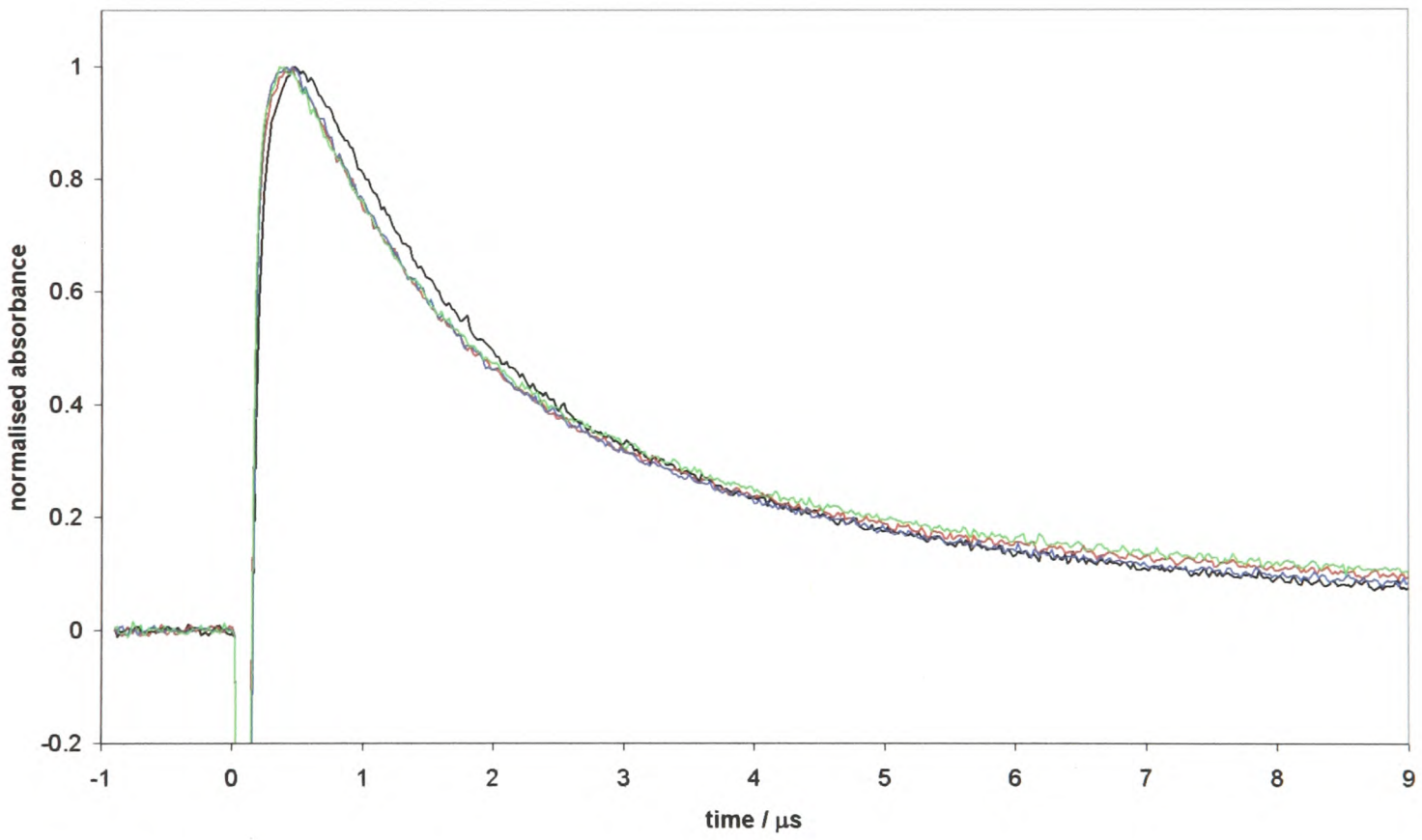


Figure 6.5: Normalised zero field time curves of 2 mM BP and DODAC concentrations of (•) 25, (•) 30, (•) 35, and (•) 40 mM

The results are similar with a BP concentration of 2.5 mM. The normalised zero field time curves are shown in figure 6.6. There were only three different concentrations of DODAC used, and figure 6.6 shows that the recombination seems to be slowest in the 40 mM sample.

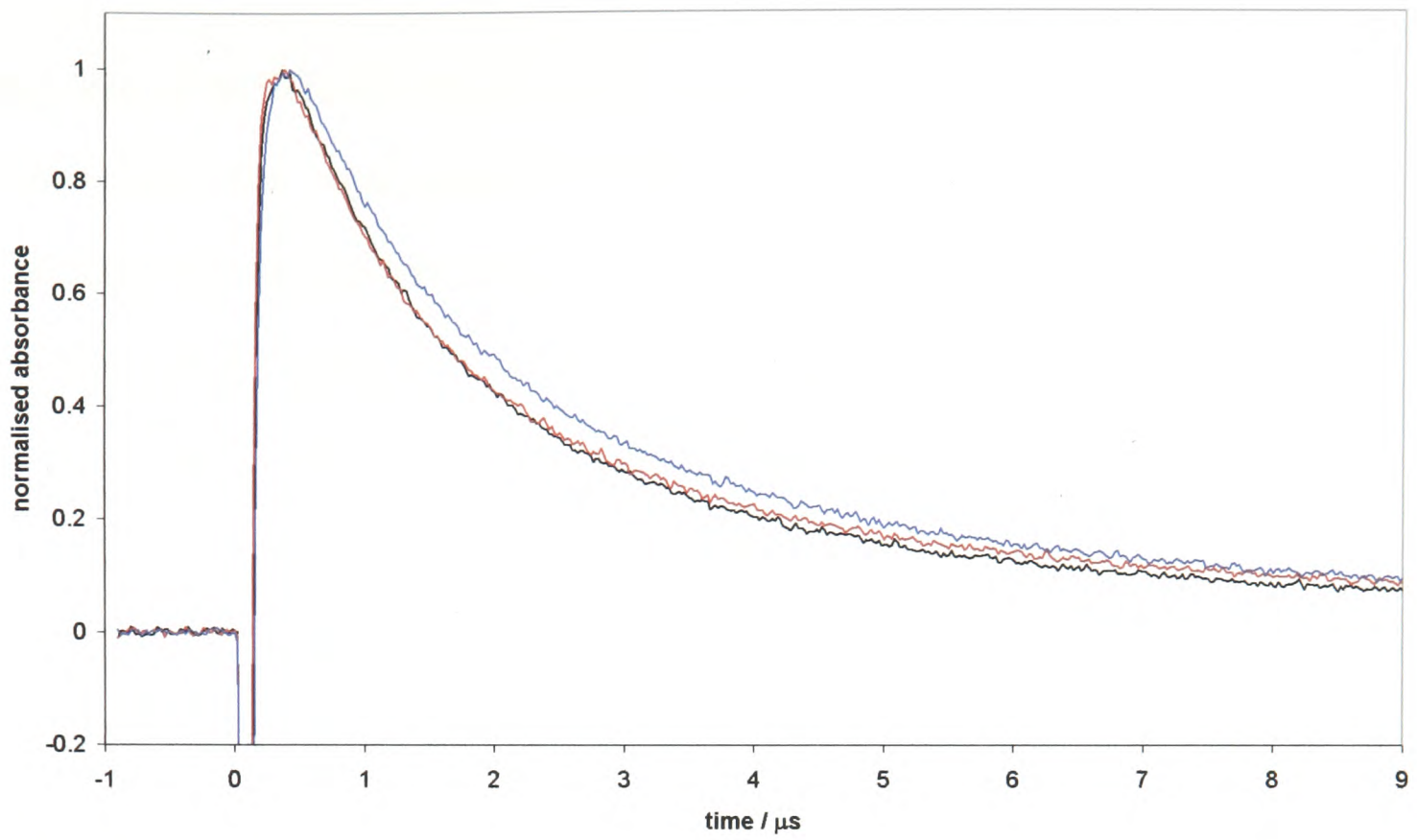


Figure 6.6: Normalised zero field time curves of 2.5 mM BP and DODAC concentrations of (•) 25, (•) 30, and (•) 40 mM

The results of changing the BP concentration are far easier to interpret and understand.

Figure 6.7 shows zero field time curves for both concentrations of BP in 40 mM DODAC. As is expected a higher concentration of BP leads to higher concentrations of $BPH^{\bullet}$ radicals and hence a larger absorption signal. However a 25% increase in BP concentration only leads to a 10% increase in size of the absorption peak, as measured from the data in figure 6.7. There are two major possibilities that could explain this lack of linearity between the BP concentration and the size of the absorbance peak seen in figure 6.7. The first involves the saturation of absorption of the laser excitation light. Figure 7.3 shows UV/vis absorption spectra for DODAC/BP, and it can be seen that the absorbance at 308 nm is fairly large. If the majority of the laser light is being absorbed by the DODAC/BP solution when the concentration of BP is at 2 mM then upon increasing the BP concentration to 2.5 mM the absorption of the laser light may have become saturated, resulting in a smaller proportion of the BP molecules being excited by the laser light at the larger concentration. The second possible reason for

the non-linearity of the system is that due to increased concentrations of BP, and the large size of the DODAC vesicles many excited ^{3}BP* molecules will be present in each vesicle. The large number of ^{3}BP* molecules could lead to triplet-triplet quenching, with no resulting radical formation. The larger concentration of BP would therefore lead to an increased amount of quenching, and hence a smaller increase in signal size than would otherwise be expected. However, from the evidence of figure 6.7 alone it is not possible to conclude which of the two possibilities is occurring in this case. One way of investigating this further would be to measure the amount of laser light that passes through the cell in both cases to find the change in transmitted light at the two concentrations of BP.

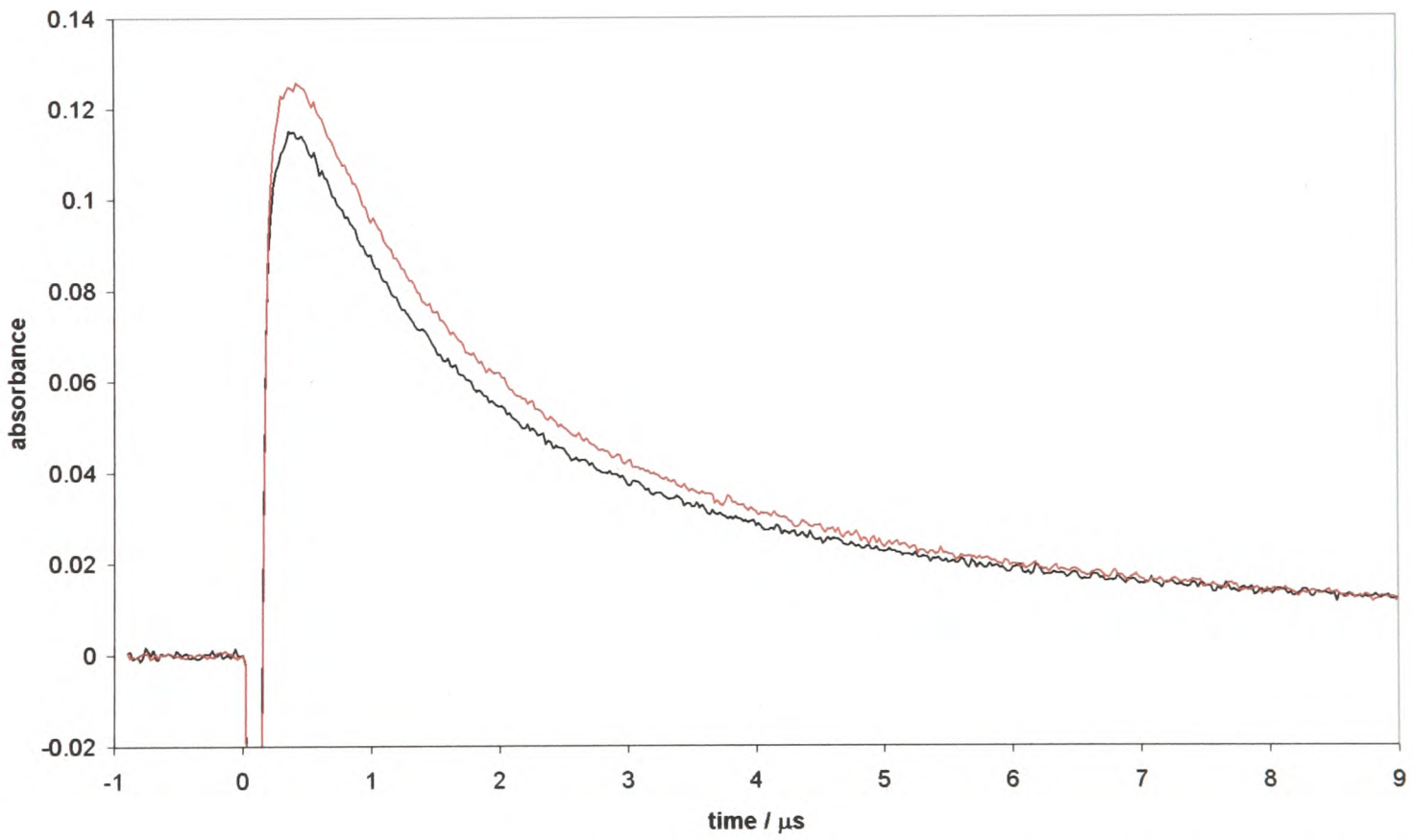


Figure 6.7: Zero field time curves of 40 mM DODAC and BP concentrations of (•) 2, and (•) 2.5 mM

If the two zero field time curves in figure 6.7 are normalised then figure 6.8 is produced. This shows that although the size of the two curves is different the shapes

are very similar and therefore the kinetics determining the absorption decay at the two concentrations must be almost identical.

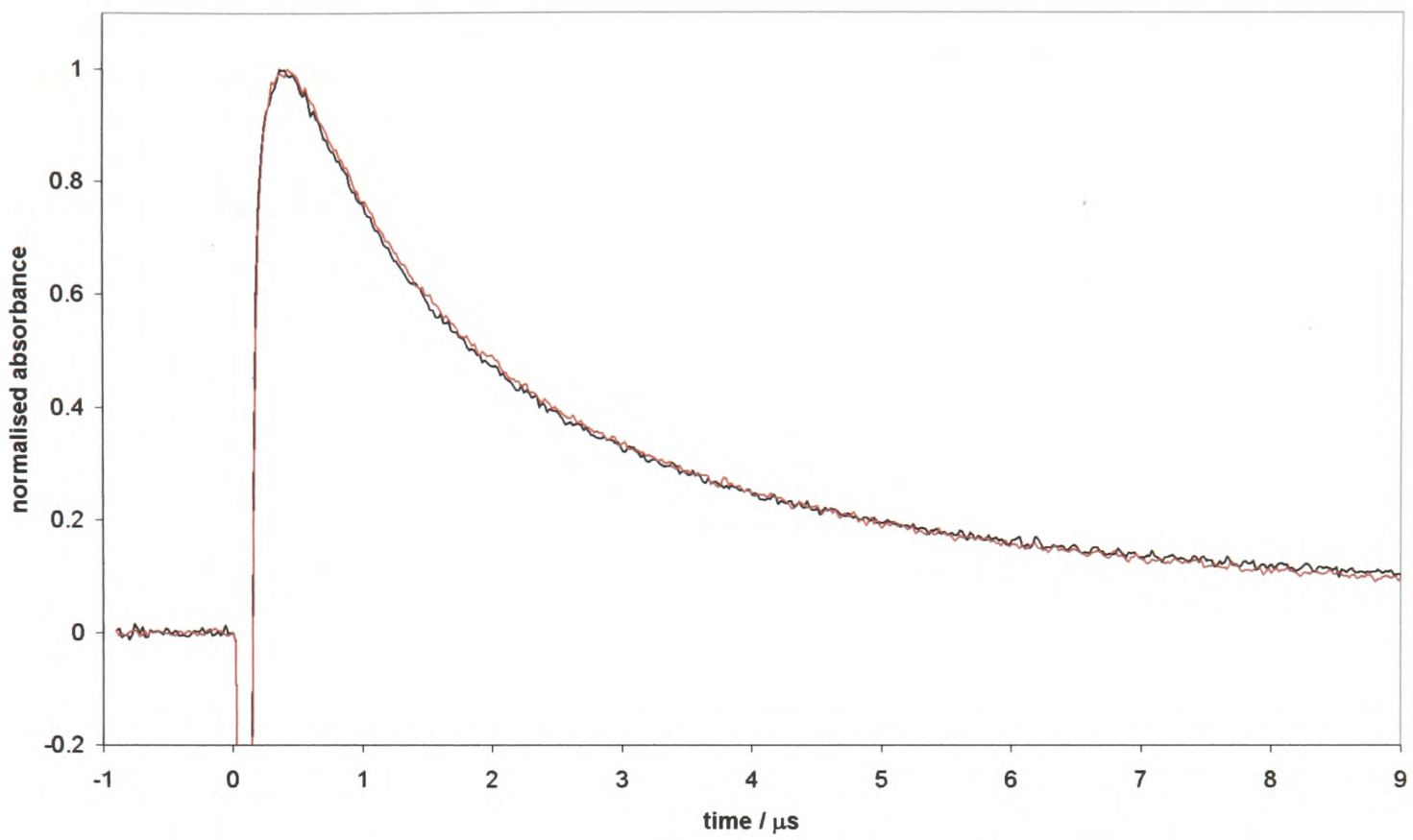


Figure 6.8: Normalised zero field time curves of 40 mM DODAC and BP concentrations of (•) 2, and (•) 2.5 mM

DODAC conc / mM	BP conc / mM	$T_{3/4}$ / μs	$T_{1/2}$ / μs	$T_{1/4}$ / μs
25	2	0.66	1.50	3.34
30	2	0.58	1.38	3.38
35	2	0.58	1.40	3.36
40	2	0.60	1.48	3.62
25	2.5	0.54	1.30	3.10
30	2.5	0.54	1.34	3.26
40	2.5	0.66	1.52	3.68

Table 6.1: Lifetime data for DODAC/BP at varying concentrations

Table 6.1 shows the lifetime data for the seven combinations of DODAC and BP concentration. As is shown by figure 6.5 changing the DODAC concentration makes little difference to the recombination rate of the radical pair, and, as both figure 6.5 and table 6.1 show, there is no trend in the lifetime data as the DODAC concentration is increased, the 25 mM and 40 mM DODAC have the longest $T_{3/4}$ lifetimes of the four DODAC concentrations. For the 2.5 mM BP the results shown in figure 6.6 are confirmed. The 40 mM DODAC has a slower recombination rate than the other two

concentrations, however the difference in lifetimes between all the concentrations is very small.

The fractional lifetimes are much longer than any of those seen for the micellar systems in the previous two chapters, indicating a much slower rate of radical recombination. $T_{3/4}$ and $T_{1/2}$ are approximately a factor of four larger than those seen for SDS/BP in chapter three, whilst $T_{1/4}$ is approximately a factor of five larger in DODAC/BP than in SDS/BP. From tables 2.1 and 2.3 it can be seen that both the size and the microviscosity of the DODAC vesicles is larger than for any of the micellar systems. The cationic micelles showed that as the micelle size and microviscosity increased (with increasing chain length) this had the general effect of increasing the fractional lifetimes, and it is seen here that the very large increase in size of the hydrophobic compartment and increase in microviscosity results in very large increases in the fractional lifetimes between the two types of structures.

6.2.2 MARY Curves

MARY curves were recorded at the same concentrations as those for the zero field time curves. Figure 6.9 shows the MARY curves for 2 mM BP and four different concentrations of DODAC.

The curves shown are all averages of seven MARY curves, each of fifty averages per point, apart from the 35 mM curve which is an average of eight separate MARY curves.

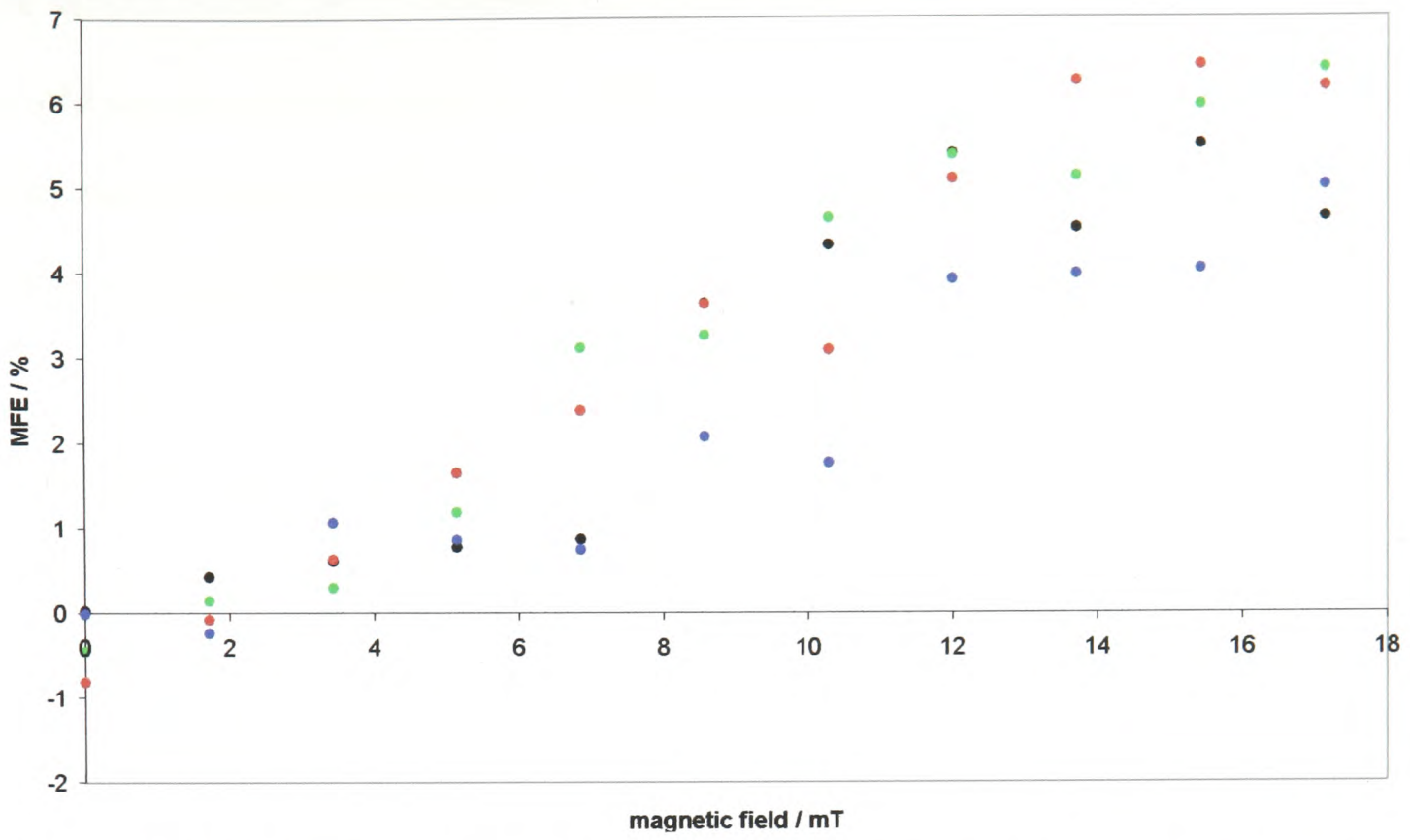


Figure 6.9: MARY curves of 2 mM BP and DODAC concentrations of (•) 25 (1.4), (•) 30 (2.6), (•) 35 (1.8), and (•) 40 mM (2.5) (figures in brackets show EE / %)

As with the zero field time curves there is no clear trend with changing concentration.

The 30 mM and 40 mM curves generally seem to have larger MFEs than the 25 mM and 35 mM curves, and it was the 30 mM and 40 mM curves from figure 6.5 which showed the slower radical recombination rates.

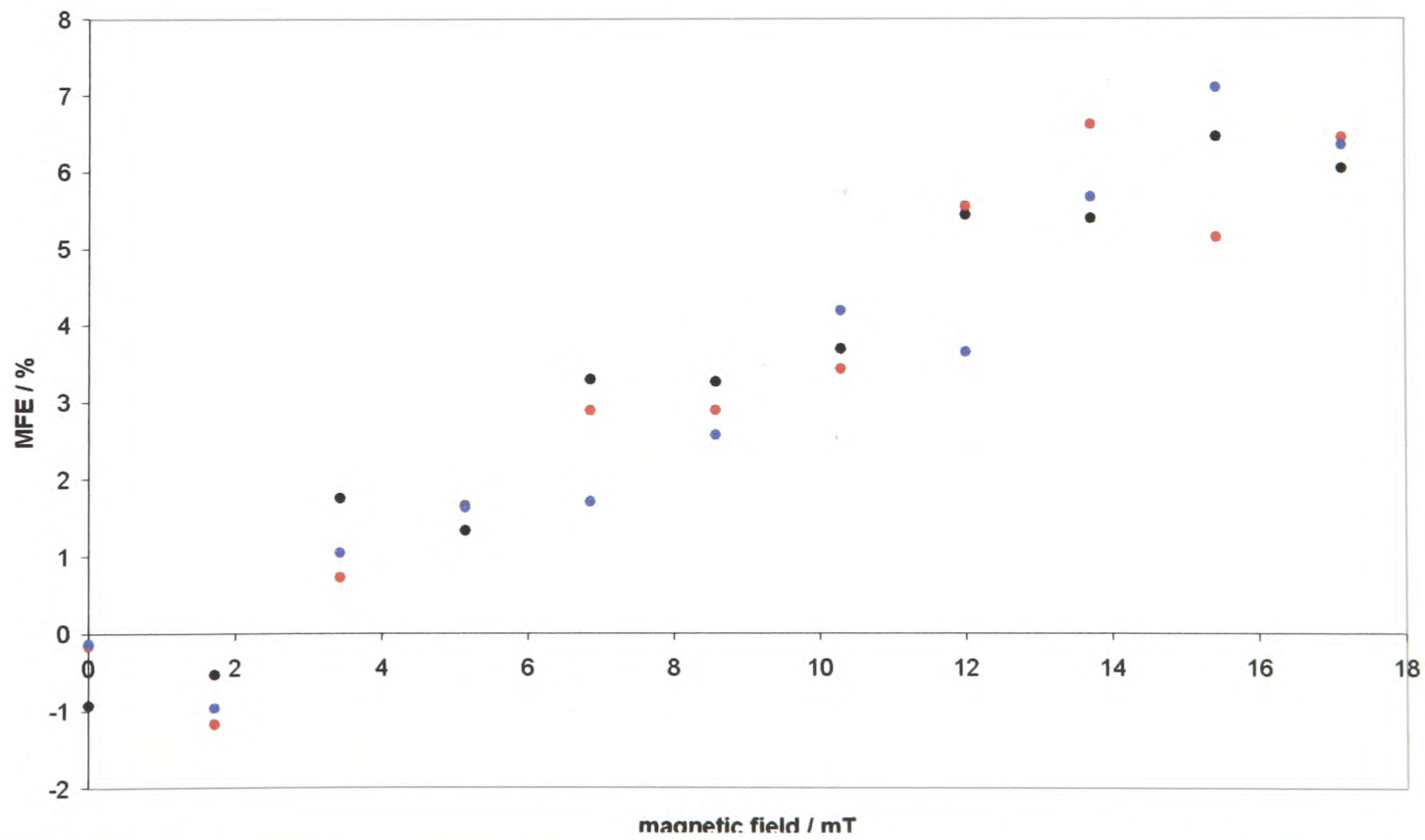


Figure 6.10: MARY curves of 2.5 mM BP and DODAC concentrations of (•) 25 (2.1), (•) 30 (1.8), and (•) 40 mM (2.2) (EE / %)

The MARY curves for 2.5 mM BP are shown in figure 6.10. The 25 mM, 30 mM, and 40 mM curves are averages of six, seven, and three MARY curves respectively. There is no real difference between the size of the MFEs for the three concentrations of DODAC, despite the difference in recombination rates seen in figure 6.6.

As would be expected from the zero field time curves seen in figure 6.8, changing the BP concentration from 2 mM to 2.5 mM makes no difference to the MARY curves. Figure 6.11 shows the MARY curves for the two different BP concentrations in 40 mM DODAC.

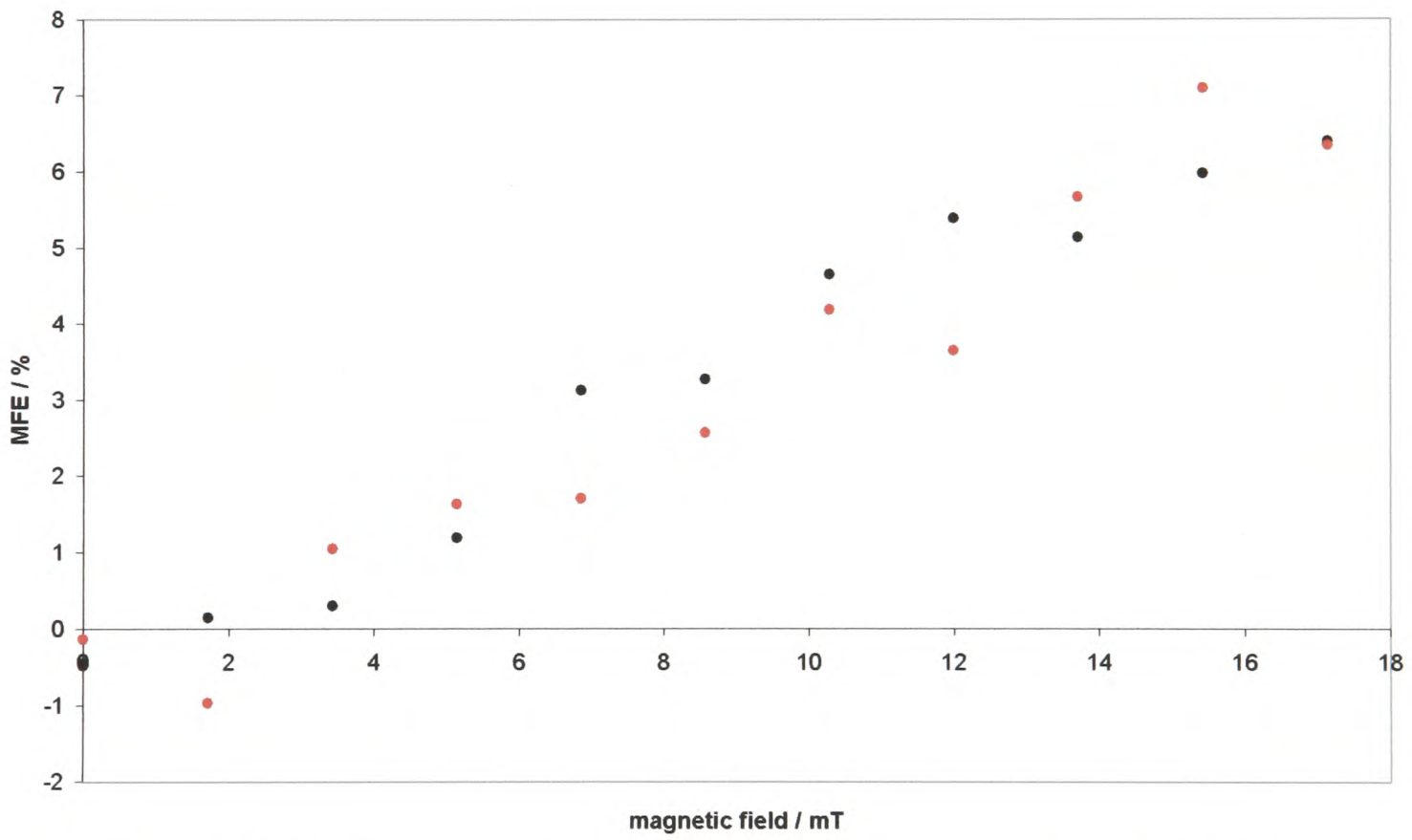


Figure 6.11: MARY curves of 40 mM DODAC and BP concentrations of (•) 2 (2.5), and (•) 2.5 mM (2.2) (EE / %)

The MFEs seen with all the concentrations of DODAC and BP are much smaller than those observed in micellar systems in the previous two chapters. At the largest magnetic field strengths investigated (around 18 mT) the MFEs for SDS/BP are of the order of 25%, with the hydrogen donor systems ranging between approximately 15%

and 35%. The cationic micelles at the same magnetic field strength also have MFEs in the region of these values. For the DODAC/BP system the MFEs at this magnetic field strength are of the order of 7%, at maximum half the size of those seen in micellar systems. The difference in physical properties between micelles and vesicles have been discussed in chapter two, and briefly in section 6.2.1, with the interior of the DODAC vesicles being both much larger and more viscous than that of the micelles studied. This agrees with the trend seen in the cationic micelles where an increase in micelle size and microviscosity (with increasing chain length) led to a decrease in the size of the MFEs.

6.3 Hydrogen Donors

As with the other 'micro-reactors' used in this study, hydrogen donors were added to the DODAC/BP system to see what effect faster hydrogen abstraction has on the time curves and magnetic field effects, for these experiments CHD was used as the hydrogen donor. The concentrations of DODAC, BP and CHD were 25 mM, 2 mM, and 40 mM respectively.

Figure 6.12 shows the zero field time curves with and without CHD. Each curve is an average of four different zero field time curves, each of fifty averages. The most striking feature about this comparison is how much larger the absorbance is in the presence of CHD. The initial peak height of the CHD curve is around 30% larger than the height of the curve in the absence of CHD.

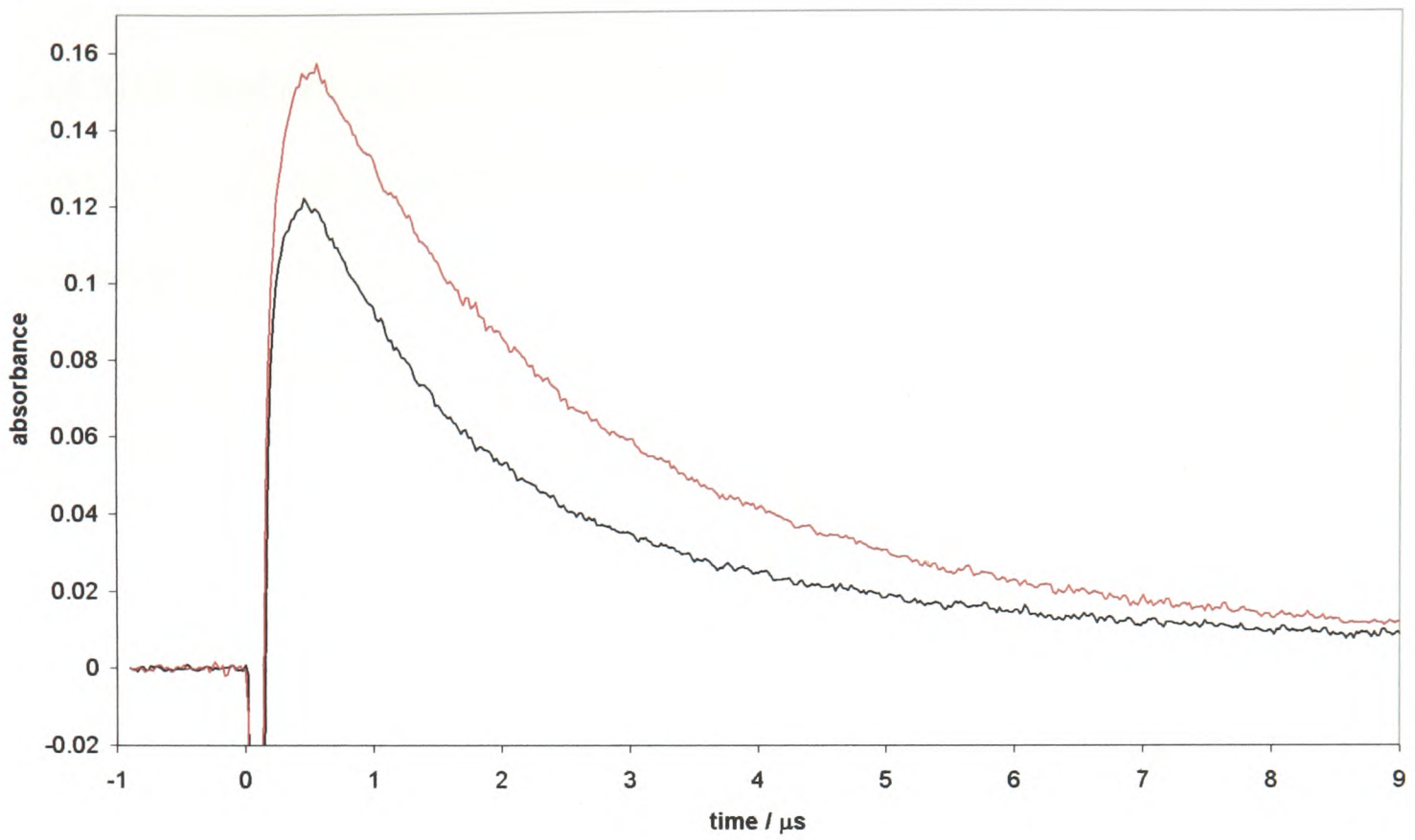


Figure 6.12: Zero field time curves of DODAC/BP (•) without CHD, and (•) with CHD

This is the opposite effect to that seen in SDS micelles where the addition of CHD caused the size of the absorption signal to decrease. This was also the case with the cationic micelles, where with both DTAC/BP and CTAC/BP addition of CHD led to a decrease in the size of the initial absorbance peak. In SDS/BP the reduction in signal was ascribed to quenching of the excited BP triplet by the CHD molecule without radical pair formation taking place. The increase in signal size with addition of CHD in DODAC/BP must either mean that the quenching by CHD is overcome by the increase in hydrogen abstraction rate, which results in the signal increase, or that the effect on the structure of the vesicle caused by the addition of such a large concentration of CHD results in the increased size of the initial absorption peak. One difference between the SDS and DODAC experiments is the relative concentration of CHD. The BP:CHD ratio is the same in both cases, but in SDS there are six CHD molecules for every ten SDS molecules, whereas in DODAC there are sixteen CHD molecules for every ten DODAC molecules. This means that, in the concentrations

used, addition of CHD will have a greater effect on the structure of DODAC than on that of SDS. Studies have been made in SDS micelles of the effect on micelle size of the addition of butane [4], where it was shown that when the concentration of butane is increased from 10% to 40% of the SDS concentration, the radius of the SDS micelles is only increased by approximately 8%. Section 6.3.1 addresses the problem of high CHD concentration in DODAC vesicles in more detail.

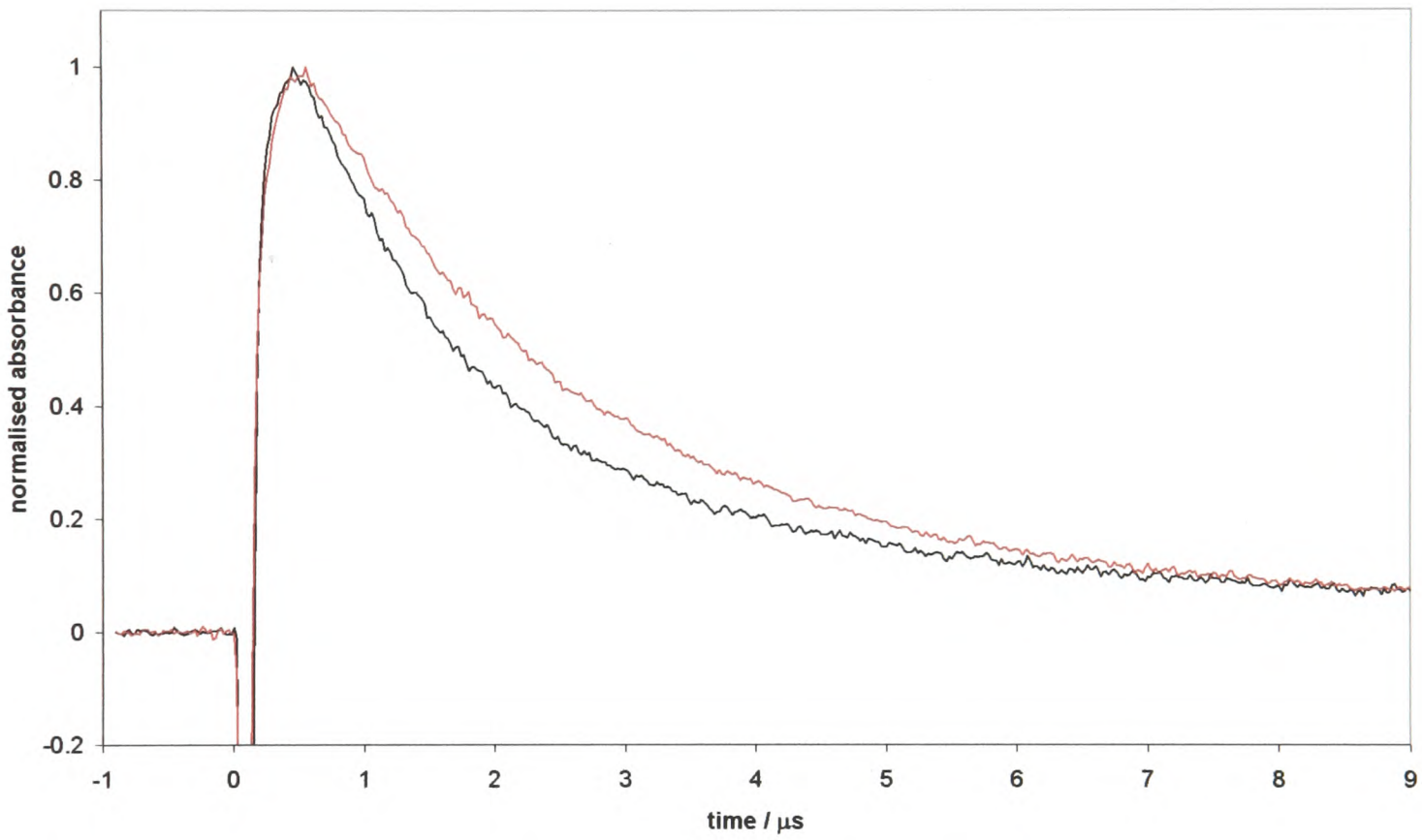


Figure 6.13: Normalised zero field time curves of DODAC/BP (•) without CHD, and (•) with CHD

If the two time curves of figure 6.12 are normalised then figure 6.13 is produced. This shows that not only does the addition of the CHD lead to larger absorption signals, but it also causes a slower rate of radical recombination. This is the same as seen in SDS micelles, where addition of CHD also causes slower recombination rates. In both the SDS and DODAC this is due to an increase in the escape of the radical pair and hence an increase in the number of F pairs and a longer lived $BPH^{\bullet}$ signal. Addition of CHD also causes a change in shape of the time curve from bi-phasic with DODAC/BP to

mono-phasic with DODAC/BP/CHD. This mirrors the change seen in figure 5.4 with the DTAC/BP system, where the addition of CHD led to a change from bi-phasic to mono-phasic kinetics.

System	$T_{3/4}$ / μs	$T_{1/2}$ / μs	$T_{1/4}$ / μs
DODAC/BP	0.66	1.5	3.34
DODAC/BP/CHD	0.76	1.72	3.7

Table 6.2: Lifetime data showing effect of CHD on DODAC/BP system

The lifetime data in table 6.2 reinforces the point made by figure 6.13 that the addition of CHD to the DODAC/BP system increases the lifetime of the RP at all three fractions of signal size. This is the same trend seen in the previous chapter with the cationic micelles DTAC and CTAC, where addition of CHD lead to increased fractional lifetimes. This suggests that, as with the cationic micelles studied, the increase in geminate recombination rate due to the addition of CHD is outweighed by the increase in the escape rate of the geminate RP.

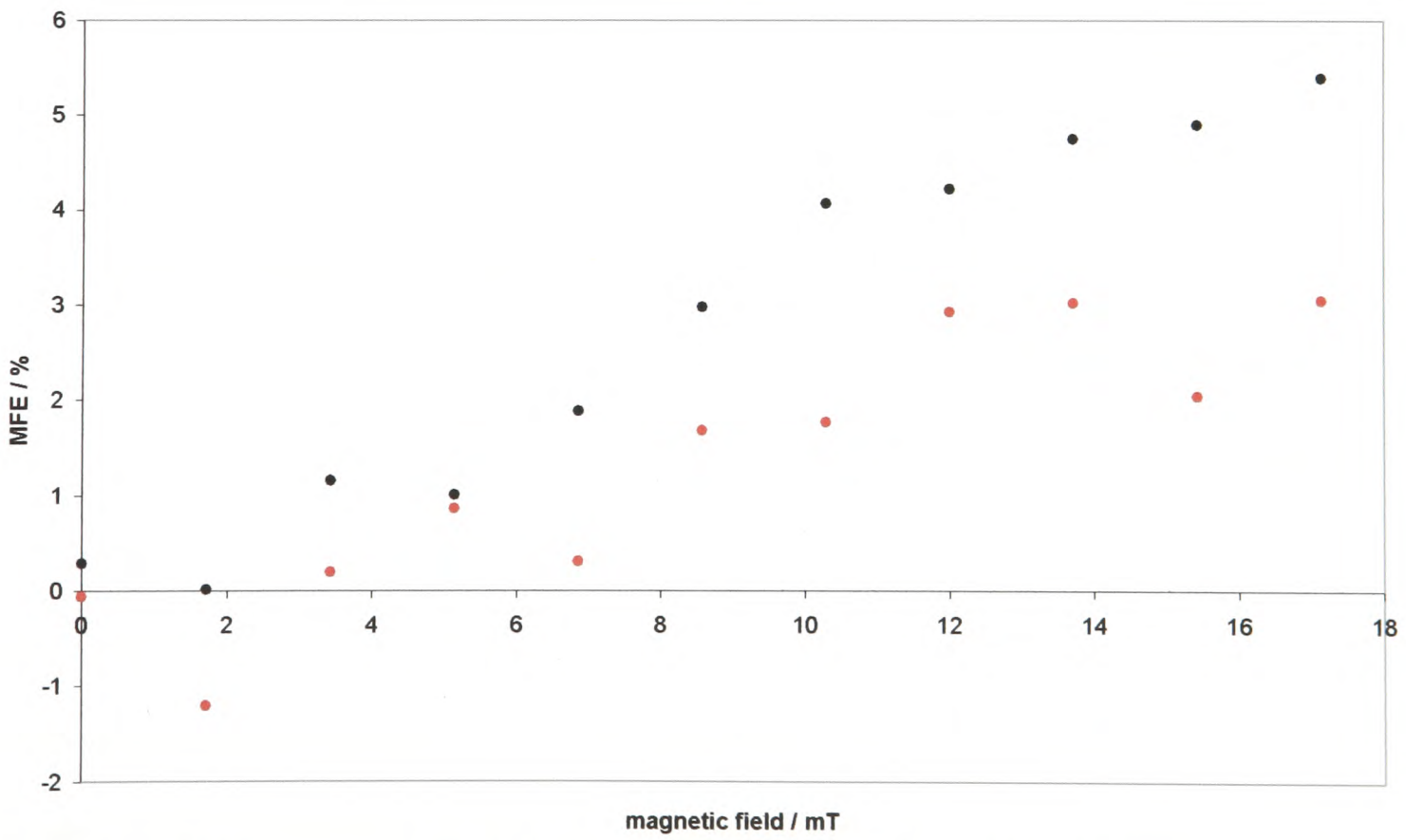


Figure 6.14: MARY curves of DODAC/BP (•) without CHD (3.5), and (•) with CHD (1.4) (EE / %)

Figure 6.14 shows the effect on the MARY curves of adding CHD to the DODAC/BP system. Each MARY curve is an average of seven curves, each of fifty averages per point. Again the effect in DODAC is the opposite from that seen in SDS micelles. The addition of CHD to DODAC/BP gives smaller MFEs than those seen in the absence of CHD. The effect on the MFEs of the cationic micelles upon addition of CHD was dependent on the micelle. DTAC showed decreased MFEs, but CTAC showed increased MFEs compared to the same systems in the absence of CHD. The decrease in MFE size in the DTAC system was ascribed to the fact that a geminate period could not be observed in the zero field time curve, and this is also the case with the DODAC system seen in figure 6.13.

The reduction in MFE size on addition of CHD to DODAC/BP could therefore be a consequence of an increased escape rate of radicals from the geminate RP. The size of the vesicle means that the radicals do not have to escape into the bulk solution to escape from the geminate RP, they can just escape into a separate area of the vesicle. This means that the hydrophobic radicals do not have to enter the aqueous part of the solution, they can stay in the hydrophobic interior of the vesicle, but far enough apart from each other not to encounter the other member of the geminate RP.

6.3.1 Lower CHD Concentrations

All the experiments above were performed with a concentration of CHD greater than that of the DODAC, which whilst altering the RP behaviour must also alter the structure of the vesicle. To investigate the effect of CHD without distorting the vesicle to the same extent experiments were also performed with concentrations of DODAC, BP, and CHD of 40 mM, 2 mM, and 10 mM respectively. This leads to a smaller

BP:CHD ratio than has been used in previous chapters, but still gives five CHD molecules for every BP molecule.

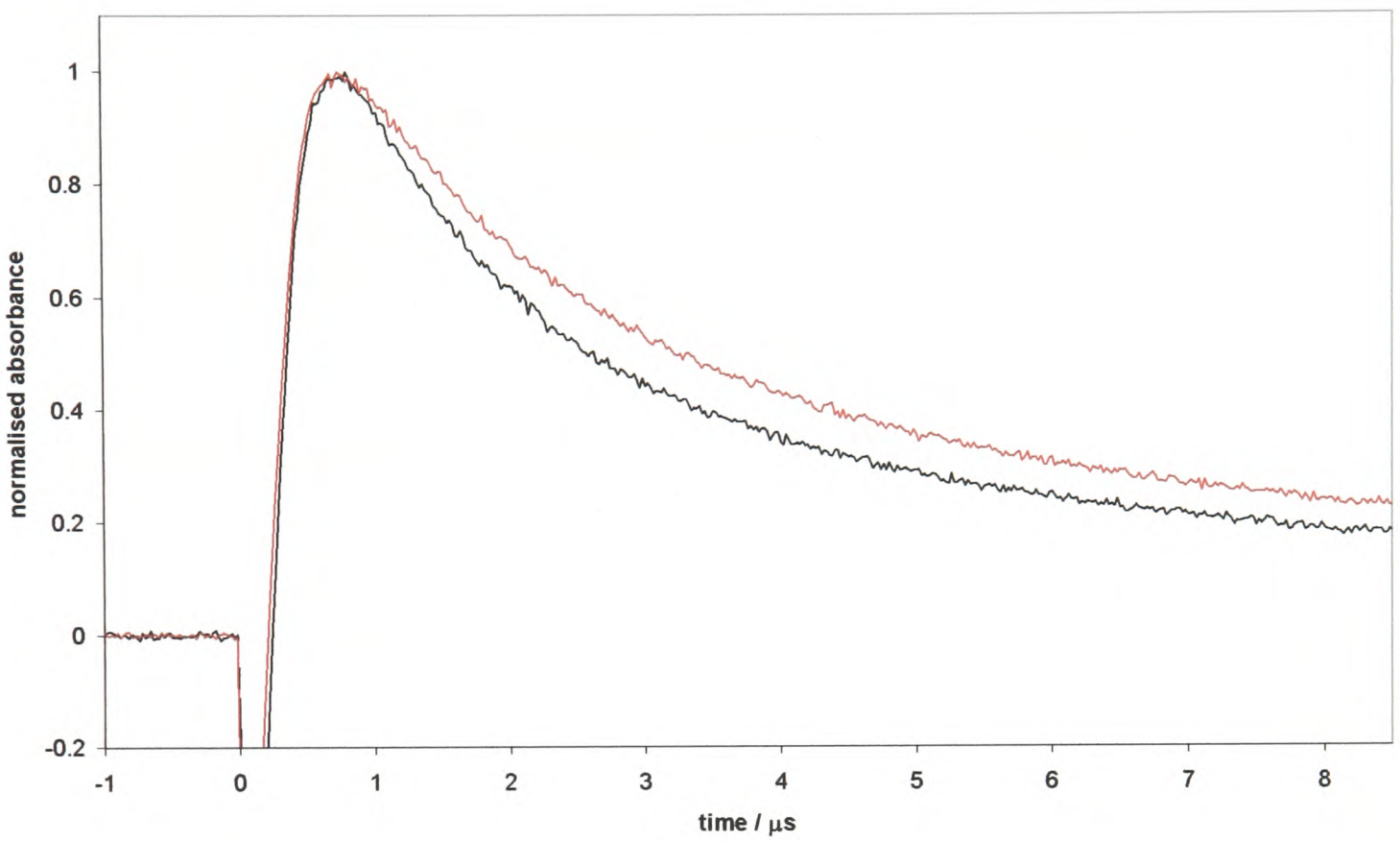


Figure 6.15: Normalised zero field time curves of DODAC/BP (•) without CHD, and (•) with CHD

Figure 6.15 shows normalised zero field time curves for DODAC/BP both in the presence and absence of CHD, and the trend is the same as that seen in figure 6.13, namely that the addition of CHD leads to a decrease in the rate of signal decay. However, the trend in the shape of the time curves is slightly different, the decay of the time curve in the presence of CHD does not follow mono-phasic kinetics, but the initial decay rate is slower than in the absence of CHD implying that less geminate recombination is occurring, as was the case in section 6.3. The trends in the MFEs are also the same as with the higher concentration of CHD, the addition of CHD to DODAC/BP leads to a decrease in the MFEs as is seen in the manually calculated MFEs shown in table 6.3. The results with the lower CHD concentration do not exclude the possibility that it is a change in structure of the vesicles upon addition of

DODAC that leads to the alterations in time curve and MFE behaviour. However, they do show that these effects are the same with a much lower CHD concentration, and a higher DODAC concentration, and hence support the conclusions drawn in the previous section.

System	MFE at 4.3 mT / %	MFE at 8.6 mT / %
DODAC/BP	2.1	7.8
DODAC/BP/CHD	1.3	3.6

Table 6.3: Manually calculated MFEs for DODAC/BP and DODAC/BP/CHD calculated from time curves of 288 averages per curve

6.4 Looking for Low Field Effects

All the work presented so far in this chapter with DODAC has been looking for magnetic field effects of any sort, and so has been over the full range of the Helmholtz coils, up to ~18 mT. MARY curves are normally taken with eleven points, so over this range only one or two points will be in the region where the LFE is expected to be.

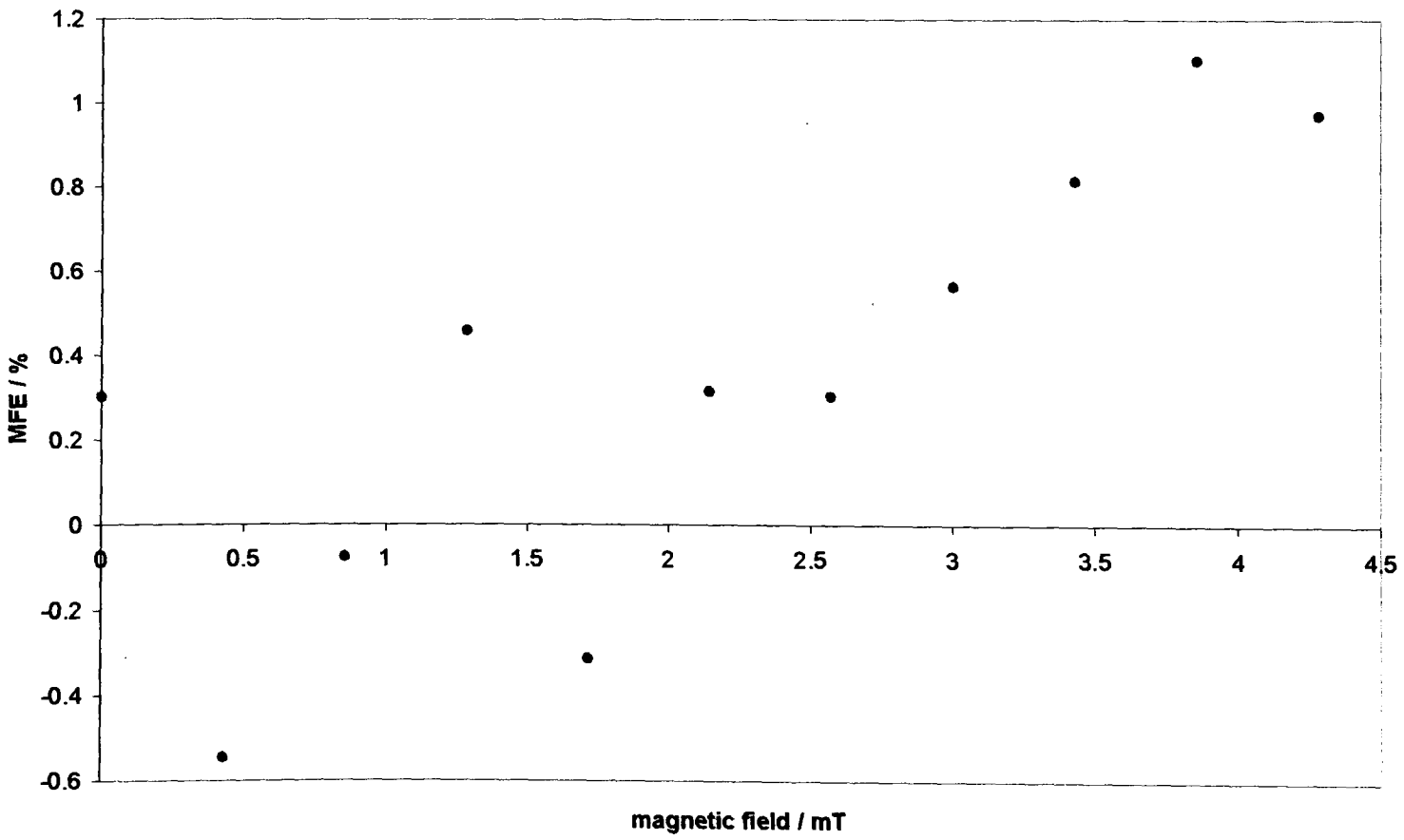


Figure 6.16: MARY curve of DODAC/BP concentrating on LFE region (EE 1.68%)

Experiments were performed concentrating on a smaller region of magnetic field in an attempt to find a LFE. The first attempts were at room temperature, as were all the DODAC experiments performed so far.

Figure 6.16 shows a MARY curve composed of the average of ten MARY curves, each of forty eight averages per point. The ten curves were obtained over two days with two separate solutions of 30 mM DODAC and 2.5 mM BP. The curves do not show conclusive proof of either the presence or absence of a LFE. The normal, positive MFEs can be seen in the last few points, but the first six points do not show the certain presence of a LFE.

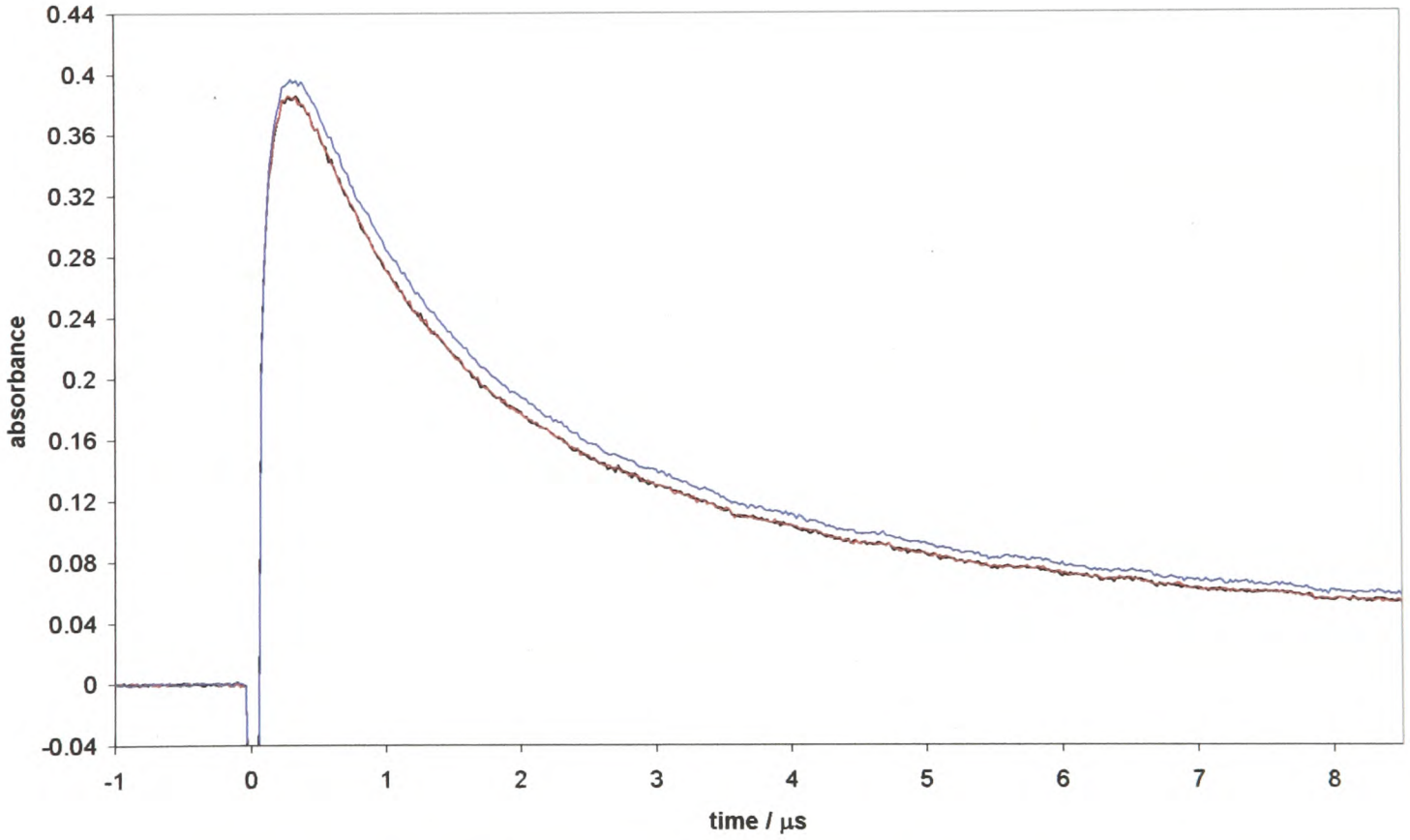


Figure 6.17: Time curves of DODAC/BP at (•) 0, (•) 1.7, and (•) 8.6 mT

The next method for looking for a LFE is to take time curves at zero magnetic field, a point in the LFE region, and at a point in the normal, positive MFE region. These time curves are shown in figure 6.17, at 0 mT, 1.7 mT, and 8.6 mT. There is an obvious

increase in signal for the 8.6 mT curve, but absolutely no difference between the curve at zero magnetic field and the curve at 1.7 mT. This evidence points to the fact that either there is no LFE present in the DODAC/BP system, or if a LFE exists it is of such a small size as not to be observable. All three curves are the average of four separate curves, each of ninety six averages, hence a total of 384 averages per curve.

6.5 TEMPERATURE EFFECTS

Investigations were also carried out into the effect of temperature on the DODAC/BP system. All the results shown in the preceding sections were obtained at 25 °C, to compare with these results experiments were performed at 60 °C, above the phase transition temperature described in section 2.3.1. Above this phase transition temperature the hydrophobic tails of the DODAC molecules are in a more disordered, liquid-like state, compared to vesicles below the transition temperature. The microviscosity of the DODAC vesicle decreases with increasing temperature, but there is also a marked decrease in microviscosity moving from below the transition temperature to above it [5]. The decrease in microviscosity means that the radicals are likely to be more mobile at the higher temperature. The temperature experiments were all carried out with a DODAC concentration of 30 mM and a BP concentration of 2.5 mM.

Figure 6.18 shows the zero field time curves for DODAC/BP at both temperatures, and it can be seen that although the higher temperature curve has the smaller initial size it decays at a slower rate than the lower temperature curves to have a larger radical concentration by the end of the measurement period.

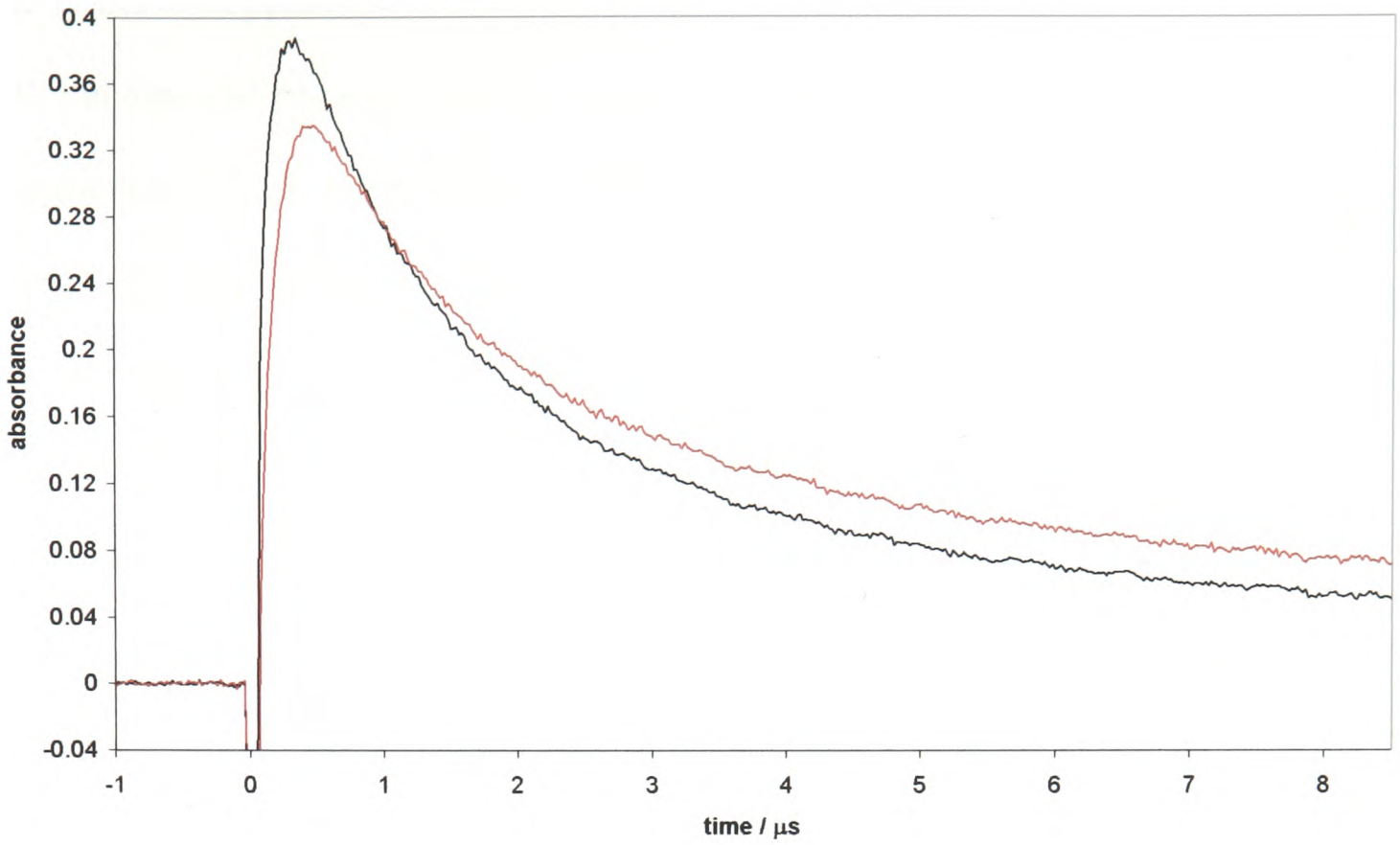


Figure 6.18: Zero field time curves of DODAC/BP at (•) 25, and (•) 60 °C

Temperature / °C	$T_{3/4}$ / μs	$T_{1/2}$ / μs	$T_{1/4}$ / μs
25	0.54	1.34	3.26
60	0.76	2.06	6.54

Table 6.4: Lifetime data for DODAC/BP at two temperatures

The lifetime data in table 6.4 emphasizes the trend shown in figure 6.18, that increasing the temperature above the phase transition temperature increases the lifetime of the $BPH^{\bullet}$ radical. This is most likely to be due to an increased escape rate of the geminate radical pair, as the interior of the vesicle has a much lower viscosity above the phase transition temperature. This is in agreement with the effect seen on addition of CHD in section 6.3, where the increase in lifetime of the $BPH^{\bullet}$ radical was ascribed to the increase in mobility of the RP as the counter radical was changed from a DODAC derived surfactant radical to the CHD derived radical. This effect on radical pair lifetime is opposite to that seen with SDS micelles, where an increase in temperature leads to an increase in recombination rate.

The effect of temperature on the MARY curves of DODAC is smaller than that seen with the time curves, as is shown in figure 6.19. In the LFE region there is a stronger suggestion of a LFE at the higher temperature, and at higher strength fields the higher temperature solution gives slightly larger MFEs. This trend would be in agreement with SDS micelles, where a higher temperature leads to both larger LFEs and also larger MFEs at higher magnetic field strengths [6]. However, the error estimation shows that the uncertainty in the higher temperature results is greater than that in the lower temperature results, and hence despite the high number of averages the difference in MFE size is not conclusive.

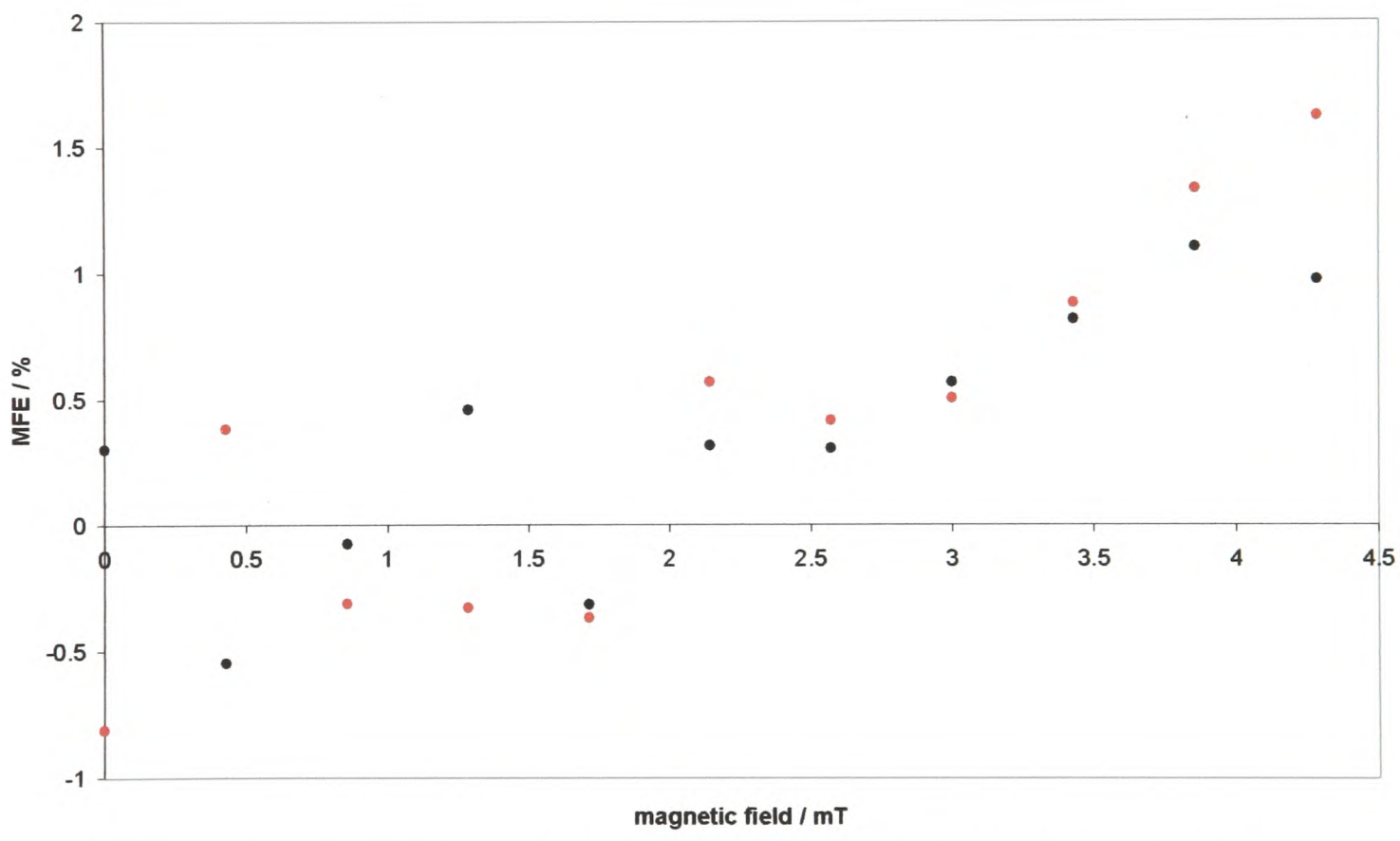


Figure 6.19: MARY curves of DODAC/BP at (•) 25 (1.68), and (•) 60 °C (4.04) (EE / %)

6.6 CONCLUSIONS

This chapter has presented results of what are believed to be the first investigations into MFEs at weak magnetic fields inside DODAC vesicles. Although experimentally quite challenging initially three areas were investigated successfully; the impact of concentration of DODAC and BP on the size of the MFE was probed, additional hydrogen donors were added to the vesicle solutions, and the effects of increasing the solution temperature, and hence changing the phase of the vesicle, were examined. The concentration studies showed that over the relatively small concentration range investigated only minor differences were observed in the kinetics of the time curves, and in the size of the MFEs in the MARY curves. Addition of CHD to the DODAC/BP system leads to increased fractional lifetimes, and reduced MFEs compared to DODAC/BP in the absence of CHD. These results were repeated when the concentration of CHD was lowered to a quarter of that used in the initial experiments, and the DODAC concentration increased. The experiments at temperatures above the phase transition showed that increasing the temperature also increased the fractional lifetimes. However, the effect on the MFEs was minimal. At both temperatures the size of the MFEs is much smaller than that seen in micellar systems. Upon close investigation the suggestion of a LFE is seen, but despite comprehensive averaging this could not be confirmed. These results do show however that it is possible to see MFEs in vesicles at relatively low magnetic field strengths, and provide a useful 'stepping stone' for progress towards biologically relevant systems. DODAC vesicles are used by other research groups as membrane mimetic agents and can therefore provide useful information on radical pair reactions in these environments.

7: Biological Micelles – Lysophospholipids

Chapters three and four described work undertaken in synthetic micelles, this chapter reports on experiments carried out in lysophospholipid micelles. The lysophospholipid used is lysophosphatidyl choline (LPC), which means that the head group is zwitterionic, as opposed to the anionic micelles used in chapter three and the cationic micelles used in chapter four. LPC also has the same head group as found in phosphatidyl choline phospholipids, hence the use of LPC as another 'stepping stone' on the way to working with phospholipid vesicles. As discussed in chapter two micelles formed from only lysophospholipids are not found in nature, but lysophospholipid molecules are constituents of many biological membranes.

7.1 Experimental Section

Solutions were prepared using the same method as in previous chapters with sonication for 59 minutes at 25 °C, unless otherwise stated. All LPC experiments were performed with concentrations of LPC at 40 mM and probe molecule at 2 mM unless otherwise stated. All SDS experiments were performed at 25 °C with an SDS concentration of 100 mM and probe molecule at 3 mM.

All time curves shown consist of an average of two data sets, with each data set being an average of 48 acquisitions, and were recorded at zero applied magnetic field unless stated otherwise.

7.1.1 Wavelength Studies

Transient absorption spectra were recorded over the range 400 nm to 700 nm. Solutions were prepared as described previously, and zero field time curves were recorded between 400 nm and 700 nm at 10 nm intervals without the use of any band pass filters. The absorbance was calculated as described in section 3.5, and absorbance values were recorded for each wavelength at specific times after the laser pulse.

7.1.2 Buffered Solutions

For the experiments where buffered solutions were required, solutions were prepared as follows. The quantities of each buffer component were calculated from table 7.1 in order to achieve the desired pH values, deionised water added, and the resulting solutions were sonicated for 5 minutes at 25 °C. The pH values of the solutions were checked, and then the buffer solutions were used in place of deionised water in the usual preparation of a micellar solution (as described in section 3.3). The pH values of the final solutions were measured after the 59 minutes of sonication, and again after the experiment, to ensure no variation during data acquisition.

Buffer	pH	Concentration / M	Mass acidic component / g	Mass basic component / g
phosphate – citrate	3.2	0.2	citric acid – 2.29	sodium phosphate, dibasic – 0.87
phosphate – citrate	6.0	0.2	citric acid – 0.97	sodium phosphate, dibasic – 2.82
phosphate – phosphate	6.0	0.1	sodium phosphate, monobasic – 1.47	sodium phosphate, dibasic – 0.39
phosphate – phosphate	7.8	0.1	sodium phosphate, monobasic – 0.095	sodium phosphate, dibasic – 2.02

Table 7.1: Composition of buffers used in pH dependence experiments

7.2 A CHANGE OF PROBE MOLECULE

7.2.1 Initial Experiments with BP

Initially lysophospholipids were used with BP as the probe molecule. The zero field time curves that were obtained display a very small signal, in comparison to other systems previously studied such as SDS and DODAC (figure 7.1). The concentrations are shown on the diagram, however, whilst the BP concentration is 50% higher in the SDS solution than in the other two solutions, the initial peak is more than double that obtained in the DODAC/BP system, and almost ten times larger than in the LPC/BP system.

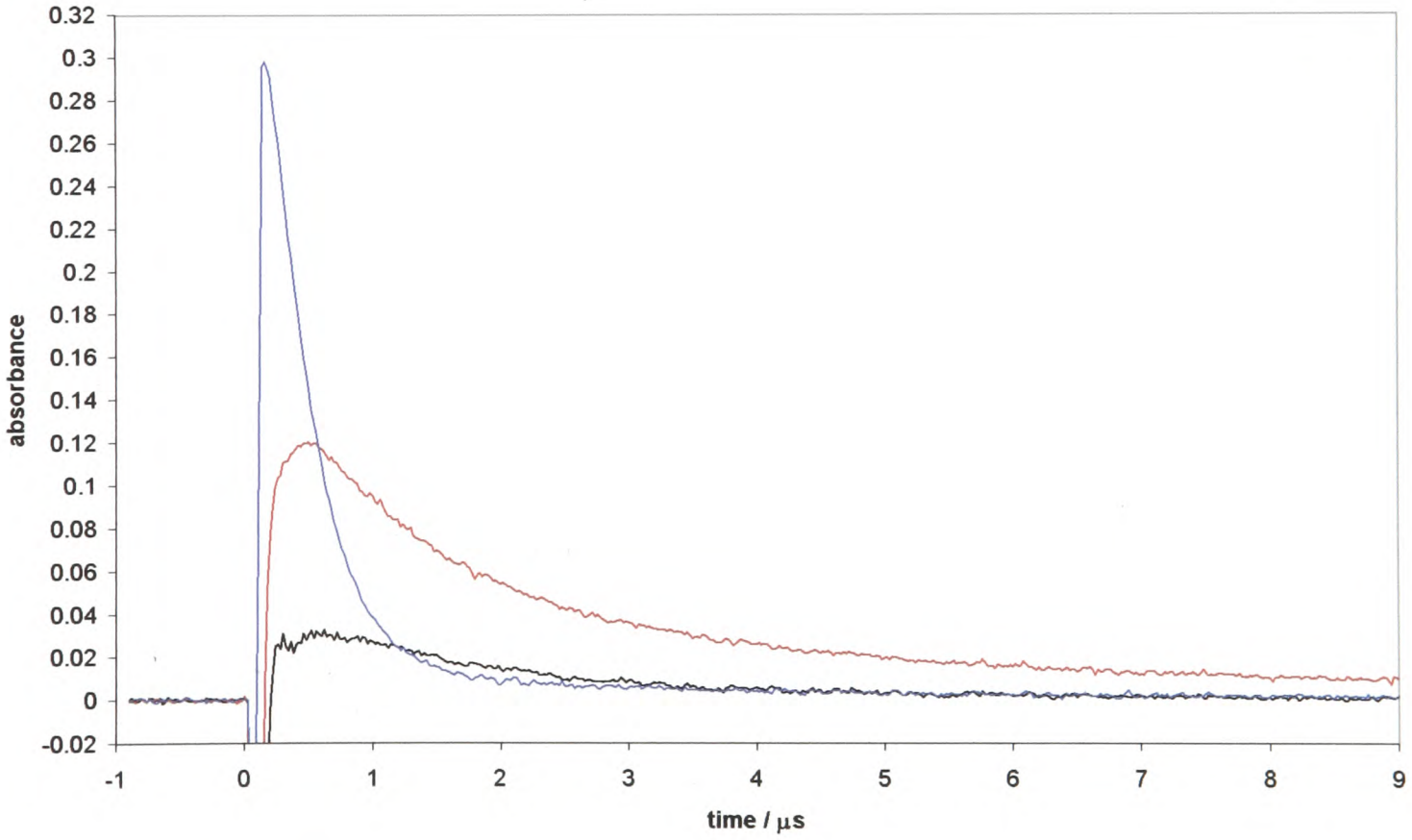


Figure 7.1: Zero field time curves of (•) LPC/BP (40/2 mM), (•) DODAC/BP (25/2 mM), and (•) SDS/BP (100/3 mM)

The reason for the small size of the LPC/BP signal is not immediately obvious, as the solution itself is less turbid than the DODAC/BP solution, hence the small signal size is not due to increased scattering of the monitoring beam. Despite the small signal size it is still possible to see suggestions of MFEs in the time curves of LPC/BP (not shown), and in the MARY curves there is an obvious increase in MFE with increasing magnetic field strength (figure 7.2), although the low signal to noise ratio means that the points on the MARY curve look scattered.

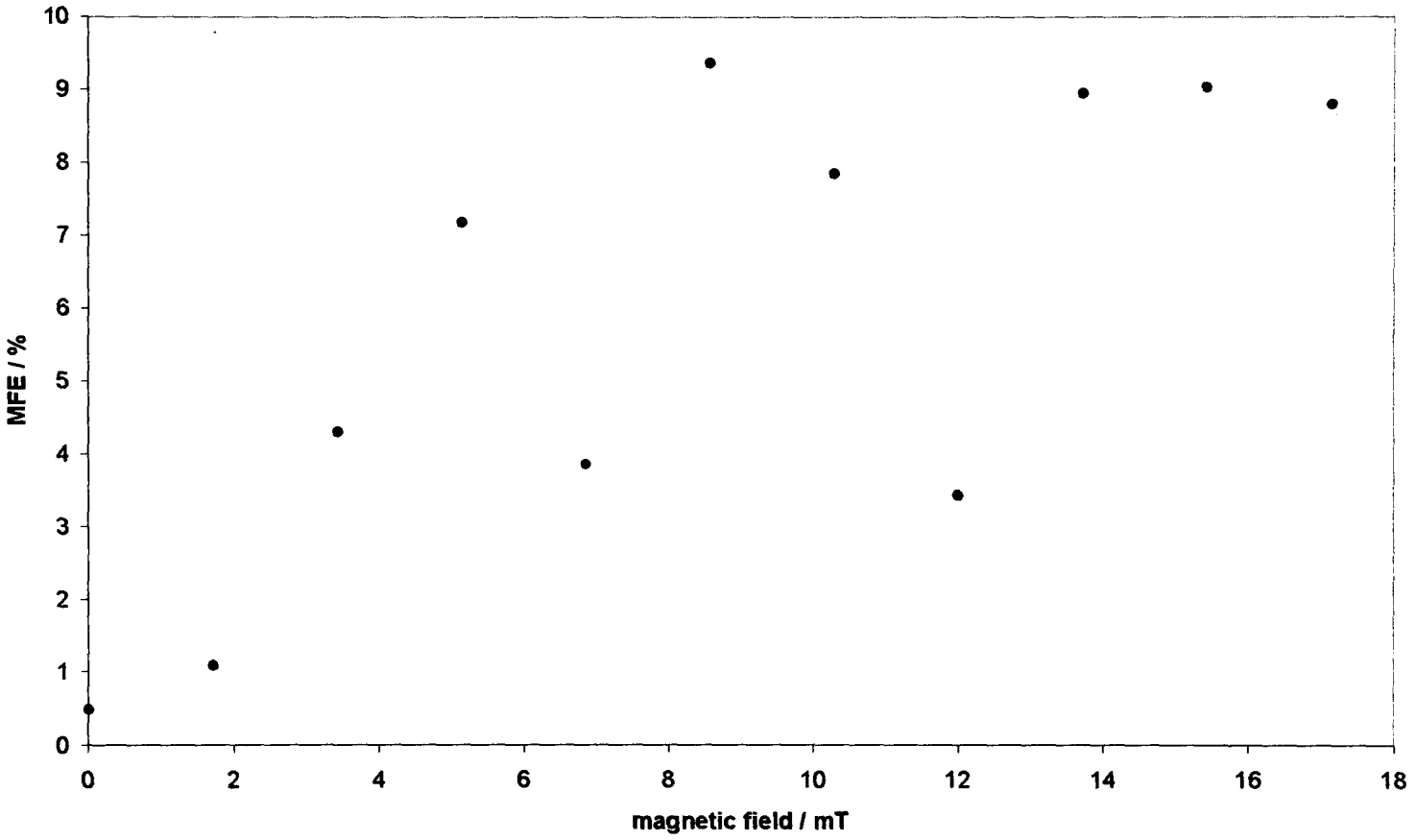


Figure 7.2: MARY curve of LPC/BP (EE 7.4%)

A superficial explanation for a small absorption signal in this type of experiment is a low concentration of radicals, however the reasons for a low concentration of radicals in this LPC/BP system require clarification. The intensity of laser light is unchanged from the DODAC/BP experiments, and the concentration of BP is also identical, suggesting that some other component of the solution is absorbing the laser light in competition with the BP, or that radical formation is less efficient in LPC micelles. To

test the hypothesis of a species other than the BP absorbing the laser light UV/vis absorption spectra for solutions of LPC, and DODAC/BP were obtained, a composite of the spectra of the two solutions is shown in figure 7.3.

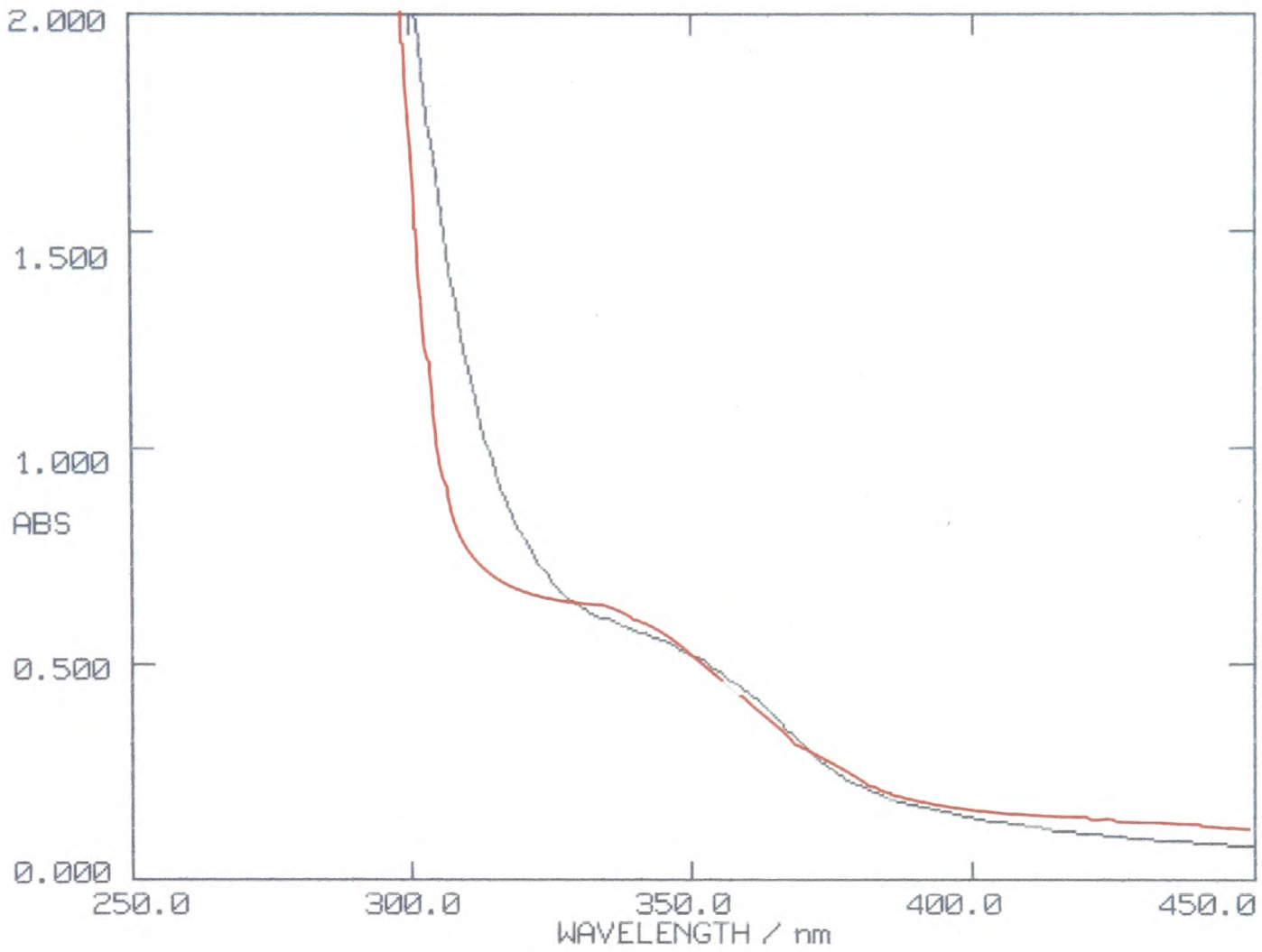


Figure 7.3: UV/vis absorption spectra of (●) LPC, and (●) DODAC/BP

The UV/vis spectra show very clearly that even in the absence of BP the LPC solution absorbs strongly at 308 nm, the wavelength of the XeCl laser. This presented a major problem, as the absorbance signals obtained with LPC/BP were very small, and made a thorough investigation of MFEs in these systems very challenging. Both lysophospholipids and phospholipids display strong absorbance at 308 nm, hence any investigation of MFEs in these systems in greater detail required alteration of the experiment and equipment. LPC displays less absorption at 355 nm than at 308 nm (figure 7.3), and so a YAG laser tuned to fire at this wavelength was employed.

However, the change of laser and excitation wavelength led to a further problem; BP displays very weak absorbance at 355 nm, and the signals obtained were too small to study MFEs. The absorption signal of the $BPH^{\bullet}$ ketyl radical measured at 555 nm obtained using excitation with the YAG laser at 355 nm is almost half the size of the signal obtained using excitation with the XeCl laser at 308 nm.

7.2.2 Experiments with 2-Benzoyl Thiophene

Any new probe molecule to be used in the experiment had to fulfil the following requirements: 1) The molecule must form a neutral radical pair, preferably by hydrogen abstraction, of which the probe molecule derived radical must absorb light in the visible region of the spectrum. 2) The ground state molecule is required to absorb light at 355 nm for excitation by the YAG laser. 3) The molecule must be hydrophobic so that it locates preferentially in the interior of micelles and vesicles. For these reasons the probe molecules considered were all derivatives or analogues of BP. The first molecule to be utilised was 2-benzoyl thiophene (BT), the structure of which is shown in figure 7.4, below. It was chosen due to its structural similarities to BP, and hence similar hydrophobicity, but BT has a greater absorbance at 355 nm.

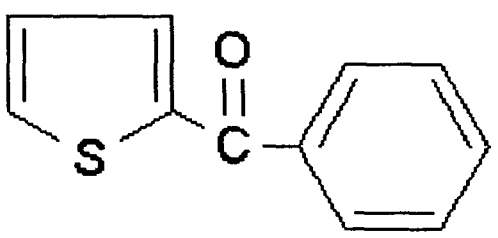


Figure 7.4: Structure of 2-benzoyl thiophene

Prior to obtaining the YAG laser, wavelength studies were performed on BT using the XeCl excimer laser. Three solutions were used, SDS/BT, SDS/BT/CHD and BT in acetonitrile (MeCN). The latter was used as the rate of hydrogen abstraction from

MeCN is very slow on the timescale of the experiment (130 M^{-1} s^{-1} for BP in MeCN [1]). As a consequence the excited triplet state of BT can be studied in MeCN, as its lifetime is much longer than in solutions where hydrogen abstraction occurs at a much faster rate (*e.g.* the hydrogen abstraction rates for BP in table 4.2, which are of the order of 10^7 M^{-1} s^{-1}). Figure 7.5A shows the spectra for four different timescales for the SDS/BT solution, and it can be seen that the absorption maximum occurs at a longer wavelength than the peak in SDS/BP, which occurs at 550 nm [2]. Figure 7.5B shows the spectra for the same four timescales, but this time for BT in MeCN. Whilst the peaks occur at the same wavelength (600 nm) and are equally broad, they differ in the speed with which the signals decay in the two systems. In SDS/BT the 1 μs and, to an extent, the 2 μs curves follow the shape of the earlier curves. However in MeCN the 1 μs and 2 μs curves are essentially flat and show no absorption.

The wavelength study for the third solution, SDS/BT/CHD, is shown in figure 7.5C. This gives a different shape for the peak, and also a longer lived signal as can be seen from the fact that 2 μs after the laser flash the absorption is still about a third of the size of the absorption at 240 ns. In both the SDS/BT and BT/MeCN solutions the maximum absorption occurred at 600 nm, whereas in SDS/BT/CHD the maximum value occurs at 580 nm.

A comparison of the shapes and positions of the absorption values from the three different systems 240 ns after the laser flash shows a similarity between the SDS/BT and BT/MeCN curves. The decrease in wavelength maxima combined with the shoulder at 540 nm suggests that the absorbing species in SDS/BT/CHD is different from that in the other two solutions, or is a combination of two or more species.

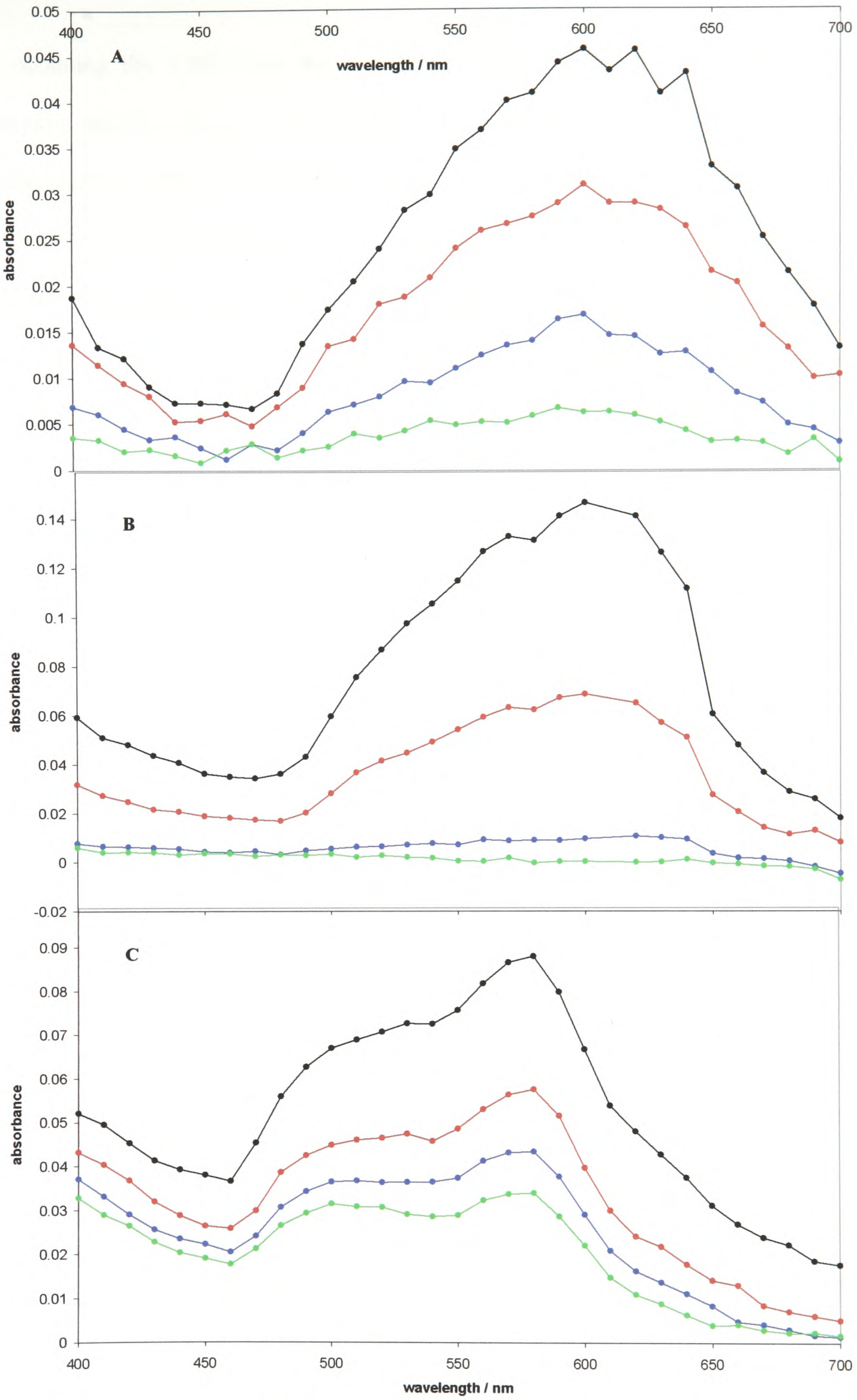


Figure 7.5: Transient absorption spectra of A) SDS/BT, B) BT/MeCN, and C) SDS/BT/CHD at (•) 240 ns, (•) 500 ns, (•) 1 μs, and (•) 2 μs after laser flash

On obtaining the YAG laser the wavelength study of SDS/BT was repeated to determine whether changing the excitation wavelength made any difference to the species formed. Figure 7.6 shows the 240 ns spectra for SDS/BT with both the XeCl and YAG lasers, normalised to their absorptions at 600 nm. The normalised spectra are shown as the absorption when the YAG laser is used is approximately five times larger than that achieved with the XeCl laser. The spectra with the two lasers show approximately the same shape, and that the absorption profiles are similar.

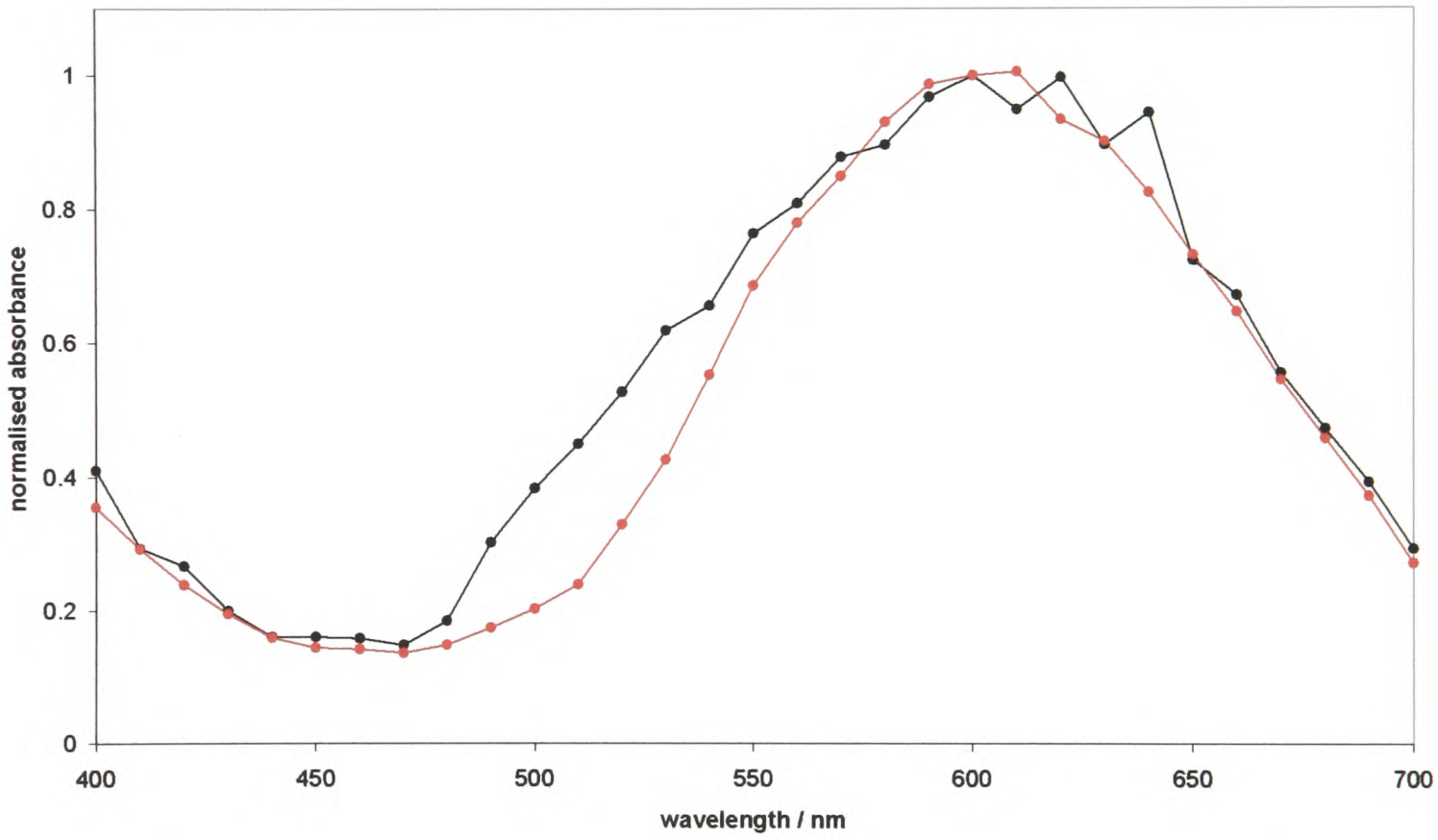


Figure 7.6: Normalised transient absorption spectra of SDS/BT at 240 ns after laser flash with excitation from (•) XeCl laser at 308 nm and, (•) YAG laser at 355 nm

If the spectrum obtained from MeCN is of the excited triplet of BT, then the similarity in the spectra could imply that no radical is formed in SDS/BT, and for radical formation a more efficient hydrogen donor, such as CHD, is needed. One way to investigate the existence of a radical pair is to look for MFEs, as they are only observed if a RP is present. Experiments were carried out with SDS/BT and using the

largest magnetic field that the Helmholtz coils would allow, no MFEs were seen. The MARY curves for this system also show a complete lack of any trends in the MFEs (see figure 7.7). The addition of a more efficient hydrogen donor to the system, CHD, resulted in MFEs that were observed in both the time curves (not shown) and MARY curves. Figure 7.7 shows a comparison between MARY curves of the SDS/BT and SDS/BT/CHD systems, which clearly demonstrates that only SDS/BT/CHD displays any MFEs.

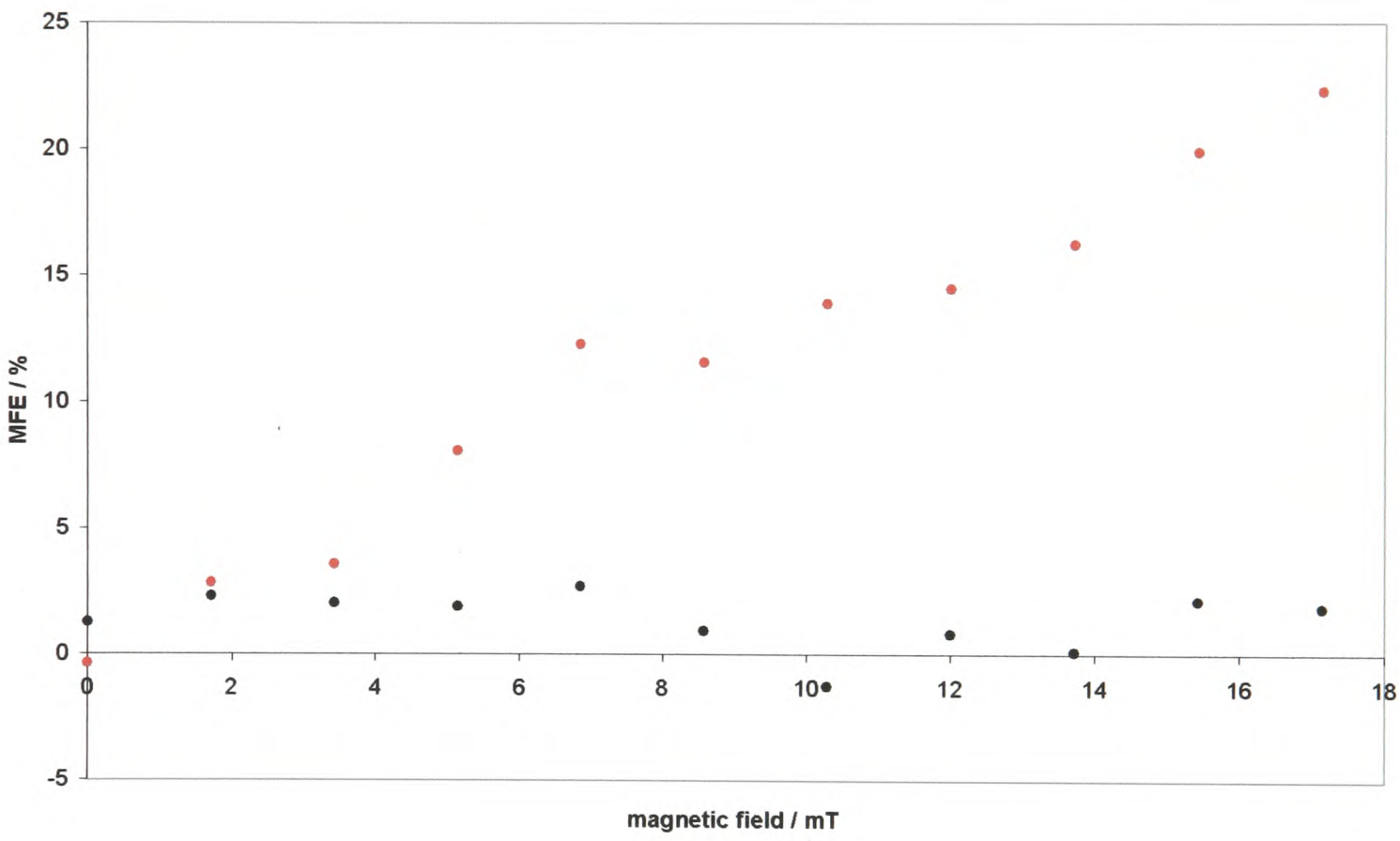


Figure 7.7: MARY curves of (•) SDS/BT (7.0) and (•) SDS/BT/CHD (6.2) (figures in brackets show EE / %)

The rate constant for hydrogen abstraction, and indeed whether any hydrogen abstraction occurs, depends on the energy and configuration of the excited triplet state of the hydrogen abstractor, as well as on the C-H bond strength of the hydrogen donor. Ketones which have lowest energy triplet states of n,π^* configuration (*e.g.* 4-fluoro-benzophenone and 3-theinyl-4'-pyridyl ketone) easily abstract hydrogen

atoms, due to their similarity to alkoxy radicals. However, ketones which have lowest energy triplet states of π,π^* configuration (*e.g.* 4-phenyl-benzophenone and 4-methoxy acetophenone) are less reactive towards hydrogen abstraction [3]. BP has a lowest energy triplet state of n,π^* configuration, whereas BT has a lowest energy triplet state of π,π^* configuration, and hence BT is a less efficient hydrogen abstractor than BP. This could provide an explanation for both the lack of MFEs with SDS/BT, and the similarity of transient absorption spectra displayed by SDS/BT and BT/MeCN. Since BT is a weaker hydrogen abstractor than BP the C-H bond strength in SDS might be too strong to allow abstraction by the excited triplet BT molecule. The strength of a C-H bond in a typical alkane molecule is around 425 kJ mol^{-1} [4], whereas the bond strength of the most labile C-H bond in CHD is 305 kJ mol^{-1} [5]. So CHD, with its weaker C-H bond strength, is available for hydrogen abstraction by BT, and hence explains why MFEs can be seen in the SDS/BT/CHD system. Any absorption in the SDS/BT system is due to the excited triplet and not to the $BTH^{\bullet}$ radical.

The transient absorption spectra provide further indication that only the BT triplet is present in the SDS/BT system. If the four curves from figure 7.5A are normalised to the maximum at 600 nm figure 7.8A is produced. Despite the noisy nature of the curves all four curves have approximately the same normalised absorption at all wavelengths, indicating the presence of only one absorbing species. Figure 7.8B shows the same for the four curves from SDS/BT/CHD (from figure 7.5C) normalised to the maximum at 580 nm. For this system it can be seen that the relative sizes of the absorption at different timescales change depending on the wavelength. At longer wavelengths (*i.e.* >580 nm) the 240 ns curve is largest, but at shorter wavelengths

(*i.e.* <580 nm) it is the 2 μs curve that is largest. This indicates a mixture of species, with peaks at different wavelengths. It is most likely due to absorption from both the excited triplet BT (λ_{max} ~600 nm) at short timescales and, the $BTH^{\bullet}$ radical at longer timescales.

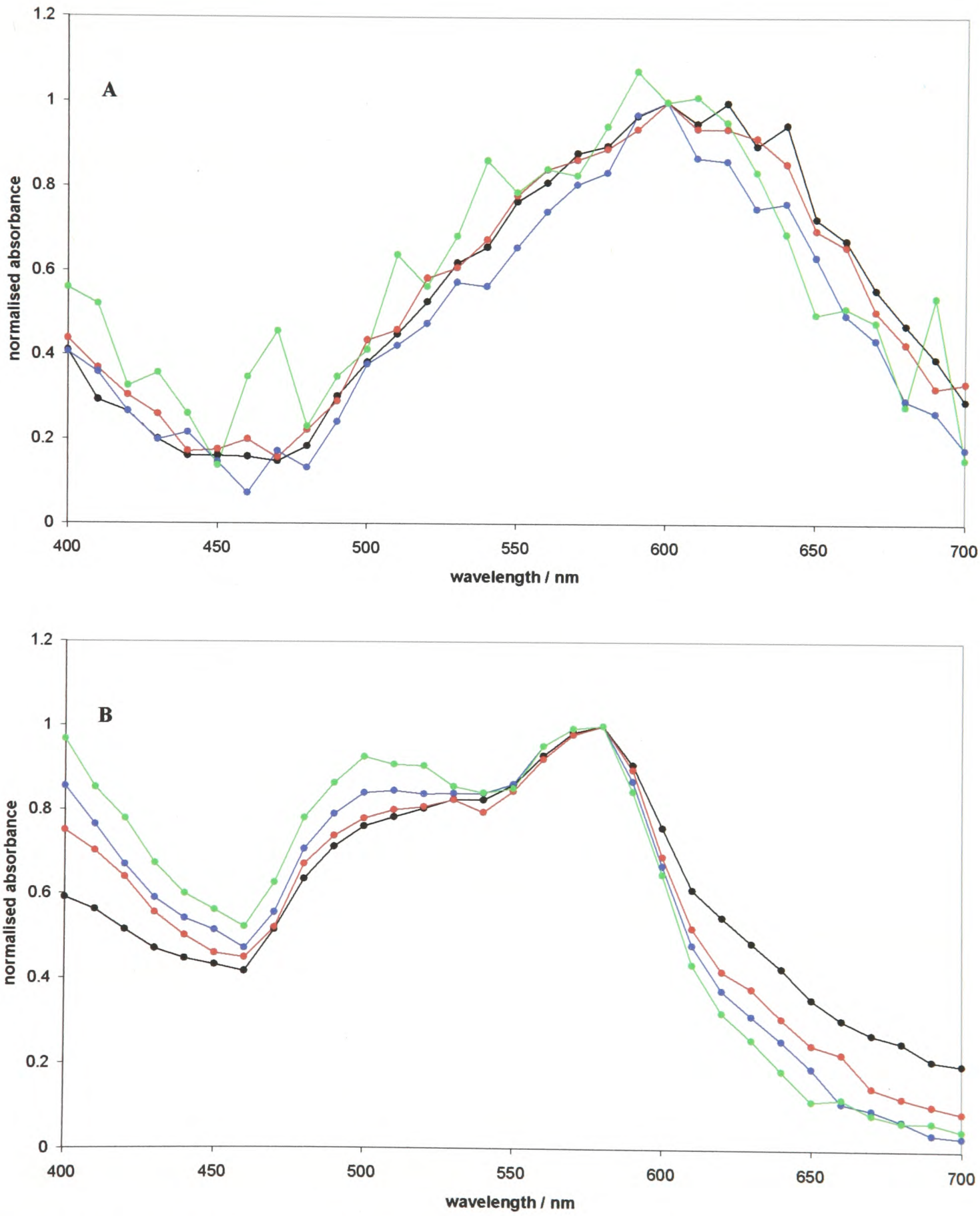


Figure 7.8: Normalised transient absorption spectra of A) SDS/BT and B) SDS/BT/CHD at (•) 240 ns, (•) 500 ns, (•) 1 μs, and (•) 2 μs after laser flash

7.2.3 Using BT with Lysophospholipids

Once it was established that MFEs could be seen in SDS micelles with BT, provided CHD was present, the next step was to investigate BT/CHD in LPC micelles. The concentration of LPC was 40 mM, as previously, and the concentration of BT was 2 mM, the same concentration as that of BP in previous experiments using LPC. The concentration of CHD was 30 mM in order to keep the BT:CHD ratio the same as that used in the SDS experiments in chapter four. With BT/CHD, as previously outlined with BP, the absorption signals obtained in LPC were much smaller than those in SDS, for the same concentration of probe molecule. However, crucially, LPC/BT/CHD with the YAG laser providing excitation light at 355 nm larger signals were obtained than from LPC/BP with the XeCl laser at 308 nm.

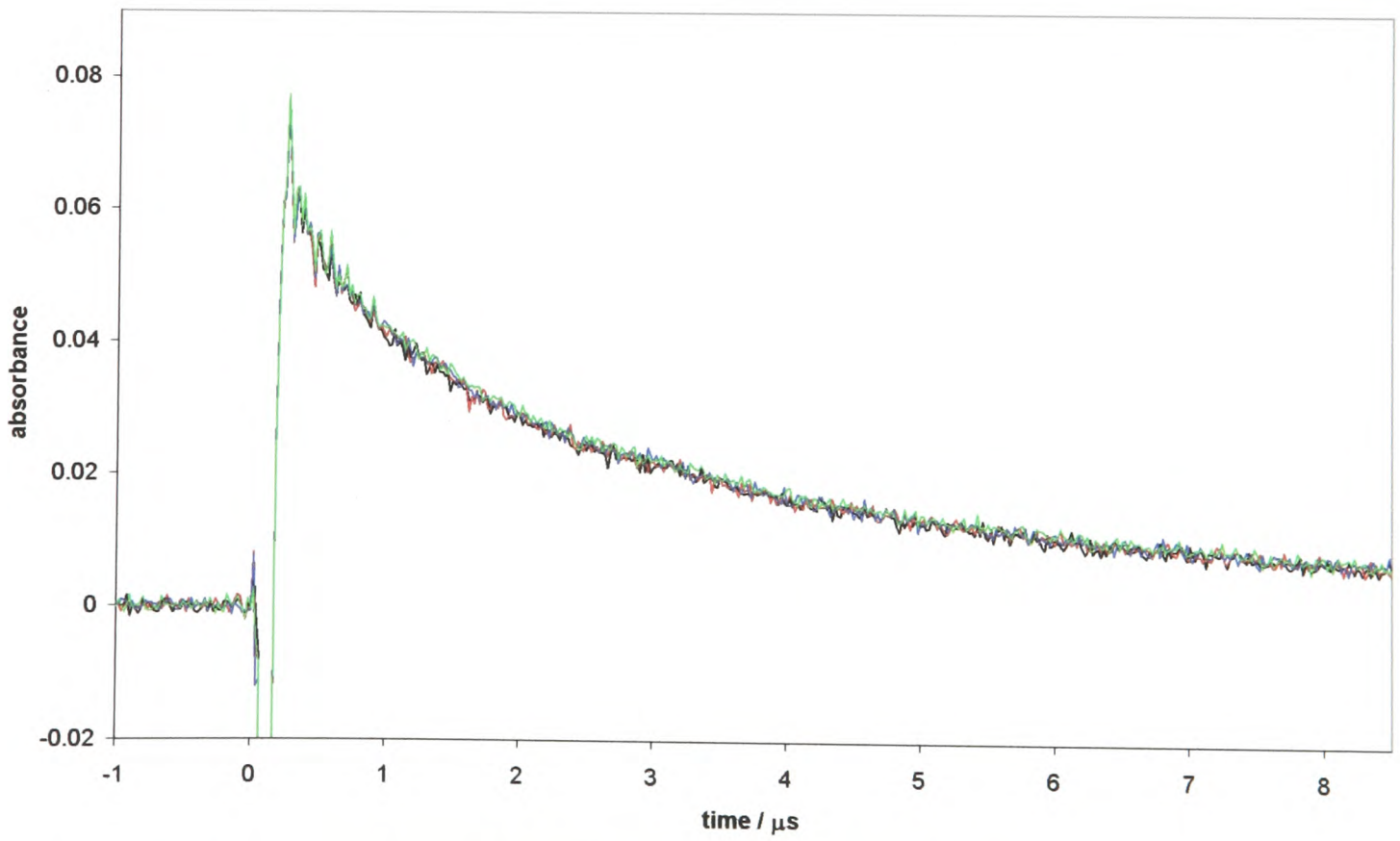


Figure 7.9: Time curves of LPC/BT/CHD at (•) 0 mT, (•) 4.3 mT, (•) 8.6 mT, and (•) 17.1 mT

It is not immediately obvious from the time curves whether a MFE is present (figure 7.9), however, manual calculation (see section 3.5.1) of the MFEs from the time curves shown in figure 7.9 gives MFEs of 1.4%, 2.2%, and 4.3% for magnetic field strengths of 4.3 mT, 8.6 mT, and 17.1 mT respectively.

The MARY curves obtained, whilst very noisy, suggest a general trend of increasing MFE with increasing magnetic field strength (figure 7.10). It is interesting to note that addition of CHD to the LPC/BT system does not result in mono-phasic kinetics as seen with the DTAC and DODAC systems. A separate geminate and F pair recombination period can be seen in the time curves of LPC/BT/CHD, however the MFEs are the smallest seen so far in this thesis.

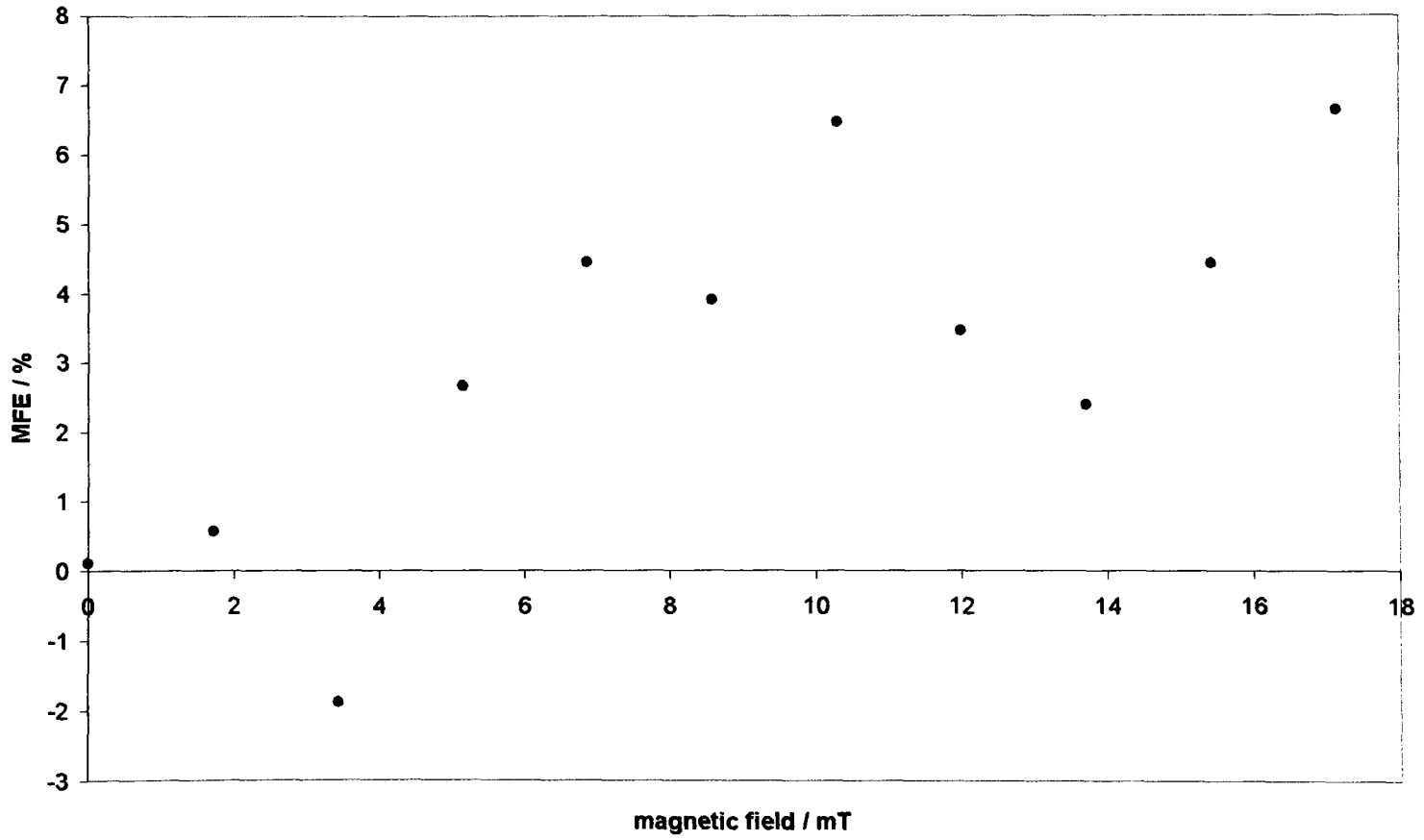
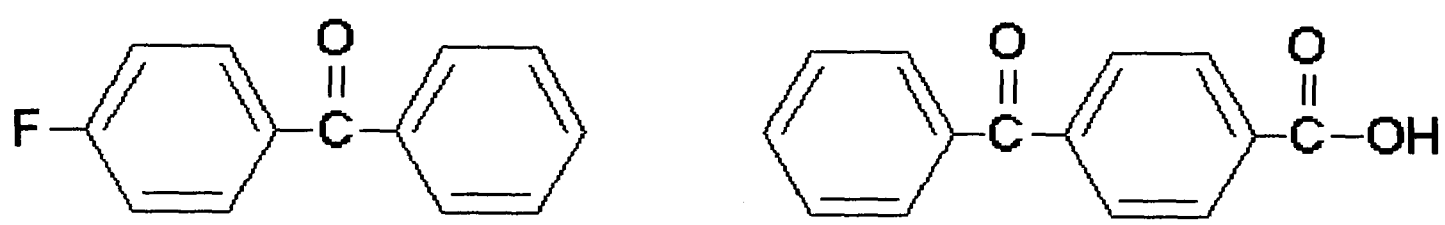


Figure 7.10: MARY curve of LPC/BT/CHD (EE 4.4%)

Whilst initial results with BT/CHD were promising it was observed that size of the absorbance signal decreased during the course of an experimental run, and from one

solution to the next, despite identical conditions. This was due to deposition of a white precipitate on the interior face of the cell nearest to the laser, blocking out the excitation light and causing the decrease in signal size. Removal of the deposit was difficult and time-consuming, requiring a strongly oxidising solution of potassium dichromate in concentrated sulphuric acid to be left in the cell overnight, or sometimes longer. This was impractical, and an alternative probe molecule was therefore required. Two possible replacements were investigated, both of which are BP derivatives, and are known to have n,π^* as the lowest energy triplet excited state, hence avoiding the necessity of an additional hydrogen donor to create a RP. These molecules are 4-fluorobenzophenone (BP-4F) and 4-benzoylbenzoic acid (BP-COOH), the structures of which are shown below in figure 7.11.



4-fluorobenzophenone 4-benzoylbenzoic acid

Figure 7.11: Structures of BP-COOH and BP-4F

7.2.4 Experiments with BP-4F and BP-COOH

The UV/vis spectra of the ground state molecules in SDS revealed BP-COOH to be the most promising replacement for BT, as it has a larger absorption at 355 nm (see figure 7.12). However, wavelength studies were also carried out on both BP-COOH and BP-4F in SDS (using the YAG laser with 355 nm excitation) to find which gave

the largest transient absorption signal. The transient spectra at four different timescales are shown in figure 7.13 for BP-COOH and BP-4F.

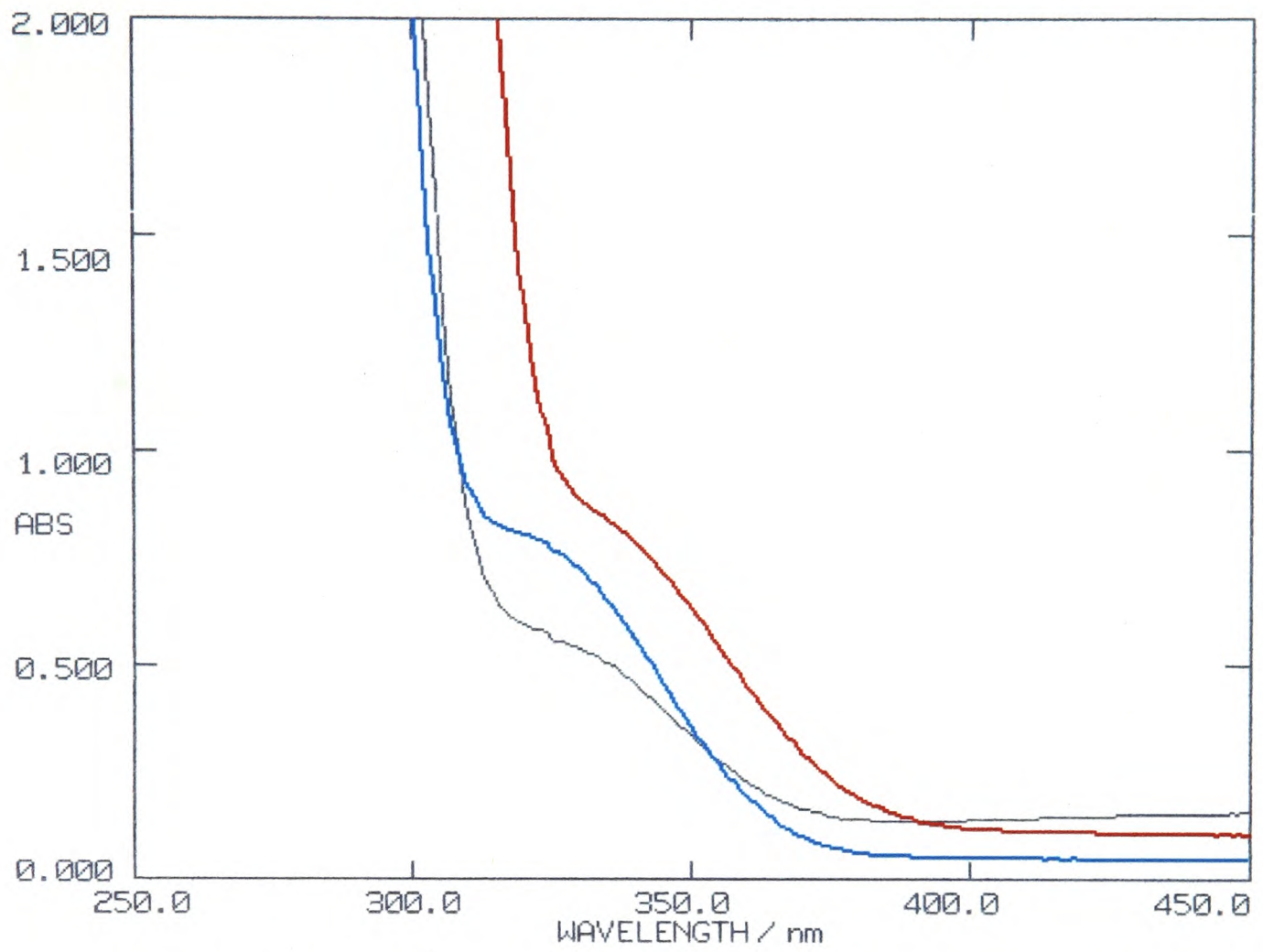
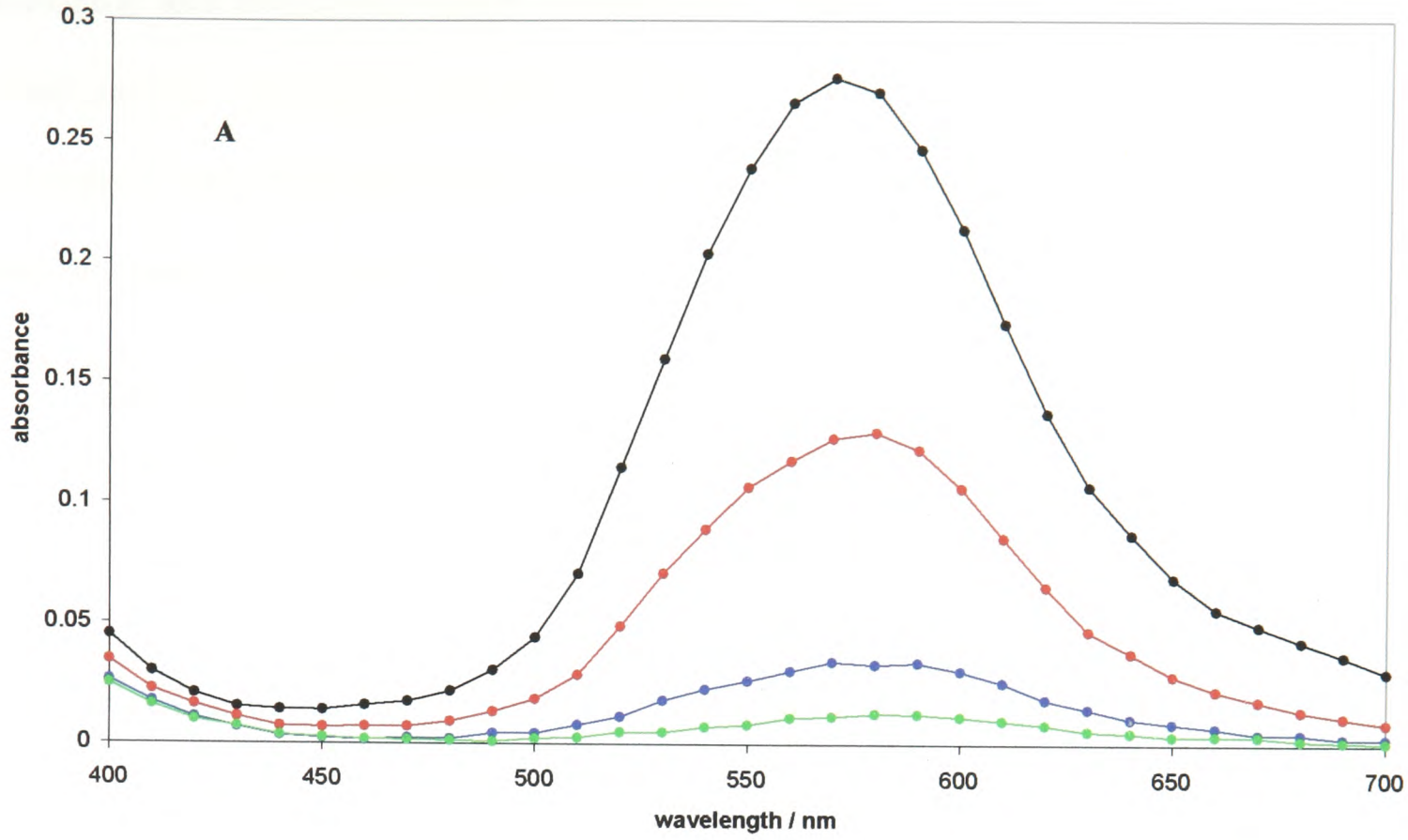


Figure 7.12: UV/vis absorption spectra of (•) SDS/BP, (•) SDS/BP-COOH, and (•) SDS/BP-4F

There are several differences between the two spectra; first is the position of the absorption peak. The absorption maximum in BP-COOH is located around 570 nm, whereas the BP-4F peak is at 530 nm. The second, and possibly more important, difference is the size of the absorption signal in the two systems. In BP-4F the absorption after 240 ns at 530 nm is around 0.13, but with BP-COOH after 240 ns at 570 nm the absorption is around 0.28, over twice as large. The final difference is the shape of the two peaks; the BP-4F is a sharper peak, with a slight shoulder at around 610 nm, compared to the broader, shoulder-less BP-COOH.



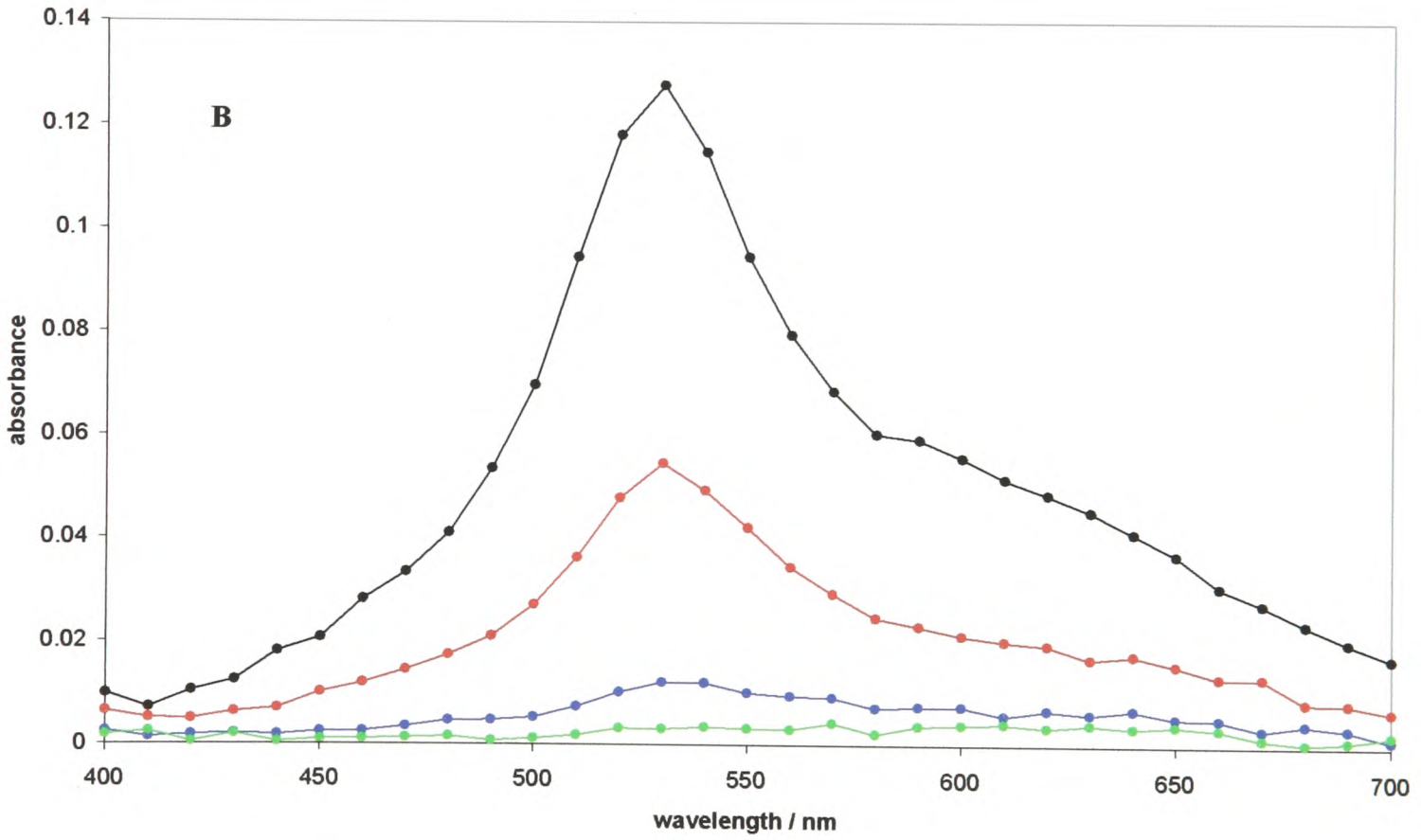


Figure 7.13: Transient absorption spectra of A) SDS/BP-COOH, and B) SDS/BP-4F at (•) 240 ns, (•) 500 ns, (•) 1 μs, and (•) 2 μs after laser flash

The transient absorption spectra were used to choose a suitable wavelength for the monochromator to investigate the MFEs of the two probe molecules in SDS solution. As the transient absorption spectra in SDS show overlapping signals from the triplet

molecular and the radical species, wavelength studies were carried out in MeCN to determine the wavelength of triplet absorption maxima. Figure 7.14 shows the spectra obtained in MeCN for BP-COOH, alongside the wavelength study in SDS. This shows that the triplet absorption maximum occurs at shorter wavelengths than the peak in SDS, implying that the maximum due to the radical occurs at longer wavelengths. This is also the case for BP-4F (not shown).

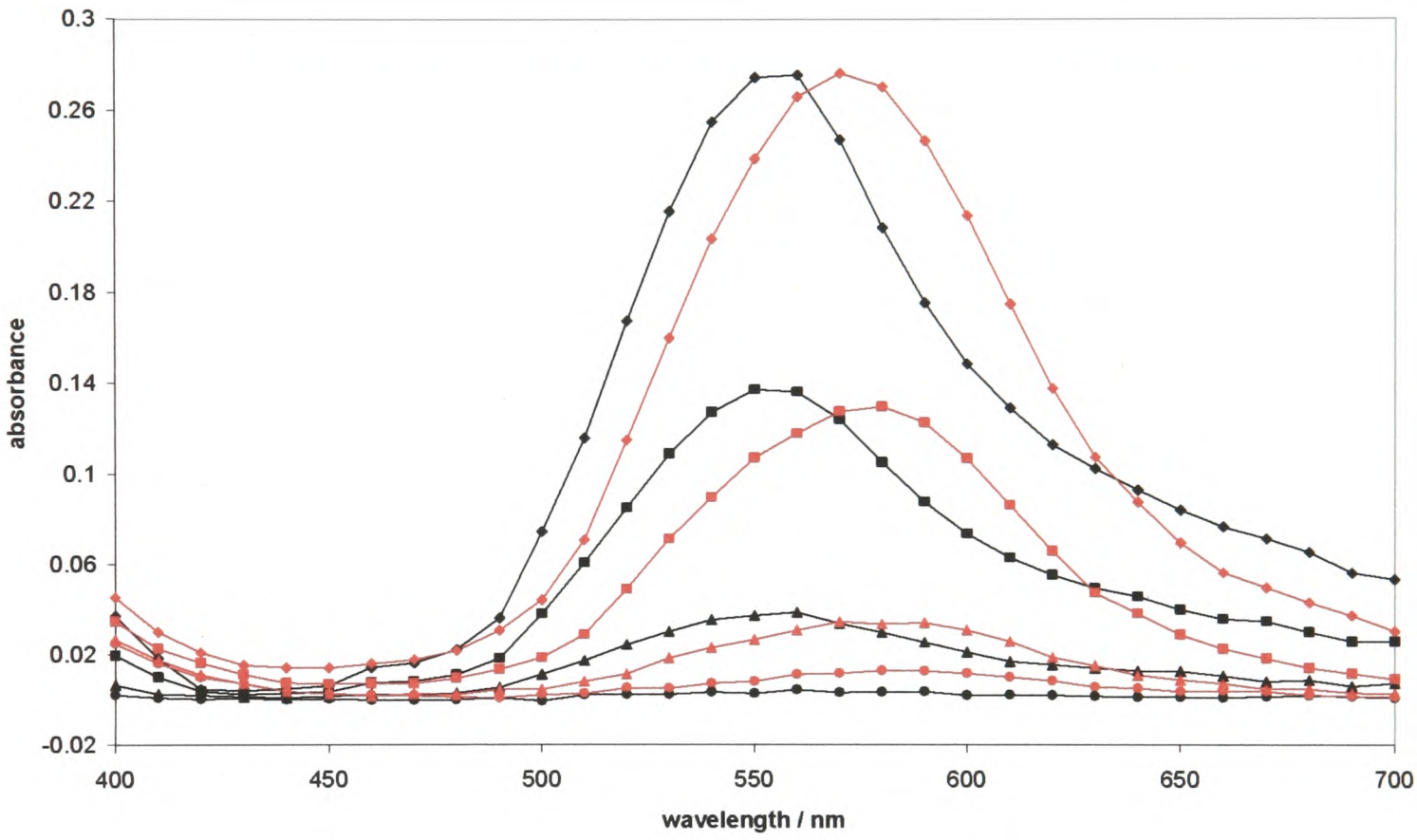
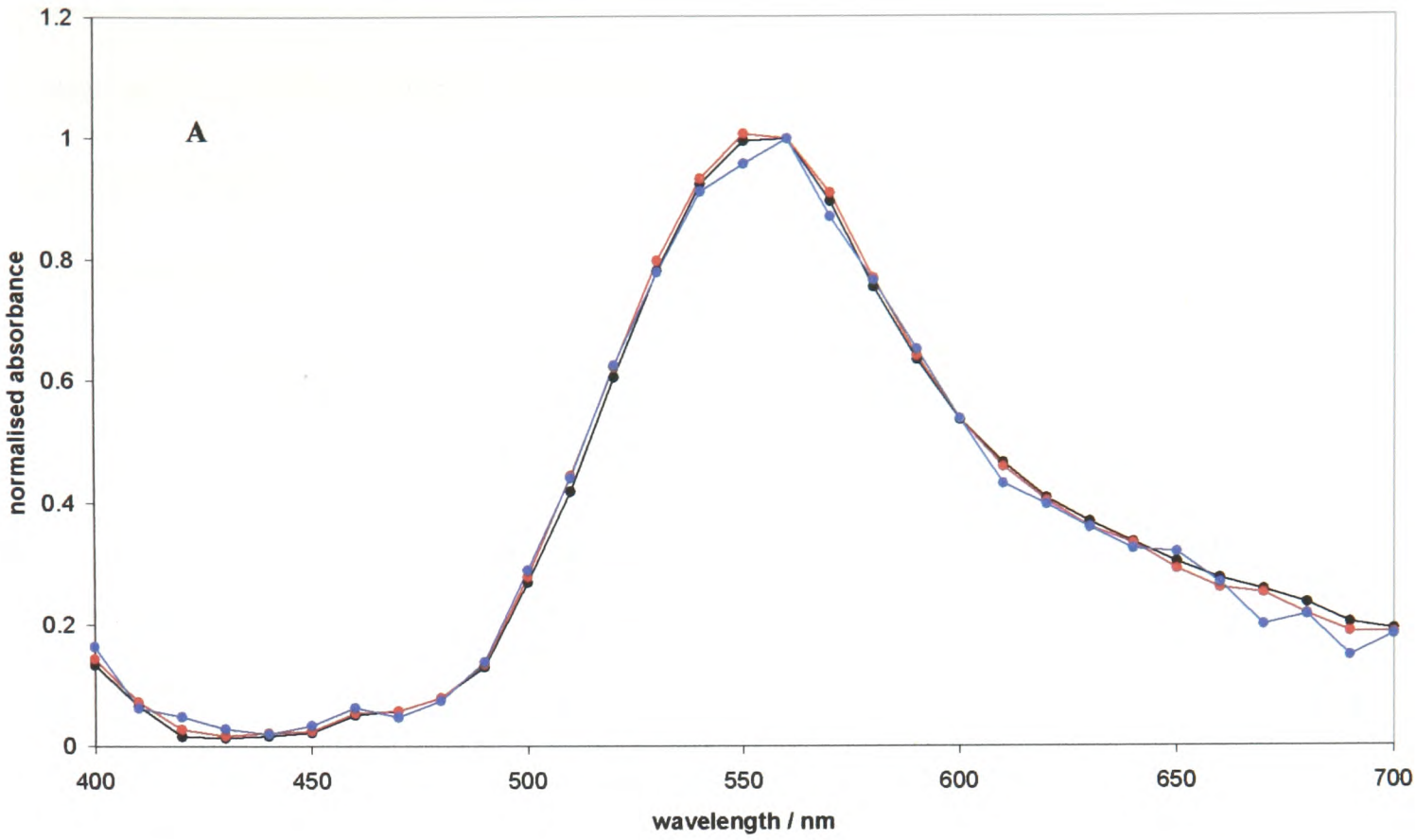


Figure 7.14: Transient absorption spectra of (+) BP-COOH/MeCN, and (+) SDS/BP-COOH at (♦/♦) 240 ns, (■/■) 500 ns, (▲/▲) 1 μs, and (●/●) 2 μs after laser flash

Whilst on initial inspection the spectra of the two solutions look similar, differences can be observed. For the three shortest timescales the size of the absorption is similar at the peak wavelengths, however at 2 μs the SDS signal exceeds the MeCN signal. The other difference is only obvious when the spectra are normalised so that each of the timescales has a maximum of unity at the absorption peak, as was seen in figure 7.8.



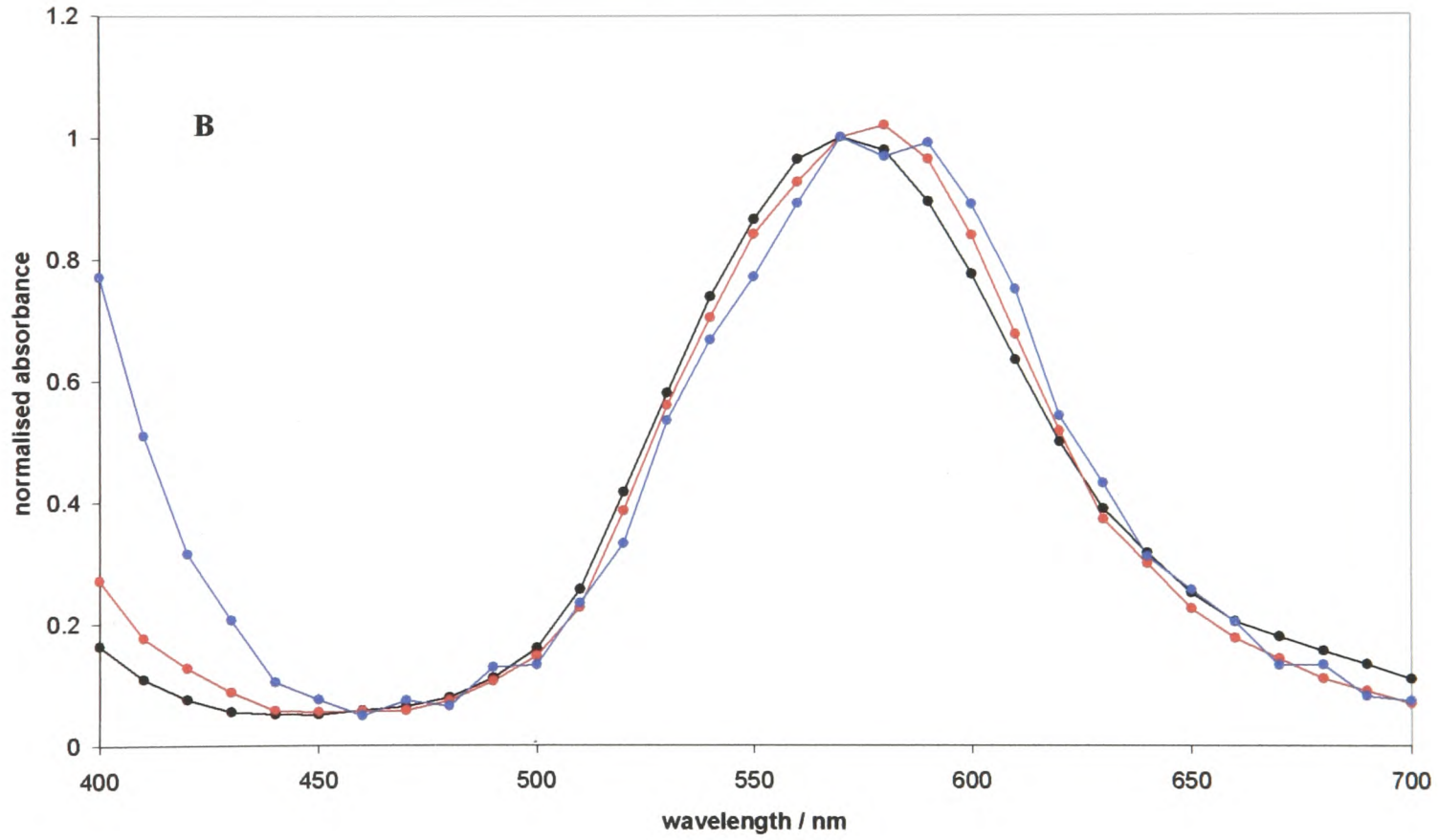


Figure 7.15: Normalised transient absorption spectra of A) BP-COOH/MeCN and B) SDS/BP-COOH at (•) 240 ns, (•) 500 ns, and (•) 1μs after laser flash

In MeCN when the first three timescales are normalised to 560 nm the curves show almost identical absorptions at all wavelengths measured, suggesting identical kinetics at all wavelengths and hence the same species (figure 7.15A). However when this

process is repeated for SDS/BP-COOH and the first three timescales are normalised to the maximum at 570 nm (figure 7.15B) the peak shifts, albeit only a small amount, to longer wavelengths at later timescales, indicating a mixture of transient species with different lifetimes. As the triplet absorbs at shorter wavelengths the species at longer wavelengths is probably the ketyl radical, so to maximise the ketyl:triplet ratio it was decided to investigate SDS/BP-COOH at 580 nm and SDS/BP-4F at 540 nm.

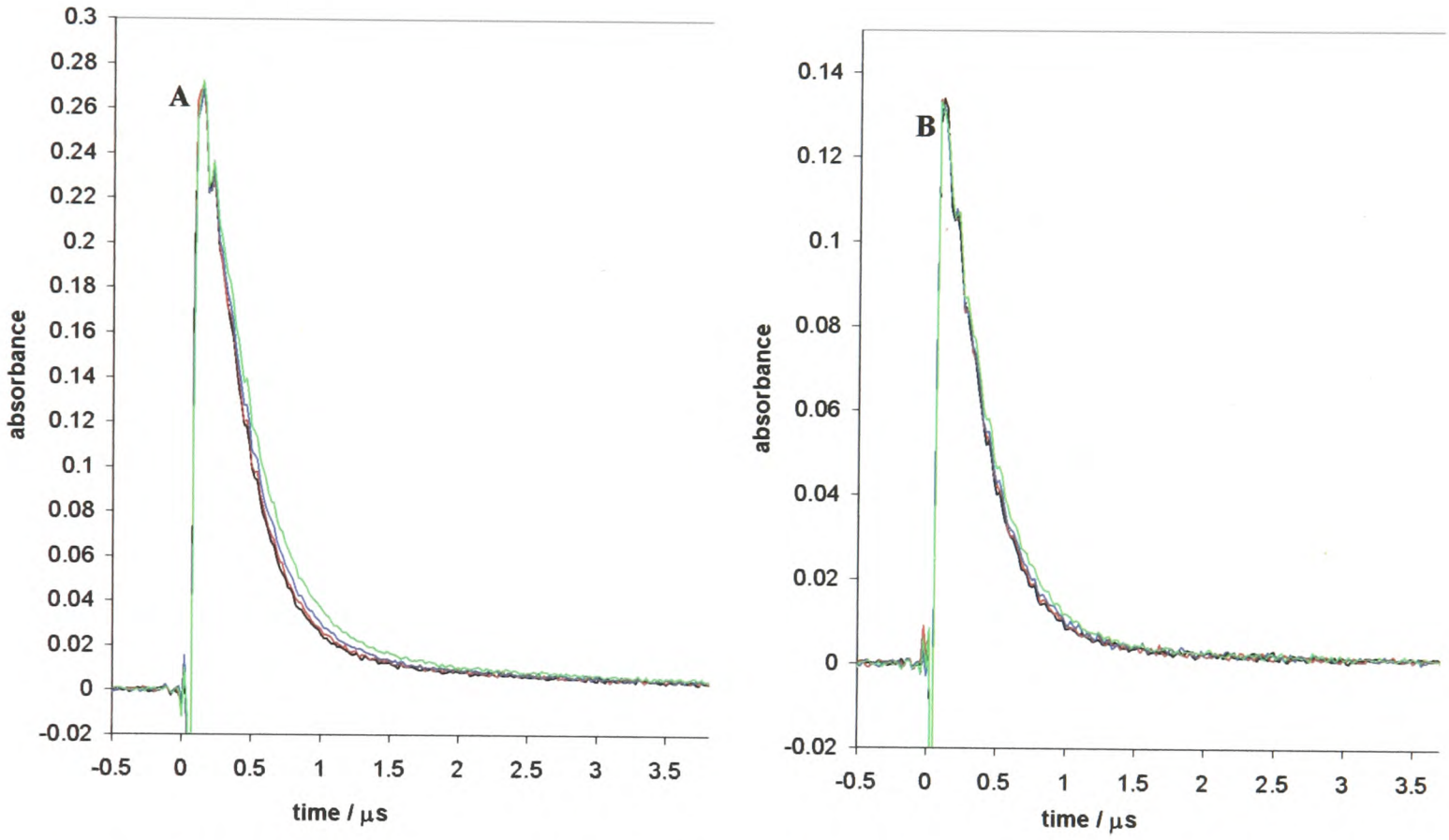


Figure 7.16: Time curves of A) SDS/BP-COOH, and B) SDS/BP-4F at (•) 0 mT, (•) 4.3 mT, (•) 8.6 mT, and (•) 17.1 mT

Experiments were carried out using these wavelengths to investigate the MFEs on the two systems. The MFEs on the time curves of both SDS/BP-COOH and SDS/BP-4F are shown in figure 7.16, concentrating on the first few microseconds following the laser pulse. Field effects can be seen in both systems, but on initial inspection the MFEs in SDS/BP-COOH seem to be larger. Manual calculation of the MFEs of the 17.1 mT curves gives 18% for BP-COOH and 8.7% for BP-4F.

7.2.5 Solubility of BP-COOH

With the carboxylic acid functional group BP-COOH is expected to be more soluble in water than BP. In addition this solubility is likely to be pH dependent as at higher values of pH the COOH group will be ionised to COO^-. The table below gives values for the solubility of BP-COOH at various pH values, and also for BP, whose solubility does not vary across the pH range indicated in table 7.2.

Molecule	pH	Solubility / mol dm^{-3}	Reference
BP-COOH	1	< 0.01	[6]
BP-COOH	4	< 0.01	[6]
BP-COOH	7	0.1 – 1	[6]
BP-COOH	8	> 1	[6]
BP-COOH	10	> 1	[6]
BP	-	4.6×10^{-4}	[7]

Table 7.2: Solubility of BP-COOH and BP at 25 ^{0}C in pure water

If the BP-COOH is resident in the water phase rather than inside the micelles then the geminate lifetime of the radical pair will be much shorter, and so the effects of a weak strength magnetic field would be expected to be greatly reduced. If a high proportion of the BP-COOH is resident in the water phase then any change in micelle properties will be less obvious, as a smaller proportion of RP will be affected.

To determine the effect of pH on BP-COOH in SDS micelles a series of experiments was undertaken using buffered solutions to hold the pH at a constant value. To obtain a wide range of pH values two buffer systems were used; a sodium phosphate buffer with pH range 5.8 to 8.0, and sodium phosphate-citrate buffer with pH range 2.6 to 7.0. Figure 7.17 shows zero field time curves at four different pH values. The curves obtained at pH values of 6 and 7.8 used the phosphate buffer, the curve at pH 3.2 used

the phosphate-citrate buffer, and that at pH 5.3 a non-buffered SDS/BP-COOH solution.

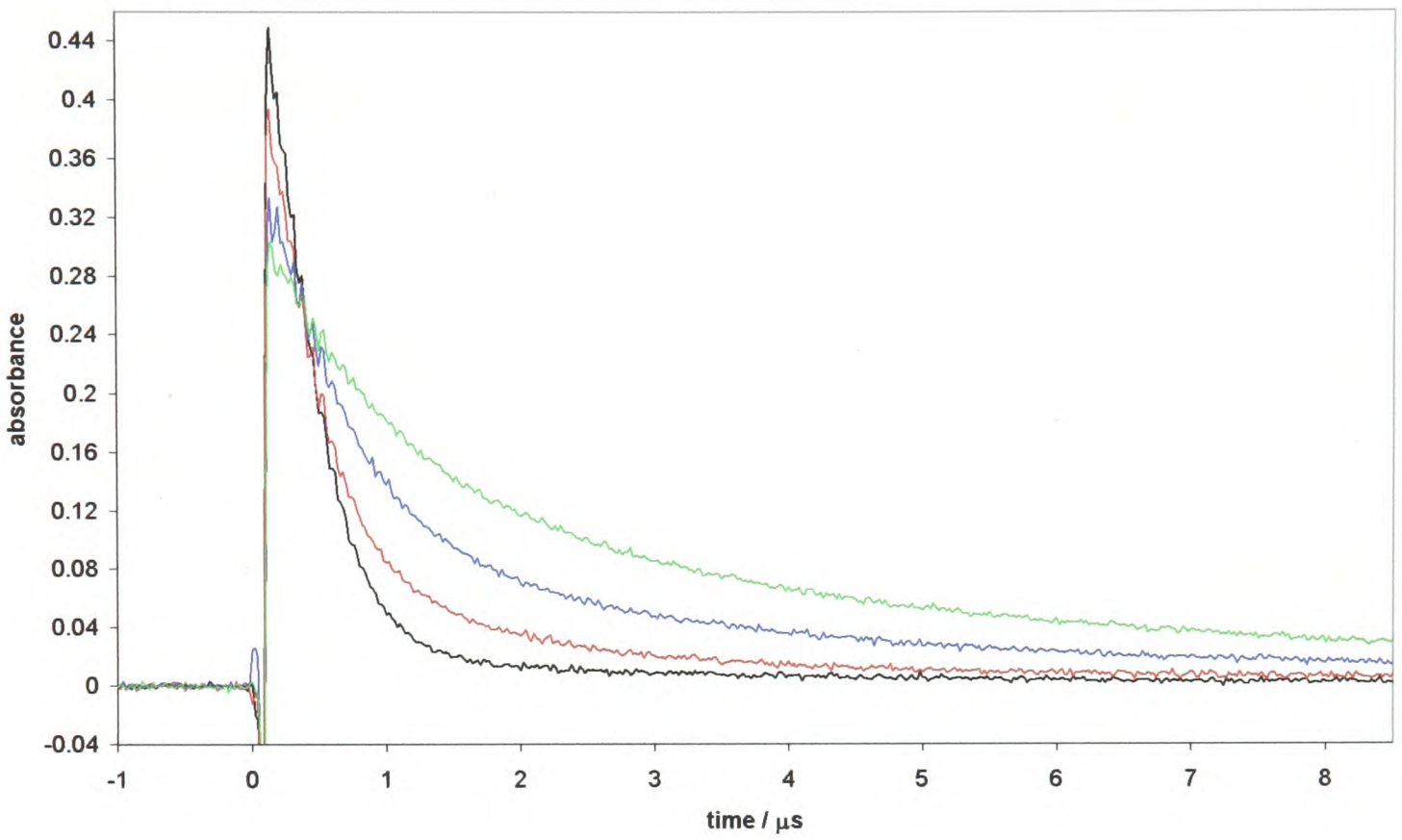


Figure 7.17: Zero field time curves of SDS/BP-COOH at (•) pH 3.2, (•) pH 5.3, (•) pH 6.0, and (•) pH 7.8

There are two trends shown in this diagram. The first is the increase in lifetime of the signal with increasing pH, and the second is the decrease in initial peak size with increasing pH. A longer lived signal means that the rate of radical recombination is slower at the larger pH values, this implies a greater rate of escape from the geminate RP, an increase in the number of F pairs, and hence a slower rate of radical recombination. Experiments on BP-COOH in pure water showed that there is no measurable hydrogen abstraction occurring, hence the longer lived signal means that the rate of escape from the micelle must be faster at higher pH. If the solubility of the BP-COOH molecule increases with pH, then this implies the solubility of the BPH-

$COOH^{\bullet}$ ketyl radical also increases with increasing pH, which would be consistent with an increase in the escape rate of this radical from the micelle.

The decrease in initial peak size with increasing pH value can be explained by considering the solubility of the BP-COOH species. As the pH is increased the solubility of BP-COOH in water also increases, leading to a larger proportion of the BP-COOH molecules being located outside the micelles. Hydrogen abstraction, and hence radical formation, can only occur in the interior of the micelle, therefore the more soluble the BP-COOH molecules are in water the fewer radicals are formed, and the smaller the absorption signal.

Figure 7.18 shows the effect of pH on the MARY curves at the four different pH values. As expected the size of the MFE decreases with increasing pH, for the reason discussed above.

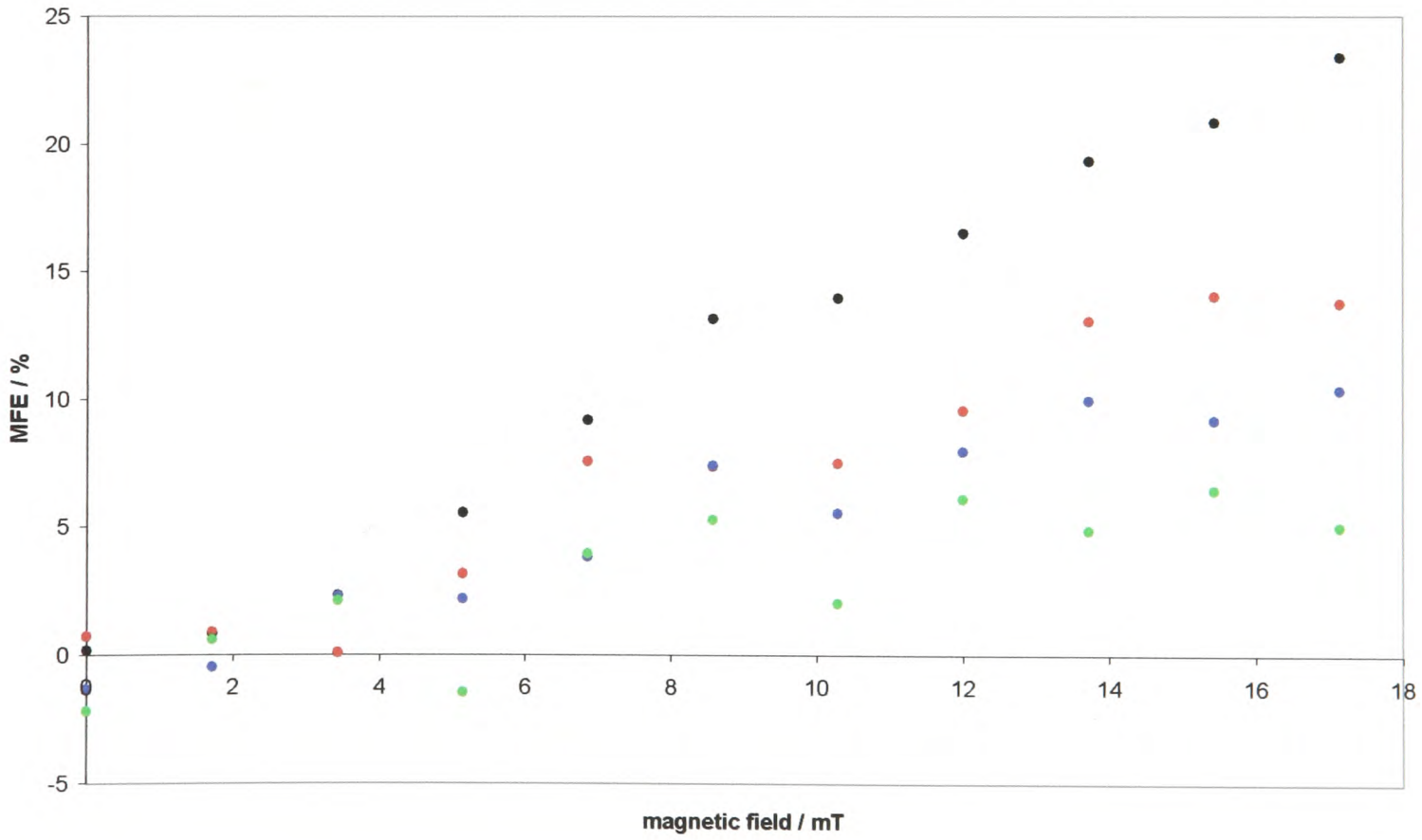


Figure 7.18: MARY curves of SDS/BP-COOH at (•) pH 3.2 (2.5), (•) pH 5.3 (6.0), (•) pH 6.0 (3.6), and (•) pH 7.8 (4.9) (figures in brackets show EE / %)

To make sure that these effects are due to pH and not the effect of a change in ionic strength the experiment was repeated with NaCl at two different concentrations to give the same concentrations, and hence ionic strengths, of the buffers. These experiments showed no change in either the time curves or MARY curves with increasing salt concentration. It has previously been shown that the presence of NaCl can have an effect on both the time curves and MARY curves [8,9], as it changes the properties of the micelle. Increasing salt concentration causes a decrease in the CMC and an increase in the aggregation number, and hence the size of ionic micelles. However, at the concentrations used in these experiments this effect is very small, and causes no observable difference in the signals. The effect of buffer composition was also studied by conducting an experiment with the phosphate-citrate buffer at pH 6 to ensure that buffer identity had no effect on the results. Both the time curves and MARY curves obtained were identical for both species of buffer (not shown).

The use of buffers has shown that even though a proportion of the BP-COOH is resident in the water phase at the non-buffered pH of 5.3, there is still enough inside the micelles to see a significant MFE.

7.3 Low Field Effects with BP-COOH

From the experiments detailed in section 7.2 it was decided to use BP-COOH as the new probe molecule for further experiments with LPC. It does not display the fouling of the cell seen when BT/CHD is used, and gives both greater absorption in the time curves and larger MFEs than BP-4F. BP-COOH also has the advantage over BT/CHD that LPC/BP-COOH is a simpler, two component system, and so has the option of

addition of CHD, or some other hydrogen donor, to investigate the effect of a faster rate of radical formation.

In all the experiments so far testing the BP replacements the whole range of the Helmholtz coils was used, with no particular attention paid to the LFE region of the magnetic field. Before investigating LFEs in LPC, and other structures it was crucial to demonstrate that LFEs can be seen with BP-COOH in SDS micelles. Experiments were conducted with SDS/BP-COOH concentrating on the LFE region, from 0 mT to 3.5 mT. Figure 7.19 shows a MARY curve obtained from averaging 19 separate MARY curves (*i.e.* 912 averages per point), which shows no real indication of LFEs in this system.

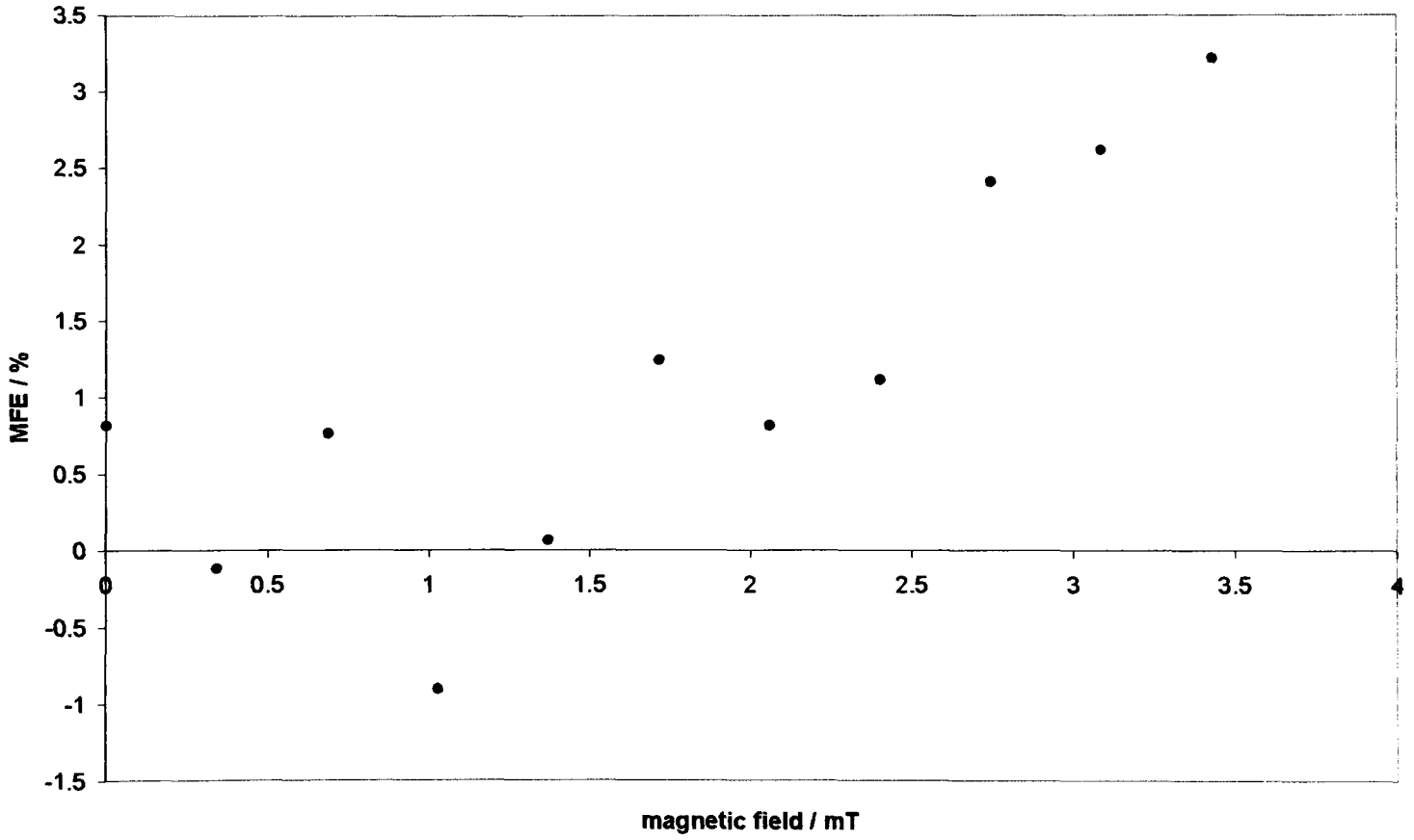


Figure 7.19: MARY curve of SDS/BP-COOH concentrating on LFE region (EE 6.9%)

Time curves were also taken at 0, 0.6, and 8.6 mT, with 384 averages at each magnetic field strength, and are shown in figure 7.20. A clear difference can be seen

between the curve at 8.6 mT and the other two curves, but there is no observable difference between the curves at 0 and 0.6 mT.

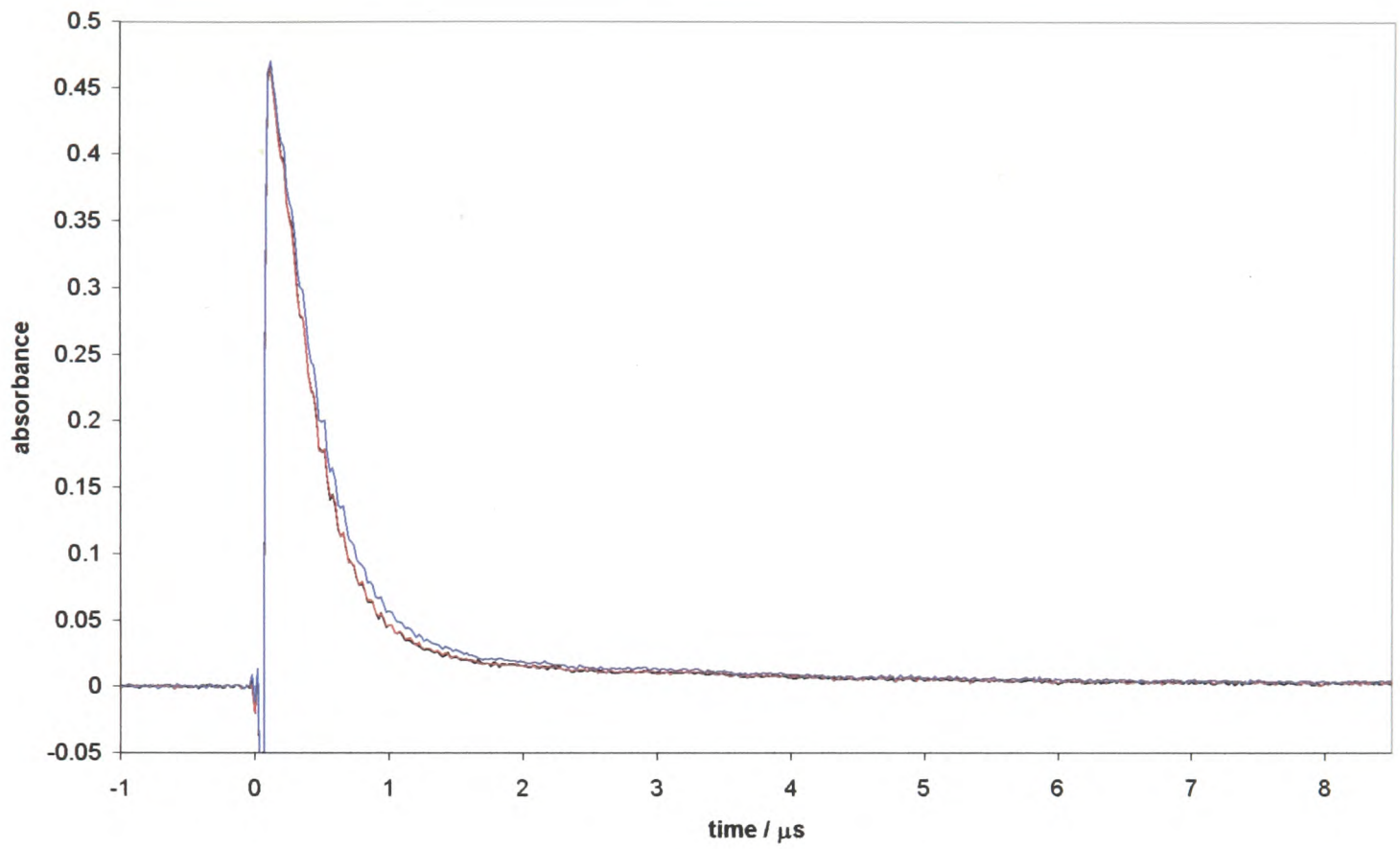


Figure 7.20: Time curves of SDS/BP-COOH at (●) 0 mT, (●) 0.6 mT, and (●) 8.6 mT

Adding the -COOH group to BP changes the hyperfine couplings of the BPH-COOH$^{\bullet}$ ketyl radical, and this could be the cause of the absence of the LFE. There are no reported HFC for the BPH-COOH$^{\bullet}$ radical in the literature, but two analogues between BPH$^{\bullet}$ and BPH-COOH$^{\bullet}$ are shown in table 7.3, below. The couplings in the BPH$^{\bullet}$ ketyl radical are also added for comparison.

For the benzyl and α-trimethylsilyl benzyl systems adding the –COOH (or –COO^{-}) group does not change the hyperfine couplings by a significant amount, as can be seen by the difference in average hyperfine coupling, a_k.

Radical	HFC / mT	$\langle a_k \rangle$ / mT	Ref.
Benzyl radical Ph – $CH_2^\bullet$	2H ($CH_2^\bullet$): 1.636; 2H (o): 0.514; 2H (m): 0.175; H (p): 0.614	2.18	[10]
^-O_2C – Ph – $CH_2^\bullet$	2H ($CH_2^\bullet$): 1.576; 2H (o): 0.507; 2H (m): 0.177	2.04	[11]
α-trimethylsilyl benzyl radical Ph – $CH^\bullet SiMe_3$	H ($CH^\bullet$): 1.50; 2H (o): 0.50; 2H (m): 0.15; H (p): 0.60	1.54	[12]
HO_2C – Ph – $CH^\bullet SiMe_3$	H ($CH^\bullet$): 1.50; 2H (o): 0.50; 2H (m): 0.15	1.45	[12]
BPH$^\bullet$ ketyl radical Ph_2 – $C^\bullet$(OH)	H (OH): 0.291; 4H (o): 0.323; 4H (m): 0.123; 2H (p): 0.364	0.79	[13]

Table 7.3: HFC in BPH$^\bullet$ and BPH-COOH$^\bullet$ analogues

This suggests that the change in size of the MFEs, and lack of a LFE, between BP and BP-COOH is not caused by the change in hyperfine couplings, but by the change of some other property of the system. The –COOH group changes the shape of the molecule, so the dynamics inside the micelle will probably be altered, and the difference in solubility caused by the carboxylic acid group will not only affect the escape rate of the radical, but could also change the location of the probe molecule inside the micelle.

The lack of a LFE in the SDS/BP-COOH system does not rule out the possibility of seeing LFEs in lysophospholipids or phospholipids with BP-COOH, indeed the different confinement conditions in the LPC micelles, or phospholipid vesicles could be a potential factor in favouring LFEs as compared with SDS micelles. The next section concentrates on investigating LPC with BP-COOH under different conditions of temperature and BP-COOH concentration.

7.4 BP-COOH in LPC

7.4.1 Initial Experiments

The first experiment with LPC/BP-COOH was carried out with LPC at a concentration of 40 mM and BP-COOH at 2 mM, to compare with the work done earlier with LPC/BT/CHD. Figure 7.21 shows zero field time curves for both BT/CHD and BP-COOH in LPC. Although the initial absorbance peak is almost identical for both systems, the shapes of the two curves are very different. The BT/CHD curve has a faster initial decay rate, but by the end of the measurement period the BP-COOH curve shows a smaller concentration of radicals. However, despite this difference both decay curves follow bi-phasic kinetics.

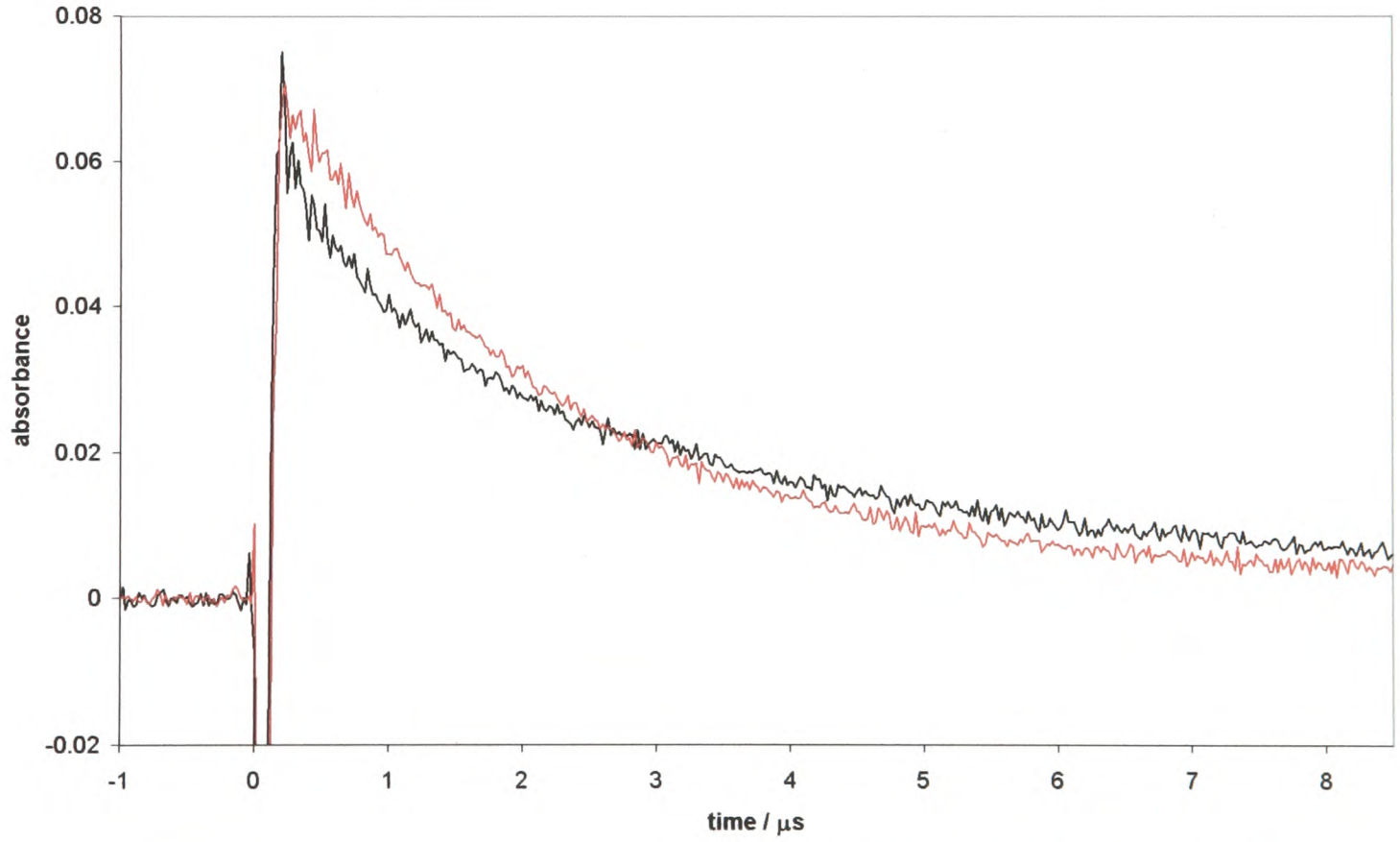


Figure 7.21: Zero field time curves of (•) LPC/BT/CHD, and (•) LPC/BP-COOH

Table 7.4 shows lifetime data for the two systems, calculated from the data in figure 7.21. The data confirms that the LPC/BT/CHD has a much faster initial decay rate as

seen by the shorter times for $T_{3/4}$ and $T_{1/2}$. However, by the time the signals have decayed to a quarter of their initial height they have crossed over, and LPC/BP-COOH has a shorter $T_{1/4}$.

System	$T_{3/4}$ / μs	$T_{1/2}$ / μs	$T_{1/4}$ / μs
LPC/BT/CHD	0.16	1.02	3.30
LPC/BP-COOH	0.58	1.48	3.16

Table 7.4: Lifetime data for LPC/BT/CHD and LPC/BP-COOH

The MFEs are slightly more obvious in the time curves of LPC/BP-COOH than in those of LPC/BT/CHD. Figure 7.22 shows time curves for LPC/BP-COOH at four different magnetic field strengths, and although the difference is hard to see, the manually calculated MFE for 17.1 mT is 6.5%. The MARY curves also show larger, and less noisy MFEs than with BT/CHD, figure 7.23 shows a MARY curve comprised of 15 separate MARY curves (each of 48 averages per point), and a clear trend in the MFEs can be seen, with the size of the MFE increasing with the magnetic field.

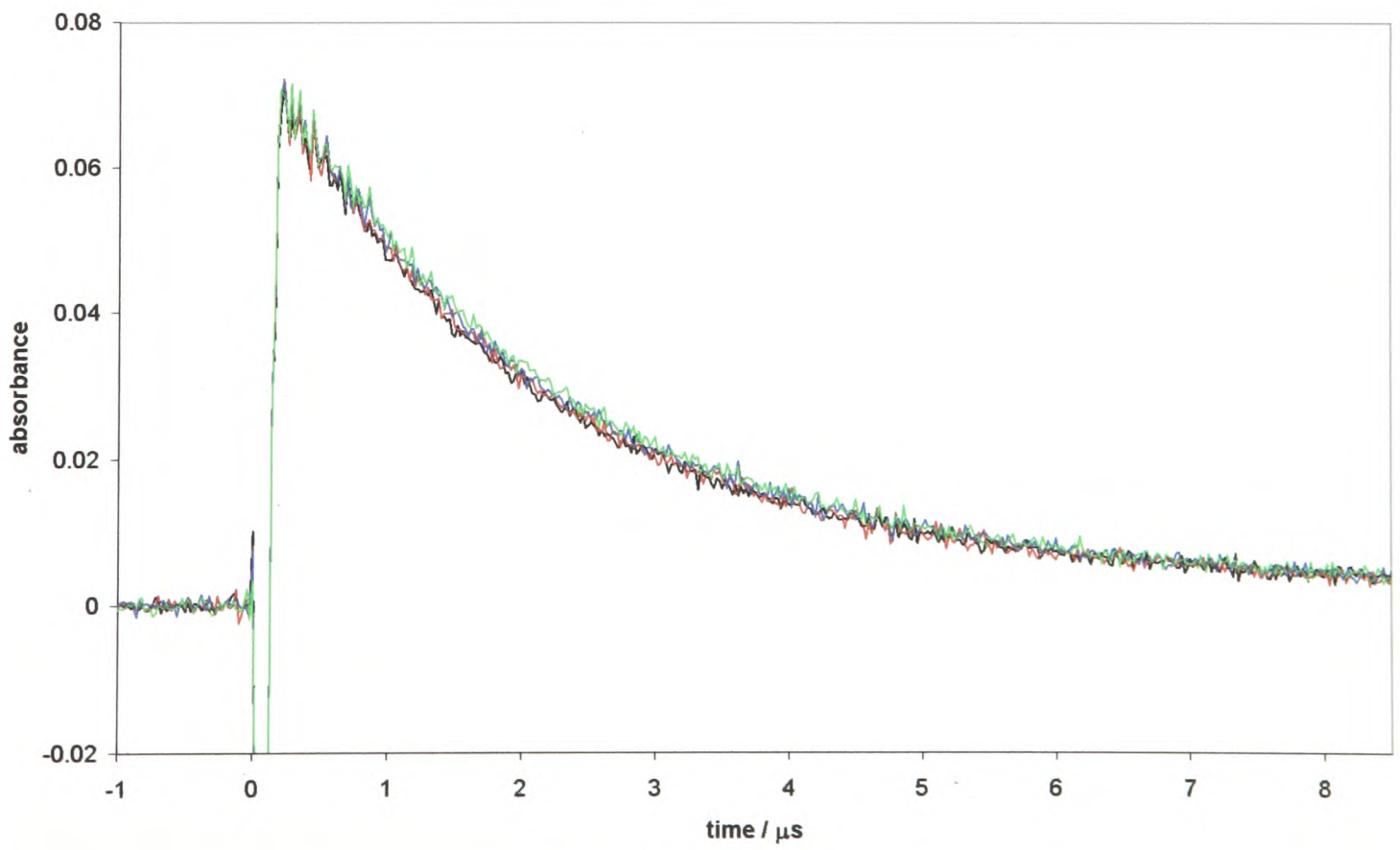


Figure 7.22: Time curves of LPC/BP-COOH at (•) 0 mT, (•) 4.3 mT, (•) 8.6 mT, and (•) 17.1 mT

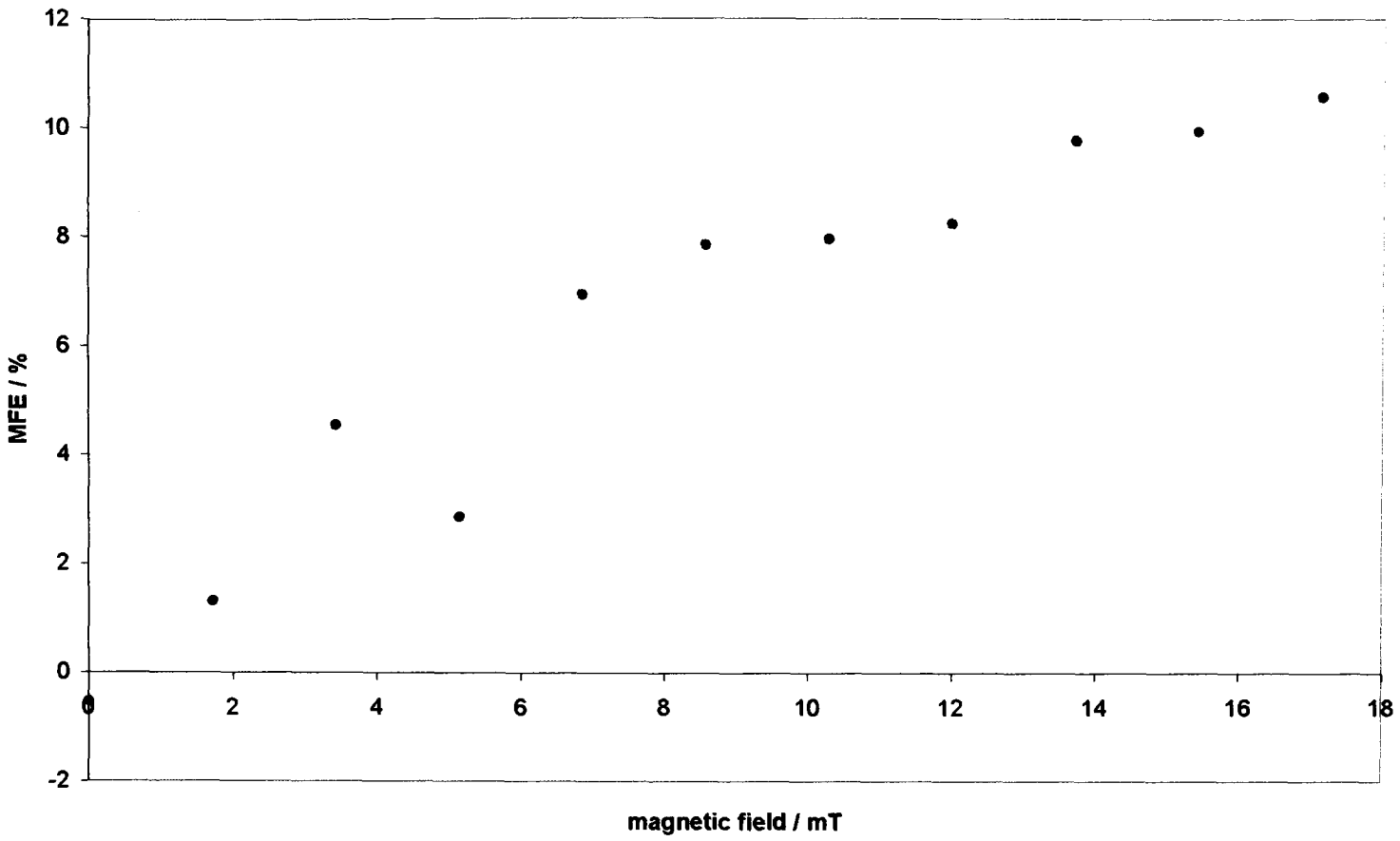


Figure 7.23: MARY curve of LPC/BP-COOH (EE 5.4%)

7.4.2 BP-COOH Concentration and Temperature Effects

In SDS micelles the ratio of surfactant:BP, or surfactant:BP-COOH, is much larger than in the LPC micelles. Also the number of BP-COOH molecules per micelle is different in SDS and LPC as they have different aggregation numbers. SDS has an aggregation number of around 65 [14], and LPC has an aggregation number of around 139 [15], so for identical concentrations of SDS and LPC there are about half as many LPC micelles. For 40 mM LPC and 2 mM BP-COOH (as has been used so far) this leads to an average of approximately seven BP-COOH molecules per micelle. This contrasts with approximately two BP molecules per micelle with 100 mM SDS and 3 mM BP. Using the information for micelle radius in table 2.1 and the occupation numbers of the probe molecules inside the micelles, the volume of micelle per probe

molecule can be calculated. This value is 10.8 nm^3 per BP molecule in SDS, and 11.5 nm^3 per BP-COOH molecule in LPC, at surfactant concentrations of 100 mM and 40 mM for SDS and LPC respectively. This means that on average the probe molecules are approximately the same distance apart in the two systems. To investigate the effect of BP-COOH concentration experiments were carried out with LPC at 40 mM and BP-COOH at 1 mM, 2 mM, and 4 mM. However, when the BP-COOH concentration was increased to 4 mM the sample was no longer soluble at 25 °C, so the experiments had to be conducted at 45 °C where all the LPC dissolved, and a transparent solution could be obtained. For comparison, and to investigate the effect of temperature on this system, experiments were also carried out at 45 °C with a BP-COOH concentration of 2 mM.

Figure 7.24 shows comparisons between zero field time curves for 1 mM and 2 mM at 25 °C and 2 mM and 4 mM at 45 °C. As would be expected, a higher concentration of BP-COOH leads to a larger absorption signal due to the increased number of RPs formed. It is interesting to note that although the initial peak height for the 4 mM curve is approximately twice that of the 2 mM curve, the initial peak for the 1 mM curve is more than half the size of the 2 mM curve. This suggests that a higher percentage of the BP-COOH molecules form radicals in the 1 mM solution than in the 2 mM or 4 mM solutions. The non-linearity in signal size between the 1 mM and 2 mM signals mirrors that seen in DODAC/BP in section 6.2.1. However in this case it is obvious that the reason for the non-linearity in absorbance between the 1 mM and 2 mM curves is not due to saturation of laser absorption (otherwise the doubling in signal size between the 2 mM and 4 mM curves would not be seen). Figures 7.3 and 7.12 also show that the absorption of any of the systems at 355 nm is far lower than

that at 308 nm, and hence the argument for saturation of the laser excitation light does not hold in this case

In SDS micelles it is known that the aggregation number of the micelles decreases with increasing temperature. Although no literature data could be acquired for LPC micelles, similar behaviour is assumed. As the temperature is increased from 25 °C to 45 °C the radical absorption decreases, which might indicate that less BP-COOH is incorporated into the micelle (this process might also be supported by an increase of the solubility of BP-COOH in water as the temperature increases).

A doubling of the BP-COOH concentration from 2 mM to 4 mM leads to consequent doubling of initial absorption size indicating linear behaviour of BP-COOH incorporation into the LPC micelle (and linearity in all absorption processes). The non-linearity of the absorption signal between the 1 mM and 2 mM curves at the lower temperature might be due to non-linearity of BP-COOH incorporation into the micelles at this temperature. A discussion of these graphs is very difficult as many parameters, often changing in opposing directions, influence the absorption intensity. Some of the parameters that influence the amount of ketyl radical observed include the changing solubility of BP-COOH in both the LPC micelles and the bulk solution with both BP-COOH concentration and temperature, the change in the degree of ^{3}BP-COOH* - ^{3}BP-COOH* quenching with concentration inside the micelles, and the change in micelle size, shape and stability with BP-COOH concentration and temperature. It is hence very difficult to give even a fully qualitative account of figure 7.24.

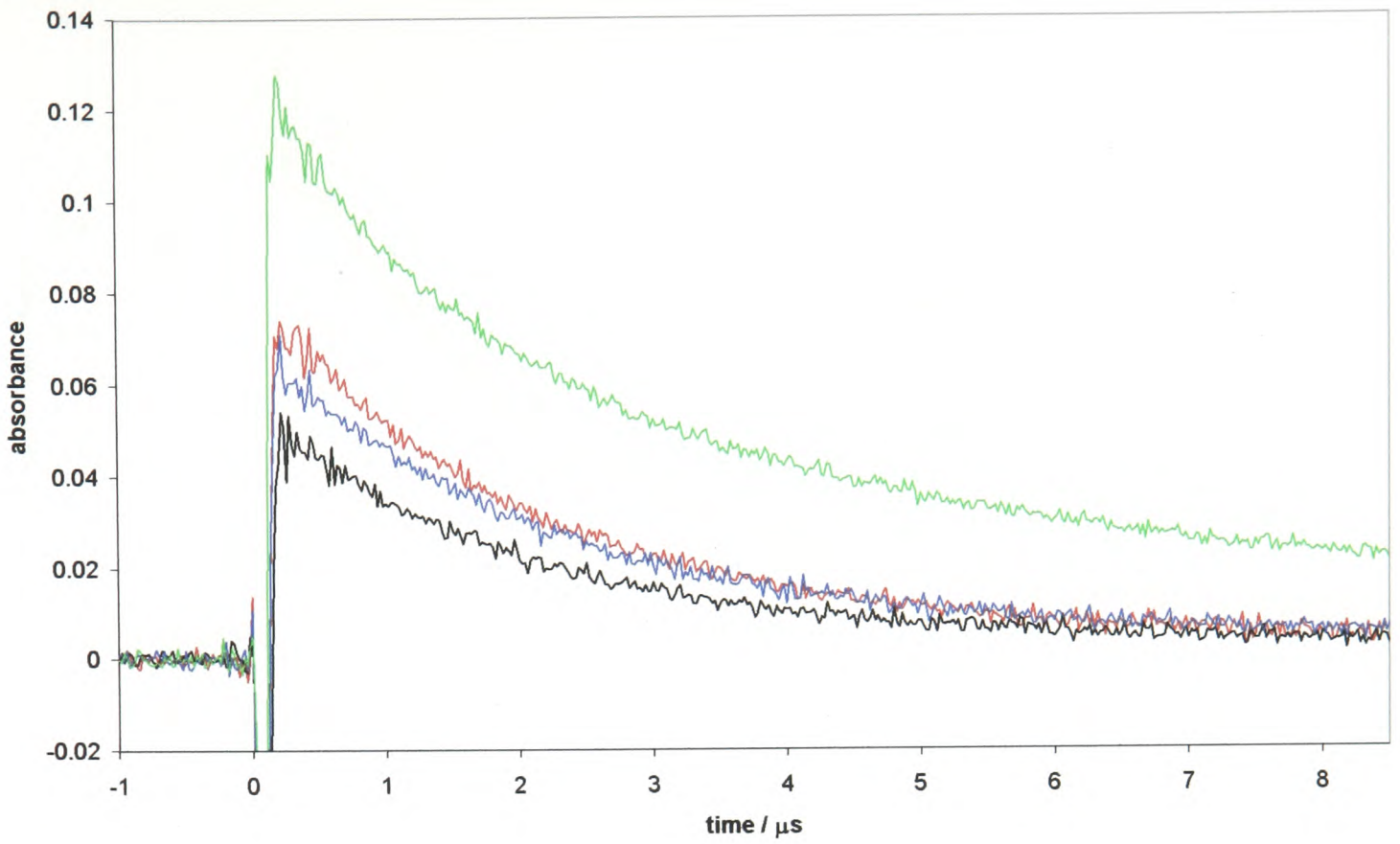


Figure 7.24: Zero field time curves of LPC/BP-COOH with temperatures / BP-COOH concentrations of (●) 25 ^{0}C / 1 mM, (●) 25 ^{0}C / 2 mM, (●) 45 ^{0}C / 2 mM, and (●) 45 ^{0}C / 4 mM

The effect of temperature on the zero field time curves of the 2 mM BP-COOH can be seen in figure 7.24. Although the higher temperature curve has the smaller initial absorption (as was the case with DODAC/BP), when the two curves are normalised to the same initial absorption (figure 7.25) it can be seen that the difference in recombination rates between the two temperatures is very small (which is not the same as the behaviour in DODAC/BP). This implies that although the initial radical concentration is larger at the higher temperature the fate of the RPs, and the kinetics of these processes, are very similar at the two different temperatures. DODAC vesicles undergo a phase transition at around 36 °C, and this accounts for the difference in rate of signal decay. There is no such phase transition in LPC micelles, and hence no large change in decay kinetics.

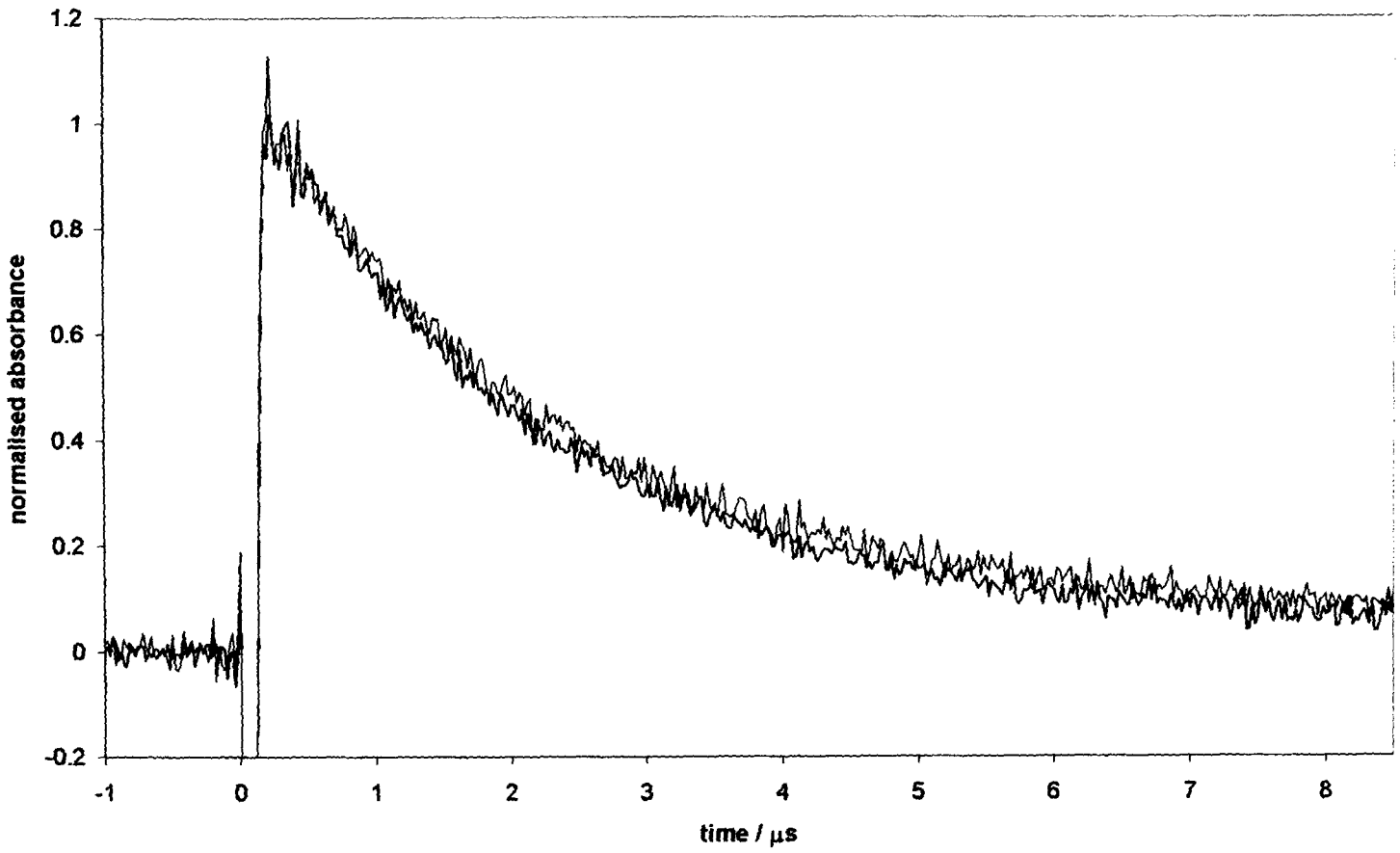


Figure 7.25: Normalised zero field time curves of LPC/BP-COOH at 40 / 2 mM at (•) 25 ^{0}C, and (•) 45 ^{0}C

The effect of temperature and BP-COOH concentration on the size of the MFE at 17.1 mT can be seen in table 7.5, below.

BP-COOH conc. / mM	Temperature / ^{o}C	MFE at 17.1 mT / %	EE / %
1	25	3	7.2
2	25	6	5.1
2	45	5	11
4	45	9	7.0

Table 7.5: Manually calculated MFE for LPC/BP-COOH at 17.1 mT

The MFEs were manually calculated from time curves (of 288 averages per curve) taken at zero applied magnetic field and 17.1 mT. However, the low signal to noise ratio in this system means that even with extensive signal averaging the values obtained for MFEs in this system are not very precise, which is the reason that the MFE values in table 7.5 are only given to one significant figure. As the EE values show, the noise in these measurements is much larger than in the synthetic micelle

systems. For this reason no real significance can be drawn from the difference in MFE size for 2 mM BP-COOH at 25 °C and 45 °C. The difference in MFE size with concentration is much larger, and at both temperatures an increase in BP-COOH concentration gives an increase in the size of the MFE at 17.1 mT.

7.4.3 LFE in LPC/BP-COOH

Despite no LFE being observed in the SDS/BP-COOH system the LFE in LPC/BP-COOH was investigated. Seven MARY curves, each of 48 averages per point, were recorded in the range 0 mT to 3.5 mT, and the average of these seven curves is shown in figure 7.26. However, the MARY curve obtained is still noisy, and no LFE is observable.

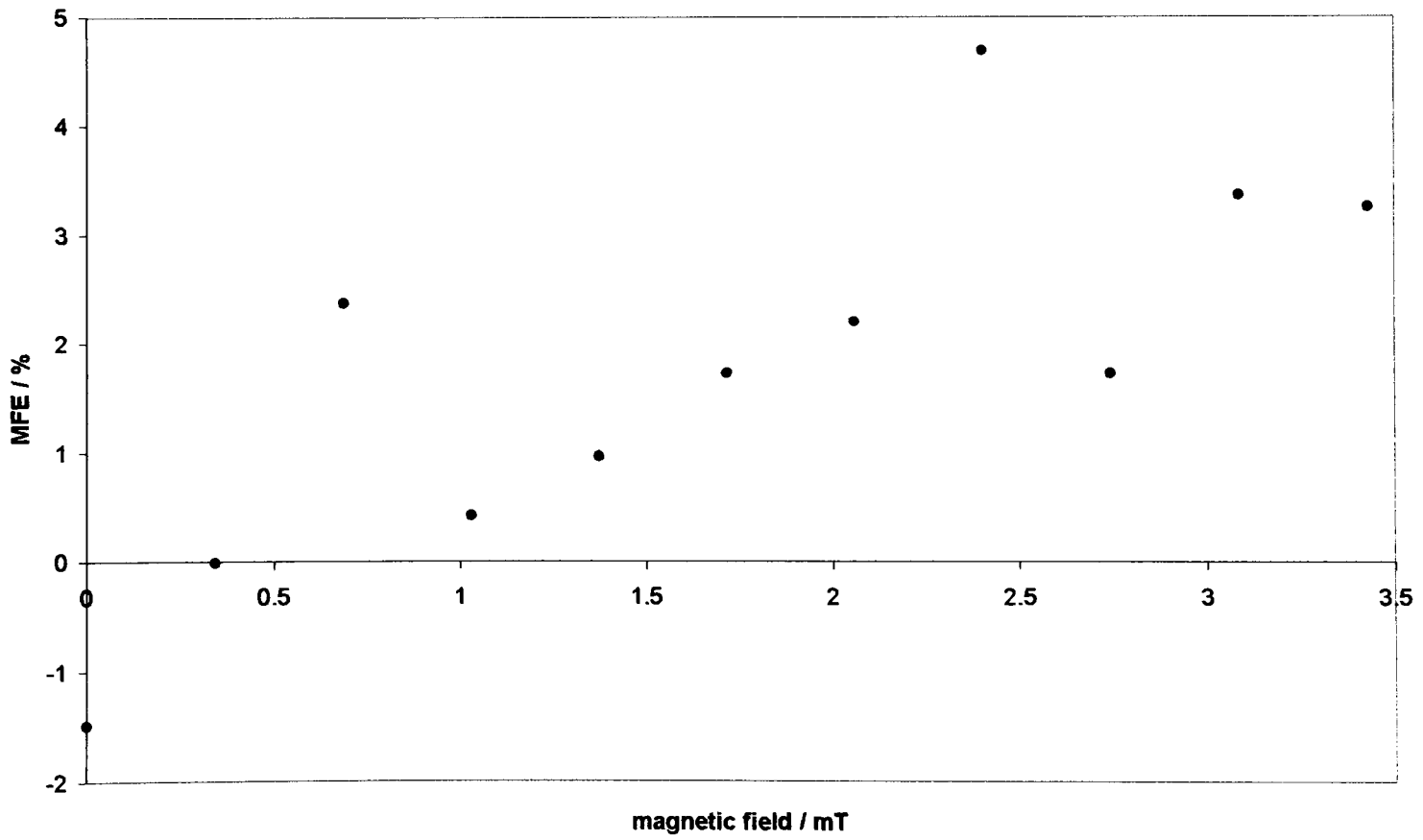


Figure 7.26: MARY curve of LPC/BP-COOH concentrating on LFE region (EE 7.1%)

There is the suggestion of the normal, positive MFE at the higher magnetic field strengths, and the magnitude of the MFE seen at around 3.5 mT in figure 1.28 are the same as those seen in figure 7.23 at the same magnetic field strengths.

7.5 Comparison Between SDS and LPC Micelles

The problems with LPC absorption at 308 nm discussed in section 7.2 prevent a comparison between SDS/BP and LPC/BP, but the preliminary experiments using BP-COOH allow a comparison between SDS and LPC micelles, using BP-COOH as the probe molecule.

Figure 7.27 shows zero field time curves of SDS/BP-COOH and LPC/BP-COOH normalised to give an absorption value of unity at the initial absorption peak. The SDS/BP-COOH time curve shows a rapid initial decay, followed by the slower F pair period, but the LPC/BP-COOH shows a slower, monophasic decay.

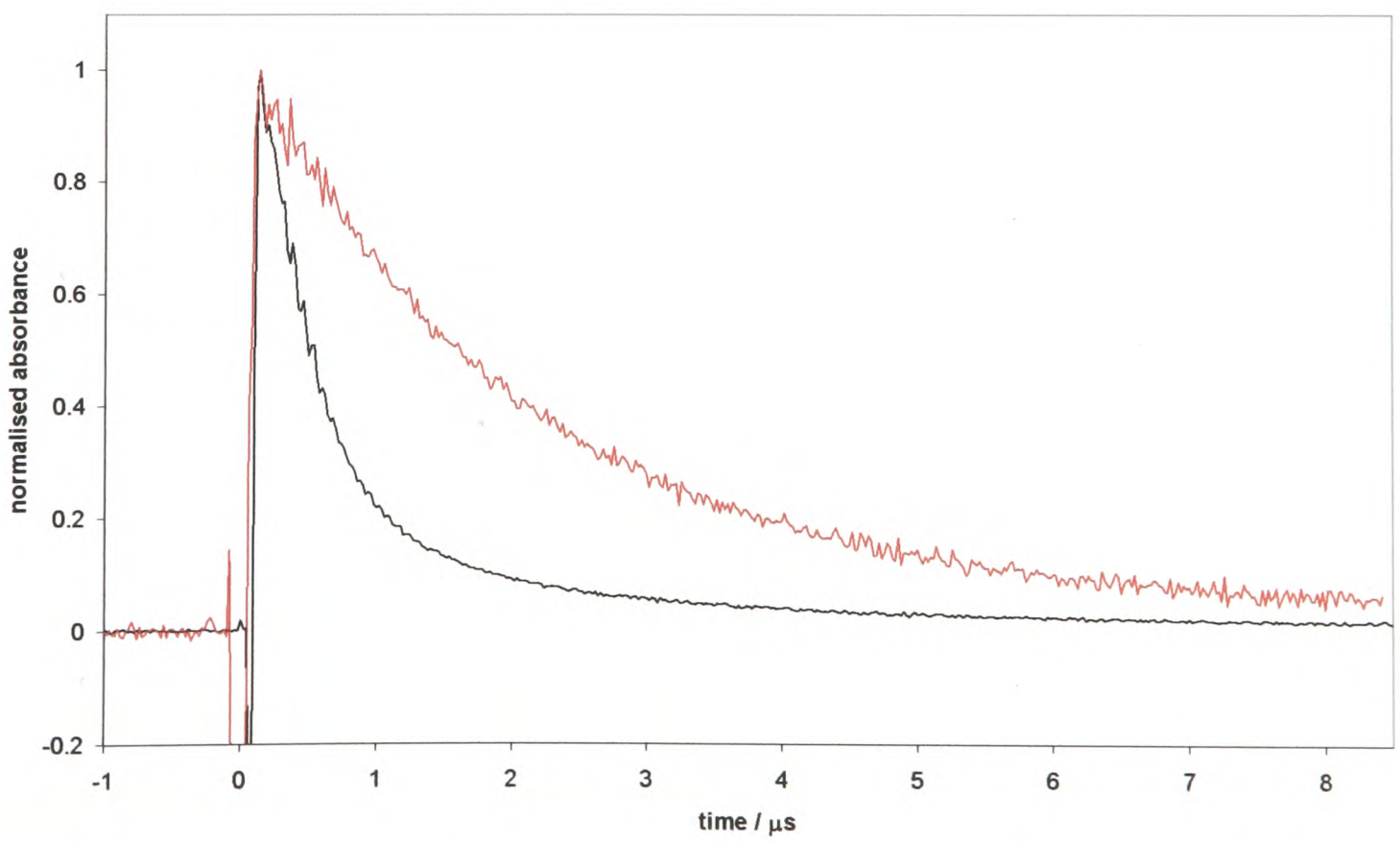


Figure 7.27: Zero field time curves of (•) SDS/BP-COOH, and (•) LPC/BP-COOH

The LPC/BP-COOH curve in figure 7.27 shows a marked similarity with the SDS/BP-COOH curve at pH 7.8 shown in figure 7.17. This could indicate that the molecule is in the same environment in both cases, however further work in LPC at varying pH values would have to be undertaken before firm conclusions could be drawn.

The fractional lifetimes of the two systems, (and those of SDS/BP for comparison) are shown in table 7.6, below.

System	$T_{3/4}$ / μs	$T_{1/2}$ / μs	$T_{1/4}$ / μs
SDS/BP-COOH	0.20	0.42	0.82
LPC/BP-COOH	0.58	1.48	3.16
SDS/BP	0.16	0.34	0.62

Table 7.6: Lifetime data for LPC/BT/CHD and LPC/BP-COOH

The fractional lifetimes confirm the differences seen in figure 7.27, and also that while the fractional lifetimes of SDS/BP-COOH are slightly larger than SDS/BP it is not by a large amount. The differences between the physical properties of SDS and LPC micelles were listed in table 2.1, which showed that whilst SDS micelles are smaller than those of LPC (a radius of 17.5 Å for SDS, and 26.7 Å for LPC) SDS micelles have a higher microviscosity than those of LPC (19 cP for SDS, and 10.4 cP for LPC). This implies that the BPH-COOH$^{\bullet}$ radicals not only have a greater volume to explore in LPC micelles, but that their movement inside the LPC micelles is less restricted than in SDS micelles, and this leads to the longer signal lifetime seen in figure 7.27.

In the previous chapter it was seen that the fractional lifetimes for DODAC/BP were also much longer than in SDS/BP, but in this case both the size of the hydrophobic compartment and also the microviscosity are much greater in DODAC vesicles than in SDS micelles. From the evidence of these three systems it would appear that the

overall rate of signal decay is therefore more dependent on the size of the structure confining the RP, rather than its microviscosity. However, many more systems would have to be studied over a wide range of sizes and microviscosities to confirm this observation.

Despite the very large differences in the appearances of the zero field time curves, the MARY curves of SDS/BP-COOH and LPC/BP-COOH are similar, as can be seen from figure 7.28, reiterating the observation that the size of the MFEs are not obviously predictable from the appearance of the zero field time curves.

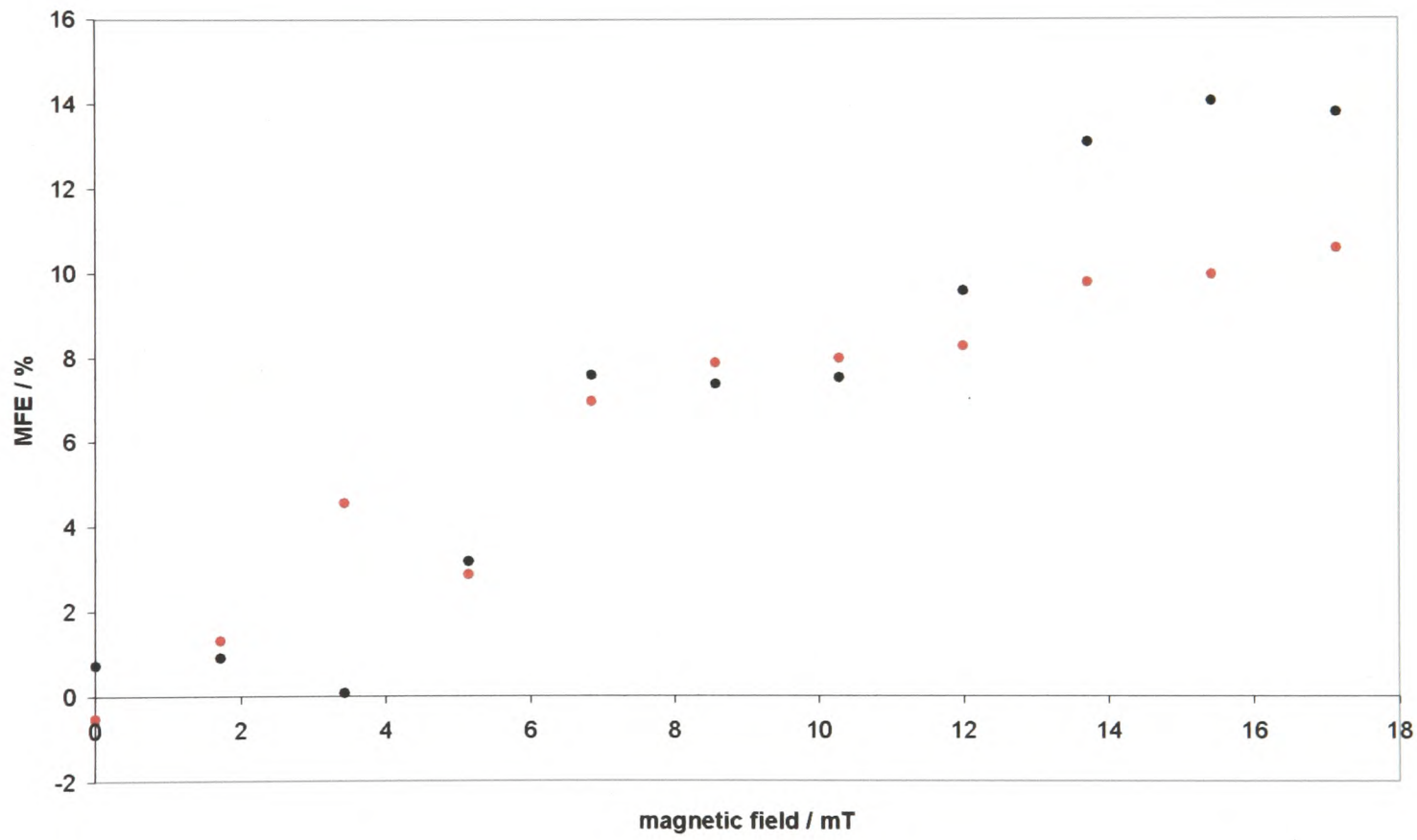


Figure 7.28: MARY curves of (•) SDS/BP-COOH (6.0), and (•) LPC/BP-COOH (5.4) (figures in brackets show EE / %)

As there is no additional hydrogen donor in either case, the RP that is formed will consist of the BPH-COOH$^{\bullet}$ radical, and a radical formed by hydrogen abstraction from one of the micelle molecules. If the BP-COOH molecule abstracts a hydrogen

atom from somewhere along the hydrophobic tail in both types of micelle, then the hyperfine couplings will be very similar in both SDS and LPC micelles. Hence, despite the differences in micelle properties, figure 7.28 suggests that it could be the hyperfine couplings in the RPs of SDS/BP-COOH and LPC/BP-COOH that determine the size of the MFEs in the magnetic field range investigated. However, this theory does not agree with the evidence shown in figure 7.18 showing the MFE dependence of SDS/BP-COOH on pH. Here the hyperfine couplings of the radicals do not change, but the size of the MFE at around 18 mT varies between approximately 5% and 25% between pH values of 3.2 and 7.8.

The MFEs seen in both the SDS/BP-COOH and LPC/BP-COOH systems in figure 7.28 are approximately twice as large as those seen in DODAC/BP in the previous chapter, over the magnetic field range investigated. With so many variables changing between three systems it is hard to pick out confidently the factor, or factors, that cause the change, but as noted before both the size and microviscosity of DODAC vesicles are much larger than those of either the SDS or LPC micelles.

7.6 Conclusions and Future Lysophospholipid Work

The unforeseen problem with LPC was that it absorbs light in the same region of the spectrum as BP, hence the necessity of changing to a different probe molecule, and changing the laser to one which provides excitation light at a different wavelength. However, once this was achieved the primary objective with lysophospholipids was to test whether or not these structure provide the right microenvironment for magnetic field dependent radical pair kinetics. The experiments performed showed MFEs in LPC micelles with BT/CHD, BP-4F and BP-COOH as probes, and with the

LPC/BP-COOH system produced MFEs that are similar in size to those in the SDS/BP-COOH system. There is still much other work which can be undertaken involving LPC at different concentrations and temperatures to those which were used in this work. Investigations at varying pH levels with LPC/BP-COOH could also be carried out for comparison with those seen in section 7.2.5 for the SDS/BP-COOH system. For detailed investigations into the effect of temperature variations, enhancements and refinements will have to be carried out on the experimental apparatus. For example the thermostating of the cell will have to be improved to ensure a higher degree of control over the solution temperature. With the old, larger volumed cell described in section 3.6.1 this was achieved by enclosing the cell in an aluminium block and flowing water around the cell, but this is not possible with the current cell design. The easiest solution would be to enclose the pipes leading to the cell in a water jacket, but the temperature of the solution in the cell would have to be carefully measured to determine the amount of heat loss as the solution leaves the jacketed pipe and enters the cell, especially at low flow rates.

No LFEs were seen with LPC, but this was most likely a consequence of using BP-COOH as the probe molecule, as discussed in section 7.3. To increase the chance of detecting a LFE in lysophospholipids another probe molecule should be used. This could also involve changing the experimental apparatus, as an excitation source other than the YAG laser may be needed.

Additionally, lysophospholipids are commercially available with varying lengths of carbon chain in the hydrophobic 'tail' of the molecule. They are also available with head groups other than those based on choline, such as those based on ethanolamine or serine, which will lead to different micelle properties, such as different micelle sizes and aggregation numbers, or different solubilities.

8: BIOLOGICAL VESICLES – PHOSPHOLIPIDS

Phospholipids are the major component of most biological membranes, hence understanding the effect of radical pair reactions inside phospholipid vesicles will go a long way towards enhancing the understanding of the behaviour of radical pairs in biological membranes, and consequently the effects of magnetic fields on these systems.

The work in this chapter forms a study into RPs in phospholipid vesicles, and investigates the possibility of observing magnetic field effects at relatively low magnetic field strengths. The work in the two previous chapters has shown that MFEs can be seen in DODAC vesicles, as well as in lysophospholipid micelles. Phospholipid molecules bear a strong chemical resemblance to lysophospholipid molecules, but contain two fatty acid chains rather than one, leading to the formation of vesicles in phospholipids, rather than the micellar structure seen with lysophospholipids.

8.1 EXPERIMENTAL SECTION

8.1.1 Phospholipid Purity and Nomenclature

As further discussed in sections 8.5 and 8.6 three different types of phospholipids were examined in the course of these experiments. All three were obtained from Sigma, and used as received. Henceforward the three different types of phospholipid will be labelled PC_A, PC_B, and PC_C. Both PC_A and PC_B are prepared from soybean, but differ in the purity of the samples. For the initial experiments PC_A was used, it has

a purity of approximately 50% phosphatidyl choline, with a mixture of different fatty acid chains attached to the glycerol group. The remainder is made up of other lipids, such as phosphatidyl ethanolamine, and other substances such as carbohydrates. For the secondary experiments PC_B was used, it has a purity of at least 99% phosphatidyl choline. PC_A and PC_B are very different in appearance; PC_A is a yellow solid whilst PC_B is a white solid, leading to solutions which are yellow and white respectively when prepared including the other components. The third type of phospholipid used was PC_C, a phospholipid prepared from egg, rather than soybean. It has the same purity of phosphatidyl choline molecules as seen with PC_B, but as it is derived from a different source the mixture of fatty acid chains will be different in the two samples. PC_B contains a higher proportion of unsaturated fatty acid chains than PC_C and has a slightly higher average molecular weight due to the mixture of hydrophobic chains. PC_C also forms a white solution when prepared with the other components for the MFE experiments.

The initial experiments were performed with the lower purity phospholipid, PC_A, to establish experimental procedures and solution preparations, to ensure that signals could be obtained from these systems, and to optimise the experimental set-up. Once this had been accomplished the purer, more expensive PC_B could be used to investigate phospholipid systems further.

8.1.2 Solution Preparation

Experiments were performed with phospholipid concentration ranging from 20 mM to 40 mM. In all cases the hydrogen abstractor molecule concentration was 2 mM; and the concentration of hydrogen donor was 10 mM, where present. Experiments were

performed at 35 °C unless stated otherwise. Two different preparation procedures were used, a more straightforward procedure for PC_A and PC_B following that used for the preparation of DODAC vesicular solutions and some literature procedures (*e.g.* [1]), and a more sophisticated procedure for PC_C following the more common literature sonication procedures (*e.g.* [2]). Other methods of vesicle preparation are used in the literature (*e.g.* injection and dialysis), but these were not utilised in the present study.

To prepare the PC_A and PC_B solutions the PC and hydrogen abstractor were weighed out and added to a volumetric flask. About 90% of the water was added and the solution was heated to 60 °C and sonicated until all solids had dissolved. The solution was then sonicated for twelve hours at room temperature. If a hydrogen donor was used it was added on the day of the experiment, and the solution sonicated for a further hour at the temperature at which the experiment was conducted. After this final sonication the remainder of the water is added to make the volume of the solution up to 250 ml.

To prepare the PC_C solutions a more lengthy procedure was used. 4 mmol PC_C and 0.4 mmol BP-COOH were dissolved in a 1:1 ratio mixture of chloroform and methanol. Minimal volumes for complete dissolution of the solid were used. The solution was sonicated in an ultrasonic bath at 60 °C for 10 minutes, and then placed under a vacuum pump for 3 hours until a dry residue remained. The sample was made up to a volume of 50 ml using distilled water, and sonicated again using a titanium tipped probe sonicator. The sonication was carried out in 50 periods, each of 1 minute duration allowing the temperature to rise from 35 °C to 42 °C during each sonication period. The temperature was not allowed to rise above 42 °C to prevent titanium oxidation, which contaminates the sample. The solution was placed under centrifuge

of 20000 rpm for 90 minutes in order to remove any solid titanium that may have entered the sample during sonication. The sample was again diluted with distilled water to achieve a final solution volume of 150 ml.

For all time curves shown there are 96 averages per curve and each curve is the average of two sets of acquisitions, unless stated otherwise. All time curves shown were recorded at zero applied magnetic field, unless stated otherwise.

8.2 Concentration of Phospholipids

The initial phospholipid experiments were performed with PC_A to ensure that an absorbance signal could be observed, and to investigate the possibility of detecting any MFEs. The first investigation probed the effect of the PC_A concentration on the success of the experiments, in an attempt to maximise the signal size, and also examined the effect of changing concentration on the appearance of the time curves. Three different concentrations of PC_A were investigated, 40 mM, 30 mM and 20 mM. Figure 8.1 shows the time curves for these three different concentrations. The absorbance signals for all three curves show a growth in signal size in the early part of the signal (up to 0.5 μs post laser flash). There are two possible explanations for this observation (which also occurs in the DODAC/BP system, *e.g.* figure 6.4) and they are as follows. Firstly the rise could be due to recovery of the PMT from overload due to the fluorescence spike immediately following the laser flash. This spike is noticeably larger for the phospholipid and DODAC systems, probably due to increased light scattering. The second possibility is that the hydrogen abstraction reaction of the BP-COOH from a phospholipid monomer could be slower than that

seen in the micellar systems. DODAC and phospholipid vesicles have a much higher microviscosity than that seen in micelles (see tables 2.1 and 2.3) and this could cause a retardation of the hydrogen abstraction reaction in comparison to the micellar systems. Due to the fact that no change in signal could be observed for the highly variable hydrogen abstraction rates in section 4.2 the first explanation is considered the more likely.

Whilst the 40 mM and 30 mM time curves have the same shape, the 20 mM curve has a different shape, with a faster rate of signal decay, and hence a faster rate of radical recombination. The 20 mM curve shows the best signal to noise ratio and also forms less turbid solutions than the higher PC_A concentrations, so the experiments which followed were performed with 20 mM PC_A.

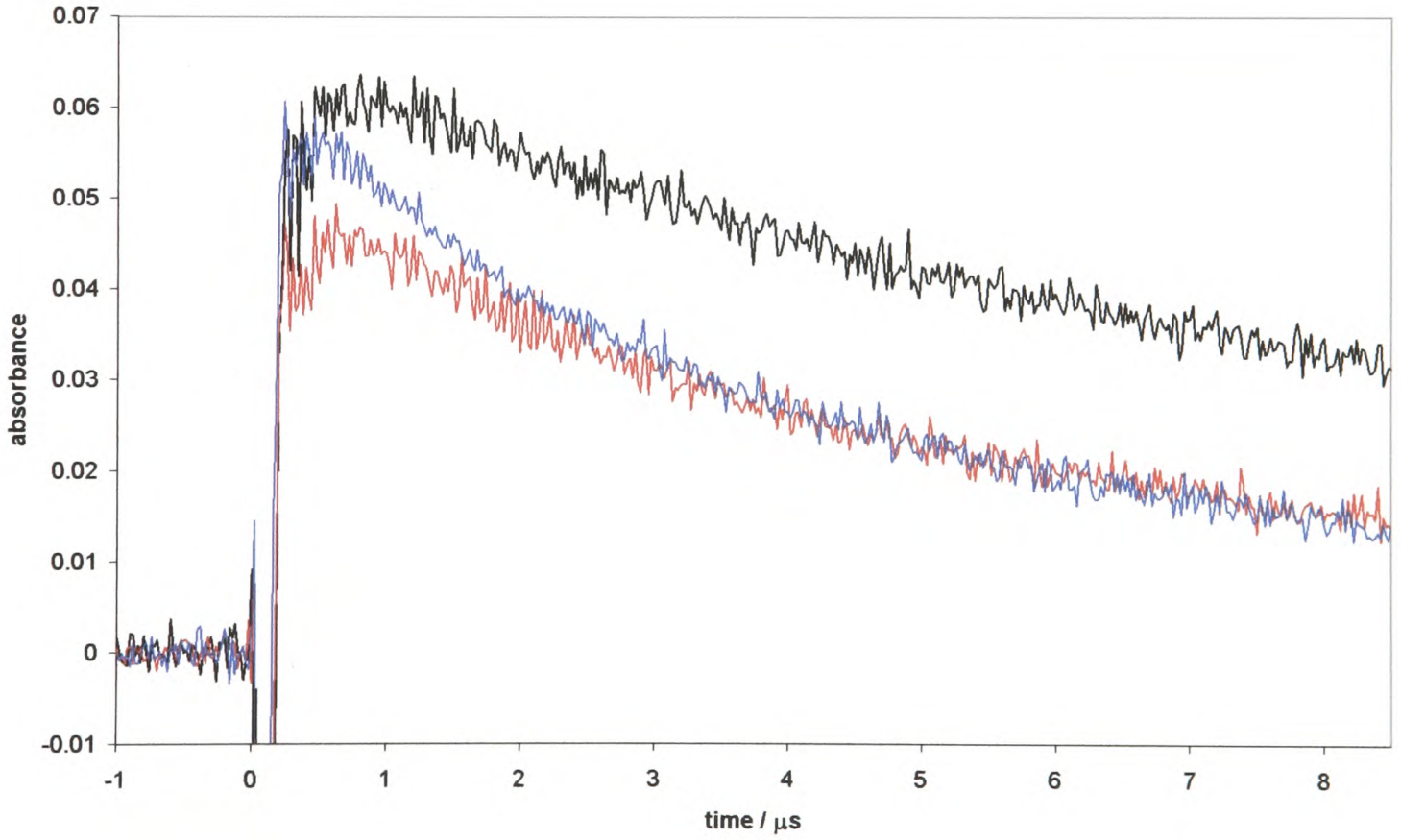


Figure 8.1: Zero field time curves of (●) 40, (●) 30, and (●) 20 mM PC_A with BP-COOH

At all three concentrations of PC_A time curves were recorded with at least 288 averages at zero applied field and 17.1 mT, the largest magnetic field the Helmholtz

coils will provide. MARY curves were also recorded between 0 mT and 17.1 mT and in no case did any of these MARY curves or time curves show any magnetic field effects.

8.3 PROBE MOLECULES

As seen in section 7.2, the best replacement found for BP, when the YAG laser is used as the excitation source, was BP-COOH. When phospholipids were first investigated BP-COOH seemed the logical choice as the hydrogen abstractor probe molecule, but BP-4F and BT/CHD were also investigated to determine whether BP-COOH is the most suitable molecule for work in phospholipid vesicles. There is also the possibility that owing to the different solubilities of the three molecules they could be located in different regions of the vesicle, and so lead to differences in radical pair behaviour.

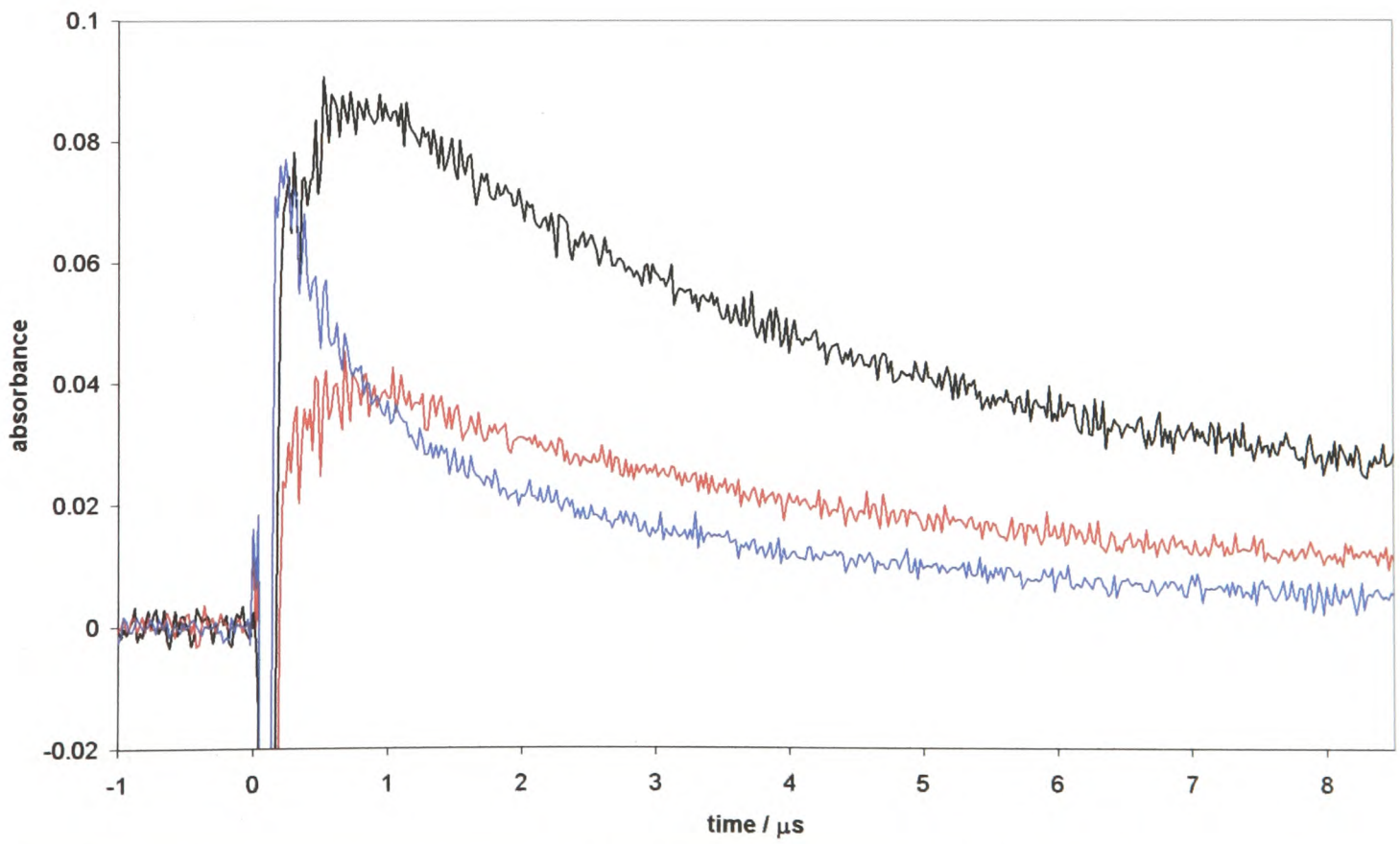


Figure 8.2: Zero field time curves of (●) BP-COOH, (●) BP-4F, and (●) BT/CHD in PC_A

Figure 8.2 shows the zero field time curves for PC_A/BP-COOH, PC_A/BP-4F and PC_A/BT/CHD. CHD was added to the BT system to increase the chance of observing MFEs, as was the case in SDS micelles in section 7.2.2.

The PC_A/BP-COOH curve shows the largest absorption signal, supporting the decision to use this as the primary system for investigating MFEs in phospholipids. The peak for the PC_A/BT/CHD system is sharper, and also occurs sooner after the laser flash. This suggests that the rate of hydrogen abstraction is faster in this system, as would be expected in the presence of CHD.

Neither the PC_A/BP-4F nor the PC_A/BT/CHD systems showed any MFEs in either their time curves or MARY spectra.

Experiments were also performed with PC_A/BP-COOH/CHD, but addition of CHD did not cause a change in shape of the zero field time curves towards that of PC_A/BT/CHD seen in figure 8.2. No MFEs were seen in either the time curves or MARY spectra of PC_A/BP-COOH/CHD.

8.4 Stronger Magnetic Fields

The lack of any observable MFEs with the PC_A systems could be due to a number of factors. For example it is possible that the absorbance signal observed is of the excited triplet of the probe molecules, and no radical formation is occurring. Another possibility is that a component of the solution (of which only 50% of the PC_A is phosphatidyl choline) is inducing rapid relaxation of the RP, and hence no MFEs are observed, as with the paramagnetic ions added to the micellar solutions in section 5.4. The signals that are observed in the PC_A systems are very noisy, and this could also be

masking any small MFEs that may be present. To maximise the possibility of observing MFEs in the PC_A systems it was decided to increase the magnetic field strength. For example a stronger magnetic field leads to increased MFEs in the SDS/BP system for magnetic fields up to field strengths of the order of 1 T [3]. Unless MFEs could be seen in the PC_A systems at higher magnetic field strengths there was very little likelihood of detecting any MFEs by optimisation of the existing apparatus. Clearly this required larger than the maximum magnetic field strength of 17.1 mT provided by the Helmholtz coils, and hence an alternate source of magnetic field was needed.

8.4.1 Horseshoe Magnet

The easiest solution to this problem was to use a permanent horseshoe magnet held close to the cell. The Helmholtz coils were removed from the experiment, and one pole of the horseshoe magnet was placed next to the cell, as shown in figure 8.3, below.

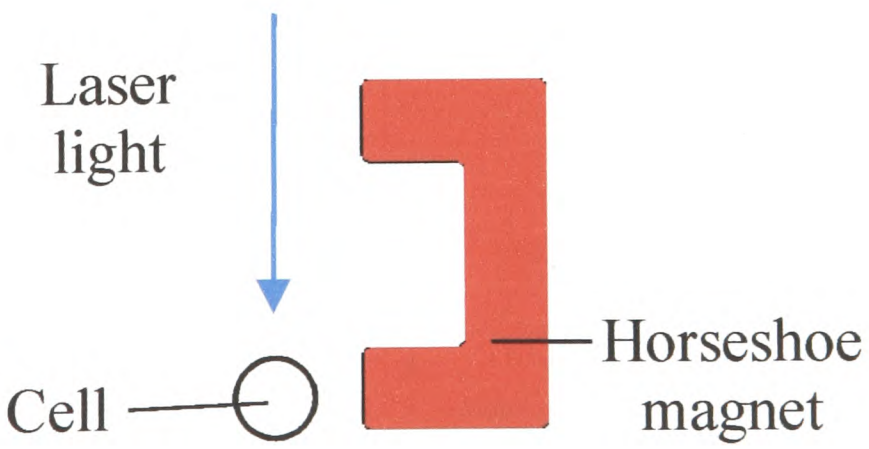


Figure 8.3: Configuration of horseshoe magnet in relation to cell as seen from above

The magnetic field produced was measured using a Hall effect probe and although the detected field was highly inhomogeneous (70 mT on the side of the cell nearest to the magnet and 40 mT on the opposite side) the observation of any MFEs would prove that the PC_A/BP-COOH system forms RPs, and is in principle capable of producing magnetic field dependent effects.

To test for MFEs time curves were obtained with the magnet in place, the laser beam was then blocked (with the laser still running) and the magnet was removed. Time curves were recorded in the absence of the magnet and the laser beam was blocked before the magnet was replaced and the procedure repeated. At the end of the experiment the curves in the presence and absence of the magnet were checked for reproducibility and, the results tested for a MFE.

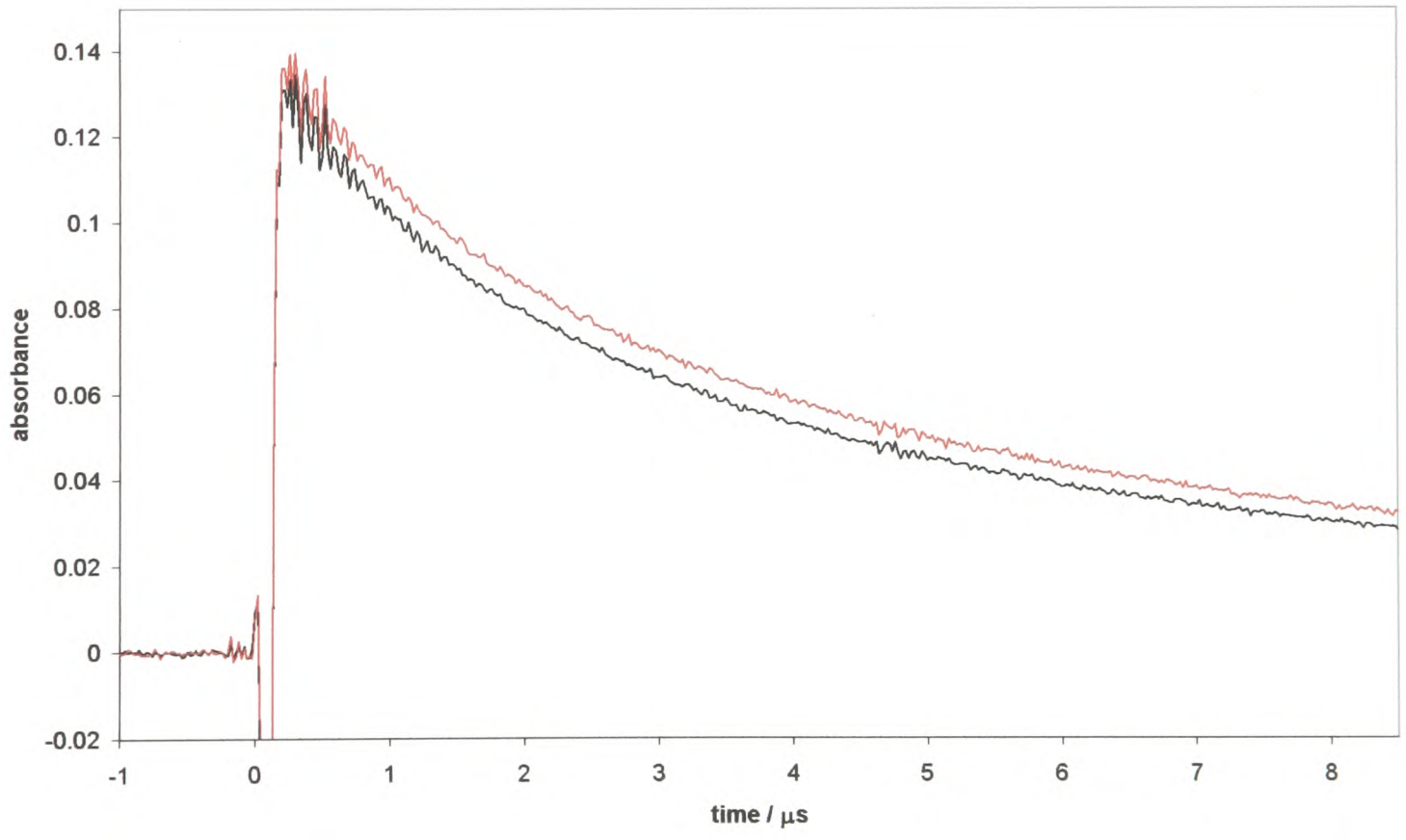


Figure 8.4: Time curves of PC_A/BP-COOH in (•) absence, and (•) presence of permanent magnet

Figure 8.4 shows the time curves for PC_A/BP-COOH with and without the permanent magnet, and the very obvious magnetic field effect that is caused by the higher

magnetic field strengths. Manually calculating the MFE using equation 3.4 and summing the areas under the two time curves the MFE is 8.9%.

There are several flaws which make this technique of observing MFEs less than ideal. The first, and probably most important, is the inhomogeneity in the magnetic field caused by using a horseshoe magnet. There is a difference of about 30 mT from one side of the cell to the other, so the magnetic field strength felt by the radical pairs on the side of the cell closest to the magnet will be much greater than that felt by the radical pairs on the other side of the cell. This leads to a range of MFEs across the cell, but the observation of a MFE, even under these less than ideal conditions, proves that the system is magnetic field sensitive.

Another problem is the exact positioning of the magnet when it is being moved and replaced during the course of the experiment. Every attempt was made to locate the magnet in the same position for every experiment and any major change in field experienced by the sample should be seen as a change in the time curves, and so be picked up when all the curves are compared at the end of the experiment. Repeating the experiments showed the MFE in this system to be reproducible, and further experiments demonstrated that the horseshoe magnet had no effect on the laser pulse, lamp, or PMT response.

To examine the size of the effect of the permanent magnet on a known system SDS/BP-COOH was used. The MFE observed was very large, as is shown in figure 8.5. Manually summing the areas under the two curves gives a field effect of 66%. To compare this with the MFEs seen with the Helmholtz coils, SDS/BP-COOH has field effects of 1.8%, 8.7% and 18% for fields of 4.3 mT, 8.6 mT and 17.2 mT respectively.

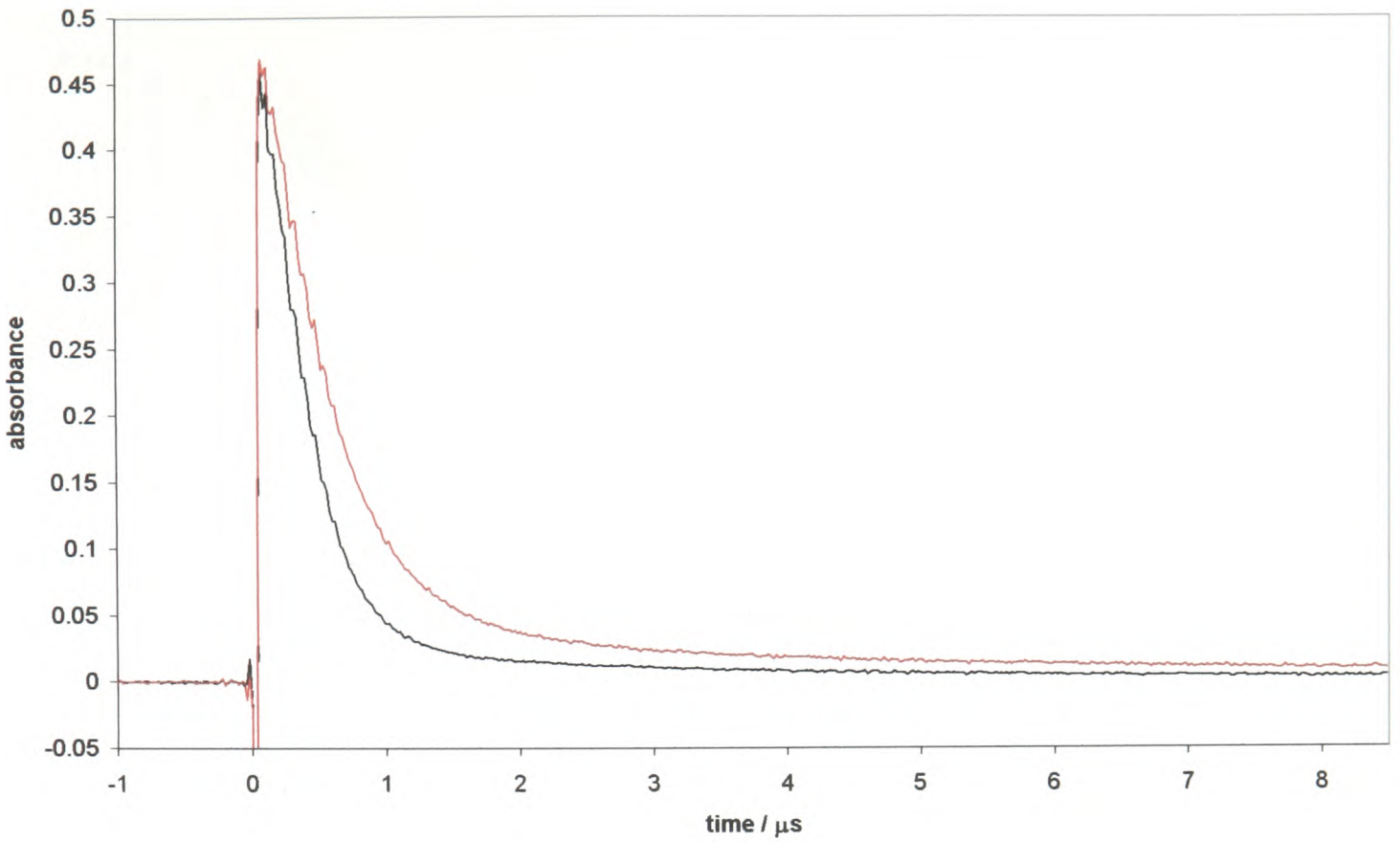
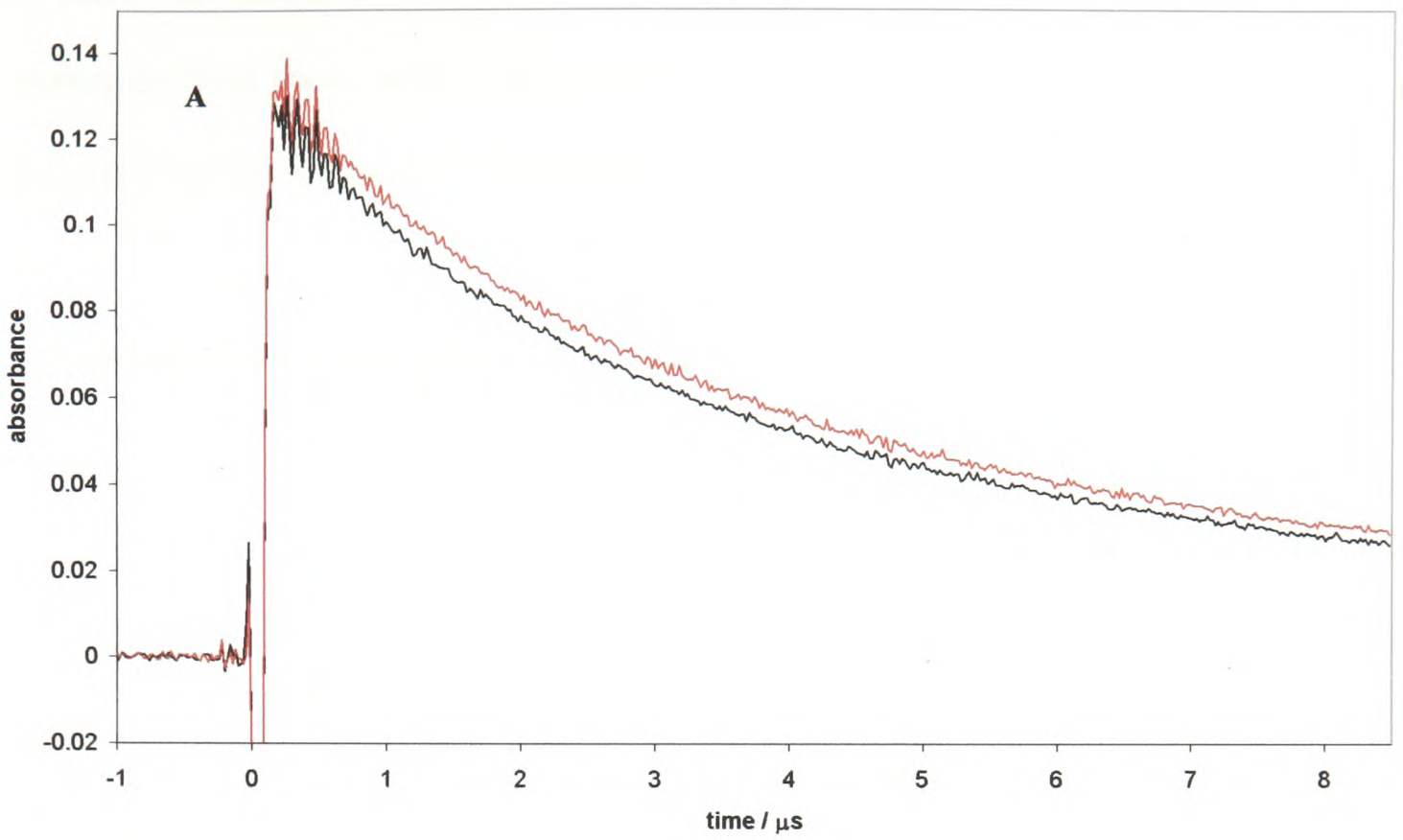


Figure 8.5: Time curves of SDS/BP-COOH in (•) absence, and (•) presence of permanent magnet

Two further phospholipid systems were investigated with the horseshoe magnet, PC_A/BP-COOH/CHD and PC_A/BP-COOH/THF. In both cases the hydrogen donors were at a concentration of 10 mM, half the concentration of phospholipid and five times the concentration of BP-COOH. As with DODAC (section 6.3) the concentration of hydrogen donor is very large compared to that of the phospholipid, and most certainly affects the vesicle structure, but it was considered that such large concentrations were needed to identify any effect on RP behaviour. The time curves showing the MFEs are shown in figure 8.6.



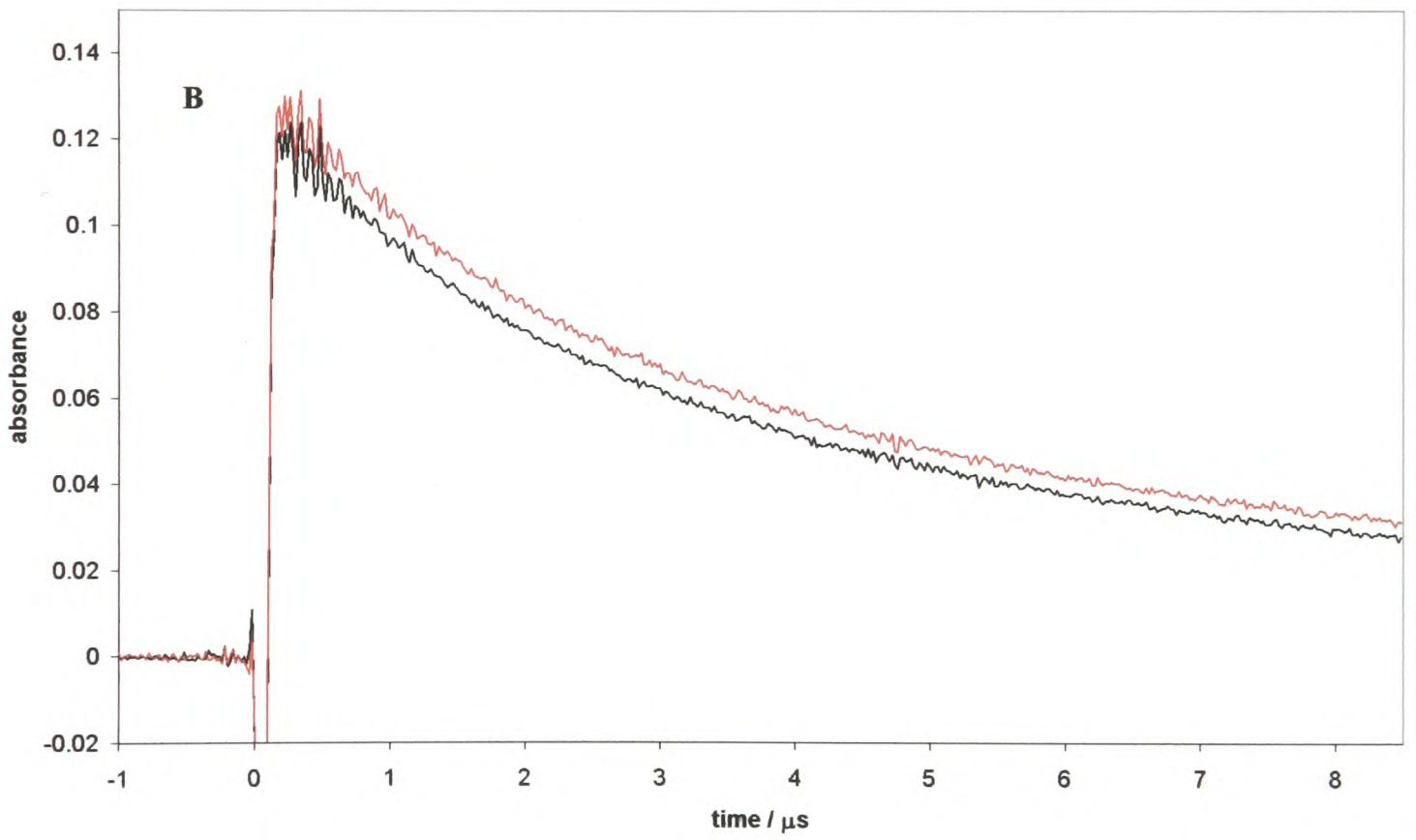


Figure 8.6: Time curves of A) PC_A/BP-COOH/CHD, and B) PC_A/BP-COOH/THF in (•) absence, and (•) presence of permanent magnet

The manually calculated field effects are 7.1% for the CHD solution and 8.8% for the THF solution. This gives a different order for the size of the MFEs than that seen in chapter four where, with SDS/BP, the MFEs were in the order SDS/BP/CHD > SDS/BP > SDS/BP/THF. However, the differences between the sizes of the MFEs are

very small between the three systems and the signal to noise ratio is poor. To take any significance from these results the experiments should be repeated, in a homogeneous field, and possibly with a lower hydrogen donor concentration.

8.5 PURITY OF PHOSPHOLIPIDS

All the experiments described so far in this chapter were performed with PC_A, with a purity of about 50% phosphatidylcholine. While MFEs were observed in these systems the signals were very noisy and this made comparisons between different systems and different conditions complicated. The purer PC (PC_B), was used to ascertain if the impurities in the PC_A solutions were contributing to the noise and the small size of the absorption signals. Because of the greater expense of the PC_B all solutions made were only 100 ml, instead of the usual 250 ml.

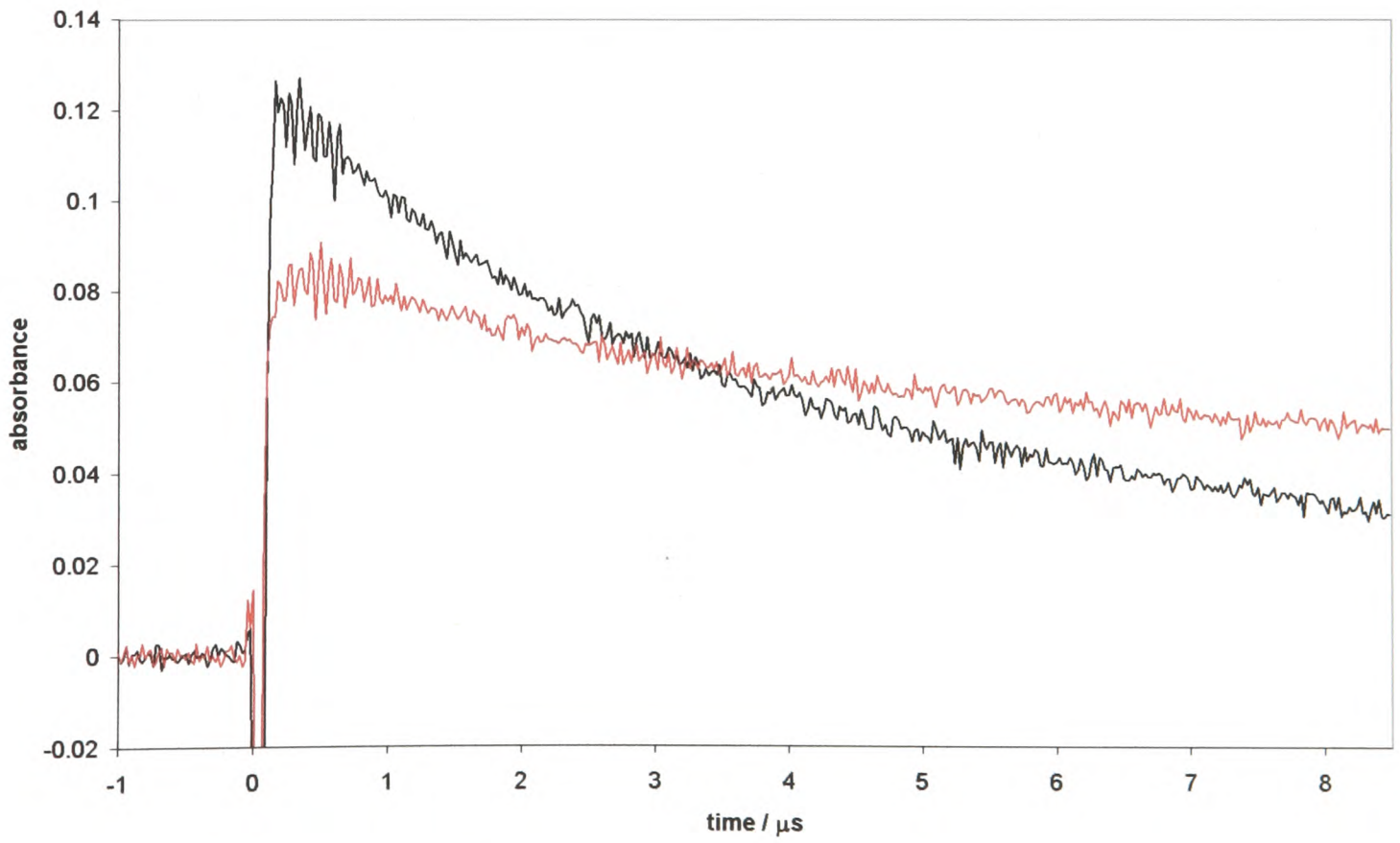


Figure 8.7: Zero field time curves of (●) PC_A, and (●) PC_B with BP-COOH

A change was seen straight away with the PC_B, the first experiments were performed with 20 mM PC_B and 2 mM BP-COOH as with the majority of the PC_A experiments, but the time curves obtained were a different shape, as can be seen in figure 8.7. The shape of the zero field time curve of PC_B/BP-COOH is closer to that of the 30 mM and 40 mM PC_A/BP-COOH time curves seen in figure 8.1. This is a conceivable result if the purities of PC_A and PC_B are taken into account. If there is a higher proportion of phospholipid in PC_B than in PC_A then it will take a smaller amount of PC_B to form solutions with the same concentration of vesicles as a solution prepared from PC_A. Not only is the absorbance smaller using the PC_B solution, but also the rate of radical recombination is much slower in PC_B compared to PC_A solutions. Table 8.1 shows the fractional lifetimes for both PC_A and PC_B with BP-COOH.

System	$T_{3/4}$ / μs	$T_{1/2}$ / μs	$T_{1/4}$ / μs
PC_A/BP-COOH	1.32	3.48	–
PC_B/BP-COOH	3.52	–	–

Table 8.1: Lifetime data for PC_A and PC_B with BP-COOH. Hyphens indicate lifetimes greater than 8.5 μs

The fractional lifetimes seen with phospholipids are greater than those seen for any other system described so far in this thesis. On the timescale shown in figure 8.7 both curves appear to undergo signal decay with mono-phasic kinetics, but this may not be the case, as is seen in section 8.6.

One further change that was seen in moving from PC_A solutions to PC_B solutions was that MFEs were observed at the magnetic field strengths provided by the Helmholtz coils. Figure 8.8 shows time curves for PC_B/BP-COOH at 0 mT, 8.6 mT and 17.1 mT. There is a clear difference between the three curves showing the effect of Zeeman splitting slowing down the rate of spin mixing, and therefore also the rate of radical

recombination. Each curve is made up from four time curves, each of 96 averages, making a total of 384 averages per curve.

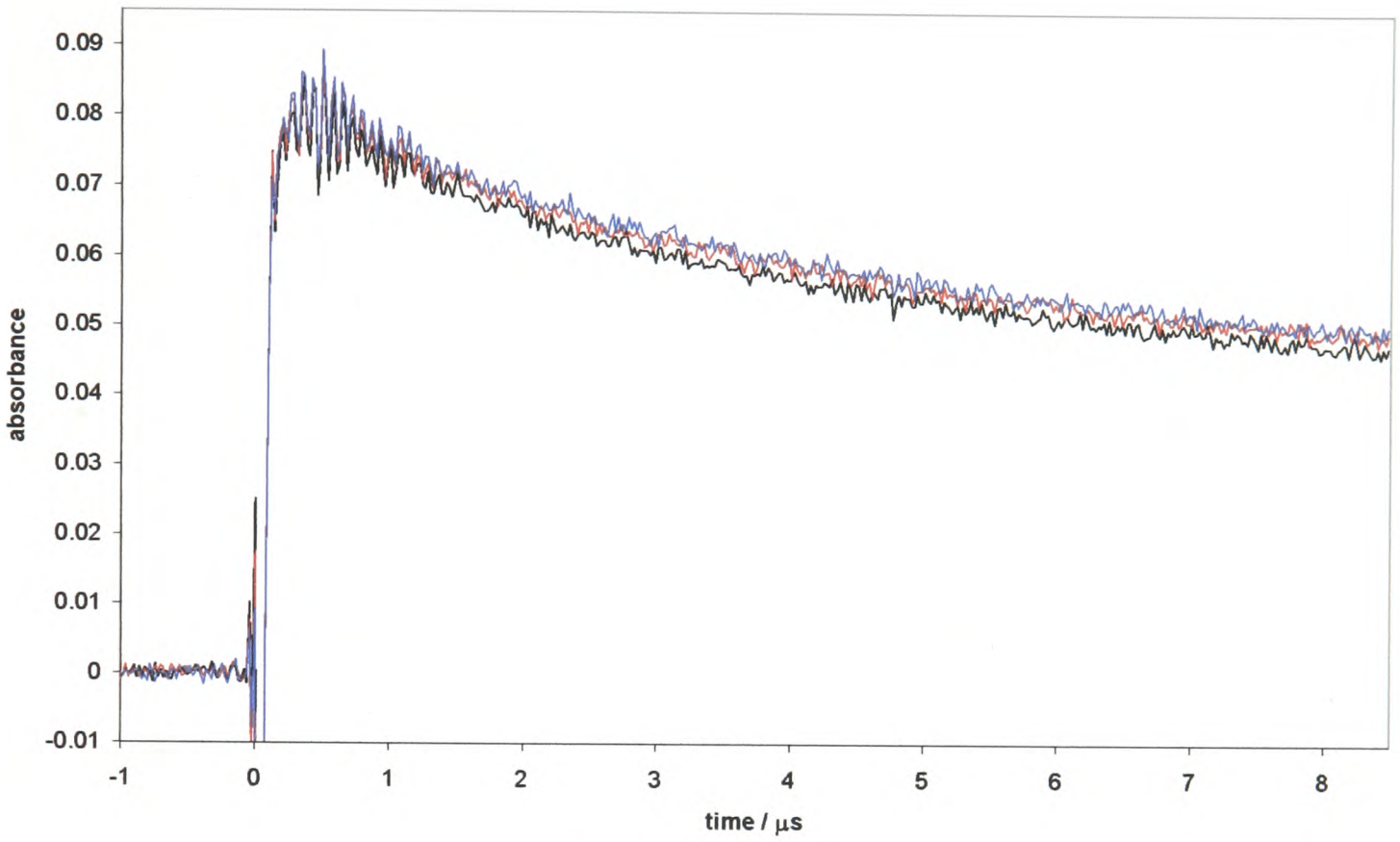


Figure 8.8: Time curves for PC_B/BP-COOH at (●) 0 mT, (●) 8.6 mT, and (●) 17.1 mT

The oscillations seen in the early part of the time curves are experimental artefacts (that are completely reproducible) and stem from ringing of the PMT due to overload by the aforementioned fluorescence spike. Attempts were made to remove them by reducing the voltage on the PMT, but no reduction could be achieved whilst still keeping the absorption signal large enough to observe MFEs. As the oscillations are completely reproducible (and not magnetic field dependent) the difference methods employed for calculation of MFE size are not affected by their presence.

The MFEs can also be seen in MARY curves. Figure 8.9 shows an average of three MARY curves for PC_B/BP-COOH, each of 48 averages per point. The MARY curve shows a clear trend of increasing MFE with increasing magnetic field strength, but no LFEs at this resolution of magnetic field strengths.

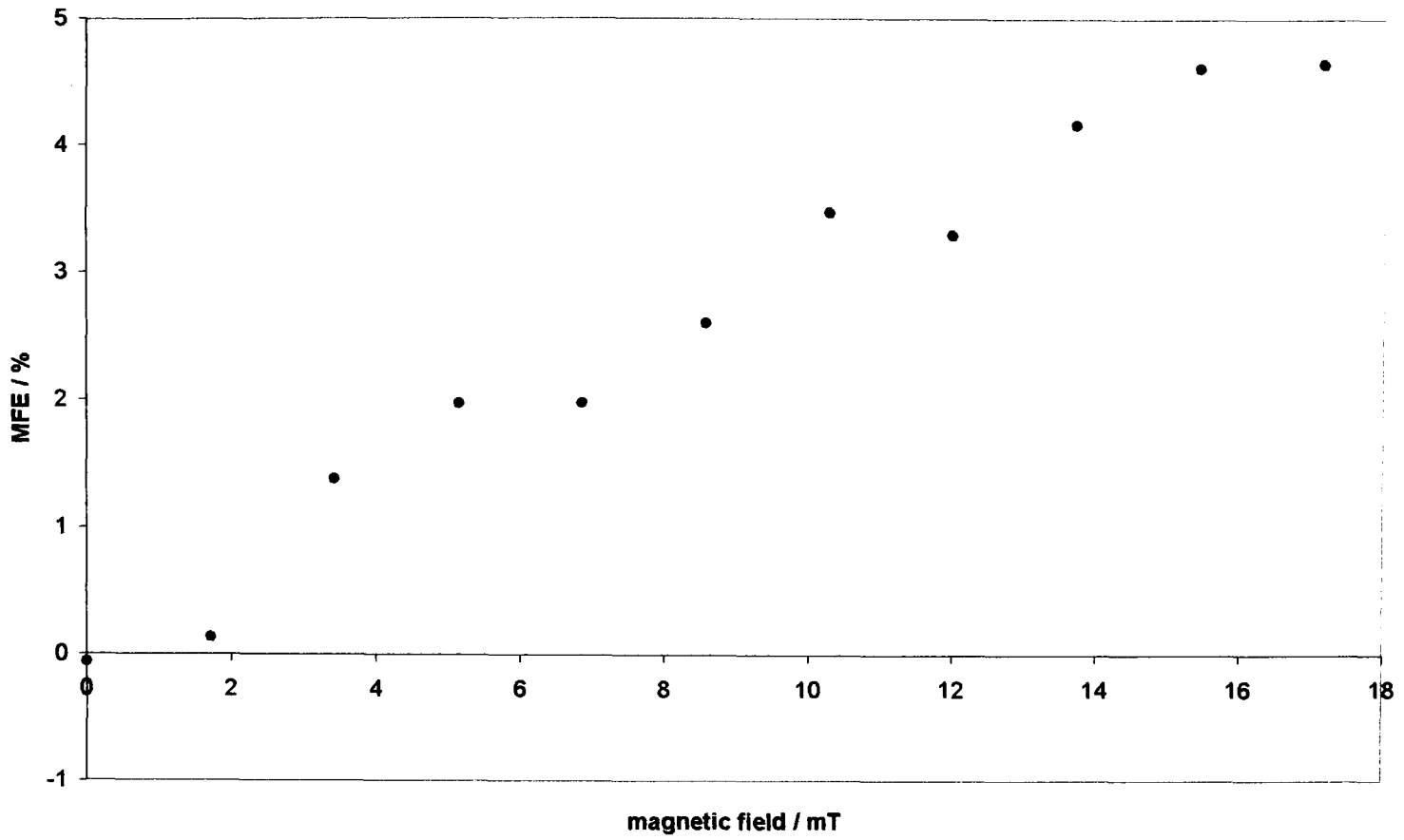


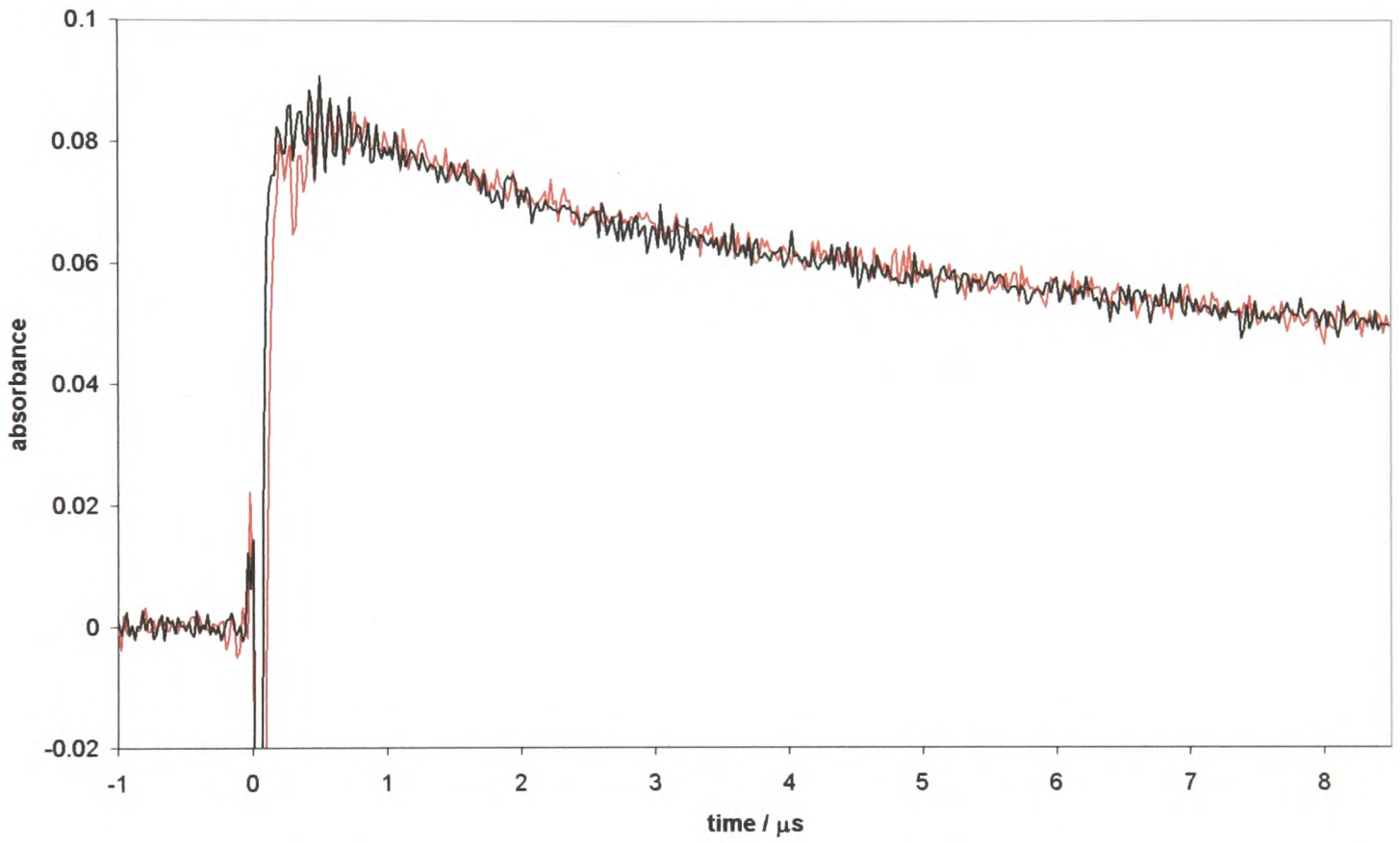
Figure 8.9: MARY curve of PC_B/BP-COOH (EE 2.0%)

The MFEs seen over this range of magnetic field strengths are the smallest seen so far in this thesis for any system that shows a reproducible MFE. At the strongest magnetic field supplied by the Helmholtz coils the MFE in PC_B/BP-COOH is approximately $^2/_3$ the size of that seen in LPC/BP-COOH and approximately half the size of the MFE seen in DODAC/BP.

8.6 Experiments with PC_C Phospholipids

The third type of phospholipid used in this preliminary study of RPs in phospholipid vesicles was PC_C. This was a phospholipid of the same purity as PC_B but with two differences. The first is that it was prepared from egg, rather than from soy like PC_A and PC_B, and hence has a slightly different mix of fatty acid chains. The second difference was in the method of solution preparation, a more complex preparation was undertaken (as described in section 8.1.2) as it was thought that this would give a

higher probability that the BP-COOH is embedded in the interior of the hydrophobic layer of the vesicles than the more simple preparation used for PC_A and PC_B. A comparison of the zero field time curves of PC_B and PC_C with BP-COOH is shown in figure 8.10, and it can be seen that the absorbance size and rate of signal decay is almost identical between the two systems. This suggests that the environment of the RP is also identical in both cases.



8.10: Zero field time curves of (●) PC_B, and (●) PC_C with BP-COOH

As would be expected from such similar time curves the MARY curves of the two systems are also very alike (but not shown here), with the MFEs of the PC_C/BP-COOH system of the same size as those of the PC_B/BP-COOH system seen in figure 8.9.

Zero field time curves of the PC_C/BP-COOH system were also obtained at longer timescales, and the results are shown in figure 8.11. From this figure it can be seen

that the PC_C/BP-COOH undergoes a biexponetnial decay, but over a much longer timescale than any of the systems seen in the previous chapters.

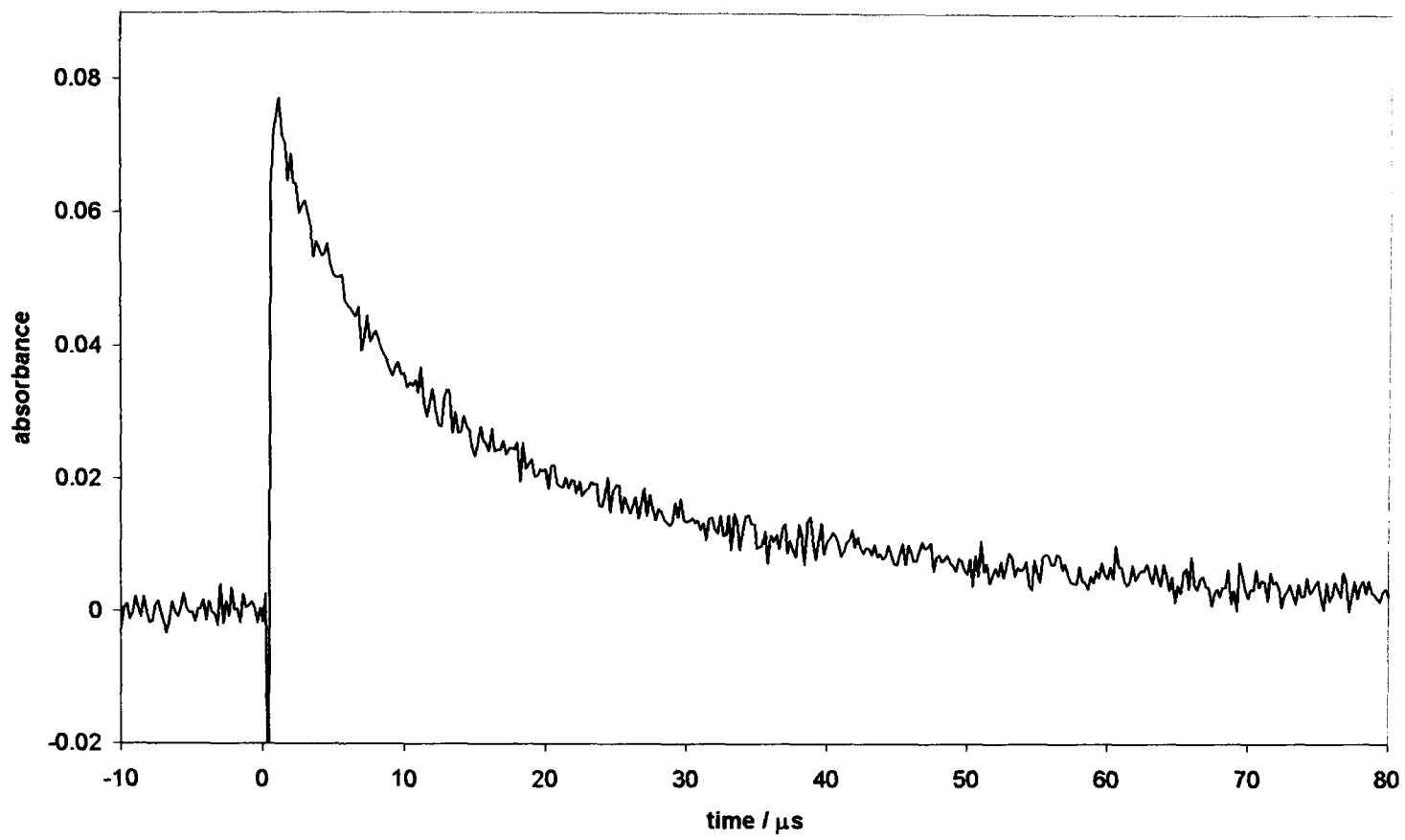


Figure 8.11: Zero field time curve of PC_C/BP-COOH at longer timescales

As great care was taken with the preparation of the PC_C solutions it is very likely that the BP-COOH probe molecules are embedded inside the vesicles. The absorbance signal of figure 8.11 shows a decay rate at least an order of magnitude slower than any other system seen in this thesis so far. The next closest system is DODAC/BP and both the phospholipid and DODAC vesicles show far larger microviscosity than the micellar systems, as is shown in tables 2.1 and 2.3. The diffusion of the radicals is expected to therefore be far slower in these vesicular systems. However, the same argument does not explain the signals seen in LPC micelles, whose microviscosity is the lowest for all of the systems investigated, but whose decay rate of absorption signal is only marginally slower than that seen in DODAC vesicles. Parameters such as aggregation number and size of hydrophobic compartment (which are much larger

in the vesicular systems) might however also contribute to these effects. In summary a very complex set of changing parameters influences the decay kinetics observed.

The final variable investigated with PC_C was the effect of temperature on the PC_C/BP-COOH system. Experiments were performed at 35 °C and 60 °C, and the effect on the normalised time curves is shown in figure 8.12.

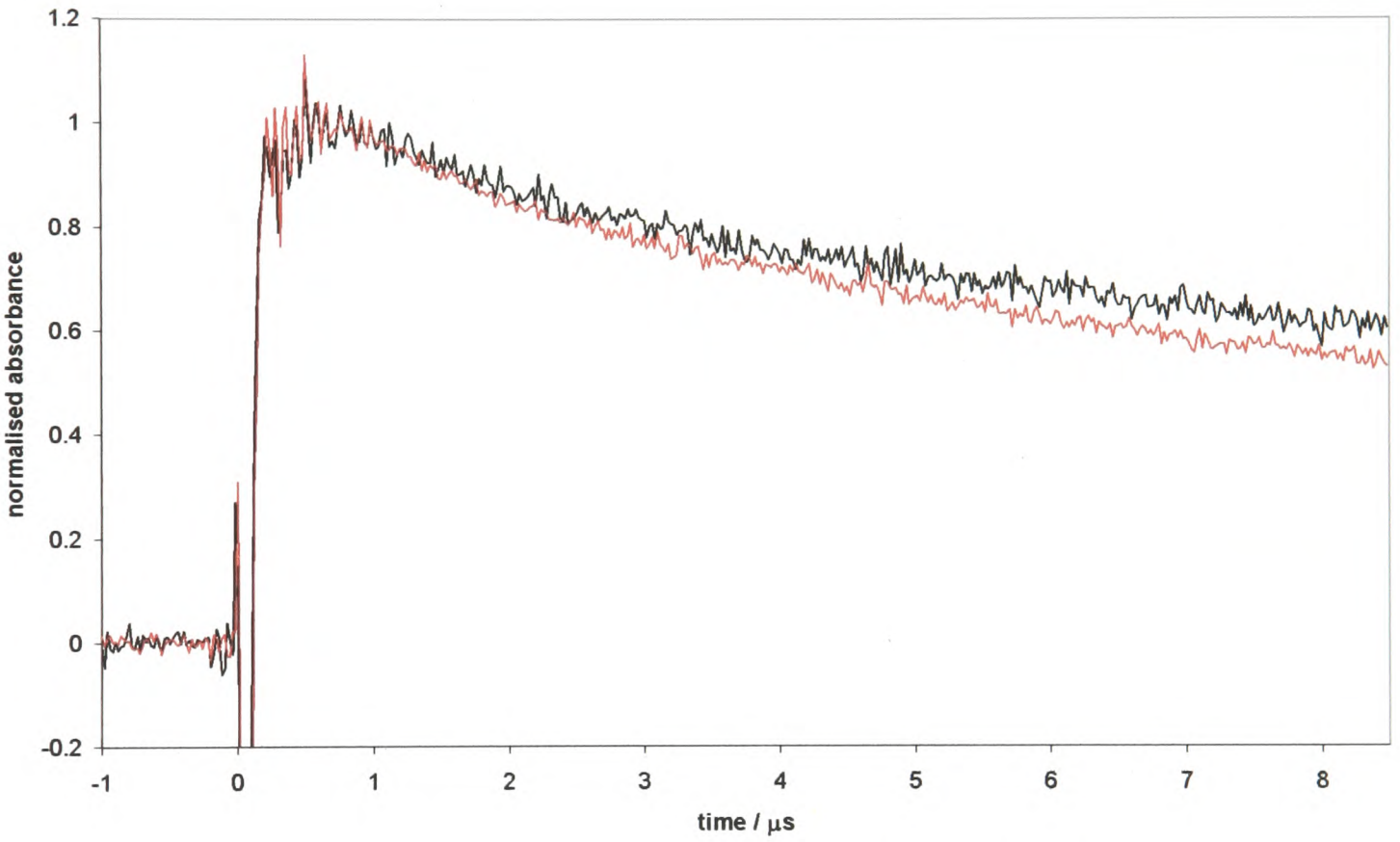


Figure 8.12: Zero field time curves of PC_C/BP-COOH at (•) 35 °C, and (•) 60 °C

The normalised times curves are shown to display the effect of increasing the temperature on the decay rate of the signal. The 60 °C curve exhibits a faster decay rate than the 35 °C curve over the time period in figure 8.12. This is the opposite effect to that seen with DODAC/BP in chapter six, where increasing the temperature from 25 °C to 60 °C resulted in a decrease in the decay rate of the absorbance signal. The DODAC experiments were performed either side of the transition temperature in the DODAC vesicles. The situation with PC_C is more complex as there is not one pure

phospholipid species, but a mixture with varying fatty acid chains. According to the suppliers the two most common components of PC_C are phosphatidyl choline molecules with two 16:0 chains and those with two 18:1 chains. Pure samples of these phospholipids have phase transition temperatures of 42 °C [4] and 20 °C [5] respectively. Studies on phospholipids derived from egg yolk have given phase transitions in the region of 30 °C [6,7]. Whilst there it is assumed that there is no phase transition in the PC_C/BP-COOH system between the temperatures studied, the microviscosity in the vesicle bilayer will decrease with increasing temperature, and hence the RP will become more mobile. However, it is unlikely that the change in environment experienced by the RP in the PC_C/BP-COOH system upon changing from 35 °C to 60 °C will be as great as that experienced by the RP in the DODAC/BP system upon changing from 25 °C to 60 °C.

The MFEs at the two temperatures for the PC_C/BP-COOH system are very similar, resulting in MARY curves that look identical within experimental error (not shown).

8.7 Conclusions and Future Phospholipid Work

The results of this initial work with phospholipid vesicles lead to the following important conclusions. Firstly, an absorption signal can be detected when BP-COOH is incorporated into the phospholipid vesicles, and magnetic field effects can be observed with magnetic field strengths lower than 5 mT. The work with PC_A showed that even with an impure phospholipid sample MFEs can be seen, but a much higher magnetic field strength is needed to overcome the poor signal to noise ratio in this system. Secondly, the results from PC_B and PC_C showed that the more elaborate preparation regime may not be necessary to prepare solutions with a substrate

molecule, such as BP-COOH, incorporated inside the vesicles in the study of magnetic field effects. However, further investigation is required to understand the effects of solution preparation method on variables such as the distribution of vesicle sizes and aggregation numbers.

There still remains a great deal of work to be done with the phospholipid systems. The main priority is to improve the signal to noise ratio and reproducibility, however this will require a redesign of the experimental apparatus, especially if detailed work is to be carried out on the temperature dependence of the time curves and MFEs. It may also be an advantage to work with synthetically derived phospholipids that do not have the mixture of fatty acid chains seen with naturally derived phospholipids. This will incur extra expense, and so any redesign that minimises the amount of solution needed for each experiment would be particularly useful.

Another large area open to further research involves the addition of other chemicals to the phospholipid systems. Not only those which have been used in the past such as hydrogen donors like CHD and THF, but also biologically relevant molecules such as lysophosphatidylcholine and cholesterol which are found in biological membranes.

If LFEs are to be observed then a probe molecule other than BP-COOH will have to be used, as even in SDS no LFE has been recorded with BP-COOH (see section 7.3). This requires a molecule that absorbs at a longer wavelength than the PC, however, this may mean using an excitation source other than the YAG laser. Additionally care will also have to be taken with the solubility of the probe molecule to ensure it resides in the hydrophobic part of the membrane.

SUMMARY

The aim of this thesis was to establish under which confinement conditions magnetic fields can affect the recombination kinetics of neutral radical pairs, to quantify the size of any observed magnetic field effects, and to correlate these with the microenvironment experienced by the radical pair.

For the first time it has been shown that MFEs can be observed on neutral radical pairs in lysophospholipid micelles, and also in phospholipid vesicles, which can be understood as membrane mimetic systems. Thorough work on less complex, and more highly characterised structures such as anionic and cationic micelles, and synthetic vesicles facilitated a systematic approach to these studies by providing a well-founded base of comparative data to guide interpretation of results in more complex systems.

It is the purpose of this last section to summarise in a comprehensive manner the results obtained in the previous chapters, and to discuss any general trends and conclusions that may be drawn from the results obtained from the comparison of these microreactor based, but highly diverse systems. Table S1 summarises the results and parameters that will be used in the discussion below.

The most obvious immediate conclusion from the table in terms of MFE size is that the systems that display the smallest MFEs are those that have the largest size (in terms of hydrophobic volume), namely the DODAC, PC_C, and LPC systems. As these structures contain the largest volumes the RPs therefore have the biggest space to explore without the necessity of either member of the RP leaving the hydrophobic region. The same conclusion is reached for the cationic micelle series, where the MFE decreases with increasing chain length and micelle size. Clearly this statement can

only hold for relatively large systems, for smaller systems (as shown in [1]) a maximum in the MFE size is reached as the micelle size decreases as would be expected for a non-negligible exchange interaction (although this was not the reason given for the maximum in [1]).

System	Size / Å [A]	$T_{3/4}$ / μs	$T_{1/2}$ / μs	$T_{1/4}$ / μs	MFE / % [B]
SDS/BP	17.5	0.16	0.34	0.62	28.3
SDS/BP/CHD		0.12	0.36	1.72	45.2
SDS/BP-COOH		0.16	0.30	0.52	17.6
DTAC/BP	17	0.20	0.40	0.82	45.3
TTAC/BP	19	0.22	0.38	0.66	28.0
CTAC/BP	22	0.28	0.48	0.78	20.7
OTAC/BP		0.3	0.58	1.02	19.0
DTAC/BP/CHD		0.7	1.78	3.76	32.8
CTAC/BP/CHD		0.34	1.22	3.46	24.6
DODAC/BP	50	0.66	1.50	3.34	10.0
DODAC/BP/CHD		0.76	1.72	3.70	5.69
LPC/BT/CHD	27	0.16	1.02	3.30	4.34
LPC/BP-COOH		0.58	1.48	3.16	6.5
PC_C/BP-COOH	37	2.4	7.6	20.8	4.3

Table S1: Parameters and results for various systems studied in this thesis. A: for micelles size indicates micelle radius, for vesicles it indicates bilayer thickness. B: MFE at a magnetic field strength of 17.1 mT

The range of systems investigated in this thesis is very diverse. Hence any attempt to apply one simple type of kinetic model, such as that seen in [1] (which in turn was based on a model by Scaiano et al. [2]), or the more versatile but fragile model introduced in section 3.8, proved impossible as the absorption characteristics of the systems studied are so vastly different, and the role of F pair recombination alters between systems (including those where geminate recombination cannot be detected, *i.e.* the absorbance decay follows mono-phasic kinetics). However, the method of comparing fractional lifetimes is completely transferable between all systems, and provides a measure of the decay rate. To demonstrate this fact figure S1 shows the

fractional lifetimes of eight different systems in four different constraining structures, and the effect that the addition of CHD has upon them.

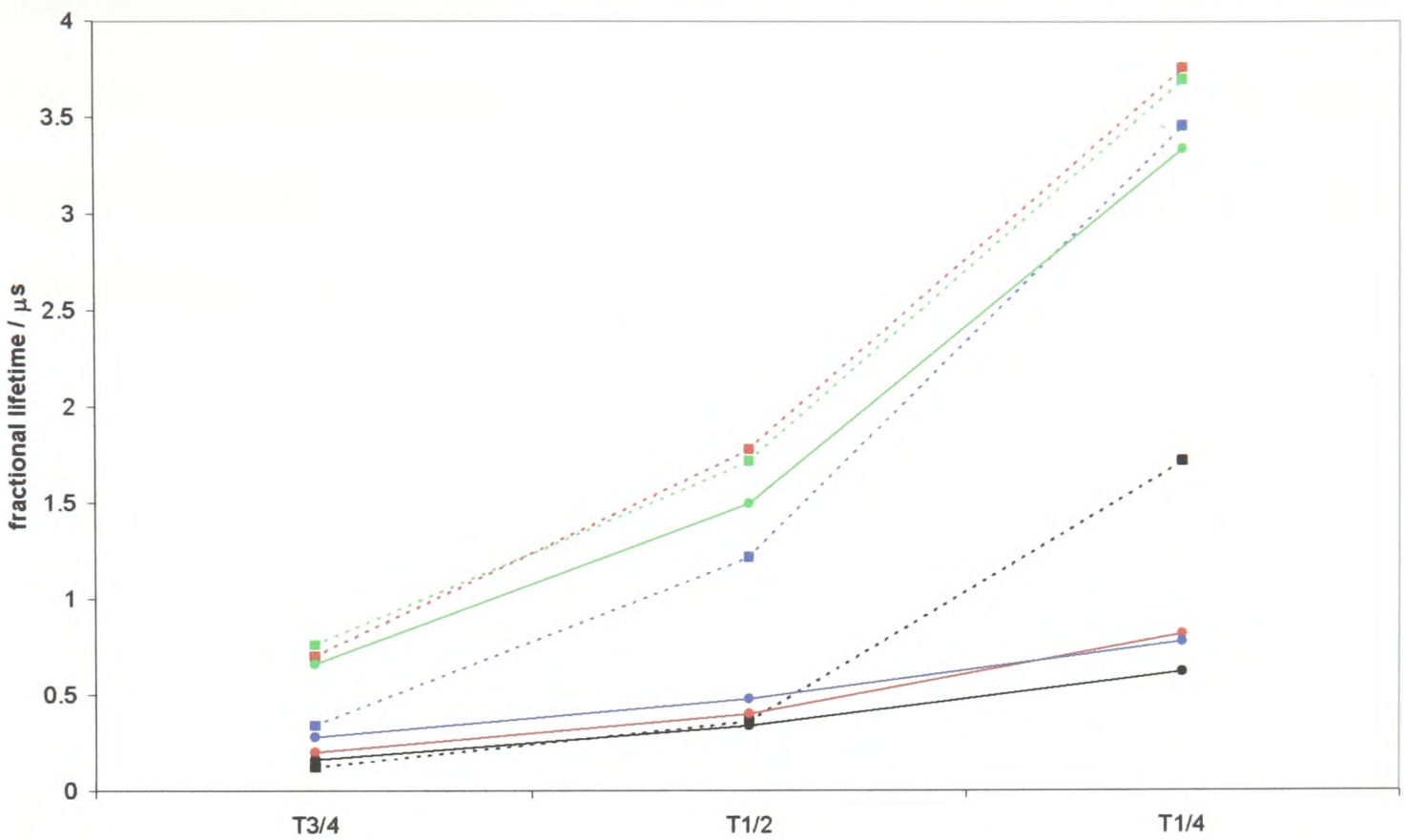


Figure S1: Fractional lifetimes of BP in structures of (•) SDS, (•) DTAC, (•) CTAC, and (•) DODAC. Solid lines are in the absence of CHD, dashed lines indicate the presence of CHD

In each case the addition of CHD causes an increase in the gradient between the $T_{1/2}$ and $T_{1/4}$ times, and in the case of the micelles addition of the CHD also causes an increase in gradient between the $T_{3/4}$ and $T_{1/2}$ times. In this type of graph a large gradient indicates a long period of time between any of the absorption fractions, and hence a slow rate of absorbance decay. It is on the longer timescales, between $T_{1/2}$ and $T_{1/4}$ that the addition of CHD seems to have most influence, causing a decrease in signal decay rates in all cases. This is presumed to be due to the increased mobility of the CHD derived radical over a surfactant derived radical, and hence a greater escape rate from the geminate radical pair. The gradients of all the curves where CHD is present in figure S1 are very similar, this means that the decay kinetics for all four systems are also similar, and hence it must be the presence of the CHD derived radical which is determining the F pair recombination kinetics.

The influence of decay kinetics does not however provide a clear link to the size of the MFEs displayed by the systems studied. Of those shown in figure S1 addition of CHD caused an increase in MFE size for SDS and CTAC, and a decrease in MFE size for DTAC and DODAC. Of the three fractional lifetimes, the one that shows the strongest correlation with MFE size is $T_{3/4}$, and a plot of $T_{3/4}$ *vs.* MFE at 17.1 mT for all the different systems studied is shown in figure S2.

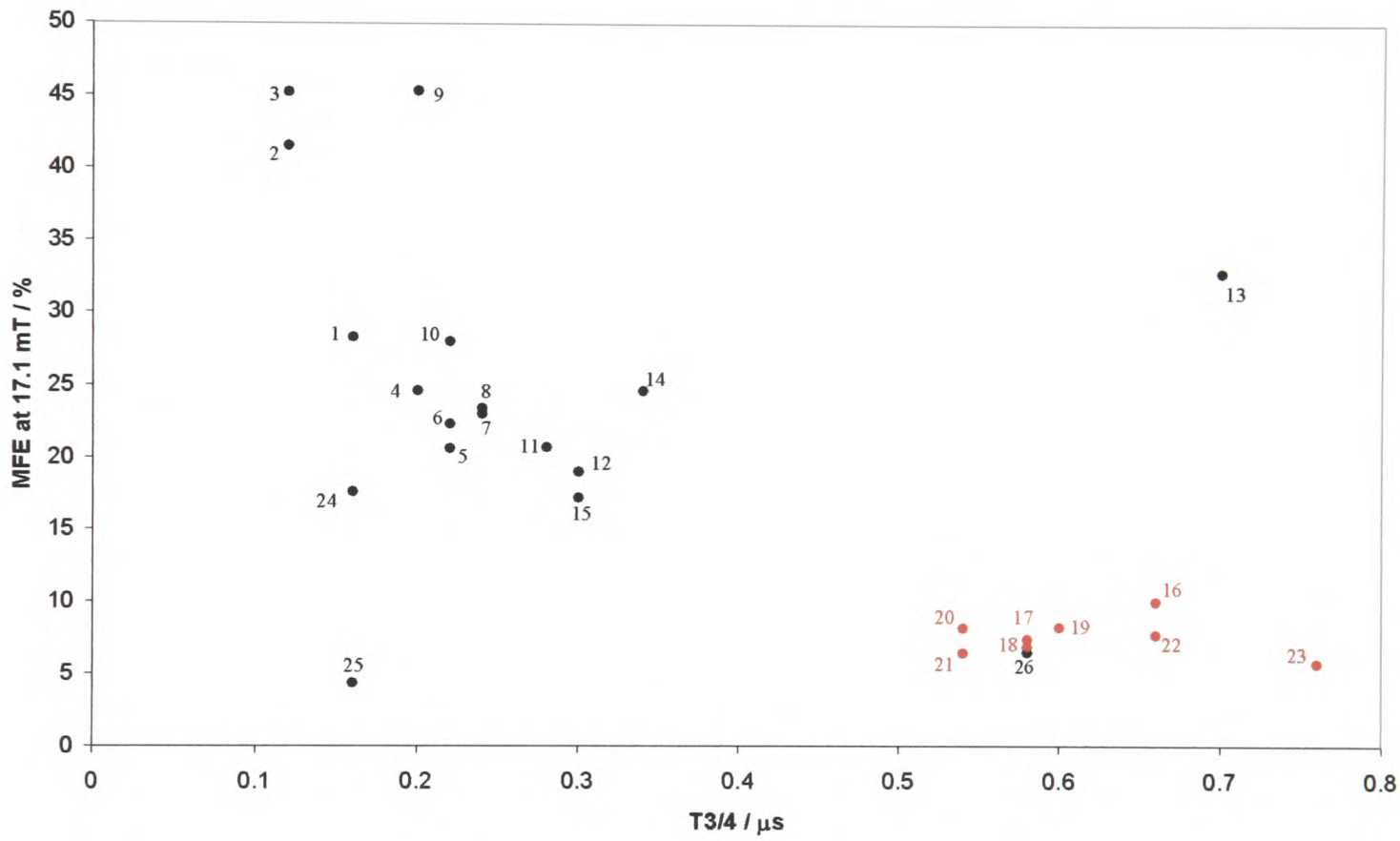


Figure S2: The correlation between $T_{3/4}$ and MFE for (•) micellar and (•) vesicular systems. The numbering refers to the labels in table S2

There is a very rough correlation that a decrease in the initial decay rate (and hence a longer $T_{3/4}$ time) leads to smaller MFE sizes, but this clearly does not hold in all cases. Of the three fractional lifetimes ($T_{3/4}$, $T_{1/2}$, and $T_{1/4}$) it is the $T_{3/4}$ times that show the strongest correlation with MFE size, implying that it is the RP behaviour at short timescales that determines the influence of the magnetic field on the recombination kinetics.

The points in figure S2 fall into two distinct groups, aside from three nonconforming points (13, 25, and 26). The first group is in the top left of the diagram and comprises the micellar systems, characterised by fast initial decay rates and large MFEs. The second group is in the bottom right and contains the vesicular systems (plus point 26, LPC/BP-COOH) with slower initial decays and lower MFEs. Both LPC points do not fit into the general scheme outlined above, with LPC/BT/CHD having an unusually fast recombination for its MFE size (or vice versa) and LPC/BP-COOH falling in with the vesicle systems. As discussed in chapter seven LPC micelles are larger than any of the other micelles studied here, and also have a zwitterionic head group, in contrast to either an anionic or cationic head group as seen in chapters four and five. The other unusual point from figure S2 is point 13, which is for DTAC/BP/CHD. As discussed in chapter five this system shows unusual behaviour in comparison to the other cationic micellar systems, possibly due to the smaller size of the DTAC micelles and hence the greater destabilising effect of a relatively large concentration of CHD on the micelle structure. As shown in chapter five the cationic micelle systems in the absence of CHD (points 9 to 12) show a very clear trend of decreasing $T_{3/4}$ time with decreasing MFE size, and these trends are made even more obvious by the method of depiction of figure S2.

It might have been expected that the transition between OTAC and DODAC would mirror that between LPC and PC systems, as in both cases the head group remains almost the same, whilst an extra hydrophobic tail was added, but the trends seen do not reflect this.

This work does show however, that the only reliable way to gauge the influence of magnetic fields on these types of radical recombination reactions is to observe the

absorbance traces at varying magnetic field strengths. This may seem tautological, but it has been shown that there is no reliable way to predict the size of the MFEs from other factors, such as the zero field absorbance curves, the size of the confining media, the hyperfine couplings of the RP, or additional hydrogen donors which may be added to the system. It is conceivable that an as yet unknown complex combination of these, and perhaps other factors holds the key to predicting the magnetic field dependent behaviour, but this thesis has shown that no simple relationship holds for any of these parameters, or any of their mutual relationships.

No	System	$T_{3/4}$ / μs	MFE / % [A]	No	System	$T_{3/4}$ / μs	MFE / % [A]
1	SDS/BP	0.16	28.3	14	CTAC/BP/CHD	0.34	24.6
2	SDS/BP/CH	0.12	41.5	15	CTAC/BP/THF	0.30	17.2
3	SDS/BP/CHD	0.12	45.2	16	DODAC/BP (25/2)	0.66	10.0
4	SDS/BP/PrOH	0.20	24.6	17	DODAC/BP (30/2)	0.58	7.41
5	SDS/BP/THF	0.22	20.6	18	DODAC/BP (35/2)	0.58	6.88
6	$SDS/BP_{d10}/THF$	0.22	22.3	19	DODAC/BP (40/2)	0.60	8.21
7	$SDS/BP/THF_{d8}$	0.24	23.0	20	DODAC/BP (25/2.5)	0.54	8.18
8	$SDS/BP_{d10}/THF_{d8}$	0.24	23.4	21	DODAC/BP (30/2.5)	0.54	6.44
9	DTAC/BP	0.20	45.3	22	DODAC/BP (40/2.5)	0.66	7.71
10	TTAC/BP	0.22	28.0	23	DODAC/BP/CHD (25/2)	0.76	5.69
11	CTAC/BP	0.28	20.7	24	SDS/BP-COOH	0.16	17.6
12	OTAC/BP	0.30	19.0	25	LPC/BT/CHD	0.16	4.34
13	DTAC/BP/CHD	0.70	32.8	26	LPC/BP-COOH	0.58	6.50

Table S2: $T_{3/4}$ times and MFE sizes for the systems shown in figure S2. A: Measured at 17.1 mT. Figures in brackets for DODAC give concentrations for DODAC/BP / mM

REFERENCES

CHAPTER 1

[1] Steiner, UE and Ulrich, T. *Chem. Rev.*, **89**, 1, 51-147, (1989)
[2] Grissom, CB. *Chem. Rev.*, **95**, 1, 3-24, (1995)
[3] Brocklehurst, B. *Chem. Soc. Rev.*, **31**, 5, 301-311, (2002)
[4] Woodward, JR. Prog. React. Kinet. Mec., 27, 3, 165-207, (2002)
[5] Timmel, CR and Henbest, KB. In Press
[6] Kaptein, R and Oosterhof, JL. *Chem. Phys. Lett.*, **4**, 4, 195-197, (1969)
[7] Closs, GL. *J. Am. Chem. Soc.*, **91**, 16, 4552-4554, (1969)
[8] Hayashi, H and Nagakura, S. *Bull. Chem. Soc. Jpn.*, **57**, 2, 322-328, (1984)
[9] Nishizawa, K et al. *Mol. Phys.*, **100**, 8, 1137-1146, (2002)
[10] Shkrob, IA et al. *Chem. Phys.*, **153**, 3, 443-455, (1991)
[11] Stass, DV et al. *Chem. Phys. Lett.*, **233**, 4, 444-450, (1995)
[12] Brockelhurst, B and McLauchlan, KA. *Int. J. Radiat. Biol.*, **69**, 1, 3-24, (1996)
[13] Timmel, CR et al. *Mol. Phys.*, **95**, 1, 71-89, (1998)
[14] Eveson, RW et al. *Int. J. Radiat. Biol.*, **76**, 11, 1509-1522, (2000)
[15] World Health Organisation, *Fact Sheet 181*, (1998)
[16] Ahlbom, A et al. *Lancet*, **342**, 8882, 1295-1296, (1993)
[17] Lacy-Hulbert, A et al. *FASEB J.*, **12**, 6, 395-420, (1998)
[18] Cheng, KK et al. *Lancet*, **354**, 9194, 1925-1931, (1999)
[19] Wiltschko, W and Wiltschko, R. *Science*, **176**, 4030, 62-64, (1972)
[20] Wiltschko, R and Wiltschko, W. *Magnetic orientation in animals*, Springer-Verlag (1995)
[21] Ritz, T et al. *Nature*, **429**, 6988, 177-180, (2004)
[22] Hoff, AJ. *Quart. Rev. Biophys.*, **14**, 4, 599-665, (1981)
[23] Harkins, TT and Grissom, CB. *Science*, **263**, 5149, 958-960, (1994)
[24] Scaiano, JC et al. *J. Am. Chem. Soc.*, **104**, 21, 5673-5679, (1982)
[25] Kitahama, Y et al. *J. Phys Chem. A.*, **108**, 5, 754-757, (2004)
[26] McLauchlan, KA and Nattrass, SR. *Mol. Phys.*, **65**, 6, 423-438, (1988)
[27] Brocklehurst, B. *Nature*, **221**, 5184, 921-923, (1969)
[28] McLauchlan, KA and Steiner, UE. *Mol. Phys.*, **73**, 2, 241-263, (1991)
[29] Timmel, C.R. D.Phil. thesis, Oxford (1998)
[30] McLauchlan, K.A. Private communication
[31] Sakaguchi, Y et al. *J. Phys. Chem.*, **86**, 16, 3177-3184, (1982)
[32] Fujiwara, Y et al. *Chem. Lett.*, **1997**, 5, 435-436, (1997)
[33] Hayashi, H. *Dynamic Spin Chemistry*, Wiley, 7-47, (1998)
[34] Wakasa, M. *J. Phys. Chem.*, **97**, 51, 13444-13446, (1993)
[35] Closs, GL and Doubleday, CE. *J. Am. Chem. Soc.*, **95**, 8, 2735-2736, (1973)
[36] Chuang, TJ et al. *Chem. Phys. Lett.*, **25**, 2, 201-205, (1974)
[37] Adrian, FJ. *J. Chem. Phys.*, **53**, 8, 3374-3375, (1970)
[38] Wakasa, M et al. *Chem. Lett.*, 1994, 10, 1941-1944, (1994)
[39] Brocklehurst, B. *J. Chem. Soc. Faraday trans. II*, **72**, 1869-1884, (1976)
[40] Till, U et al. *Chem. Phys. Lett.*, **298**, 1-3, 7-14, (1998)
[41] Kleinman, MH et al. *Photochem. and Photobiol.*, **67**, 2, 198-205, (1998)
[42] Batchelor, SN et al. *J. Phys. Chem.*, **97**, 50, 13250-13258, (1993)
[43] Mohan, H and Mittal, JP. *Chem. Phys. Lett.*, **235**, 5-6, 444-450, (1995)
[44] Grampp, G et al. *Mol. Phys.*, **100**, 8, 1063-1070, (2002)

[45] Henbest, KB et al. *J. Am. Chem. Soc.*, **126**, 26, 8102-8103, (2004)
[46] Turro, NJ and Weed, GC. *J. Am. Chem. Soc.*, **105**, 7, 1861-1868, (1983)
[47] Sakaguchi, Y and Hayashi, H. *J. Phys. Chem.*, **88**, 7, 1437-1440, (1984)
[48] Woodward, JR and Sakaguchi, Y. *J. Phys. Chem. A*, **105**, 16, 4010-4018, (2001)
[49] Kleinman, MH. *Photochem. and Photobiol.*, **68**, 5, 710-718, (1998)
[50] Barra, M et al. *Langmuir*, **8**, 10, 2390-2395, (1992)
[51] Baretz, BH and Turro, NJ. *J. Am. Chem. Soc.*, **105**, 5, 1309-1316, (1983)
[52] Turro, NJ et al. *J. Am. Chem. Soc.*, **107**, 12, 3739-3741, (1985)
[53] Turro, NJ. *Tetrahedron*, **43**, 7, 1589-1616, (1987)
[54] Staerk, H and Razi Naqvi K. *Chem. Phys. Lett.*, **50**, 3, 386-388, (1977)

CHAPTER 2

[1] McLauchlan, KA and Steiner, UE. *Mol. Phys.*, **73**, 2, 241-263, (1991)
[2] Southall, NT et al. *J. Phys. Chem. B*, **106**, 3, 521-533 (2002)
[3] Tanford, C. *The Hydrophobic Effect: Formation of Micelles and Biological Membranes*, Wiley-Interscience (1980)
[4] Zhao, S et al. *Colloid Polym. Sci.*, **276**, 12, 1125-1130, (1998)
[5] Fennel-Evans, D and Wennerstrom, H. *The colloidal domain*, VCH (1994)
[5A] Han, B et al. *J. Coll. Interf. Sci.*, **218**, 1, 145-151, (1999)
[6] Eveson, RW et al. *Int. J. Radiat. Biol.*, **76**, 11, 1509-1522, (2000)
[7] Nishizawa, K et al. *Mol. Phys.*, **100**, 8, 1137-1146, (2002)
[8] Scaiano, JC et al. *J. Am. Chem. Soc.*, **104**, 21, 5673-5679, (1982)
[9] Woodward, JR and Sakaguchi, Y. *J. Phys. Chem. A*, **105**, 16, 4010-4018, (2001)
[10] Cozens, FL and Scaiano, JC. *J. Am. Chem. Soc.*, **115**, 12, 5204-5211, (1993)
[11] Turro, NJ et al. *J. Phys. Chem.*, **92**, 2, 433-437, (1988)
[12] Plueckthun, A and Dennis, EA. *Biochemistry*, **21**, 8, 1743-1750, (1982)
[13] Bergelson, LD et al. *FEBS Letters*, **2**, 2, 87-90, (1968)
[14] Lianos, P and Zana, R. *J. Coll. Interf. Sci.*, **84**, 1, 100-107, (1981)
[15] Roelants, E and De Schryver FC. *Langmuir*, **3**, 2, 209-214, (1987)
[16] Hayashi, H et al. *Chem. Lett.*, **23**, 12, 2407-2410, (1994)
[17] Fennell Evans, D. *Langmuir*, **4**, 1, 3-12, (1988)
[18] Cang, H et al. *J. Phys. Chem. B*, **105**, 41, 10007-10015, (2001)
[19] Sepulveda, L and Cortes, J. *J. Phys. Chem.*, **89**, 24, 5322-5324, (1985)
[20] Kang, KH et al. *Bull. Kor. Chem. Soc.*, **22**, 9, 1009-1014, (2001)
[21] Onda, M et al. *J. Biochem.*, **130**, 5, 613-620, (2001)
[22] Szajdzinska-Pietek, E et al. *J. Am. Chem. Soc.*, **120**, 17, 4215-4221, (1998)
[23] Nakagaki, M et al. *Chem. Pharm. Bull.*, **34**, 11, 4486-4493, (1986)
[24] Duplatre, G et al. *J. Phys. Chem.*, **100**, 41, 16608-16612, (1996)
[25] Imae, T and Ikeda, S. *J. Phys. Chem.*, **90**, 21, 5216-5223, (1986)
[26] Pignol, D et al. *J. Biol. Chem.*, **275**, 6, 4220-4224, (2000)
[27] Stilbs, P et al. *J. Phys. Chem.*, **87**, 23, 4762-4769, (1983)
[28] Malliaris, A et al. *J. Phys. Chem.*, **89**, 12, 2709-2713, (1985)
[29] McConnell, HM and Kornberg, RD. *Biochemistry*, **10**, 7, 1111-1120, (1971)
[30] Shaw, JM et al. *Biochemistry*, **16**, 19, 4156-4163, (1977)
[31] Saunders, L et al. *J. Pharm. Pharmacol.*, **14**, 567-572, (1962)
[32] Fendler, JH. *Acc. Chem. Res.*, **13**, 1, 7-13, (1980)

[33] Smith, R and Tanford, C. *J. Mol. Biol.*, **67**, 1, 75-83, (1972)
[34] Haberland, ME and Reynolds, JA. *J. Biol. Chem.*, **250**, 17, 6636-6639, (1975)
[35] Lee, AG. *Biochim. Biophys. Acta*, **472**, 237-281, (1977)
[36] Kano, K et al. *J. Am. Chem. Soc.*, **101**, 15, 4030-4037, (1979)
[37] Kajiyama, T et al. *Chem. Lett.*, **1979**, 6, 645-648, (1979)
[38] Barra, M et al., *Langmuir*, **8**, 10, 2390-2395, (1992)
[39] Kleinman, MH et al. *Photochem. Photobiol.*, **68**, 5, 710-718, (1998)
[40] Van Golde, LMG. et al. *Chem. Phys. Lipids*, 1, 3, 282-293, (1967)
[41] Shafirovich, VY et al. *Photochem. Photobiol.*, **55**, 3, 473-476, (1992)
[42] Shafirovich, VY et al. *J. Am. Chem. Soc.*, **117**, 22, 6093-6100, (1995)
[43] Herrmann, U and Fendler, JH. *Chem. Phys. Lett.*, **64**, 2, 270-274, (1979)
[44] Tran, CD et al. *J. Am. Chem. Soc.*, **100**, 5, 1622-1624, (1978)
[45] Huang, C and Mason, JT. *Proc. Natl. Acad. Sci. USA*, **75**, 1, 308-310, (1978)

CHAPTER 3

[1] Sakaguchi, Y et al. *Chem. Phys Lett.*, **72**, 3, 420-423, (1980)
[2] Hayashi, H. et al., *Chem. Lett.*, 9, 1149-1152 (1980)
[3] Sakaguchi, Y et al. *Chem. Phys. Lett.*, **82**, 2, 213-216, (1981)
[4] Scaiano, JC et al. *J. Am. Chem. Soc.*, **104**, 21, 5673-5679, (1982)
[5] Sakaguchi, Y et al. *J. Phys. Chem.*, **86**, 16, 3177-3184, (1982)
[6] Tanimoto, Y et al. *J. Phys. Chem.*, **87**, 5, 724-726, (1983)
[7] Sakaguchi, Y and Hayashi, H. *J. Phys. Chem.*, **88**, 7, 1437-1440, (1984)
[8] Levin, PP and Kuzmin, VA. *Chem. Phys.*, **162**, 1, 79-93, (1992)
[9] Woodward, JR and Sakaguchi Y. *J. Phys. Chem. A*, **105**, 16, 4010-4018, (2001)
[10] Gould, IR et al. *J. Am. Chem. Soc.*, **107**, 16, 4607-4612, (1985)
[11] Turro, NJ et al. *J. Phys. Chem.*, **92**, 2, 433-437, (1988)
[12] Tarasov, VF et al. *Chem. Phys.*, **135**, 3, 391-404, (1989)
[13] Cozens, FL and Scaiano, JC. *J. Am. Chem. Soc.*, **115**, 12, 5204-5211, (1993)
[14] Shkrob, IA et al. *Chem. Phys.*, **153**, 3, 443-455, (1991)
[15] Tarasov, VF et al. *Z. Phys. Chem.*, **182**, S, 227-244, (1993)
[16] Eveson, RW et al. *Int. J. Radiat. Biol.*, **76**, 11, 1509-1522, (2000)
[17] Kiryukhin, YI, et al. *Khimiya Vysokikh Energii*, **13**, 6, 515-521, (1979)
[18] Wolf, MW et al. *J. Am. Chem. Soc.*, **99**, 2, 526-531, (1977)
[18A] Taylor, JW et al. *J. Phys. Chem. A*, **108**, 35, 7193-7203, (2004)
[19] Batchelor, SN et al. *J. Phys. Chem.*, **97**, 50, 13250-13258, (1993)
[20] Grampp, G et al. *Mol. Phys.*, **100**, 8, 1063-1070, (2002)
[21] Sakaguchi, Y and Woodward, JR. *Appl. Magn. Reson.*, **23**, 3, 319-331, (2003)

CHAPTER 4

[1] Curtis, AF. D.Phil. thesis, Oxford, 2002
[2] Scaiano, JC et al., *J. Am. Chem. Soc.*, **104**, 21, 5673-5679, (1982)
[3] Encinas, MV and Scaiano, JC. *J. Am. Chem. Soc.*, **103**, 21, 6393-6397, (1981)
[4] Lutz, H et al. *J. Phys. Chem.*, **76**, 6, 821-822, (1972)
[5] Urruti, EH and Kilp, T. *Macromolecules*, **17**, 1, 50-54, (1984)
[6] Griller, D et al. *J. Am. Chem. Soc.*, **103**, 3, 619-623, (1981)

[7] Konishi, Y and Okazaki, M. *Appl. Magn. Reson.*, **17**, 4, 597-608, (1999)
[8] Woodward, JR and Sakaguchi, Y. *J. Phys. Chem. A*, **105**, 16, 4010-4018, (2001)
[9] Kometani, N et al. *Phys. Chem. Chem. Phys.*, **4**, 20, 5142-5147, (2002)
[10] Cohen, SG et al. *Chem. rev.*, **73**, 2, 141-161, (1973)
[11] Cohen, SG and Cohen, JI. *J. Am. Chem. Soc.*, **89**, 1, 164-165, (1967)
[12] P_{ow} data from SciFinder Scholar , calculated using ACD Software
[13] Eveson, RW et al. *Int. J. Radiat. Biol.*, **76**, 11, 1509-1522, (2000)
[14] Sakaguchi, Y and Woodward, JR. Appl. Magn. Reson., 23, 3, 319-331
[15] Brocklehurst, B and McLauchlan, KA. *Int. J. Radiat. Biol.*, **69**, 1, 3-24, (1996)
[16] Stass, DV et al. *Chem. Phys. Lett.*, **233**, 4, 444-450, (1995)
[17] Norman, S. Private Communication
[18] Timmel, CR et al. *Mol. Phys.*, **95**, 1, 71-89, (1998)
[19] Weller, A et al. *Chem. Phys. Lett.*, **96**, 1, 24-27, (1983)
[20] Sakaguchi, Y and Hayashi, H. *Chem. Lett.*, **1993**, 7, 1183-1186, (1993)
[21] Hayashi, H and Nagakura, S. *Bull. Chem. Soc. Jap.*, **57**, 2, 322-328, (1984)
[22] Tominaga, K et al. *J. Phys. Chem.*, **95**, 9, 3671-3676, (1991)
[23] Justinek, M et al. *J. Am. Chem. Soc.*, **126**, 17, 5635-5646, (2004)
[24] Gatenby M.P. Part II Thesis, Oxford, 2001
[25] Wilson, R. *J. Chem. Soc. B*, **1968**, 84-90, (1968)
[26] Sakaguchi, Y et al. *Chem. Phys. Lett.*, **82**, 2, 213-216, (1981)
[27] Sakaguchi, Y et al. *J. Phys. Chem.*, **86**, 16, 3177-3184, (1982)
[28] Paul, H and Fischer, H. *Helv. Chim. Acta*, **56**, 5, 1575-1594, (1973)
[29] Gilbert, BC and Trenwith, M. *J. Chem. Soc. Perkin Trans. II*, **1975**, 10, 1083-1090, (1975)
[31] Maeda, K et al. *RIKEN Rev.*, **44**, 85-87, (2000)
[30] Cirelli, G et al. *Chem. Phys.*, **72**, 1-2, 15-34, (1982?)
[32] de Kanter, FJJ et al. *Mol. Phys.*, **34**, 3, 857-874, (1977)
[33] Till, U et al. *Chem. Phys. Lett.*, **298**, 1, 7-14, (1998)

CHAPTER 5

[1] Tarasov, VF et al. *J. Am. Chem. Soc.*, **114**, 24, 9517-9526, (1992)
[2] Eveson, RW et al. *Int. J. Radiat. Biol.*, **76**, 11, 1509-1522, (2000)
[3] Thomas, PG. Part II Thesis, Oxford, 2000
[4] Cozens, FL and Scaiano, JC. *J. Am. Chem. Soc.*, **115**, 12, 5204-5211, (1993)
[5] Turro, NJ et al. *J. Am. Chem. Soc.*, **101**, 24, 7435-7437, (1979)
[6] Turro, NJ and Weed, GC. *J. Am. Chem. Soc.*, **105**, 7, 1861-1868, (1983)
[7] Sakaguchi, Y and Hayashi, H. *Chem. Phys.*, **162**, 1, 119-129, (1992)

CHAPTER 6

[1] Barra, M et al. *Langmuir*, **8**, 10, 2390-2395, (1992)
[2] Fendler, JH. *Acc. Chem. Res.*, **13**, 1, 7-13, (1980)
[3] Herrmann, U and Fendler, JH. *Chem. Phys. Lett.*, **64**, 2, 270-274, (1979)
[4] Han, B et al. *J. Coll. Interf. Sci.*, **218**, 1, 145-151, (1999)
[5] Kano, K et al. *J. Am. Chem. Soc.*, **101**, 15, 4030-4037, (1979)
[6] Thomas, PG. Part II Thesis, Oxford, 2000

CHAPTER 7

[1] Naguib, YMA et al. *J. Phys. Chem.*, **91**, 11, 3033-3036, (1987)
[2] Kawai, A et al. *J. Phys. Chem. A*, **105**, 42, 9628-9636, (2001)
[3] Ortica, F et al. *J. Phys. Chem. A*, **103**, 10, 1335-1341 (1999)
[4] Seetula, JA and Slagle, IR., *Chem. Soc. Faraday Trans.*, 93, 9, 1709-1719, (1997)
[5] Griller D and Wayner DDM., *Pure. Appl. Chem.*, **61**, 4, 717-724, (1989)
[6] Solubility data from SciFinder Scholar , calculated using ACD Software
[7] Woodward, JR. D.Phil. Thesis, Oxford, 1997
[8] Levin, PP and Kuzmin, VA. *Chem. Phys.*, **162**, 1, 79-93, (1992)
[9] Thomas, PG. Part II Thesis, Oxford, 2000
[10] Neta, P and Schuler, RH. *J. Phys. Chem.*, **77**, 11, 1368-1370, (1973)
[11] Neta, P et al. *J. Phys. Chem.*, **76**, 6, 847-853, (1972)
[12] Hudson A and Hussain HA. *J. Chem. Soc. B*, **1969**, 793-796, (1969)
[13] Woodward, JR and Sakaguchi, Y. *J. Phys. Chem. A*, **105**, 16, 4010-4018, (2001)
[14] Lianos, P and Zana, R. *J. Colloid. Interf. Sci.*, **84**, 1, 100-107, (1981)
[15] Hayashi, H et al. *Chem. Lett.*, **23**, 12, 2407-2410, (1994)

CHAPTER 8

[1] Czarniecki, MF and Breslow, R. *J. Am. Chem. Soc.*, **101**, 13, 3675-3676, (1979)
[2] Shafirovich, VY et al. *J. Am. Chem. Soc.*, **117**, 22, 6093-6100, (1995)
[3] Nishizawa, K et al. *Mol. Phys.*, **100**, 8, 1137-1146, (2002)
[4] Simon, S et al. *Bioch. et Bioph. Acta*, **375**, 3, 317-326, (1975)
[5] Barton, P and Gunstone, F. *J. Biol. Chem.*, **250**, 12, 4470-4476, (1975)
[6] Gruzderv, A et al. *FEBS Lett.*, **137**, 2, 227-230, (1982)
[7] Brandenburg, K and Seydel, U. *Zeit. fur Natur.*, **41c**, 4, 463-467, (1986)

SUMMARY

[1] Eveson, RW et al. *Int. J. Radiat. Biol.*, **76**, 11, 1509-1522, (2000)
[2] Scaiano, JC et al., *J. Am. Chem. Soc.*, **104**, 21, 5673-5679, (1982)

APPENDIX – PROGRAM LISTINGS

Code principally written by Christopher Rodgers

FitMany_Plot.m

```
% load /home/laplace/pgt/PhilODE/FitMany

Tolerance=8;

% Find a point which worked
for idx=1:1000
  if isempty(ERRORS{idx})
    worked_idx=idx;
    break;
  end
end

% Fix any errors!
for idx=1:1000
  if ~isempty(ERRORS{idx})
    disp('Fitting encountered errors! "Fixing"...')
    EXITFLAG{idx}=0;
    RESIDUAL{idx}=RESIDUAL{worked_idx};
    RESNORM{idx}=0;
    X{idx}=X{worked_idx};
  end
end

figure(1)
clf
```

```
EXITFLAG_ARRAY=cell2mat(EXITFLAG);

for idx=1:10
  surf(1:10,(1:10).',repmat(idx,10,10),EXITFLAG_ARRAY(:,:,idx))
  hold on
end

colorbar

title('Exitflag values: 1-->success');
view([-24.5, 6])

%%%%%%%%%%%%%%%%

figure(2)
clf

RESNORM_ARRAY=cell2mat(RESNORM)*100;
RESNORM_ARRAY(EXITFLAG_ARRAY<=0)=NaN;

for idx=1:10
  surf(1:10,(1:10).',repmat(idx,10,10),RESNORM_ARRAY(:,:,idx))
  hold on
end

colorbar

title('Residual norm for converged initial guesses');
```

```
view([-24.5, 6])

%caxis([2.5444 2.5456])
cmintmp=floor(min(RESNORM_ARRAY(:))*1000)/1000;
caxis([cmintmp, cmintmp+0.002])
colorbar

%%%%%%%%%%%%%%%%


figure(3)
clf

X_ARRAY=permute(cell2mat(reshape(X,1,1,10,10,10)),[3 4 5 2 1]);

mask=repmat((EXITFLAG_ARRAY<=0 | RESNORM_ARRAY>Tolerance),[1,1,1,3]);

X_ARRAY(mask)=NaN;

for idx=1:10
  surf(1:10,(1:10).',repmat(idx,10,10),X_ARRAY(:,:,idx,1))
  hold on
end

colorbar

title('X1 for well-converged guesses')
view([-24.5, 6])

%caxis([2.5444 2.5456])
colorbar

XTmp=X_ARRAY(:,:,:,1);
XTmp=XTmp(~isnan(XTmp));

minval=min(XTmp(:));
maxval=max(XTmp(:));
stdval=std(XTmp(:));
meanval=mean(XTmp(:));

xlabel(sprintf('min=%g, max=%g, mean=%g,
stdev=%g',minval,maxval,meanval,stdval));

%%%%%%%%%%%%%%%%


figure(4)
clf

for idx=1:10
  surf(1:10,(1:10).',repmat(idx,10,10),X_ARRAY(:,:,idx,2))
  hold on
end

colorbar

title('X2 for well-converged guesses')
view([-24.5, 6])

%caxis([2.5444 2.5456])
```

```
colorbar

XTmp=X_ARRAY(:,:,:,2);
XTmp=XTmp(~isnan(XTmp));

minval=min(XTmp(:));
maxval=max(XTmp(:));
stdval=std(XTmp(:));
meanval=mean(XTmp(:));

xlabel(sprintf('min=%g, max=%g, mean=%g,
stdev=%g',minval,maxval,meanval,stdval));

%%%%%%%%%%%%%%%


figure(5)
clf

for idx=1:10
  surf(1:10,(1:10).',repmat(idx,10,10),X_ARRAY(:,:,idx,3))
  hold on
end

colorbar

title('X3 for well-converged guesses')
view([-24.5, 6])

%caxis([2.5444 2.5456])
colorbar
```

```
XTmp=X_ARRAY(:,:,:,3);
XTmp=XTmp(~isnan(XTmp));

minval=min(XTmp(:));
maxval=max(XTmp(:));
stdval=std(XTmp(:));
meanval=mean(XTmp(:));

xlabel(sprintf('min=%g, max=%g, mean=%g,
stdev=%g',minval,maxval,meanval,stdval));

%%%%%%%%%%%%%%%


figure(6)
clf

for idx=1:10
  for jdx=1:10
    for kdx=1:10
      if (EXITFLAG{idx,jdx,kdx}>=1) &
((RESNORM{idx,jdx,kdx}*100)<Tolerance)
        plot(datatimes,RESIDUAL{idx,jdx,kdx}+data,'r-');
        hold on;
      end
    end
  end
end
```

```
plot(datatimes,data,'k.');
```

FitMany.m

```
% Use lsqcurvefit to fit to Phil's data

function Fit(filename)

[data]=dlmread([filename '.txt']);
datatimes=data(:,1)*1e9;
data=data(:,2);

% $$$ [data]=dlmread('XTAC.txt');
% $$$ datatimes=data(1:40,1)*1e9;
% $$$ data=data(1:40,5);

% $$$ [X,RESNORM,RESIDUAL,EXITFLAG,OUTPUT]=...
% $$$ lsqcurvefit(@PhilODESolve,[0.001 0.001
0.001],datatimes,data,...
% $$$             [0.0001 0.0001 0.0001],[0.1 0.1 0.1],[],data)

X1vals=logspace(-1,-4,10);
X2vals=logspace(-1,-4,10);
X3vals=logspace(-1,-4,10);

X=cell(prod(size(X1vals)),prod(size(X2vals)),prod(size(X3vals)));
RESNORM=X;
EXITFLAG=X;
OUTPUT=X;
ERRORS=X;
```

```
for X1dx=1:prod(size(X1vals))
  for X2dx=1:prod(size(X2vals))
    for X3dx=1:prod(size(X3vals))
      disp('.')
      try

[X{X1dx,X2dx,X3dx},RESNORM{X1dx,X2dx,X3dx},RESIDUAL{X1dx,X2dx,X3dx},E
XITFLAG{X1dx,X2dx,X3dx},OUTPUT{X1dx,X2dx,X3dx}]=...
          lsqcurvefit(@PhilODESolve,[X1vals(X1dx) X2vals(X2dx)
X3vals(X3dx)],datatimes,data,...
                      [0 0 0],[0.1 0.1 0.1],[],data)
      catch
        ERRORS{X1dx,X2dx,X3dx}=lasterr;
      end
    end
  end
end

% Save the results for later analysis and quit to free up the
licence...
save(['FitMany_' filename])
```

PhilODESolve.m

```
function [YSum,Y]=PhilODESolve(params,timeswanted,ydata)

% ODEFUN, TSPAN, Y0, OPTIONS, PARAMS
[T,Y]=ode45(@PhilODEFun,timeswanted,[1 0],[],params);
```

```
clf
plot(timeswanted,ydata,'b.');
hold on
plot(T,Y);
YSum=sum(Y,2);
plot(T,YSum,'r-');
legend('Expt','[R\cdot P\cdot]','[R\cdot]','Sum');
xlabel('Time / ns')
ylabel('Concentration / units?')
title(num2str(params))
drawnow;
```

PhilODEFun.m

```
% Define radical pair coupled kinetic equations suitable for use with
% e.g. ode45 (Runge-Kutta numerical integration).
%
% params(1): k_recombination
% params(2): k_escape
% params(3): k_F

function [dxy] = PhilODEFun(t,xy,params)

dxy=zeros(2,1);

% dx/dt = -(k_recombination + k_escape) x:
dxy(1)=-(params(1)+params(2))*xy(1);

% dy/dt = k_escape x - k_F y^2:
dxy(2)=params(2)*xy(1) - params(3) * xy(2)^2;
```